Modelling the fluid-structure coupling caused by a far-field underwater explosion

Damien Mavaleix-Marchessoux

INSTITUT POLYTECHNIQUE DE PARIS

NNT : 2020IPPAE012

Thèse de doctorat

Modelling the fluid-structure coupling caused by a far-field underwater explosion

Thèse de doctorat de l'Institut Polytechnique de Paris
préparée à l'École Nationale Supérieure de Techniques Avancées

École doctorale n°574 Mathématiques Hadamard (EDMH)
Spécialité de doctorat : Mathématiques appliquées

Thèse présentée et soutenue à Palaiseau, le 10 décembre 2020, par

Damien Mavaleix-Marchessoux

Composition du Jury :

Marion Darbas Professeur, Université Paris 13 (LAGA)	Présidente
Régis Cottereau Chargé de recherche (HDR), CNRS (LMA)	Rapporteur
Christophe Geuzaine Professeur, Université de Liège, Belgique	Rapporteur
François Alouges Professeur, École Polytechnique (CMAP)	Examinateur
Marc Bonnet Directeur de recherche, CNRS (POEMS)	Directeur de thèse
Stéphanie Chaillat Chargée de recherche (HDR), CNRS (POEMS)	Co-directrice de thèse
Bruno Leblé Ingénieur de recherche, Naval Group Research	Encadrant industriel
Guillaume Barras Ingénieur de recherche, Direction Générale de l'Armement	Invité

Remerciements

Les travaux réalisés durant cette thèse, et présentés dans ce document, ont requis la précieuse contribution d'un grand nombre de collaborateurs, collègues et amis.

Je souhaite tout d'abord remercier les membres de mon jury pour leur participation à ma soutenance, en particulier Madame Marion Darbas pour l'avoir pilotée en qualité de Présidente, Messieurs Régis Cottereau et Christophe Geuzaine pour avoir relu avec attention ce mémoire et fourni des rapports très précis qui soutiennent les contributions de ce travail, et Messieurs François Alouges et Guillaume Barras pour l'attention qu'ils ont portée au sujet.

J'ai eu la chance d'être remarquablement bien encadré. Je remercie Bruno Leblé, mon encadrant industriel, pour avoir initié ce projet, pour le temps qu'il y a consacré, pour les formations qu'il m'a permis de suivre, et pour les visites des lieux de fabrication et d'entretien des navires (peu de personnes ont l'opportunité et le privilège de visiter un sous-marin et une frégate !). Je remercie également Marc Bonnet, mon directeur de thèse, pour son importante contribution à notre travail, en particulier à nos articles ; pour tous ses éclaircissements sur le plan théorique, notamment lors de nos longues discussions à l'ENSTA ou au téléphone ; et pour sa patience pendant nos échanges. Merci encore pour les relectures du mémoire et les nombreuses répétitions pour ma soutenance. Ma profonde gratitude va à ma directrice de thèse, Stéphanie Chaillat. Elle m'a apporté une aide précieuse, notamment sur le plan numérique et par ses très nombreuses relectures attentives de toutes mes contributions, et du mémoire en particulier. De plus, travailler avec elle pendant ces quatre années fut un réel bonheur ! Elle a été l'encadrante parfaite, aussi bien sur le plan humain que scientifique. Elle a su me guider au quotidien de manière bienveillante, m'accompagner dans les moments difficiles, m'encourager continuellement, me féliciter toujours. Pour tout cela, un grand merci !

Le contexte CIFRE de ma thèse m'a permis d'évoluer dans deux mondes assez différents : académique et industriel. Dans le premier, j'ai eu le privilège d'échanger avec différents chercheurs et étudiants. Je remercie tous mes collègues du laboratoire POEMS, et plus largement de l'UMA, pour la bonne ambiance, les discussions au coin café et au Magnan. Je remercie plus spécifiquement ceux qui m'ont aidé durant la thèse en répondant à mes diverses questions : Nicolas, Maurice et Christophe pour leur aide toujours très rapide et efficace concernant les problèmes informatiques ; Axel, Marc, Maryna et Eliane pour leurs explications concernant certains points théoriques précis ; Adrien pour avoir répondu à mes diverses questions et m'avoir fourni gracieusement un programme pour l'interpolation de maillage ; Nicolas pour m'avoir expliqué l'algorithme de la CQM ; Faisal pour nos échanges enrichissants. Merci à Corinne pour tout le temps passé à gérer mes venues à l'ENSTA, en particulier à me trouver un logement, et à Damien, Lucas, Xavier qui m'ont hébergé, souvent en dernière minute, quand je n'avais pas d'autre solution. Je remercie également Robin, mon homologue dirigeable/air, pour nos discussions très instructives concernant

les problèmes d'écoulement potentiel. Un remerciement spécial à mon camarade Émile pour sa gentillesse et ses réponses toujours très précises à mes questions scientifiques et administratives. Un clin d'oeil sympathique à Jean-François pour son sprint mémorable avec ma lourde valise dans l'Aéroport Charles de Gaulle pour m'éviter de manquer ma correspondance ! Enfin, je remercie Alice pour avoir accepté de continuer nos travaux dans le cadre de sa thèse, et je lui souhaite bon courage.

Dans le milieu industriel, j'ai découvert de nombreuses thématiques en lien avec le monde maritime grâce à mes collègues de Naval Research avec qui j'ai eu le plaisir d'échanger au quotidien. Je remercie Cédric, spécialiste de mon sujet de thèse, pour son savoir sur les aspects mathématiques appliquées qui m'a été très précieux ; Quentin et Ladya pour avoir accepté de travailler avec moi sur un cas de validation de nos procédures numériques ; Éric pour son assistance dans l'utilisation du CSE d'Abaqus® et son aide sur des points précis d'implémentation. Merci à tous mes collègues de Sirehna, dont Maïté, Adrien, Luc, Jean-Jacques, Pierre et Pol pour leurs réponses à mes questions ; et Guillaume et Charles-Edouard qui m'ont permis d'améliorer mon niveau d'implémentation en m'expliquant avec patience et pédagogie la bonne méthode et le bon outil pour aborder chaque problème. Merci à Romain et Maud pour leurs conseils sur la vie en entreprise et la gestion de ma carrière ; Thomas, mon manager, qui m'a fait confiance pour gérer mon temps ; Damien, Maud, Yann, Christian, Mikaël, Jean-Michel, Pierre et tous ceux qui ont fait leur possible pour m'aider à trouver un financement pour continuer mes travaux au sein de Naval Group ; Julia et Camille pour leurs conseils pour mes présentations ; Nicolas et Gilles pour nos échanges sur les problématiques de fonctions de Green et rayonnement acoustique ; Laurent, Alexis, mes collègues de l'usine du futur et ceux de Sirehna qui m'ont aidé pour la rétro-construction de CAO à partir d'un maillage ; Stéphane, Nicolas, Killian, Florent et Sébastien pour leur soutien sur les outils informatiques et le cluster. Un remerciement chaleureux aux doctorants, stagiaires, jeunes permanents et intérimaires avec qui j'ai passé de bons moments : Étienne pour nos extravagantes parties de Age Of Empires, très utiles pour décompresser ; Quentin pour avoir soutenu la science avant tout ; Ronan, Julie, Matthieu, Julia et tous les autres ! Enfin, merci à tous les collègues du cross-training pour leur bonne humeur pendant que nous faisions du gainage !

Je veux maintenant remercier ceux qui n'ont pas contribué directement à mon sujet pendant cette thèse, mais qui m'ont guidé tout au long de ma scolarité vers le doctorat : mes professeurs de sciences de collège, de lycée, de prépa, de l'ENSTA et de l'École Polytechnique. Je n'oublie pas mes camarades de l'ENSTA qui, dans un cadre convivial et bienveillant, m'ont donné envie de continuer mes études ; et mes amis d'enfance, toujours fidèles malgré l'éloignement nécessaire pour le besoin de mes études, qui ont accepté et compris l'importance que j'accordais à ces dernières. Je remercie ma famille, notamment mes parents, mes grands-parents, mon frère et Lulu pour m'avoir soutenu tout au long de mon éducation et de mon instruction, et pour m'avoir toujours exprimé sans réserve leur fierté.

Pour conclure ces remerciements, je veux exprimer ma profonde gratitude et mon admiration pour ma camarade, collègue, amie, compagne Léa. Je la remercie pour ses enseignements sur la maîtrise de Git et du développement logiciel, et je lui suis infiniment reconnaissant pour son soutien au quotidien dans cette longue aventure de la thèse, d'abord à Paris puis à Nantes. Tu as été exactement ce dont j'avais besoin : toi.

Résumé étendu

Contexte

Les sous-marins militaires doivent résister aux sollicitations induites par une explosion sous-marine. La simulation numérique des effets d'une explosion sous-marine lointaine sur une structure donnée est d'une importance capitale, compte tenu du coût très élevé des campagnes expérimentales. Une explosion sous-marine lointaine est un événement complexe qui a deux effets distincts (voir Figure 1.1, Snay, 1956) : elle libère une onde de choc, puis crée une bulle de gaz oscillante qui pousse une grande quantité d'eau plus lentement.

Les deux phénomènes ont des caractéristiques et des échelles de temps assez différentes (Cole, 1948). L'onde de choc est libérée au moment de la détonation, et son échelle de temps typique est la milliseconde. Ensuite, une bulle de gaz brûlés, qui résulte de la réaction chimique de l'explosion, oscille sous l'eau avec une pseudo-période de l'ordre d'une demi-seconde, à la recherche d'un équilibre entre ses pressions interne et externe.

Dans ce travail, nous supposons que l'explosion est suffisamment éloignée pour (i) que la présence du navire affecte peu l'explosion, et (ii) permettre une séparation temporelle des deux phénomènes, tels que perçus par le navire. Notre objectif est de développer, dans ces conditions, une méthodologie de simulation pour le problème d'interaction fluide-structure prenant en compte les deux phénomènes. En plus de la phase de conception théorique, nous recherchons une implémentation numérique efficace de la procédure, dans le cadre du calcul haute performance, puis la validation de celle-ci sur des cas simples, et enfin l'application à des cas industriels réalistes.

Chapitre 1 : L'onde de choc et la bulle de gaz oscillante

La première partie de cette étude commence par un aperçu global du problème physique, dans la Section 1.1. L'objectif est double : (i) se familiariser avec les phénomènes de l'onde de choc et de la bulle, en s'appuyant notamment sur des études expérimentales disponibles dans la littérature, et (ii) poser le cadre de notre analyse, en précisant notamment les hypothèses. Certaines de ces hypothèses (comme par exemple celle d'écoulement potentiel) sont simplement énoncées dans le texte principal, et justifiées dans l'Annexe A.

L'onde de choc est une sollicitation rapide, qui vient impacter localement la structure dans la région qui fait face à l'explosion, provoquant des déformations élastiques, voire plastiques, de la coque du sous-marin. Le passage de l'onde autour du navire dure quelques millisecondes, et, sur cette durée, on observe de petits déplacements et de petites déformations. Le cas d'une explosion proche (étudié par exemple dans Barras 2012), dont l'onde de choc peut engendrer de grandes déformations plastiques, voire la rupture de la coque, n'est pas considéré.

La Section 1.2 se concentre sur l'onde de choc et ses théories de propagation (en l'absence du sous-marin). Nous y expliquons pour quelles raisons et dans quelle mesure la théorie de l'acoustique linéaire est pertinente pour modéliser la propagation de l'onde de choc suffisamment loin de l'explosion. Une étude complémentaire, introduisant notamment la théorie de propagation des ondes de choc de Kirkwood-Bethe (Brinkley and Kirkwood, 1947a,b) est proposée en Annexe B.

Consécutivement à l'onde de choc, des gaz chauds, libérés par la réaction chimique de l'explosion (principalement du CO_2), forment une bulle de gaz. Initialement, la pression interne de la bulle est plus élevée que la pression hydrostatique qui appuie sur sa surface ; la bulle gonfle. Après un certain temps, la pression interne est égale à la pression externe, et la surface de la bulle, qui a acquis une vitesse dans le processus d'expansion, entame un mouvement de décélération. Lorsque la surface a une vitesse nulle, la pression interne est inférieure à la pression hydrostatique, et on observe alors le processus inverse : la bulle se contracte. Cette oscillation quasi-périodique autour d'un équilibre des pressions interne et externe, dont la pseudo-période est de l'ordre d'une demi-seconde, s'accompagne d'une migration de la bulle vers la surface (voir Figure 1.2, Brett et al., 2003). En oscillant, la bulle de gaz provoque de grands déplacements d'eau, qui engendrent un mouvement d'ensemble du sous-marin, de type flexion. Cette déformation peut s'avérer très dommageable si la pseudo-période de la bulle est proche de la première période propre de flexion de la structure (Zong, 2005; Zhang and Yao, 2008).

La Section 1.3 s'intéresse à la modélisation de la dynamique de bulle (en l'absence du sous-marin). De nombreux modèles de bulle sont disponibles dans la littérature (Geers and Hunter, 2002; Wang and Khoo, 2004; Barras et al., 2012). Pour donner une idée du comportement de la bulle, nous présentons un modèle simple : une bulle sphérique qui oscille dans un fluide parfait, où l'écoulement est supposé incompressible et potentiel, en migrant vers une surface supposée infiniment éloignée (Leblond, 2007). Nous décidons de ne pas développer de modèle de bulle, et choisissons de traiter le problème dans le cadre simplifié d'écoulement potentiel incompressible.

Le chapitre se termine par une discussion sur le raccordement des deux phénomènes physiques. En s'appuyant sur une méthode multi-échelles, nous justifions le traitement séquentiel des deux perturbations dans le cas d'explosions lointaines d'une part, et montrons, dans (1.43), que l'influence de l'onde de choc sur la phase de bulle oscillante se manifeste par le terme d'*after flow* introduit dans (1.12).

Chapitre 2 : Transformée en $\mathcal{Z}$ et approximations hautes fréquences pour les problèmes 3D transitoires rapides

Le Chapitre 2 se concentre sur la résolution de problèmes d'interaction fluide-structure non couplés, qui constitue une première étape avant de s'intéresser au couplage fluide-structure pour la phase de l'onde de choc.

Le contexte industriel, et en particulier l'application visée (interaction fluide-structure entre un sous-marin et une explosion sous-marine), nous conduit à introduire la théorie des équations intégrales (Lenoir, 2016; Sayas, 2016; Nédélec, 2001) pour traiter le problème fluide. Nous rappelons donc, dans la Section 2.2, les principales étapes conduisant à l'obtention de l'équation intégrale (2.14) qui exprime la valeur du potentiel dans le fluide par une intégrale (sur Γ) de produits de convolutions temporelles avec les solutions fondamentales (fonctions de Green) de l'équation des ondes.

La Section 2.3 est dédiée à la reformulation de l'équation intégrale espace-temps en

un ensemble d'équations intégrales posées dans le domaine des fréquences complexes de Laplace. Pour ce faire, nous proposons une dérivation simple combinant la méthode de quadrature de convolution (CQM) (Lubich, 1988a,b) et la transformée en $\mathcal{Z}$ (Sayas, 2016). D'autres approches sont disponibles dans la littérature (Betcke et al., 2017). La procédure numérique obtenue, que nous nommons $\mathcal{Z}$-BEM, est résumée dans la Section 2.3.4 : pour un intervalle de temps discret $\{0, \Delta t, \ldots, T = M\Delta t\}$, les valeurs discrètes de l'inconnue ϕ sont obtenues par transformée en $\mathcal{Z}$ inverse numérique de sa transformée en $\mathcal{Z}$. La partie centrale de la procédure (qui concentre la quasi-totalité du temps de calcul) est la résolution de $M+1$ équations intégrales à fréquences complexes qui gouvernent la transformée en $\mathcal{Z}$ de ϕ.

Après une rapide présentation, dans la Section 2.4, de la méthode des éléments de frontière (BEM) (Banerjee, 1994; Bonnet, 1999) et de sa version accélérée par méthode multipole rapide (Chaillat, 2008; Darve, 2000; Nishimura, 2002), la Section 2.5 présente notre démarche d'amélioration de la $\mathcal{Z}$-BEM pour traiter efficacement des problèmes transitoires rapides. L'objectif est de réduire drastiquement les coûts de calcul en réduisant le nombre de problèmes BEM à résoudre (initialement $M+1$). Pour ce faire, nous recourons à une approximation haute fréquence pour traiter les problèmes BEM haute fréquence issus de la CQM. Une de nos principales contributions est la construction d'une approximation haute fréquence empirique pour les problèmes de diffraction d'ondes par un obstacle immobile. La procédure obtenue, nommée *HFA-enhanced $\mathcal{Z}$-BEM*, possède une complexité avantageuse en $O(1)$ par rapport à la discrétisation temporelle. La méthode est validée dans la Section 2.6, d'abord sur le cas de rayonnement d'une onde par une sphère pulsante en eau, puis sur le problème de diffraction de l'onde de choc d'une explosion sous-marine par un cylindre infini. Enfin, la Section 2.7 démontre la performance de la procédure sur un cas d'application représentatif de l'objectif industriel : un sous-marin immergé soumis à une explosion sous-marine lointaine.

Chapitre 3 : Interaction fluide-structure pour l'onde de choc

L'objectif du Chapitre 3 est de résoudre le problème d'interaction fluide-structure (FSI) couplé pour la phase de l'onde de choc. Dans la Section 3.1, nous introduisons les procédures de couplage classiques itératives et monolithiques. Nous présentons ensuite les contraintes spécifiques liées à notre sujet, et expliquons en quoi elles orientent notre choix vers une procédure itérative FEM/BEM qui ne peut pas se faire pas-de-temps par pas-de-temps. Ainsi, nous envisageons une procédure itérative FEM/BEM qui alterne des résolutions FEM-structure et $\mathcal{Z}$-BEM-fluide sur l'intervalle de temps complet $[0, T]$. Inspirés par les méthodes de décomposition de domaines (Dolean et al., 2015; Toselli and Widlund, 2006) et par la méthode *LArge Time INcrement* (LATIN) (Néron, 2004), nous construisons un procédé itératif piloté par des conditions de transmission de type Robin (3.13). Malheureusement, des contraintes pratiques liées au contexte industriel de la thèse CIFRE nous obligent à utiliser le code Abaqus® pour la partie FEM-structure, qui ne permet pas de considérer des conditions de transmission de type Robin. Par conséquent, nous ne pouvons pas implémenter notre procédure itérative $\mathcal{Z}$-BEM/FEM qui alterne des résolutions sur l'intervalle de temps complet.

Étant donné les contraintes pratiques rencontrées, nous adoptons, Section 3.3, une procédure de remplacement de type monolithique FEM/FEM pour la partie couplée du problème (pression rayonnée dans le fluide), tout en conservant la $\mathcal{Z}$-BEM pour calculer la composante réfléchie de la pression (voir Figure 2.8). La procédure résultante, nommée *Hybrid $\mathcal{Z}$-BEM/FEM/FEM*, fournit des résultats satisfaisants au regard de l'objectif industriel,

comme démontré dans la Section 3.5 sur le cas d'un cylindre infini déformable soumis à une explosion sous-marine lointaine. En particulier, nous comparons les résultats obtenus avec notre méthode à ceux obtenus avec une procédure semi-analytique (Rakotomalala et al., 2021; Leblond et al., 2009; Sigrist and Leblond, 2008) et une méthodologie de couplage entièrement FEM/FEM (Khoun, 2021) développée dans Code_Aster Open Source (2020).

Chapitre 4 : Interaction fluide-structure pour la bulle de gaz

Le but de ce quatrième chapitre est de traiter l'interaction fluide-structure pour la phase de pulsation de bulle. Nous choisissons le modèle simplifié de Hicks (Hicks, 1970; Leblond, 2007) pour décrire la dynamique de bulle, qui fournit le champ (potentiel des vitesses) ambiant ϕ^{amb} constituant la donnée d'entrée de notre procédure de couplage.

Nous décidons de traiter le problème FSI avec une procédure classique de couplage FEM/BEM pas-de-temps par pas-de-temps (voir Figure 4.1), présentée dans la Section 4.2. Ensuite, nous expliquons comment accélérer les résolutions BEM côté fluide dans la Section 4.3, notamment en réutilisant les opérateurs BEM à chaque pas-de-temps. L'indépendance vis-à-vis du temps de ces opérateurs n'est pas vraie dans le cas général, mais s'avère être une hypothèse raisonnable dans notre contexte particulier (domaine fluide infini isotrope, petites déformations du navire,...). La méthode multipole rapide n'est alors pas la plus efficace pour accélérer les résolutions BEM, car elle ne stocke pas les opérateurs BEM, et donc ne permet pas de les réutiliser à chaque pas-de-temps. Nous choisissons plutôt la technique des matrices hiérarchiques ($\mathcal{H}$-matrices) (Hackbusch, 1999; Chaillat et al., 2017b), qui fournit une forme compressée des opérateurs BEM, pour accélérer les résolutions BEM.

Notre méthodologie de résolution du problème fluide-structure, résumée dans la Section 4.4, est validée dans la Section 4.5 sur le cas simple d'une sphère rigide mobile immergée dans un écoulement potentiel uniforme dont l'amplitude dépend du temps. En particulier, nous étudions comment diminuer le nombre de sous-cycles par incrément de temps (voir Figure 4.1) en construisant une bonne approximation de la solution à l'incrément courant à partir des solutions des incréments précédents (voir Figure 4.14).

La Section 4.6 traite le cas d'une structure raidie (type coque de sous-marin) soumise aux sollicitations induites par une bulle de gaz oscillante (voir Figure 4.15). Les résultats issus de la simulation numérique sont cohérents vis-à-vis des comportements classiquement observés : la structure se déforme principalement selon son premier mode de flexion. Une phase de validation de la procédure par comparaison avec les résultats issus de campagnes expérimentales a été initiée pendant cette thèse, mais n'est pas présentée dans ce document.

Chapitre 5 : Application industrielle : coque raidie soumise à une explosion sous-marine

Le dernier chapitre présente le traitement d'un cas d'étude d'ingénierie de l'application principale de nos travaux : une coque raidie soumise à une explosion sous-marine lointaine. La Section 5.1 rappelle brièvement toutes les étapes de la procédure globale (pour les deux phases : onde de choc et bulle de gaz), qui sont illustrées sur la Figure 5.4. Nous y exposons également les modèles numériques, et proposons une méthode simple de jonction entre les deux phases, illustrée Figure 5.2.

Les résultats numériques sont présentés dans la Section 5.2. Nous sommes très satisfaits du calcul préliminaire de la pression réfléchie par la structure immobile qui fait face à

l'onde de choc : le front d'onde est bien marqué et le champ total respecte la causalité (voir Figures 5.6 à 5.8). Nous sommes également satisfaits du calcul pour la structure déformable (voir Figures 5.10 à 5.13).

L'état final de la structure après cette phase d'onde de choc sert ensuite d'état initial pour la phase de pulsation de bulle. Pour faciliter la transition entre les deux simulations, nous avons essayé d'introduire un léger amortissement numérique de type Rayleigh pour réduire l'agitation de la structure à la fin de la procédure de l'onde de choc. Cependant, nous n'avons pas encore réussi à résoudre le problème d'interaction fluide-structure pour la phase de bulle oscillante en prenant en compte l'état de la structure à la fin de l'interaction avec l'onde de choc. La fin du chapitre explique les difficultés numériques rencontrées et fournit des pistes de recherche pour les résoudre.

Conclusion et perspectives

Conclusion. Ce mémoire synthétise le traitement numérique (modélisation et simulation) d'un problème industriel concret : l'interaction fluide-structure entre une explosion sous-marine lointaine et un sous-marin. Nous avons tout d'abord étudié les phénomènes qui entrent en jeu : (i) l'onde de choc, perturbation rapide dont la propagation est modélisée dans le cadre de l'acoustique linéaire, et (ii) la bulle de gaz oscillante, perturbation plus lente étudiée sous l'hypothèse d'un fluide potentiel incompressible. Ensuite, nous avons développé une procédure éléments de frontière accélérée, basée sur une combinaison de la méthode de quadrature de convolution avec une approximation haute fréquence empirique originale. Plus largement, cette procédure permet de simuler efficacement des problèmes transitoires rapides 3D de propagation d'ondes en milieu non-borné, et offre une complexité très favorable : $O(1)$ par rapport à la discrétisation temporelle et $O(N \log N)$ par rapport à la discrétisation spatiale. Enfin, nous avons ensuite mis en place des stratégies performantes de couplage éléments finis/éléments de frontière (FEM/BEM) pour le traitement séparé de la phase d'interaction fluide-structure de l'onde de choc puis celle de la bulle de gaz. La procédure globale, validée sur des problèmes académiques, fournit des résultats très prometteurs sur des cas industriels réalistes.

Perspectives. Cette première étude sur la conception et l'implémentation d'une méthodologie numérique pour résoudre le problème d'interaction fluide-structure considéré a ouvert de nombreuses perspectives. À court terme, nous proposons d'améliorer la procédure pour la phase de bulle oscillante, notamment au niveau numérique pour réduire les temps de calcul. À moyen terme, nous voulons continuer notre travail sur la procédure de couplage $\mathcal{Z}$-BEM/FEM introduite pour traiter l'interaction fluide-structure pour la phase d'onde de choc, afin de résoudre le problème complet sans recourir à un maillage volumique du fluide. Nous avons aussi commencé une phase de validation des outils développés par comparaison avec des campagnes expérimentales. À long terme, nous envisageons d'améliorer le raccordement entre les deux phases du problème (onde de choc et bulle de gaz) en proposant un traitement plus unifié.

D'autres perspectives portent sur l'amélioration des capacités numériques des codes développés et utilisés, ainsi que leur généralisation, pour pouvoir traiter toujours plus rapidement et précisément les diverses problématiques industrielles d'interaction fluide-structure rencontrées dans le monde maritime.

Annexes

Le mémoire se termine avec quatre annexes qui donnent des détails sur :

- l'analyse dimensionnelle des problèmes de l'onde de choc et de la bulle de gaz,
- une analyse complémentaire de l'onde de choc,
- des preuves et calculs de résultats énoncés dans le corps principal du document,
- des tables qui fournissent les informations et paramètres numériques de l'étude comparative effectuée dans la Section 3.5.

Principales publications associées à ce travail

Articles. Le travail présenté dans cette thèse a fait l'objet d'une publication dans une revue avec comité de lecture :

- D. Mavaleix-Marchessoux, M. Bonnet, S. Chaillat, B. Leblé. A fast boundary element method using the Z-transform and high-frequency approximations for large-scale three-dimensional transient wave problems. *Int J Numer Methods Eng.* 2020; 121(21): 4734 – 4767. https://doi.org/10.1002/nme.6488

et deux publications sont actuellement en préparation : (i) sur l'interaction fluide-structure pour la phase d'onde de choc, correspondant au contenu du Chapitre 3, et (ii) sur l'interaction fluide-structure pour la phase de bulle oscillante, correspondant au contenu du Chapitre 4.

Conférences. Ce travail a été présenté lors d'une conférence internationale et deux conférences nationales.

Contents

List of Figures

List of Tables

Notations

In the entire document, the following notations are used:

Definitions and relations

- $:=$: definition of a new mathematical or physical quantity;
- $\equiv$: attribution of a symbol to a known physical quantity or mathematical object;
- $\simeq$ or $\approx$: $a \simeq b$ means a is approximately equal to b;
- $\sim$: $a \sim 10^6$ means the order of magnitude of a is 10^6.

Operations

- Δ : spatial Laplacian;
- H : Heaviside step function;
- Let $\mathbf{n}$ denote the outward normal to a certain closed surface $S \subset \mathbb{R}^3$ and $f : \mathbb{R}^3 \to \mathbb{R}$, then $\dfrac{\partial f}{\partial n} \equiv \nabla f \cdot \mathbf{n}$.

Sets

- $\mathbb{N}$: set of non-negative integers;
- $\mathbb{R}$: set of real numbers; $\mathbb{R}^+ := \{x \in \mathbb{R} | x \geq 0\}$;
- For $\Omega \subset \mathbb{R}^3$,

$$
\begin{aligned}
L^2(\Omega) &:= \left\{ f : \Omega \to \mathbb{R} \,\middle/\, \int_\Omega f^2 < \infty \right\}, \\
H^1(\Omega) &:= \left\{ f : \Omega \to \mathbb{R} \,\middle/\, f \in L^2(\Omega), \nabla f \in \left(L^2(\Omega)\right)^3 \right\}, \\
H_0^1(\Omega) &:= \left\{ f : \Omega \to \mathbb{R} \,\middle/\, f \in H^1(\Omega),\ f = 0 \text{ on } \partial\Omega \right\}, \\
H^1(\Delta;\Omega) &:= \left\{ f : \Omega \to \mathbb{R} \,\middle/\, f \in H^1(\Omega),\ \Delta f \in L^2(\Omega) \right\}.
\end{aligned}
$$

Generic notations

- $\mathbf{x}$: position vector;
- t : time;
- $\mathbf{g}$: gravity;
- $p(M)$: pressure at point M in the fluid or at the fluid-structure interface;
- $\mathbf{v}(M)$: fluid particle velocity at point M;
- $u(M)$: projection of $\mathbf{v}(M)$ on a unit vector $\mathbf{n}$ (e.g., normal vector to a surface);

- $\phi(M)$: velocity potential. If the flow is potential then $\mathbf{v}(M) = +\nabla\phi(M)$;
- $e(M)$: specific internal energy per unit mass at point M;
- σ : Cauchy stress tensor;
- ε : strain tensor.

Specific notations relative to underwater explosion analyses

Consider an underwater explosion occurring far from a submarine. The effects on the structure depend on several parameters, depicted in Figure 1.

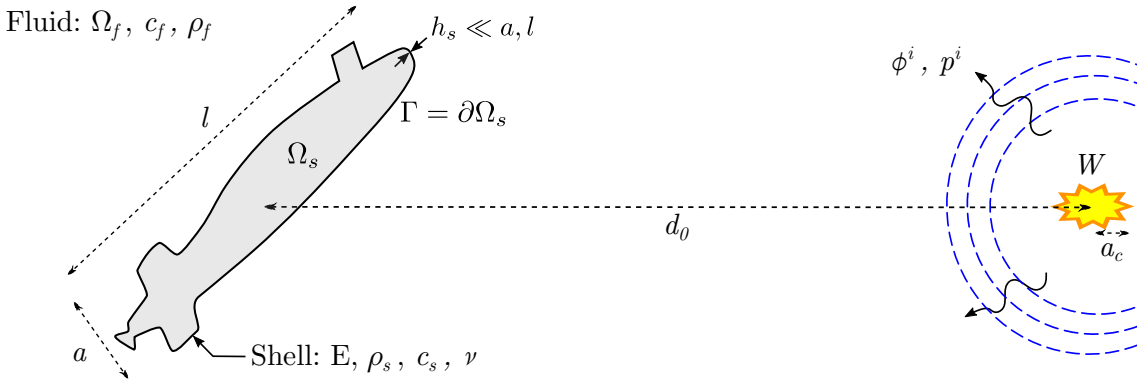

Figure 1: Shell submerged in water, subjected to a remote underwater explosion: notations.

- d_s : shortest distance between the shell and the explosion, termed *standoff distance*. The distance to the structure centre d_0 is rather used in this work (e.g., for a cylinder of radius a, $d_s = d_0 - a$);
- W : charge mass;
- a_c : charge radius;
- ξ_{exp} : positive water depth of the explosion;
- a, l : characteristic lengths of the structure (submarine);
- h_s : thickness of the structure (submarine);
- E : Young's modulus of the structure (steel);
- ν : Poisson's ratio of the structure (steel);
- ρ_s : volumetric mass density of the structure (steel);
- c_s : sound speed in the solid (steel);
- c_f or c : sound speed in the fluid (water);
- ρ_f or ρ : volumetric mass density of the fluid (water);
- $p_m(r)$: jump magnitude of the shock wave at distance r from the explosion;
- $\tau(r)$: time characterising the temporal decline of the pressure at distance r from the explosion;
- t_r : retarded time, it expresses causality for the shock wave;
- $f_{\mathcal{W}}$: denotes the part of a total quantity f which is due to the shock wave (e.g., $\rho_{\mathcal{W}}$, $p_{\mathcal{W}}$, ...);
- $f_{\mathcal{B}}$: denotes the part of a total quantity f which is due to the oscillating bubble (e.g., $\rho_{\mathcal{B}}$, $p_{\mathcal{B}}$, ...);

- ξ_M : positive water depth at point M;
- p_h : hydrostatic pressure;
- P_0 : atmospheric pressure;
- $\xi_{\text{atm}} \equiv P_0/\rho_f\, g$: contribution of the atmospheric pressure P_0 to the hydrostatic pressure;
- T : quasi-period of the bubble oscillation;
- $R_{\max}$: maximum radius of the oscillating gas bubble.

Numerical parameters

- N : number of spatial degrees of freedom;
- M : number of time steps;
- Δt : time step;
- T : simulation duration.

Introduction

CONSIDER a smart trout, standing still in a narrow river of the Limousin[1] (see Figure 2). At an initial time instant $t = 0$, the fishing float of a clumsy fisherman enters the water, near the fish. Consequently, a perturbation starts propagating in the fluid. After a while, it reaches the fish and makes him vibrate. Aware of this perturbation, the prudent trout inevitably flees. The coveted river fish is gone forever.

The problem studied in this dissertation is somehow similar to the scene depicted above. The fish is replaced by a submarine or a ship (a submarine is used in the following), the fishing float by an underwater explosion, bursting at $t = 0$, and the river by a sea or an ocean. Resulting from the explosion, some perturbations propagate through the water and reach the hull of the submarine after a certain time, notably depending on the sound speed c_f in the acoustic medium. Then, these perturbations affect the shell in a way depending on the kind of the explosive material, the charge weight of the explosion, the water depth, and the distance that separates the submarine and the initial bursting point.

The purpose of this PhD work is to model the fluid-structure coupling between a structure (submarine) and the water, caused by an underwater explosion. More precisely, it intends to (i) provide a comprehensive theoretical modelling of the problem, (ii) design and implement an efficient numerical procedure that simulates the effects of a remote underwater explosion on a submarine in deep water. It was supported by the French institute ANRT and the industrial company Naval Group, and is part of a collaboration between the latter and the research laboratory POEMS (ENSTA Paris – INRIA – CNRS).

What is a far-field underwater explosion? A remote (or far-field) underwater explosion is a complex event that has two distinct effects: it sends a shock wave, then creates an oscillating gas bubble that sets water in slower motion. The two phenomena have quite different characteristics and time scales. The shock wave, initially sent by the blast, is the result of a sudden release of energy, which propagates as a *wave* in the fluid, namely through a transfer of energy, but no transport of matter. The typical time scales involved are of some milliseconds. Consecutively, a bubble of burnt gases results from the chemical reaction of the explosion. As it oscillates under water, seeking a balance between its internal and external pressures, it generates an ebb and flow of water, with a pseudo-period of typically half a second.

In this work, only *far-field underwater explosions* are considered. It consists in two hypotheses: (i) the presence of the submarine only marginally affects the explosion, and (ii) there is a temporal separation of the two phenomena (shock wave and oscillating bubble), as experienced by the ship. Our overall goal is to develop, under these conditions, a computational solution methodology for the fluid-structure interaction (FSI) problem, taking into account both phenomena.

[1] One of the most beautiful regions of France, located in the centre of the country.

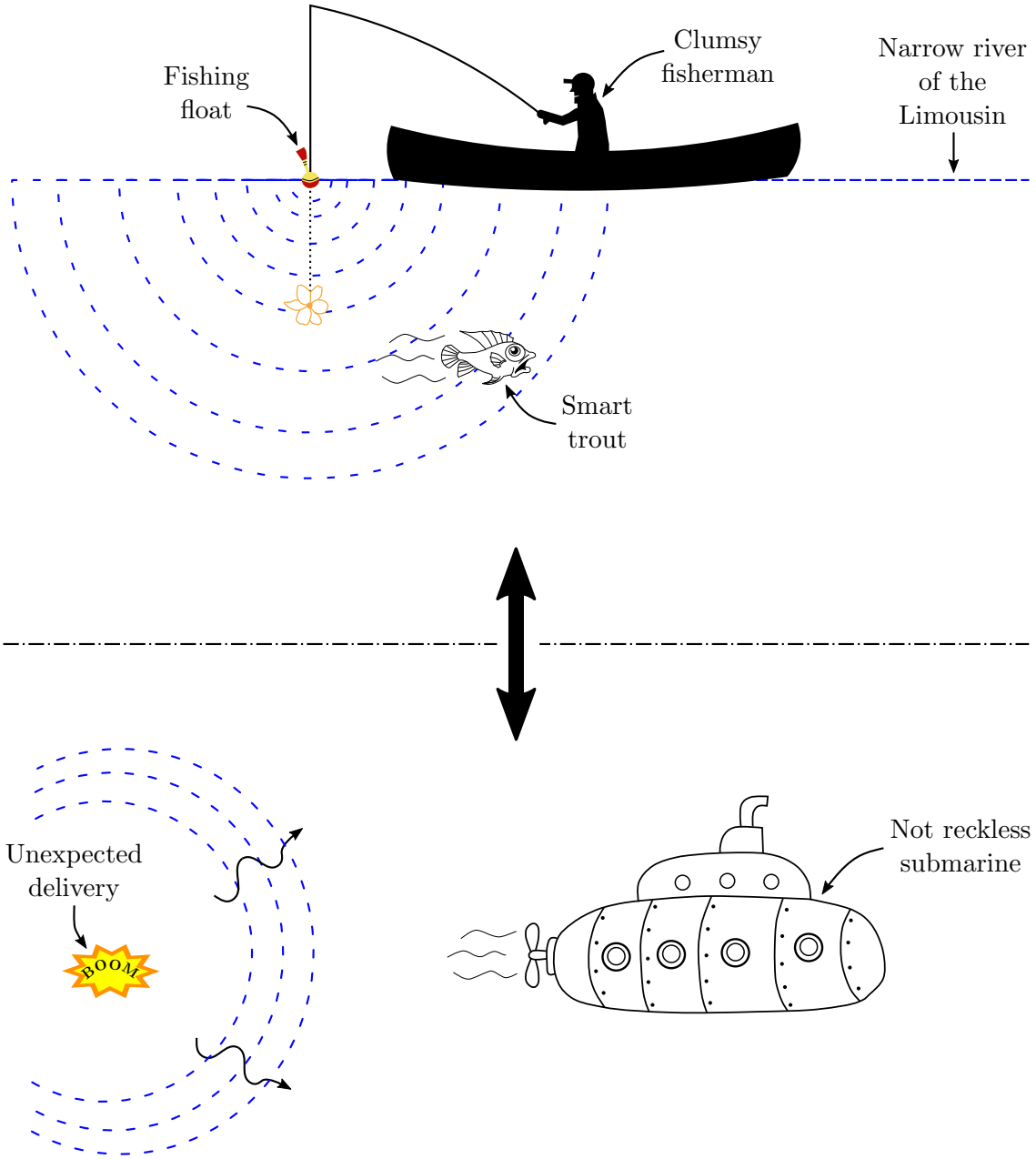

Figure 2: Upper part: a clumsy fisherman fails to catch a trout. Lower part: an unexpected delivery bursts before reaching its destination.

Why simulate the effects of a far-field underwater explosion? Submarines must withstand the effects of rapid dynamic loads induced by underwater explosions. This lends great importance on the numerical simulation of the effects of a remote underwater blast on a given structure, in view of the very high cost of full-scale experimental testing. Of course, it cannot be a substitute to experimental investigations, but allows to predict, with a certain degree of accuracy, the results of a given experiment. Thus, once a numerical method has been validated through comparisons with experimental data, the simulation can be used as an alternative to numerous, costly and difficult experimental tests, to validate some specific criteria of resistance. Therefore, for Naval Group, one of the French industrial group specialised in naval defence, that notably designs warships and submarines, the topic

has been and will remain widely studied in its Research and Development departments.

How do we address the problem? The first step of the story is to well understand the physical phenomena underlying the effects of an underwater explosion, because only a sharp comprehension of the physical problem permits the choice of the most appropriate modelling. This is the task of Chapter 1, in which both the shock wave and the oscillating bubble are under scrutiny, in a mostly bibliographic study. The shock wave propagation is found to be governed by the wave equation, within the framework of linear acoustics, whereas the perturbation induced by the oscillating bubble is dealt with in the context of incompressible potential flow, with the Laplace equation. The end of the chapter is dedicated to the study of the junction between the two phenomena and their mutually exclusive modelling.

Building on the knowledge gathered in this first chapter, we then address the shock wave phenomenon. Chapter 2 lays down the foundation for a first approach, termed FEM/BEM coupling, in which the fluid part is treated in the framework of the *Boundary Element Method (BEM)*, whereas the structure part is dealt with using the *Finite Element Method (FEM)*. We focus on the fluid part, and propose a numerical method to efficiently deal with 3D rapid transient acoustic problems set in large exterior domains. Using the $\mathcal{Z}$-transform and the convolution quadrature method (CQM), we present a straightforward way to reframe the problem to the solving of a large amount (the number of time steps, M) of frequency-domain BEMs. Then, taking advantage of a well-designed high-frequency approximation (HFA), we drastically reduce the number of frequency-domain BEMs to be solved, with little loss of accuracy. The complexity of the resulting numerical procedure turns out to be $O(1)$ in regards to the time discretisation and $O(N \log N)$ for the spatial discretisation (N being the number of spatial degrees of freedom), the latter being prescribed by the complexity of the used fast BEM solver, based on the Fast Multipole Method (FMM) in our case. Examples of applications are proposed to illustrate the efficiency of the procedure in the case of fluid-structure interaction: the radiation of an acoustic wave into a fluid by a deformable structure with prescribed velocity, and the scattering of an abrupt wave by simple then realistic geometries.

Chapter 3 deals with the FSI coupling for the shock wave part. First, inspired by domain decomposition methods, we propose a FEM/BEM coupling using the procedure developed in Chapter 2, and explain why it is not perfectly appropriate given the industrial constraints tied to our problem. Then, taking advantage of the fluid decomposition into a radiated (radiation problems) and a reflected (scattering problems) components, we examine the characteristics of the radiated pressure, which concentrates the coupled part of the FSI problem. As a result of this analysis, we adapt the procedure in such a way that the coupled part of the FSI problem is now solved with a FEM/FEM coupling. Far from being the ideal solution, the obtained computational method nonetheless efficiently tackles the difficult FSI problem, as it is illustrated in the reference case of a long cylinder subjected to an underwater explosion. In particular, a comparison to other numerical methods validates our procedure, with very promising results.

Once the shock wave phenomenon considered, Chapter 4 focuses on the oscillating bubble phase. We first stress the time-(in)dependence aspects of the fluid problem, in contrast to the acoustic case (shock wave phase). Then, we introduce the hierarchical matrices ($\mathcal{H}$-matrices), an acceleration technique for the BEM that is efficient when dealing with multiple right hand-sides. Thereafter, we present the step-by-step FEM/BEM coupling procedure we choose to solve the FSI problem. We validate the method on the simple problem of a sphere in a uniform time-dependent flow, before solving the FSI problem

of a gas bubble impacting a stiffened submarine hull. We pay particular attention to the numerical techniques enabling a faster convergence of the iterative FEM/BEM coupling procedure, such as relaxation techniques and the use of well-chosen initial guesses.

This work concludes with the treatment of an industrial case: a submarine stiffened hull subjected to a remote underwater explosion. The purpose of this Chapter 5 is to show the efficiency of the computational method, when gathering all the results obtained throughout this work. The engineering study conducted represents a prime example of the target applications of this work.

The conclusion of this PhD work is divided in four parts. Firstly, we summarise all of the content presented in this dissertation. Secondly, we stress our contributions, notably by identifying our start and end points, both in terms of knowledge and software development. Thirdly, we discuss the consequences of some choices made in the industrial context. Finally, we give some prospects for future studies (some being already investigated).

Chapter 1

The shock wave and oscillating bubble phenomena

This chapter is dedicated to the presentation of the characteristics of the two phenomena resulting from an underwater explosion (UNDEX): the shock wave and the oscillating bubble (see the Introduction). The goal is to well understand those phenomena, to infer appropriate hypotheses and identify well suited models, hence setting the governing equations of each event.

This chapter is composed of four sections. Section 1.1 is dedicated to an overview of the characteristics of an underwater explosion. The shock wave phenomenon and the oscillating gas bubble are introduced, and an energetic study shows that they both have to be taken into account for fluid-structure interaction problems (i.e., one is *a priori* not marginal compared to the other). Thereafter, a more thorough analysis is conducted in Section 1.2 for the shock wave, and in Section 1.3 for the oscillating gas bubble. Finally, we explain how to perform the junction between the two events in Section 1.4.

1.1 Global overview

As stated in the Introduction, only far-field underwater explosions, also termed remote underwater explosions, are considered. For instance, an explosion of $W = 100$ kg of TNT, located at a distance $d_s = 100$ m from a submerged ship, at a water depth $\xi_{\text{exp}} = 100$ m, satisfies the two conditions to be a remote underwater explosion:

- the effects of the shock wave can be temporally separated from those of the oscillating bubble, as experienced by the ship;
- the oscillating bubble behaviour is only marginally affected by the presence of the structure.

In the following, this set of explosion parameters ($W = 100$ kg, $d_s = 100$ m, $\xi_{\text{exp}} = 100$ m) is used as a reference to estimate the magnitude of the physical parameters characterising the shock wave and the bubble phenomena.

The accurate understanding of the consequences of an UNDEX constitutes an essential step prior to the study of the related fluid-structure couplings. Hence, in the following, we examine the effects of an UNDEX at a point P in the fluid, in the absence of any obstacle.

1.1.1 Brief presentation of the shock wave

An explosion is a sudden release of a high amount of energy, typically due to an exothermic chemical reaction. Right after the explosion, the energy released creates a *wave*, called *shock wave* or primary wave, that starts propagating in the fluid medium Ω_f, approximately (in a sense specified in Section 1.2) governed by the linear *wave equation* (Cole, 1948), but at a speed v initially higher than the sound speed in the fluid. Over a very short distance of about 20 times the charge radius a_c (typically, $a_c \simeq 10$ cm), the shock wave speed declines and reaches the sound speed $c \equiv c_f \simeq 1500$ m/s in water. As the shock wave speed v converges to the sound speed c, the energy carried by the wave, corresponding to approximately half the total energy released by the explosion, reduces before reaching a quasi-stable value (Arons and Yennie, 1948). When the shock interacts with a structure, during a typical duration of 10^{-2} s, the induced deformations are mostly localised on the part of the shell that faces the explosion.

To study the propagation of the blast, the simplest approximation is to state that the supersonic shock wave turns into a common acoustic wave that propagates in the fluid, governed by the *wave equation*. The study of the supersonic shock wave near the explosion is not performed in this work, since we focus on far-field explosions. The reader may refer to (Barras, 2012) for more details about near-field underwater explosions. Even in the case of a far-field explosion, the phenomenon is not exactly depicted by an ideal wave, in the sense that some of the energy of the shock wave is dissipated during the propagation. This matter is discussed in Section 1.2.2.

The characteristics of the shock wave have been studied in the middle of the past century, notably in (Cole, 1948; Arons and Yennie, 1948; Brinkley and Kirkwood, 1947a,b). Experimental results suggest that the expression of the incident pressure associated to the primary wave is characterised by a sudden jump, within less than 10^{-7} s, to a magnitude p_m, of typically 1 to 10 MPa, followed by an exponential decay of time constant τ, with typically $\tau \sim 10^{-4} - 10^{-3}$ s. More precisely, at a point P within the fluid, the incident pressure is expressed as (Cole, 1948)

$$p_{\mathcal{W}}(r,t) = p_m(r) \exp\left(-\frac{t_r(r,t)}{\tau(r)}\right) H(t_r(r,t))\,, \tag{1.1}$$

where

- H is the Heaviside step function,
- $p_m(r) = K_1 \left(\dfrac{W^{1/3}}{r}\right)^{a_1}$ is the jump magnitude,
- $\tau(r) = K_2 W^{1/3} \left(\dfrac{W^{1/3}}{r}\right)^{a_2}$ characterises the temporal decline of the pressure,
- $t_r(r,t) := t - r/c$ is the retarded time, which expresses causality,
- r is the distance between the field point P and the initial bursting point.

K_1, K_2, a_1, a_2 are parameters that depend on the kind of the explosive material, and are given later in Table 1.1 for some common explosive materials. The parameters p_m and τ are related to W and r, and so the wave at distance r can be characterised by either pair of parameters. In other words, for a given experimental configuration in which W and the kind of the explosive are known (*we* launch a torpedo), the form of the induced incident pressure can be inferred at distance r; and in another experiment in which $p_{\mathcal{W}}$ is measured (*they* launch a torpedo), the corresponding charge weight and distance may be computed provided that the kind of explosive material is known/guessed.

The severity of an UNDEX at the standoff point is measured by a physical quantity, namely the *shock factor* K, determined from a similitude principle (Cole, 1948; Arons and Yennie, 1948), and expressed as[1]:

$$K = \frac{\sqrt{W}}{d_s}\,. \tag{1.2}$$

Two different explosions with the same explosive material and similar shock factor are assumed to lead to similar damages. A value of $K < 0.1$ kg$^{1/2}$/m is said to imply limited damages, whereas $K > 1$ kg$^{1/2}$/m is seen as a severe shock that induces plastic deformations of the hull (Brochard, 2018). For our reference explosion of $W = 100$ kg at $d_s = 100$ m, $K \simeq 0.1$ kg$^{1/2}$/m. A more detailed analysis of the primary wave is given in Section 1.2. Before that, we introduce the oscillating bubble phenomenon.

1.1.2 Brief presentation of the oscillating gas bubble

A shock wave is the phenomenon commonly considered when thinking about a blast in air, but in water another substantial phenomenon has to be taken into account. Resulting from the chemical reaction that releases the energy, the detonation produces large amounts of hot gases[2] that form a bubble (Brett et al., 2003). The typical pressure and temperature in the product gases are of the order of 50 000 bar and 3 000°C, respectively (Cole, 1948). Initially, the internal pressure of the bubble is higher than the ambient hydrostatic pressure, so the bubble starts by expanding, pushing away the water. As it expands, its internal pressure decreases and the velocity of the bubble surface increases. After a while, the internal pressure is exactly equal to the water pressure, but the bubble continues growing because of its high surface velocity. As it grows, its velocity drops. When its speed reaches zero, the reverse phenomenon appears, the bubble collapses. After a while, the bubble expands again and the process starts again. This oscillating phenomenon is similar to that of a spring-mass system initially compressed. During the process, some of the energy of the bubble is irreversibly transmitted to the water (Arons and Yennie, 1948). Consequently, the phenomenon is not exactly periodic, but *quasi-periodic*. Therefore, the bubble quasi-oscillates around an *equilibrium* position corresponding to the equality between internal and external pressures. The quasi-period of this oscillation depends on the type of the explosive material and the charge parameters (charge weight, water depth, charge radius). The time scale of the oscillations is approximately 0.1 to 0.5 s (Snay, 1962; Swisdak, 1978). As the bubble oscillation makes the water move, it generates a transport of both matter and energy. Consequently, the propagation of the created perturbation is not governed by the wave equation, but *a priori* by the common *Euler equations* of fluid dynamics (viscous effects are neglected, see Appendix A). When affecting a slender structure, this process, involving half the energy resulting from the explosion, generates a quasi-periodic structural load on the hull, whose frequency may be close to the resonant frequency of a warship. Hence, the shell globally vibrates due to this phenomenon and the induced damages may be significant (Zong, 2005; Zhang and Yao, 2008).

In addition to the ebb and flow generated by the oscillations, secondary pressure waves are created when the bubble is the most contracted (see Figure 1.1). These waves, also termed bubble pulses, are less abrupt than the shock wave, namely the magnitude of the incident pressure induced by secondary waves is (i) reached more smoothly and (ii) smaller

[1] Another definition takes into account the depression angle α (angle between vessel axis and charge), so that $K = (1 + \sin\alpha)/2\,\sqrt{W}/d_s$.

[2] The types of gases depend on the reagents involved in the chemical reaction. Common gases are CO, N_2, CO_2 or CH_4.

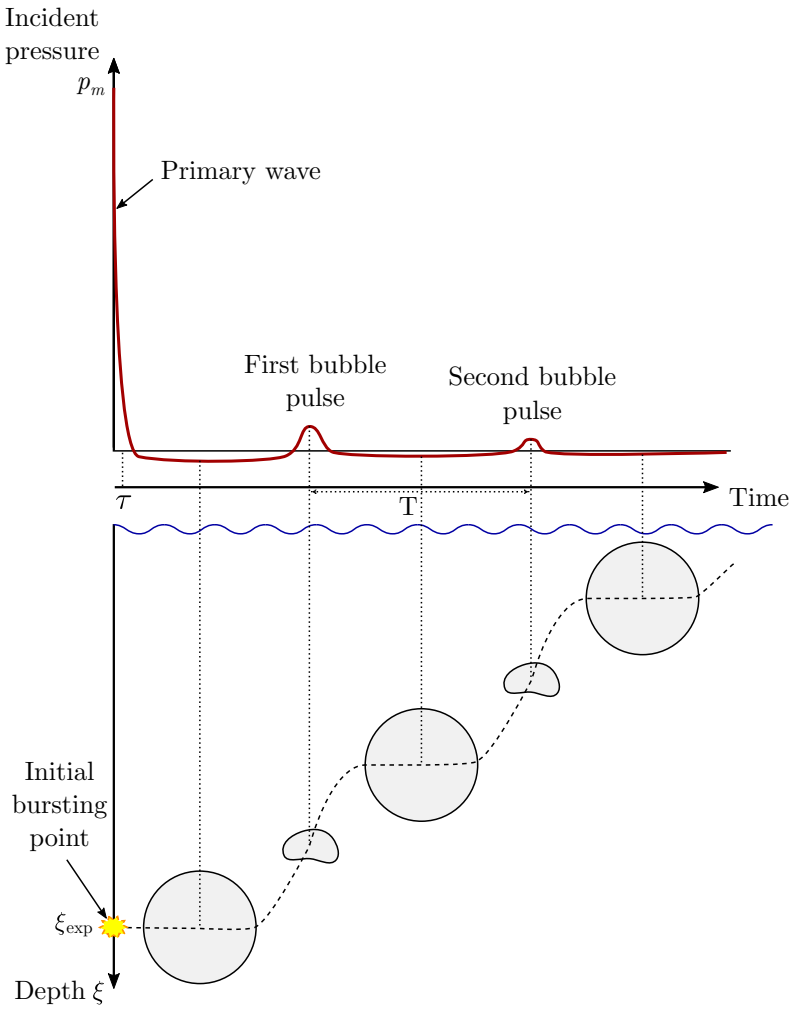

Figure 1.1: Schematic representation of the bubble motion and the pressure history, after (Snay, 1956).

than that of the primary wave. Therefore, some of the energy of the bubble is radiated, and consequently not stored as reversible potential energy in the fluid. This loss of energy implies that the maximum radius of the bubble reduces as the number of oscillations increases.

Due to Archimedes' principle, the bubble migrates to the surface. This vertical motion is not linear in time and depends on the bubble oscillations. It is observed that the bubble moves faster towards the surface when it is contracted, which is not obvious *a priori* since the buoyant force linearly rises with the occupied volume. This acceleration is explained by considering the fluid resistance, which evolves proportionally to the square of the velocity and the square of the bubble radius.

The motion of a gas bubble formed by the detonation of 0.5 kg of composition B (60/40 RDX/TNT) is illustrated in Figure 1.2 (Brett et al., 2003). It is noticeable that the gas bubble surface remains smooth and spherical during the first expansion, until snapshot 8. When it fully collapses, its shape is deformed, the bubble becomes asymmetric, especially on snapshots 12 and 13, and it may even be split in two parts (Best, 2002). This change of shape is notably due to the formation of a high-speed liquid jet upon collapse, noticeable on

snapshot 14. This fluid jet is caused by the variation of hydrostatic pressure, whose action on the bubble depends on its water depth. At the time of second maximum expansion (see snapshot 18) the bubble surface is not perfectly symmetric, as some instabilities arise.

So far, the shock wave and the oscillating bubble appear to be fundamentally different phenomena. Their motion is not governed by the same equations and their effects on the structure are not of the same type (one is local, the other one global). Therefore, the modelling of their effects is mainly studied separately in the remainder of this dissertation. However, it is important to keep in mind that the two phenomena are intrinsically linked since they both emerge from the same explosion. Trying to deal with them strictly separately, or considering one of them marginal compared to the other, would be a mistake in some configurations, and nowadays it is well known that, for fluid-structure interaction purposes involving a submarine, both phenomena have to be taken into account and unified as much as possible (Geers and Hunter, 2002; Graham et al., 2017). The energy repartition discussed next emphasises this point.

1.1.3 Energy repartition

The repartition of the energy of an underwater TNT explosion has been studied in (Arons and Yennie, 1948), and is sketched in Figure 1.3. The values have been obtained through analyses based on experimental results, notably in (Arons et al., 1948). The method was to compute the energy flow associated to each phenomenon, and then to infer the energy losses from a global energy balance. The computation is briefly explained in Appendix B.3. Note that the values provided in Figure 1.3 are given with an uncertainty of at least 10%, making the relevance of some values open to discussion. Also, the values in Figure 1.3 have been obtained using as a zero energy reference the state of infinite adiabatic expansion of the product gases. See (Arons and Yennie, 1948) for more details about the latter two remarks.

Figure 1.3 shows that the energy released by the explosion is nearly evenly divided between the shock wave and the oscillating bubble. Moreover, it stresses that the oscillating bubble affects the submerged structure not only through the ebb and flow it generates, but also through the secondary waves created when the bubble is fully contracted. Indeed, on the one hand the energy carried out by the primary wave is approximately 26% of the total energy of the explosion, while on the other hand the first secondary wave created by the bubble carries 11% of the total energy. It is then noticeable that the first secondary wave, produced by the first maximum contraction of the bubble, is not negligible, in terms of energy, compared to the primary wave.

With this in mind, it is however important to stress that secondary waves are less abrupt than the primary wave, namely they are smoother than the latter, and so the effects on a structure could be reduced, compared to that of the shock wave. Yet, a recent paper (Graham et al., 2017) carried out a study claiming that the bubble pulses could be *"much more damaging"* than the initial shock wave. This reminds the community that the topic is still open, and may suggest that improving the modelling of the bubble dynamics, by considering bubble pulses as waves for instance (Leblond, 2007), and determine whether it is relevant in the case of far-field underwater explosions, is among future prospects.

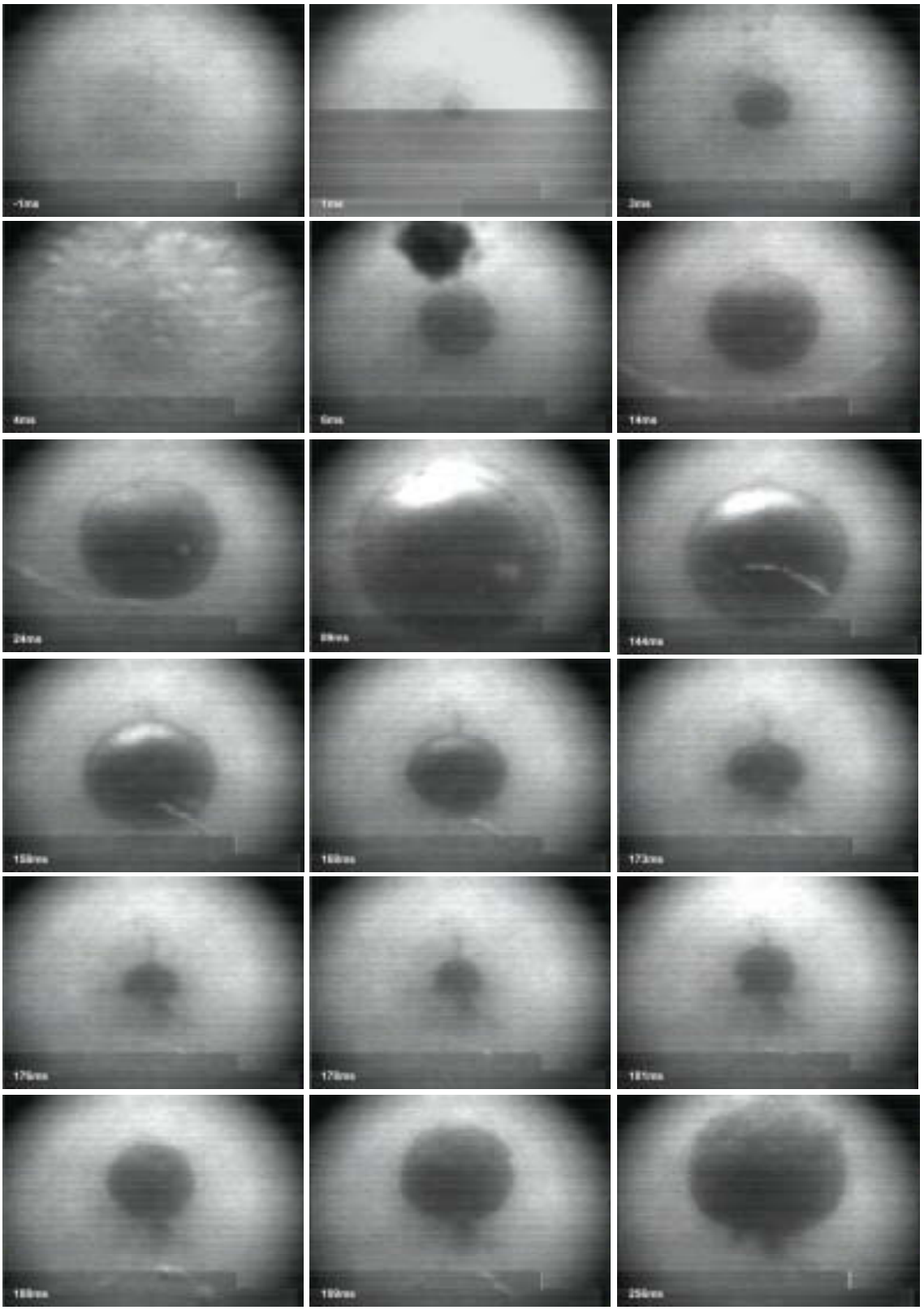

Figure 1.2: **Motion of the gas bubble formed by the detonation of 0.5 kg of composition B (60/40 RDX/TNT) at a depth of 5 m, from $t = 0$ to $t = 256$ ms. The maximum bubble diameter is about 2.3 m. Snapshots from (Brett et al., 2003).**

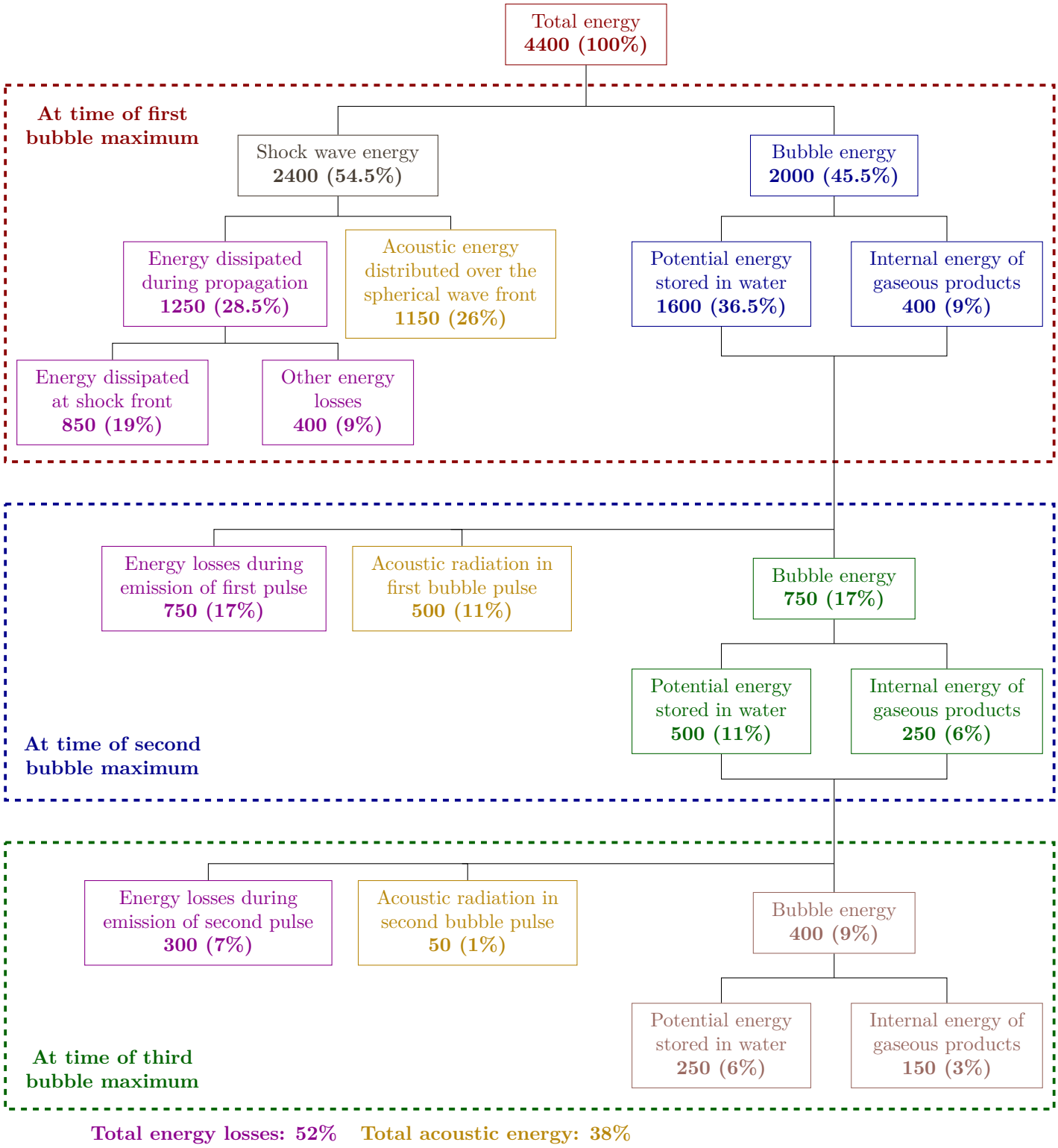

Figure 1.3: **Energy repartition of an underwater TNT explosion, from the values obtained in (Arons and Yennie, 1948), representation inspired from (Brochard, 2018). Energy values given in J/g. For W expressed in kg, the acoustic radiation and the energy dissipated at the shock wave front are evaluated at a distance $r = W^{1/3} \times 0.665$ m from the initial bursting point.**

1.1.4 Summary: what problems are considered? What are the hypotheses?

So far, two distinct phenomena (arising in far-field of explosions) have been briefly presented: a *shock wave*, also termed primary wave or blast, and an *oscillating gas bubble*. Since their characteristics are very different, proposing an efficient numerical method that covers the effects of both phenomena is challenging. Instead, it is helpful to treat them separately and find a way to combine their analysis. Again, this is possible only because *far-field underwater explosions* are considered, namely explosions far enough so that

- the effects of the shock wave can be temporally distinguished from those of the oscillating bubble, as experienced by the ship;
- the oscillating bubble behaviour is only marginally affected by the presence of the shell.

The first hypothesis allows to decompose the global study in two sequential phases. The second makes it reasonable to uncouple the shell behaviour from the bubble dynamics. Also, the fluid domain (the ocean) is treated as unbounded, so that reflections of the shock wave by the water surface and the seabed are disregarded. It corresponds fairly well to the study of a military submarine fight in deep water[3].

The study reported in Appendix A permits to specify the relevant approximations for both the shock wave and the gas bubble. For both phenomena, the Reynolds number is sufficiently high for viscous effects to be negligible. For the shock wave, the strains and the displacements may be considered small. We choose to study the bubble part under the assumption of small strains but possibly (large) finite rigid displacement. In both cases, the water is considered as a *perfect fluid*, *homogeneous*, *isotropic*, where the flow is *irrotational or potential*. These hypotheses, known to be relevant approximations, are also discussed in (Cole, 1948). As they satisfactorily depict reality, these assumptions are the basis on which the modelling is performed in Section 1.2 and Section 1.3.

1.2 The shock wave and its theory of propagation

The purpose of this section is to find and justify an adequate modelling for the shock wave phenomenon. All the concepts and results presented therein are available in the literature, but we try to enhance the way they are introduced. In particular we attempt to specify and justify properly any assumption or approximation. The study proposed is not quite comprehensive, notably because it does not analyse the behaviour of a shock wave near the explosion. However, we believe it offers a fairly thorough examination of the characteristics of a shock wave far from the explosion.

1.2.1 Impulsion of the shock wave, single- and double-exponential fits

As stated in Section 1.1, the shock wave stems from a sudden release of energy at the surface of the explosive charge when detonating. Far from the explosion, the resulting incident pressure may be represented by an exponential decay (see Section 1.1.1). Actually, after a more detailed analysis of the experimental results presented in (Coles et al., 1946), it was noticed that the pressure decay is better approximated by a double-exponential

[3] Modern nuclear attack submarines have a maximum operating depth greater than 400 meters.

decay of the form[4] (Geers and Hunter, 2002)

$$p_{\mathcal{W}}(r,t) = p_m\, f(t_r(r,t))H(t_r(r,t))\,, \tag{1.3}$$

$$f(t) = \alpha_1\, e^{-\beta_1\, t/\tau} + \alpha_2\, e^{-\beta_2\, t/\tau}\,, \quad \forall t \leq 7\tau\,, \tag{1.4}$$

where $\alpha_1, \beta_1, \alpha_2, \beta_2$ are numerical coefficients, obtained from experimental data, that depend on the type of the explosive material, and

$$p_m(r) = K_1 \left(\frac{W^{1/3}}{r}\right)^{a_1}\,, \qquad \tau(r) = K_2 W^{1/3} \left(\frac{W^{1/3}}{r}\right)^{a_2}\,. \tag{1.5}$$

According to (Geers and Hunter, 2002), the new form (1.4) of the shock wave pressure is fairly accurate for TNT for a retarded time smaller than 7τ, whereas a single-exponential decay remains accurate only before τ. Also, the double-exponential fit allows a better junction with the effects of the bubble (see Section 1.4.1). Therefore, it seems that this double-exponential fit is to be preferable for more accurate results. On the other hand, the single exponential fit is still widely used in the literature, and especially in industry, and so remains of interest. If the explosive material is TNT, the numerical coefficients in (1.4) are experimentally set to $\alpha_1 = 0.8251$, $\beta_1 = 1.338$, $\alpha_2 = 1 - \alpha_1 = 0.1749$ and $\beta_2 = 0.1805$. Otherwise, since the literature mainly considers the case of TNT, it is difficult to find the proper coefficients for other explosive materials.

So far, the fits proposed in (1.1) and (1.4) introduce a typical time scale τ and a typical pressure p_m, for a wave propagating at speed c. They characterise the exponential decay of the wave at a point P located at distance r from the explosion locus. Another formulation of (1.3) may be written as (Coles et al., 1946; Price, 1979; Geers and Hunter, 2002):

$$p_{\mathcal{W}}(r,t) = P_c \left[\frac{a_c}{r}\right]^{1+b_1} \tilde{f}\left(\frac{v_c}{a_c}\left[\frac{a_c}{r}\right]^{b_2} t_r\right) H(t_r)\,, \tag{1.6}$$

where $\tilde{f}(u) = \alpha_1\, e^{-\beta_1 u} + \alpha_2\, e^{-\beta_2 u}$ for $u \leq 7$. The parameters P_c, v_c, b_1 and b_2 are related to the former parameters through

$$b_1 \equiv a_1 - 1\,, \qquad b_2 \equiv -a_2\,, \tag{1.7a}$$

$$P_c \equiv K_1 \left(\frac{W^{1/3}}{a_c}\right)^{a_1}\,, \qquad v_c \equiv \frac{1}{K_2}\left(\frac{a_c}{W^{1/3}}\right)^{1+a_2}\,. \tag{1.7b}$$

Some authors prefer to consider the form (1.6) rather than (1.4). In this work, we adopt (1.4). Obviously, this does not introduce any theoretical issue, since the two forms are equivalent and (1.7) allows to move from one representation to the other.

Two very important quantities related to an acoustic wave are its impulsion and the total acoustic energy it carries. The impulsion per unit area I of a wave is defined as the integral over time of the associated incident pressure. For an underwater explosion, the pulse duration of the pressure is usually chosen equal to 7τ, to avoid to take into consideration the effects of the bubble (Cole, 1948). Hence, the impulsion per unit area of the wave at distance r may be obtained through a time integration of (1.3) for a retarded time t_r going from 0 to 7τ. Using the single-exponential fit (1.1), the wave impulsion I_s is given by

$$I_s := \int_0^{7\tau} p_m e^{-t/\tau}\, \mathrm{d}t \simeq p_m\, \tau\,. \tag{1.8}$$

[4] Setting $\alpha_1 = 1$, $\alpha_2 = 0$ and $\beta_1 = 1$ provides the single-exponential fit.

Using the double-exponential fit (1.4), the wave impulsion I_d is given by

$$I_d := \int_0^{7\tau} p_m \left(0.8251\, e^{-1.338\, t/\tau} + 0.1749\, e^{-0.1805\, t/\tau}\right) \mathrm{d}t \simeq 1.30\, p_m\, \tau\,. \tag{1.9}$$

A difference of about 30% is observed between the impulsions produced by the single- and the double-exponential fits. This difference is significant as regards the effects of the shock wave on a submerged structure, and reflects the difference between the two fits. Using (1.5), the dependence of the impulsion on r is obtained, for instance for the double-exponential fit, as

$$I_d(r) = 1.30\, K_1 K_2\, W^{(1+a_1+a_2)/3}\, r^{-(a_1+a_2)}\,,$$

which, using the values given in Table 1.1, approximately corresponds to a $1/r$ spatial decay, which is consistent with the linear acoustic wave model.

1.2.2 Acoustic compressional energy of the shock wave

Let us compute the compressional energy carried by the primary wave. Consider a sphere $\mathcal{S}$ in water, of radius r and centred at the initial bursting point. When the shock wave goes through an elementary surface $\mathrm{d}S$ of $\mathcal{S}$, the particles of fluid are subjected to an elementary force $\mathrm{d}\mathbf{F}(r,t) = p_{\mathcal{W}}(r,t)\,\mathrm{d}S\,\mathbf{n}$, where $\mathbf{n}$ denotes the outward normal to $\mathcal{S}$ at the centre of $\mathrm{d}S$. The associated elementary power is:

$$\mathrm{d}P = \; p_{\mathcal{W}}(r,t)\,\mathbf{n}\cdot\mathbf{v}_{\mathcal{W}}\,\mathrm{d}S\,, \tag{1.10}$$

where $\mathbf{v}_{\mathcal{W}}$ is the fluid-particle velocity. The total power of the forces induced by the primary wave on the sphere is then given by

$$P = \int_{\mathcal{S}} p_{\mathcal{W}}(r,t)\,\mathbf{n}\cdot\mathbf{v}_{\mathcal{W}}\,\mathrm{d}S \;= S\, p_{\mathcal{W}}(r,t)\, u_{\mathcal{W}}\,, \tag{1.11}$$

where $S = 4\pi r^2$ is the surface of $\mathcal{S}$ and $u_{\mathcal{W}} \equiv \mathbf{n}\cdot\mathbf{v}_{\mathcal{W}}$ is independent of the considered point on the sphere, because of the spherical symmetry of the problem. In the case of water, the acoustic approximation (with spherical symmetry) is such that $u_{\mathcal{W}}$ satisfies (Lamb, 1932; Arons and Yennie, 1948)

$$u_{\mathcal{W}}(r,t) \simeq \frac{p_{\mathcal{W}}(r,t)}{\rho\, c} + \frac{1}{r\,\rho}\int_0^t p_{\mathcal{W}}(r,\theta)\,\mathrm{d}\theta\,, \tag{1.12}$$

where ρ denotes the mass density of the initially unperturbed fluid. It is then noticeable that, though the limit $\lim_{t\to\infty} p_{\mathcal{W}}(r,t)$ is zero, the limit $\lim_{t\to\infty} u_{\mathcal{W}}(r,t)$ is not zero and corresponds to the limit when t grows to infinity of the second term in (1.12). For that reason, this second term in (1.12) is termed *after flow* (Arons and Yennie, 1948). The approximation (1.12) stems from the linearised Euler momentum equation, which provides

$$\frac{\partial u_{\mathcal{W}}}{\partial t} + \frac{1}{\rho}\frac{\partial p_{\mathcal{W}}}{\partial r} \simeq 0\,. \tag{1.13}$$

For an acoustic wave, with $p_{\mathcal{W}} \sim \frac{1}{r}e^{-(t-r/c)/\tau}$, it holds

$$\frac{\partial p_{\mathcal{W}}}{\partial r} = -\frac{p_{\mathcal{W}}}{r} + \frac{p_{\mathcal{W}}}{\tau\, c} = -\frac{p_{\mathcal{W}}}{r} - \frac{1}{c}\frac{\partial p_{\mathcal{W}}}{\partial t}\,,$$

and then (1.13) becomes

$$\frac{\partial u_{\mathcal{W}}}{\partial t} \simeq \frac{p_{\mathcal{W}}}{r\,\rho} + \frac{1}{\rho\, c}\frac{\partial p_{\mathcal{W}}}{\partial t}\,. \tag{1.14}$$

(1.12) is obtained through time integration of (1.14) from 0^- to t.

At the wave shock front, at $t = r/c$, so $t_r = 0$, (1.12) provides

$$u_{\mathcal{W}}(r, t_r = 0) = \frac{p_{\mathcal{W}}(r, t_r = 0)}{\rho\, c} = \frac{p_m(r)}{\rho c}\,. \tag{1.15}$$

(1.15) reminds us of the Rankine-Hugoniot condition for conservation of momentum (Hugoniot, 1887 - 1888; Rankine, 1870), that is presented in Appendix B. We stress that the relation $u_{\mathcal{W}} = p_{\mathcal{W}}/(\rho c)$ holds approximately for any time far from the source, where the spherical wave front is locally approximated by a plane wave front, and then the relation (1.12) reduces to the plane wave approximation.

More precisely, in our case, where

$$p_{\mathcal{W}} \sim 10^6 \text{ Pa},\ r \sim 10^2 \text{ m},\ c \sim 1.5\ 10^3 \text{ m/s},\ \rho \sim 10^3 \text{ kg/m}^3,$$
$$\int_0^t p_{\mathcal{W}}(r, \theta)\mathrm{d}\theta < I \overset{(1.8)}{\sim} p_m \tau \sim 10^3 \text{ SI},$$

the first term in (1.12) is of order 1 m/s, whereas the after flow term is of order $1/r \sim 10^{-2}$ m/s. Therefore, for remote UNDEX, where $r > 50$, the after flow term is negligible.

In the plane wave approximation, keeping only the first term in the right hand side of (1.12), and using the double-exponential fit (1.4), the compressional energy carried by the wave is obtained through integration of (1.11) over time

$$E_c = \frac{4\pi r^2}{\rho\, c} \int_0^{7\tau} p_m^2 \left(0.8251\, e^{-1.338\, t/\tau} + 0.1749\, e^{-0.1805\, t/\tau}\right)^2 \mathrm{d}t \simeq 0.522\, \frac{4\pi r^2}{\rho\, c}\, \tau\, p_m^2\,. \tag{1.16}$$

Using a single-exponential fit, the obtained energy E_{sc} is close to that with the double-exponential fit (1.16) ($E_{sc} = S/(2\rho\, c)\tau\, p_m^2 \simeq 0.96\, E_c$). The compressional energy carried by the primary wave is conserved if it is independent of r. Using (1.5), it comes

$$E_c \simeq 0.522\, \frac{4\pi}{\rho\, c}\, K_1^2 K_2\, W^{(1+2a_1+a_2)/3}\, r^{2-2a_1-a_2}\,, \tag{1.17}$$

and so the compressional energy is conserved if and only if $2 - 2a_1 - a_2 = 0$. As stated previously, the values of a_1 and a_2 depend on the kind of the explosive material. For some types of explosive materials, with a given mass density, the values of the parameters K_1, K_2, a_1 and a_2 provided by (Swisdak, 1978) are presented in Table 1.1.

It is noticeable that the power of r in (1.17) is strictly negative for any of the explosives presented in Table 1.1, which means that the expression of the energy obtained using experimental results (the form of the incident pressure (1.4) and of its parameters are obtained from experimental data) accounts for the small losses of energy during the wave propagation.

To validate the computation, it is checked that the value obtained for the acoustic energy distributed over the spherical wave front in Figure 1.3, and so in (Arons and Yennie, 1948), may be inferred, in terms of order of magnitude, from (1.17):

$$\begin{aligned} E_c &\simeq 0.522\, \frac{4\pi}{\rho\, c}\, K_1^2 K_2\, W^{(1+2a_1+a_2)/3} \left(0.665\, W^{1/3}\right)^{2-2a_1-a_2} \\ &= 0.522\, \frac{4\pi}{\rho\, c}\, K_1^2 K_2\, W (0.665)^{2-2a_1-a_2}. \end{aligned}$$

Explosive material	K_1 (SI)	a_1	K_2 (SI)	a_2	$2-2a_1-a_2$
TNT, mass density 1.6 g/cm^3	5.24 10^7	1.13	8.4 10^{-5}	−0.23	−0.03
Pentolite, mass density 1.71 g/cm^3 (50/50 PETN/TNT)	5.65 10^7	1.14	8.4 10^{-5}	−0.23	−0.05
H-6, mass density 1.76 g/cm^3 (45/30/20/5 RDX/TNT/A1/D-2 Wax)	5.92 10^7	1.19	8.8 10^{-5}	−0.28	−0.10
HBX-1, mass density 1.72 g/cm^3 (40/38/17/5 RDX/TNT/A1/D-2 Wax)	5.67 10^7	1.15	8.3 10^{-5}	−0.29	−0.01
HBX-3, mass density 1.84 g/cm^3 (31/29/35/5 RDX/TNT/A1/D-2 Wax)	5.03 10^7	1.14	9.1 10^{-5}	−0.218	−0.062

Table 1.1: Values of the shock wave parameters for various kinds of explosive materials, extracted from (Swisdak, 1978), expressed in SI units.

Using the parameter values of TNT and those of water ($\rho = 10^3$ kg/m^3 and $c = 1.5\ 10^3$ m/s), it comes, with $W = 10^{-3}$ kg,

$$E_c \simeq 1050\,\mathrm{J}\,, \tag{1.18}$$

which is fairly close to the value of 1150 J obtained in Figure 1.3.

Remark 1 *Since the values of a_1 and a_2 slightly vary from one explosive material to another, the units of K_1 and K_2 vary accordingly for two different explosive materials. This is because the empirical form of the shock wave incident pressure is purely based on fittings with experimental data, and it is shown in Section 1.2.3 that the empirical form (1.1) does not even provide an incident pressure that satisfies the wave equation.*

Remark 2 *The precision of the values of a_1 and a_2 is not enough to accurately predict the decay of the acoustic energy of the shock wave. Actually, such a decay is not easy to experimentally assess, as the acoustic energy depends very weakly on r.*

When studying the effects of a far-field UNDEX on a shell, the dissipation of the acoustic energy due to propagation when the shock wave passes through the shell is usually not taken into account. This is justified by the fact that the absolute value of the power of r in (1.17) is less than 0.1, and so the energy of the acoustic wave is almost the same at $r = d_0$ and $r = d_0 + a$ or $d_0 + l$, for a, l of the same order of magnitude or less than d_0. The acoustic energy of the wave when it reaches the shell is given by

$$E_{0c} \simeq 0.522\,\frac{4\pi}{\rho\, c}\,K_1^2 K_2 W^{1/3+2a_1/3+a_2/3} d_0^{2-2a_1-a_2}, \tag{1.19}$$

and the associated energy flux per unit area of surface is obtained through division by $4\pi d_0^2$. Multiplying this energy flux by the cross section of the shell provides the acoustic energy that impacts the structure.

Remark 3 *For $2a_1 + a_2 \simeq 2$, the shock factor K defined in (1.2) is proportional to the square root of the energy flux per unit area. Then, in FSI context, K measures the shock severity by assessing the quantity of energy transmitted to the structure.*

The fact that the compressional energy is not conserved seems to indicate that the incident pressure is not exactly that of an ideal wave, since the compressional energy of the latter would be conserved. Then, two questions arise: how well the empirical form of the incident pressure conforms with the wave equation, which is addressed next in Section 1.2.3, and how to take into account the energy transfer between the shock wave and the fluid during propagation, which is discussed in Appendix B.3.

1.2.3 Is the shock wave propagation governed by the wave equation?

If it is assumed that the shock wave is an ideal acoustic wave, then its propagation is supposed to be governed by the wave equation, which may be written for both the velocity potential and the pressure. For the incident pressure, it holds

$$\Delta p_{\mathcal{W}} - \frac{1}{c^2}\frac{\partial^2 p_{\mathcal{W}}}{\partial t^2} = 0\,. \tag{1.20}$$

Regularity of the incident pressure. For the type of problems studied in this thesis, with a fluid domain Ω_f exterior to a structure bounded by the surface Γ, the typical initial boundary value problem associated to (1.20) is

$$\text{Find } \psi \text{ such that } \begin{cases} \Delta\psi - \dfrac{1}{c^2}\dfrac{\partial^2\psi}{\partial t^2} = 0 & (\mathbf{x},t) \in \Omega_f \times [0,T]\,, \\ \psi(\mathbf{x},0) = 0 & \mathbf{x} \in \Omega_f\,, \\ \dfrac{\partial\psi}{\partial t}(\mathbf{x},0) = 0 & \mathbf{x} \in \Omega_f\,, \\ \text{Boundary condition} & \mathbf{x} \in \Gamma, \end{cases} \tag{1.21}$$

with $T > 0$ a finite duration. Usually, ψ does not need to be regular enough so that all the derivatives written above are meaningful in the sense of functions. Instead, (1.21) is rather to be understood in the sense of distributions (see Section 2.2). Typically, the application

$$\Psi : \begin{array}{ccc} [0,T] & \longrightarrow & E \\ t & \longmapsto & \psi(t,\cdot) \end{array}$$

is expected to have enough regularity to make the variational form of (1.21) meaningful. For instance, with Dirichlet boundary condition $\psi = 0$ on Γ in (1.21), introducing the standard function spaces

$$L^2(\Omega) \equiv \left\{ f \,\middle/ \int_\Omega f^2 < \infty \right\}, \quad H_0^1(\Omega) \equiv \left\{ f \,\middle/ f \in L^2(\Omega), \nabla f \in \left(L^2(\Omega)\right)^3, f = 0 \text{ on } \partial\Omega \right\},$$

Ψ is usually sought in $\mathcal{E} \equiv \mathcal{C}^0([0,T]; H_0^1(\Omega)) \cap \mathcal{C}^1([0,T]; L^2(\Omega))$ (Allaire, 2012), where Ω is a regular bounded domain, exterior of the structure Γ, and large enough to prevent any wave emitted by a point of Γ to reach the exterior boundary of Ω within the time duration T, due to causality (both the sound speed c and the time duration T are finite, see Section 2.2).

The discontinuous fit (1.3) chosen for $p_{\mathcal{W}}$ is not in $\mathcal{E}$. Then, to gain some regularity, the wave equation should preferably be written for the velocity potential $\phi_{\mathcal{W}}$ only, related to the pressure through the acoustic relation $p_{\mathcal{W}} = -\rho\partial_t\phi_{\mathcal{W}}$ (linearised form of the Euler momentum equation (C.21)). However, the discontinuous aspect of $p_{\mathcal{W}}$ is related to its modelling, which could be slightly modified, so that the jump to the magnitude p_m is smoothly performed during a very short time (see Section 2.6.2). Then, in the rest of this thesis, the fact that $p_{\mathcal{W}}$ satisfies the wave equation or not is dealt with independently of regularity issues.

Wave equation for the incident pressure. In Appendix C.1, we show that the incident pressure satisfies the wave equation if the empirical coefficients satisfy

$$\begin{cases} a_1 + a_1^2 - 2a_1 = 0\,, \\ a_1a_2 + a_2(1-a_2) + a_2a_1 - 2a_2 = 0\,, \\ -a_1(a_2+1) + a_2(a_2+1) - a_1(a_2+1) + 2(a_2+1) = 0\,, \\ a_2^2 = 0\,, \\ -2a_2(a_2+1) = 0\,, \\ (a_2+1)^2 - 1 = 0\,, \end{cases} \tag{1.22}$$

whose unique solution is $(a_1 = 1, a_2 = 0)$. For TNT for instance, using the values provided in Table 1.1, we find

$$\begin{cases} a_1 + a_1^2 - 2a_1 = 0.15\,, \\ a_1a_2 + a_2(1-a_2) + a_2a_1 - 2a_2 = -0.34\,, \\ -a_1(a_2+1) + a_2(a_2+1) - a_1(a_2+1) + 2(a_2+1) = -0.38\,, \\ a_2^2 = 0.05\,, \\ -2a_2(a_2+1) = 0.35\,, \\ (a_2+1)^2 - 1 = -0.41\,, \end{cases} \tag{1.23}$$

and therefore the wave equation is not exactly satisfied by the empirical form (1.3) of the incident pressure for TNT, the shock wave is not an ideal wave!

This observation raises the question of a new propagation theory. In (Cole, 1948), the Kirkwood-Bethe propagation theory is presented. This theory, summarised in Appendix B.1, results in the propagation equation

$$\Delta\phi - \frac{1}{c^2}\frac{\partial^2\phi}{\partial t^2} = \frac{1}{c^2}\left(\frac{\partial v^2}{\partial t} + \frac{1}{2}(\mathbf{v}\cdot\nabla)v^2\right), \tag{1.24}$$

where $v = \|\mathbf{v}\| = \|\nabla\phi\|$. (1.24) shows a correction compared to the wave equation

$$\Delta\phi - \frac{1}{c^2}\frac{\partial^2\phi}{\partial t^2} = 0\,,$$

since a (non-zero) right hand side is considered in (1.24). It also reflects that the wave equation is obtained from a linearisation of the Euler equations, since the right-hand side of (1.24) is composed of non-linear terms in v. Equation (1.24) may be used to numerically quantify the error in considering the propagation of a far-field UNDEX as given by the wave equation, by checking that the right-hand side is marginal compared to the term $\frac{1}{c^2}\frac{\partial^2\phi}{\partial t^2}$ of the left-hand side. The purpose is then not to use the Kirkwood-Bethe theory to evaluate the propagation of the shock wave, but rather to justify that the use of the wave equation is relevant to appreciate the shock wave propagation for far-field explosions.

1.2.4 Conclusion, choice of a model for the shock wave

In this section, the shock wave specifications were under examination. The shock wave resulting from an underwater explosion is a supersonic wave that propagates through the fluid and whose speed quickly drops to the sound speed in the fluid. Its associated radiated acoustic energy decreases during a very short distance of typically 10 times the charge radius, and then is quasi-stable during the rest of the propagation. Far from the explosion, the pressure-time curves of the phenomenon may be fitted with a single- or double-exponential fit, (1.1) or (1.4).

In the middle of the 20th century, experimental studies of shock waves led to the introduction of some parameters that depend on the type of the explosive material, and whose values are tabulated (see Table 1.1). Theoretically, for an ideal wave, the coefficients a_1 and a_2 in (1.5) are given by $a_1 = 1$ and $a_2 = 0$, so that the wave equation is satisfied for the single- and double-exponential fits, and the acoustic wave energy (1.17) is conserved. In practice, measurements provide pressure-time curves at some points located at various distances d from the source. These measurements, together with principles of similitude, allow to fit the curves with a chosen exponential fit and provide a value of (a_1, a_2) slightly different from $(1, 0)$. This is due to the fact that the measurements take into account the real phenomenon, which is not an ideal wave but a shock wave whose characteristics are not exactly that of a wave, like discussed in Section 1.2.3, Appendix B.1 and Appendix B.3.

On the one hand, considering the shock wave as an ideal acoustic wave is a theoretical issue, because it does not satisfy the wave equation, but on the other hand the empirical form of the incident pressure, that aims to stick to reality as best as possible, shows that, far from the explosion, this hypothesis yields a fair approximation. Indeed, the acoustic energy (1.17) depends very mildly on r and the low value of the numerical coefficients computed in (1.23) suggests the experimental fit is not far from a wave. Also, the right hand side of (1.24) may be used to assess the relevance of the wave equation.

Finally, the study carried out in Appendix B resulted in a final set of relations (B.18), that offers a basis to the unification between the shock wave and the oscillating bubble, in Section 1.4. Naturally, the next step of this work, before that unification, is the study of the oscillating bubble, in Section 1.3.

1.3 The oscillating gas bubble and its various models

Several bubble models are available in the literature (Geers and Hunter, 2002; Wang and Khoo, 2004; Barras et al., 2012). Most of them, even the most sophisticated, provide results in accordance with experimental data only before the third oscillation. In order to understand the overall trend of the bubble motion, we choose to present the case of a spherical bubble, moving in an infinite perfect fluid, where the flow is assumed to be incompressible and potential.

1.3.1 Gas bubble, physical parameters of first oscillation

As explained in Section 1.1, an explosion leads to the formation of hot gases that form an oscillating bubble. The study of experimental results allows to establish some principles of similitude that relate the physical parameters governing the bubble oscillation to those of the explosion. The quasi-period and the maximum radius of the first bubble oscillation are given by (Snay, 1962; Swisdak, 1978)

$$T = K_3 \frac{W^{1/3}}{(\xi_{\text{exp}} + \xi_{\text{atm}})^{5/6}}, \quad R_{\max} = K_4 \frac{W^{1/3}}{(\xi_{\text{exp}} + \xi_{\text{atm}})^{1/3}}, \tag{1.25}$$

where ξ_{exp} is the positive depth of the charge, $\xi_{\text{atm}} \equiv P_0/(\rho\, g)$ corresponds to the contribution of the atmospheric pressure P_0 to the hydrostatic pressure, and K_3 and K_4 are two empirical parameters given in Table 1.2 for various kinds of explosive materials.

Explosive material	K_3 (SI)	K_4 (SI)
TNT, mass density $1.6\,\mathrm{g/cm^3}$	2.11	3.50
Pentolite, mass density $1.71\,\mathrm{g/cm^3}$ (50/50 PETN/TNT)	2.11	3.52
H-6, mass density $1.76\,\mathrm{g/cm^3}$ (45/30/20/5 RDX/TNT/A1/D-2 Wax)	2.52	4.06
HBX-1, mass density $1.72\,\mathrm{g/cm^3}$ (40/38/17/5 RDX/TNT/A1/D-2 Wax)	2.41	3.95
HBX-3, mass density $1.84\,\mathrm{g/cm^3}$ (31/29/35/5 RDX/TNT/A1/D-2 Wax)	2.63	4.27

Table 1.2: Values of the first bubble oscillation parameters for various kinds of explosive materials, extracted from (Swisdak, 1978), expressed in SI units.

After the first oscillation, the gas bubble is no longer spherical and some perturbations appear at the bubble surface (see Figure 1.2), typically Rayleigh-Taylor instabilities (Sharp, 1984). To accurately model the phenomena, both heat and mass transfers must be taken into account. However, it is very difficult, not to say impossible, to practically measure such effects inside the bubble or at its surface during an experiment. On the other hand, assuming for simplicity that the bubble remains spherical allows a simple model providing a fair idea of the behaviour of the gas bubble.

1.3.2 Simple example of spherical bubble model

In this section, the dynamics of an oscillating bubble $\mathcal{B}$ that migrates toward an **infinitely remote** water surface is considered. The equations of motion are obtained in the case of a **spherical bubble**, moving in an **infinite perfect fluid**, where the flow is assumed to be **incompressible** and **potential**. In particular, the last two hypotheses imply

$$\mathbf{v} = \nabla\phi\,, \quad \nabla\cdot\mathbf{v} = 0 \quad \Longrightarrow \quad \Delta\phi = 0\,, \tag{1.26}$$

where ϕ is the velocity potential and Δ denotes the spatial Laplacian. The computational details are provided in Appendix C.2, and we rather focus on the physical meaning of the results in this section.

The assumed motion is such that the bubble vertically translates along $\mathbf{e}_z$, toward the (infinitely remote) water surface, while its surface oscillates with radial symmetry. The bubble position is then provided by its radius $R(t)$ and its centre position $Z(t)$ (see Figure 1.4). Under these assumptions, the solution to $\Delta\phi = 0$ is composed of only two terms: a source term ϕ_0 for the bubble oscillation and a dipole $\phi_1\cos(\theta)$ for the translation (Landau and Lifshitz, 1987):

$$\phi(r,\theta,t) = -\frac{R^2(t)\dot{R}(t)}{r} - \frac{R^3(t)\dot{Z}(t)}{2r^2}\cos\theta\,. \tag{1.27}$$

(1.27) means that knowing $R(t)$ and $Z(t)$ and their time derivatives is enough to compute the velocity potential at any point $P(r,\theta)$ in the fluid surrounding the bubble. This remains approximately true for more sophisticated bubble models (Leblond, 2007), and so, in the context of FSI with remote UNDEX, the main information of interest is $R(t)$ and $Z(t)$.

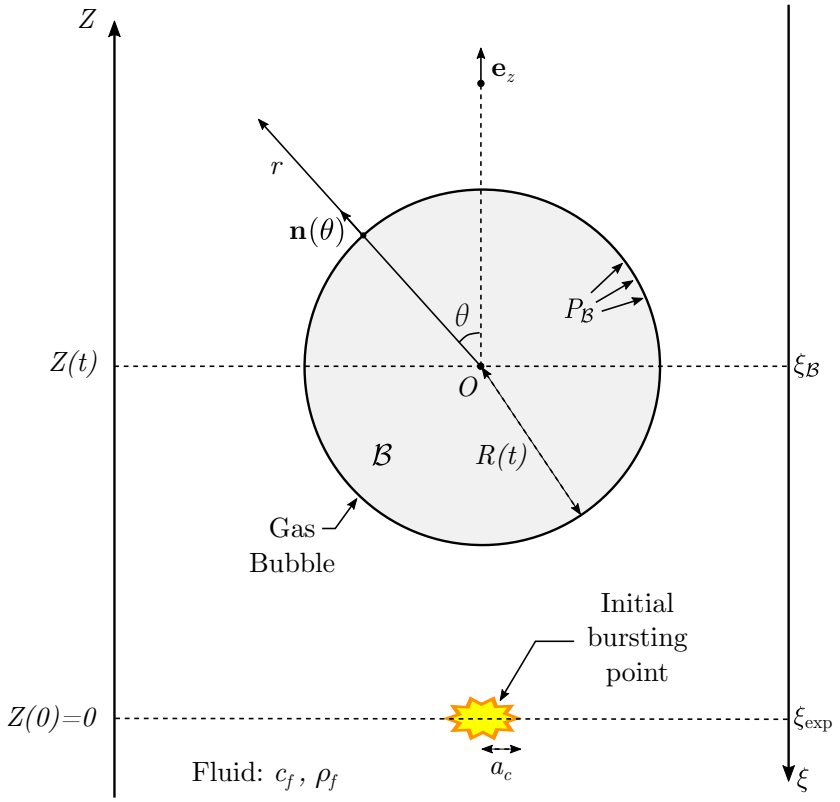

Figure 1.4: Cross-section of the (assumed spherical) gas bubble created by an underwater explosion.

The time evolution of R and Z is found (see Appendix C.2.3) to be governed by the ordinary differential equations

$$3\frac{\dot{R}}{R}\dot{Z} + \ddot{Z} + \frac{3}{4}C_D\frac{\dot{Z}^2}{R} = 2g\,, \tag{1.28a}$$

$$R\ddot{R} + \frac{3}{2}\dot{R}^2 - \frac{\kappa_c}{\rho}\left(\frac{a_c}{R}\right)^{3\gamma} = -\frac{P_{\text{exp}}}{\rho} + \frac{\dot{Z}^2}{4} + gZ\,, \tag{1.28b}$$

that notably depend on the internal bubble gas pressure

$$P_{\mathcal{B}} = \kappa_c\left(\frac{V_c}{V}\right)^{\gamma} = \kappa_c\left(\frac{a_c}{R}\right)^{3\gamma}\,,$$

gravity g, and a drag coefficient C_D (see details in Appendix C.2.3).

The equations of motion (1.28) are solvable if suitable initial conditions are also provided. Basic intuition would suggest to set those initial conditions to $Z(0) = 0$, $\dot{Z}(0) = 0$, $R(0) = a_c$ and $\dot{R}(0) = 0$. However, these initial conditions lead to numerical results that differ from the experimental ones, notably regarding the maximum radius of the bubble (Best, 2002; Leblond, 2007). To deal with this issue, the initial conditions are instead set such that the maximum radius numerically predicted corresponds to the one experimentally measured, given by (1.25). This maximum radius may be obtained via energy conservation arguments, following the steps given in (Best, 2002) (see details in Appendix C.2.4).

Far from the explosion, the bubble pressure is obtained (see Appendix C.2.5) from the generalised Bernoulli equation

$$\frac{\partial\phi}{\partial t} + \frac{1}{2}|\nabla\phi|^2 + \frac{1}{\rho}p - g\,\xi_P = 0\,, \tag{1.29}$$

and is provided by

$$p(P(r,\theta,\psi),t) \underset{r\to\infty}{\sim} \rho g\,\xi_P + \frac{\rho}{r}\frac{\partial(R^2\dot{R})}{\partial t} = \rho g\,\xi_P + \frac{\rho}{4\pi r}\frac{\partial^2 V_{\mathcal{B}}}{\partial t^2}\,, \tag{1.30}$$

where $V_{\mathcal{B}}(t) = \frac{4\pi}{3}R^3(t)$ is the current bubble volume. The pressure induced by the bubble at point P of distance d from the centre of the bubble is proportional to $1/d$, like for the shock wave, and to the second time derivative of the bubble volume. The pressure profile (1.30) is discussed in (Geers and Hunter, 2002), where it is noticed that it does not depend on the sound velocity in the fluid c and is therefore independent of the liquid compressibility. This is a consequence of the assumption of incompressible flow.

The relevance of the various model hypotheses are discussed in (Leblond, 2007). For instance, it is notably noticed that the hypothesis of an infinitely remote water surface is not true if the maximal bubble radius (1.25) is not small compared to the water depth, typically $R_{\max} < \xi_{\text{exp}}/10$. For example, in the experiment illustrated on Figure 1.2, the condition $R_{\max} < \xi_{\text{exp}}/10$ is not satisfied and the pressure record given in (Brett et al., 2003) shows the influence of the water surface. Also, the bubble must be able to oscillate several times before it reaches the water surface, which is usually the case in deep water because the bubble oscillates quicker than it vertically migrates to the water surface, at least during the first oscillations (see Figure 1.2).

The hypothesis of spherical shape is not perfectly accurate, as the gas bubble shape becomes toroidal when it is fully contracted, during the rebound (Best, 2002), and the spherical symmetry is also broken by the formation of a vertical fluid jet when the bubble enters the phase of first contraction. Moreover, not considering material and thermal transfers between the bubble and water could also result in a significant error.

The simple modelling summarised in this section, with supporting derivations given in Appendix C.2, is quite inaccurate in many cases, but it may provide a bubble dynamics not too far from reality during the first oscillation, in the case of a far-field underwater explosion in deep water. More refined bubble models are available in the literature (refer to Leblond, 2007, for a detailed bibliography). We decided not to work on developing a bubble model, considering the models available in the literature to be adequate enough as regards the engineering purpose of this thesis. Developing or improving a bubble model could nonetheless be an interesting outlook for future work.

1.3.3 Conclusion, choice of a model for the oscillating bubble

From the study presented in this section, two main results should be remembered. Firstly, the dynamics of the oscillating gas bubble (when alone in the ocean, i.e., without the ship), provided by a so-called bubble model, is not yet totally well understood today. The literature abounds with bubble models, more or less complicated, more or less accurate, and we do not wish to develop yet another one. Instead, a simple existing bubble model was presented, to give an idea of the bubble behaviour. The numerical procedure we aim to design shall be compatible with any bubble models, so that the choice of the latter remains free for the user.

Secondly, the choice of the equation for the velocity potential of the bubble-induced perturbation deserves attention. The hypothesis of incompressible flow leads to the Laplace equation for the velocity potential. In the context of FSI, we choose to stick to this equation to solve the coupling between the bubble and the submarine.

1.4 Junction between the two phenomena

As stated in Section 1.1, dealing with the shock wave and the oscillating bubble strictly separately, or considering one of them marginal compared to the other, would be a mistake in some configurations. Instead, both phenomena have to be taken into account and unified as much as possible.

During this work, we tried to link the two phenomena, notably to find a proper way to perform the junction between their two very different theories. In near-field UNDEX theory, the purpose is to obtain a single set of equations for the entire phenomenon, taking into account both the primary wave and the oscillating bubble as a single unified phenomenon. For far-field UNDEX, the goal is rather to find and justify a simple way to blend the two events.

1.4.1 Partitioning concept for the total incident pressure

Consider an explosion in a fluid, resulting in the formation of a shock wave and an oscillating bubble. In this section, d refers to the distance between the considered point P and the moving bubble centre, whereas r refers to the distance between P and the initial bursting point. The total incident pressure takes into account both the shock wave and the oscillating bubble. For short times (milliseconds), it is provided by (1.3), whereas, after a long enough time of typically one-tenth of a second, it is provided by the considered bubble model. For instance, in the case of the simple model presented in Section 1.3.2, the bubble contribution is provided by (1.30), and so the incident pressure is expressed as:

$$p^i(r,d,t) \underset{\text{short times}}{\sim} p_{\mathcal{W}}(r,t) = p_m(r) f(t_r(r,t)) H(t_r(r,t))\,,$$
$$p^i(r,d,t) \underset{\text{longer times}}{\sim} p_{\mathcal{B}}(d,t) = \frac{\rho}{4\pi d}\frac{\partial^2 V_{\mathcal{B}}}{\partial t^2}(d,t)\,.$$

Because the time constant τ of the primary wave (1.5) is much smaller than the quasi-period T of the gas bubble (1.25), the simplest way to perform the junction consists in adding both contributions. First the effects of the primary wave are considered, until a retarded time t_{rI} of typically 3τ to 7τ, so a time t_I of $3\tau + r/c$ to $7\tau + r/c$; and only then those of the bubble, such that

$$p^i(r,d,t) = p_m(r) f(t_r(r,t)) \mathbb{1}_{r/c \le t \le t_I} + \frac{\rho}{4\pi d}\frac{\partial^2 V_{\mathcal{B}}}{\partial t^2}\mathbb{1}_{t>t_I}\,. \tag{1.31}$$

The separation (1.31) must not introduce a substantial discontinuity in the form of the total incident pressure, and it is the role of the double-exponential fit (1.4) to reduce the junction jump. Also, some bubble models may provide smoother junctions compared to others. Of course, in practice, the two contributions are smoothly connected, using a smooth step function, to avoid an unwanted discontinuity.

(1.31) was originally introduced in (Geers and Hunter, 2002), where the two authors check the validity of what they call the *partitioning concept*. They consider the junction of the two phenomena at a fixed point P in the fluid, with the retarded time being the temporal variable. Then, the causality effect introduced by the fact that the junction time t_I depends on the distance r is not explicitly highlighted in their paper.

Applying the partitioning concept, Leblond (2007) performed the junction between his own bubble model and the shock wave, fitted by the double-exponential. Like in (Geers

and Hunter, 2002), the procedure was validated by checking that the value of $t_{rI} = \alpha\tau$ does not affect the final result when $\alpha \in [3, 7]$.

An example of incident pressure signal obtained using the procedure performed in (Leblond, 2007) is illustrated on Figure 1.5 for an explosion of $W = 100$ kg of TNT, located at distance $d = 100$ m, at a water depth $\xi_P = 100$ m. Figure 1.5 shows the result of (1.31) in this case. The two pressure trends seem to be fairly compatible at the junction. We purposely use a discontinuous step function in Figure 1.5, instead of a smooth junction, to show the two phases.

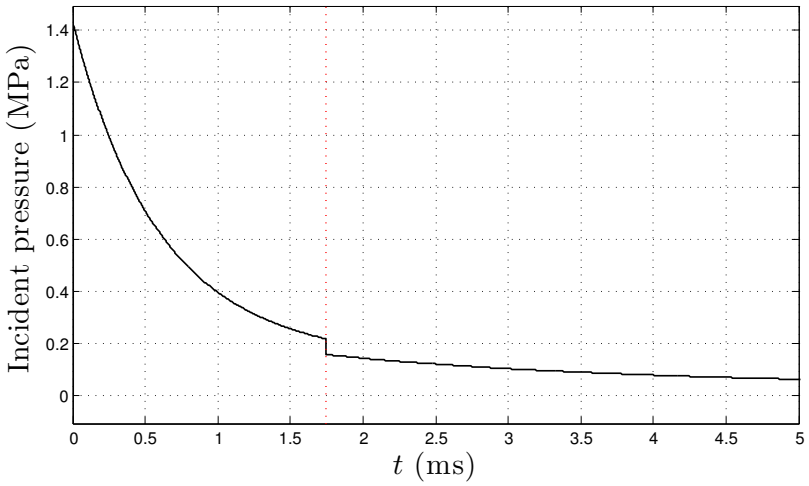

Figure 1.5: Illustration of the partitioning concept junction in the case of an explosion of $W = 100$ kg of TNT, located at $d = 100$ m, at a water depth $\xi = 100$ m.

Regarding the comparison performed in (Leblond, 2007) between numerical simulations emerging from the partitioning concept and experimental data from (Arons and Yennie, 1948), the simple junction with a smooth step function seems to be a possible way to unify the shock wave and the oscillating bubble, but it lacks a reliable theoretical basis.

1.4.2 The multi time scale method

In this section, we try to find a way to perform the junction, not only based on numerical and experimental data, contrary to the partitioning introduced in Section 1.4.1. For a sufficiently remote UNDEX, we assume it is possible to decompose the variables in terms of the contributions of the shock wave ($\mathcal{W}$) and the oscillating bubble ($\mathcal{B}$):

$$p = p_h + p_{\mathcal{W}} + p_{\mathcal{B}}\,, \tag{1.32a}$$
$$\rho = \rho_0 + \rho_{\mathcal{W}} + \rho_{\mathcal{B}}\,, \tag{1.32b}$$
$$\phi = \phi_0 + \phi_{\mathcal{W}} + \phi_{\mathcal{B}}\,, \tag{1.32c}$$
$$e = e_0 + e_{\mathcal{W}} + e_{\mathcal{B}}\,. \tag{1.32d}$$

$(p_h, \rho_0, \phi_0, e_0)$ describes the state of the fluid before the explosion, where the presence of an initial stationary flow may be taken into account through $\nabla\phi_0$. We however set ϕ_0 to zero for simplicity in the theoretical analyses carried out in this chapter. $(p_{\mathcal{W}}, \rho_{\mathcal{W}}, \phi_{\mathcal{W}}, e_{\mathcal{W}})$ describes the modifications of the quantities due to the shock wave, whereas $(p_{\mathcal{B}}, \rho_{\mathcal{B}}, \phi_{\mathcal{B}}, e_{\mathcal{B}})$ describes those due to the bubble phenomenon. For the shock wave phenomenon, we also

define $u_{\mathcal{W}} = \nabla\phi_{\mathcal{W}} \cdot \mathbf{OM}/\|\mathbf{OM}\|$ as the radial projection of the fluid velocity relative to the initial bursting point O.

The fluid, supposed perfect, is assumed for simplicity to be at rest before the explosion, so that $\mathbf{v}_0 = \mathbf{0}$ and e_0 does not depend on time. Then, ρ_0 is assumed to be constant with respect to space and time, and the hydrostatic pressure at point M is provided by $p_h(M) = \rho_0\, g(\xi_M + \xi_{\text{atm}})$. The surface is assumed to be very far from the region of interest in the fluid, and so is not taken into account. The flow is assumed to be potential for both phenomena, so three velocity potentials are defined as

$$\mathbf{v} = \nabla\phi\,, \quad \mathbf{v}_{\mathcal{W}} = \nabla\phi_{\mathcal{W}}\,, \quad \mathbf{v}_{\mathcal{B}} = \nabla\phi_{\mathcal{B}}\,.$$

The flow created by the bubble is assumed to be incompressible, like in Section 1.3, which implies

$$\rho_{\mathcal{B}} \ll \rho_0\,, \quad \nabla\cdot\mathbf{v}_{\mathcal{B}} \simeq 0\,, \tag{1.33}$$

and the induced pressure is provided by the chosen bubble model. For instance, in the case of the simple bubble model presented previously, the incident bubble pressure is provided by (1.30).

The shock wave speed is assumed to be the common sound speed c in the fluid, which, in view of the empirically-verified approximation (B.12) of the shock wave velocity, is valid if the jump magnitude p_m of the pressure at the considered point, at distance r from the explosion, satisfies $p_m(r) \ll 1$ GPa. The pressure due to the shock wave is assumed to be given by the double-exponential fit (1.4), for any time such that the retarded time is less than 7τ.

Euler equations of fluid dynamics. The linear acoustic and incompressible flow theories are two limiting cases of the Euler equations. To treat both the shock wave and the gas bubble, we therefore go back to the Euler equations of fluid dynamics

$$\begin{cases} \dfrac{\mathrm{d}\rho}{\mathrm{d}t} + \rho\nabla\cdot\mathbf{v} = \dfrac{\partial\rho}{\partial t} + \rho\nabla\cdot\mathbf{v} + (\mathbf{v}\cdot\nabla)\rho = 0 & \text{conservation of mass,} \quad (1.34a) \\ \dfrac{\mathrm{d}\mathbf{v}}{\mathrm{d}t} + \dfrac{1}{\rho}\nabla p = \dfrac{\partial\mathbf{v}}{\partial t} + (\mathbf{v}\cdot\nabla)\mathbf{v} + \dfrac{1}{\rho}\nabla p = \mathbf{g} & \text{conservation of momentum,} \quad (1.34b) \\ \dfrac{\mathrm{d}e}{\mathrm{d}t} + \dfrac{p}{\rho}\nabla\cdot\mathbf{v} = \dfrac{\partial e}{\partial t} + (\mathbf{v}\cdot\nabla)e + \dfrac{p}{\rho}\nabla\cdot\mathbf{v} = 0 & \text{conservation of energy.} \quad (1.34c) \end{cases}$$

Using the decomposition (1.32), and the orders of magnitude (B.18e) and (B.18f), i.e.

$$p_{\mathcal{W}} \sim 10^6 \text{ Pa} \ll \rho_0 c^2 \sim 10^9 \text{ Pa}\,, \quad \rho_{\mathcal{W}} \sim 1 \text{ kg/m}^3 \ll \rho_0 \sim 10^3 \text{ kg/m}^3\,,$$
$$e_{\mathcal{W}} \sim 1 \text{ m}^2/\text{s}^2 \ll c^2 \sim 10^6 \text{ m}^2/\text{s}^2\,, \quad u_{\mathcal{W}} \sim 1 \text{ m/s} \ll c \sim 10^3 \text{ m/s}\,,$$

together with (1.33), the set (1.34) is written as

$$\begin{cases} \dfrac{\partial}{\partial t}(\rho_{\mathcal{W}} + \rho_{\mathcal{B}}) + \rho_0\nabla\cdot\mathbf{v}_{\mathcal{W}} + (\mathbf{v}_{\mathcal{W}} + \mathbf{v}_{\mathcal{B}})\cdot\nabla(\rho_{\mathcal{W}} + \rho_{\mathcal{B}}) \simeq 0\,, & (1.35a) \\ \dfrac{\partial}{\partial t}(\mathbf{v}_{\mathcal{W}} + \mathbf{v}_{\mathcal{B}}) + ((\mathbf{v}_{\mathcal{W}} + \mathbf{v}_{\mathcal{B}})\cdot\nabla)(\mathbf{v}_{\mathcal{W}} + \mathbf{v}_{\mathcal{B}}) + \dfrac{1}{\rho_0}\nabla(p_{\mathcal{W}} + p_{\mathcal{B}}) \simeq \mathbf{0}\,, & (1.35b) \\ \dfrac{\partial}{\partial t}(e_{\mathcal{W}} + e_{\mathcal{B}}) + ((\mathbf{v}_{\mathcal{W}} + \mathbf{v}_{\mathcal{B}})\cdot\nabla)(e_{\mathcal{W}} + e_{\mathcal{B}}) + \dfrac{p_{\mathcal{W}} + p_{\mathcal{B}} + p_h}{\rho_0}\nabla\cdot\mathbf{v}_{\mathcal{W}} \simeq 0\,. & (1.35c) \end{cases}$$

The quantities relative to the shock wave and the oscillating bubble do not temporally vary over the same time scales. Hence, to deal with the set (1.35), the multi scale method (Cousteix and Mauss, 2006) may be of great use.

Multi time scale method. In (Guillard and Abgrall, 2001), the multi time scale method is introduced for dealing with the coexistence of acoustic and incompressible phenomena. The method is based on the decomposition of each physical quantity into "slow" and "fast" contributions. In the case of a far-field underwater explosion, the "slow" contribution corresponds to that of the bubble phenomenon, and the "fast" one to the primary wave.

Two time variables are then introduced: a slow time $t_{\mathcal{B}}$, that will be chosen as the common time variable t, and a fast time $t_{\mathcal{W}} := t/(\tau/T) = t/\mathcal{T}$, where the small non-dimensional parameter $\mathcal{T} := \tau/T$ has a value of typically 10^{-4} to 10^{-3} for a far-field UNDEX. Then, any time-dependent quantity f is described by means of a function $\tilde{f}(t = t_{\mathcal{B}}, t_{\mathcal{W}})$, such that a differentiation with respect to time t is expressed as

$$\frac{\mathrm{d}f(t)}{\mathrm{d}t} \Longleftrightarrow \frac{\partial t_{\mathcal{B}}}{\partial t}\frac{\partial \tilde{f}(t_{\mathcal{B}},t_{\mathcal{W}})}{\partial t_{\mathcal{B}}} + \frac{\partial t_{\mathcal{W}}}{\partial t}\frac{\partial \tilde{f}(t_{\mathcal{B}},t_{\mathcal{W}})}{\partial t_{\mathcal{W}}} = \frac{\partial \tilde{f}(t_{\mathcal{B}},t_{\mathcal{W}})}{\partial t_{\mathcal{B}}} + \frac{1}{\mathcal{T}}\frac{\partial \tilde{f}(t_{\mathcal{B}},t_{\mathcal{W}})}{\partial t_{\mathcal{W}}}\,. \tag{1.36}$$

Using the assumed decomposition (1.32), a physical quantity f is decomposed in three parts

$$\tilde{f}(t, t_{\mathcal{W}}, \mathbf{x}) = \tilde{f}^s(t, \mathbf{x}) + \tilde{f}^f(t_{\mathcal{W}}, \mathbf{x}) = \tilde{f}_0(t, \mathbf{x}) + \tilde{f}_{\mathcal{B}}(t, \mathbf{x}) + \tilde{f}_{\mathcal{W}}(t_{\mathcal{W}}, \mathbf{x})\,,$$

where the slow part $\tilde{f}^s$ does not vary over the time scale τ of the shock wave. Omitting the tilde symbol $\sim$ on the various quantities, (1.35) is rewritten as, using (1.36),

$$\begin{cases} \dfrac{1}{\mathcal{T}}\dfrac{\partial \rho_{\mathcal{W}}}{\partial t_{\mathcal{W}}} + \dfrac{\partial \rho_{\mathcal{B}}}{\partial t} + \rho_0 \nabla\cdot\mathbf{v}_{\mathcal{W}} + (\mathbf{v}_{\mathcal{W}} + \mathbf{v}_{\mathcal{B}})\cdot\nabla(\rho_{\mathcal{W}} + \rho_{\mathcal{B}}) \simeq 0\,, & \text{(1.37a)} \\ \dfrac{1}{\mathcal{T}}\dfrac{\partial \mathbf{v}_{\mathcal{W}}}{\partial t_{\mathcal{W}}} + \dfrac{\partial \mathbf{v}_{\mathcal{B}}}{\partial t} + ((\mathbf{v}_{\mathcal{W}} + \mathbf{v}_{\mathcal{B}})\cdot\nabla)(\mathbf{v}_{\mathcal{W}} + \mathbf{v}_{\mathcal{B}}) + \dfrac{1}{\rho_0}\nabla(p_{\mathcal{W}} + p_{\mathcal{B}}) \simeq \mathbf{0}\,, & \text{(1.37b)} \\ \dfrac{1}{\mathcal{T}}\dfrac{\partial e_{\mathcal{W}}}{\partial t_{\mathcal{W}}} + \dfrac{\partial e_{\mathcal{B}}}{\partial t} + ((\mathbf{v}_{\mathcal{W}} + \mathbf{v}_{\mathcal{B}})\cdot\nabla)(e_{\mathcal{W}} + e_{\mathcal{B}}) + \dfrac{p_{\mathcal{W}} + p_{\mathcal{B}} + p_h}{\rho_0}\nabla\cdot\mathbf{v}_{\mathcal{W}} \simeq 0\,. & \text{(1.37c)} \end{cases}$$

To deal with (1.37), the quantities are assumed to be expandable in power of $\mathcal{T}$ (Cousteix and Mauss, 2006), namely two quantities $f_{\mathcal{W}}$ and $f_{\mathcal{B}}$ are given as expansions

$$f_{\mathcal{W}}(t_{\mathcal{W}}, \mathbf{x}) = f^0_{\mathcal{W}}(t_{\mathcal{W}}, \mathbf{x}) + \mathcal{T} f^1_{\mathcal{W}}(t_{\mathcal{W}}, \mathbf{x}) + \mathcal{T}^2 f^2_{\mathcal{W}}(t_{\mathcal{W}}, \mathbf{x}) + \dots\,, \tag{1.38a}$$

$$f_{\mathcal{B}}(t, \mathbf{x}) = f^0_{\mathcal{B}}(t, \mathbf{x}) + \mathcal{T} f^1_{\mathcal{B}}(t, \mathbf{x}) + \mathcal{T}^2 f^2_{\mathcal{B}}(t, \mathbf{x}) + \dots\,. \tag{1.38b}$$

For the shock wave part, the pressure is of the form

$$p_{\mathcal{W}} \sim \exp(-t/\tau) = \exp(-t_{\mathcal{W}}/T)\,,$$

so only the first (0) component is not zero in the decomposition (1.38a). Using relations (B.18), the same reasoning holds for $\rho_{\mathcal{W}}$ and $e_{\mathcal{W}}$, and therefore the decomposition (1.38a) is not very useful for these quantities. However, for $u_{\mathcal{W}}$, if we consider the after flow term in (1.12), the latter introduces a component of order $\mathcal{T}$:

$$u_{\mathcal{W}}(t_{\mathcal{W}}, \mathbf{x}) = \frac{p_{\mathcal{W}}}{\rho_0\, c} + \frac{1}{r\,\rho_0}\int_0^t p_{\mathcal{W}}(r,\theta)\,\mathrm{d}\theta \sim \frac{p_{\mathcal{W}}}{\rho_0\, c} + \mathcal{T}\alpha\,\frac{T\,p_m(r)}{r\,\rho_0}\,, \tag{1.39}$$

where α is a numerical coefficient of typical value 1.30 for the double-exponential fit (see (1.9)) or 1 for the single-exponential fit. In the absence of the after flow term, all the shock wave quantities vanish when $t_{\mathcal{W}} \to \infty$, and so the multi time scale method is not relevant, because the slow and fast contributions do not really coincide (the fast contribution is zero before the slow contribution starts).

Introducing (1.38) into (1.37) leads to several equations corresponding to different orders in $\mathcal{T}$. The order $1/\mathcal{T}$ yields

$$\boxed{\begin{aligned} \text{mass:} \quad & \frac{\partial \rho^0_{\mathcal{W}}}{\partial t_{\mathcal{W}}} = 0\,, && \text{(1.40a)}\\ \text{momentum:} \quad & \frac{\partial \mathbf{v}^0_{\mathcal{W}}}{\partial t_{\mathcal{W}}} = \mathbf{0}\,, && \text{(1.40b)}\\ \text{energy:} \quad & \frac{\partial e^0_{\mathcal{W}}}{\partial t_{\mathcal{W}}} = 0\,. && \text{(1.40c)} \end{aligned}}$$

(1.40) provides a less refined approximation than (B.18). Indeed, it implies that $\rho^0_{\mathcal{W}}(\mathbf{x})$ and $e^0_{\mathcal{W}}(\mathbf{x})$ do not depend on $t_{\mathcal{W}}$. We then retrieve the simplest hypotheses of linear acoustics: $\rho^0_{\mathcal{W}} = 0$ and $e^0_{\mathcal{W}} = 0$, while (B.18) provides a more refined approximation (where the limit when $t_{\mathcal{W}} \to \infty$ is zero, but $\rho^0_{\mathcal{W}} \neq 0$ and $e^0_{\mathcal{W}} \neq 0$). Hence, any quantity $f^0_{\mathcal{W}}$ is either zero or exponentially decaying with $t_{\mathcal{W}}$.

For the order 0, it comes:

$$\begin{aligned} \text{mass:} \quad & \frac{\partial \rho^1_{\mathcal{W}}}{\partial t_{\mathcal{W}}} + \frac{\partial \rho^0_{\mathcal{B}}}{\partial t} + \mathbf{v}^0_{\mathcal{B}} \cdot \nabla \rho^0_{\mathcal{B}} = 0\,, && \text{(1.41a)}\\ \text{momentum:} \quad & \frac{\partial \mathbf{v}^1_{\mathcal{W}}}{\partial t_{\mathcal{W}}} + \frac{\partial \mathbf{v}^0_{\mathcal{B}}}{\partial t} + (\mathbf{v}^0_{\mathcal{B}} \cdot \nabla)\mathbf{v}^0_{\mathcal{B}} + \frac{1}{\rho_0}\nabla p^0_{\mathcal{B}} = \mathbf{0}\,, && \text{(1.41b)}\\ \text{energy:} \quad & \frac{\partial e^1_{\mathcal{W}}}{\partial t_{\mathcal{W}}} + \frac{\partial e^0_{\mathcal{B}}}{\partial t} + (\mathbf{v}^0_{\mathcal{B}} \cdot \nabla) e^0_{\mathcal{B}} = 0\,. && \text{(1.41c)} \end{aligned}$$

Again, the quantities $\rho_{\mathcal{W}}$, $p_{\mathcal{W}}$ and $e_{\mathcal{W}}$ are at most exponentially decaying according to (B.18), and so the coefficients in their decomposition of power of $\mathcal{T}$ are zero at any non-zero order. For the velocity $\mathbf{v}_{\mathcal{W}}$, the after flow term in (1.12) introduces a non-zero coefficient in (1.39), that is independent of time, so the set (1.41) simply reduces to the Euler equations for an incompressible flow for the 0-component of the bubble quantities

$$\boxed{\begin{aligned} \text{mass:} \quad & \frac{\partial \rho^0_{\mathcal{B}}}{\partial t} + \mathbf{v}^0_{\mathcal{B}} \cdot \nabla \rho^0_{\mathcal{B}} = 0\,, && \text{(1.42a)}\\ \text{momentum:} \quad & \frac{\partial \mathbf{v}^0_{\mathcal{B}}}{\partial t} + (\mathbf{v}^0_{\mathcal{B}} \cdot \nabla)\mathbf{v}^0_{\mathcal{B}} + \frac{1}{\rho_0}\nabla p^0_{\mathcal{B}} = \mathbf{0}\,, && \text{(1.42b)}\\ \text{energy:} \quad & \frac{\partial e^0_{\mathcal{B}}}{\partial t} + (\mathbf{v}^0_{\mathcal{B}} \cdot \nabla) e^0_{\mathcal{B}} = 0\,. && \text{(1.42c)} \end{aligned}}$$

The equations for the order $\mathcal{T}$ shows the impact of the non-zero component $\mathbf{v}^1_{\mathcal{W}}(\mathbf{x})$ of the shock wave on the bubble components

$$\boxed{\begin{aligned} \text{mass:} \quad & \frac{\partial \rho^1_{\mathcal{B}}}{\partial t} + (\mathbf{v}^1_{\mathcal{W}} + \mathbf{v}^1_{\mathcal{B}}) \cdot \nabla \rho^0_{\mathcal{B}} + \mathbf{v}^0_{\mathcal{B}} \cdot \nabla \rho^1_{\mathcal{B}} = 0\,, && \text{(1.43a)}\\ \text{mom.:} \quad & \frac{\partial \mathbf{v}^1_{\mathcal{B}}}{\partial t} + ((\mathbf{v}^1_{\mathcal{W}} + \mathbf{v}^1_{\mathcal{B}}) \cdot \nabla)\mathbf{v}^0_{\mathcal{B}} + (\mathbf{v}^0_{\mathcal{B}} \cdot \nabla)(\mathbf{v}^1_{\mathcal{W}} + \mathbf{v}^1_{\mathcal{B}}) + \frac{1}{\rho_0}\nabla p^1_{\mathcal{B}} = \mathbf{0}\,, && \text{(1.43b)}\\ \text{energy:} \quad & \frac{\partial e^1_{\mathcal{B}}}{\partial t} + (\mathbf{v}^1_{\mathcal{W}} + \mathbf{v}^1_{\mathcal{B}}) \cdot \nabla) e^0_{\mathcal{B}} + (\mathbf{v}^0_{\mathcal{B}} \cdot \nabla) e^1_{\mathcal{B}} = 0\,. && \text{(1.43c)} \end{aligned}}$$

Conclusion. The three sets (1.40), (1.42) and (1.43) show that only the after flow term of the shock wave phenomenon impacts the bubble part. This makes sense as it is the only shock wave contribution that do not vanish when $t_{\mathcal{W}} \to \infty$. (1.42) shows that, even for a non-zero after flow term, the first order contribution of the bubble phenomenon is not affected by the shock wave. This notably suggests that the strong assumption (1.32) is justified for the first order of the decomposition, but it is not valid for higher orders.

In Section 1.2.2, we computed orders of magnitudes to show that the after flow term does not need to be taken into account for the cases we study. Then, if this after flow term is not considered, the multi scale method confirms the possibility of two separated treatments, with a junction numerically performed when the shock wave contribution to the pressure is almost zero, and that of the oscillating bubble has not yet reached a significant value. In other words, if the after flow is neglected, the fluid-structure interaction problems associated to the shock wave phenomenon and the oscillating bubble may be treated one by one. However, they should not be treated strictly separately, in the sense that the initial conditions for the oscillating bubble problem (in particular, the structure state) should be set to the output of the shock wave problem.

In this work, the junction, illustrated in Figure 1.5 is rather performed once the shock wave incident pressure has sufficiently decreased, so a bit later than on Figure 1.5. Also, to avoid to introduce a discontinuity in the pressure, a smoothing process is used at the junction between the two phenomena. This will be discussed later in Chapter 5.

1.5 Conclusion and outline of this thesis

The overall conclusion of this chapter may be summed up concisely: for far-field underwater explosions, (i) the shock wave propagation is governed by the wave equation, within the framework of linear acoustics, and (ii) the perturbation induced by the oscillating bubble is dealt with in the context of incompressible potential flow, with the Laplace equation. For far-field UNDEX, the transition between the two phenomena is performed once the shock wave incident pressure is zero, and smooth step functions are used to avoid discontinuous pressure jumps. For both phenomena, this work is restricted to the case of an infinite ocean, i.e., the free (water) surface and the seabed are not taken into account.

Under these assumptions, the fluid-structure interaction for the shock wave part is efficiently treated with a FEM/BEM coupling. Chapter 2 lays down the foundation for this first approach, in which the fluid part is treated in the framework of the *Boundary Element Method (BEM)*, whereas the structure part is dealt with using the *Finite Element Method (FEM)*. We notably propose a numerical method to efficiently deal with 3D rapid transient acoustic problems set in large exterior domains, with $O(1)$ time complexity and $O(N \log N)$ space complexity (N being the number of spatial degrees of freedom). The method efficiency is illustrated on some examples of applications in the case of fluid-structure interaction: the radiation of an acoustic wave into a fluid by a deformable structure with prescribed velocity, and the scattering of an abrupt wave by simple and realistic geometries.

Chapter 3 deals with the FSI coupling for the shock wave part. First, inspired by domain decomposition methods, we propose a FEM/BEM coupling using the procedure developed in Chapter 2, and explain why it is not perfectly appropriate given the industrial constraints tied to our problem. Then, taking advantage of the fluid decomposition into a radiated (radiation problems) and a reflected (scattering problems) components, we examine the characteristics of the radiated pressure, which concentrates the coupled part of the FSI problem. As a result of this analysis, we adapt the procedure in such a way that the coupled part of the FSI problem is now solved with a FEM/FEM coupling. Far

from being the ideal solution, the obtained computational method nonetheless efficiently tackles the difficult FSI problem, as it is illustrated in the reference case of a long cylinder subjected to an underwater explosion. In particular, a comparison to other numerical methods validates our procedure, with very promising results.

Based on the modelling we retained for the bubble part, Chapter 4 focuses on FSI problems for incompressible flows. We first stress the time-(in)dependence aspects of the fluid problem, in contrast to the acoustic case (shock wave phase). Then, we introduce the hierarchical matrices (Hmat), an acceleration technique for the BEM that is efficient when dealing with multiple right hand-sides. Thereafter, we present the step-by-step FEM/BEM coupling procedure we choose to solve the FSI problem. We validate the method on the simple problem of a sphere in a uniform time-dependent flow, before solving the FSI problem of a gas bubble impacting a stiffened submarine hull. We pay particular attention to the numerical techniques enabling a faster convergence of the iterative FEM/BEM coupling procedure, such as relaxation techniques and the use of well-chosen initial guesses.

This work concludes with the treatment of an industrial case: a submarine stiffened hull subjected to a remote underwater explosion. The purpose of this Chapter 5 is to show the efficiency of the computational method, when gathering all the results obtained throughout this work. The engineering study conducted represents a prime example of the target applications of this work, but remains an example: the tools developed during this work can actually address a wide variety of problems.

Chapter 2

$\mathcal{Z}$-transform and high-frequency approximations for large-scale 3D rapid transient wave problems

BUILDING on the available knowledge surveyed in Chapter 1, the purpose of this chapter is to design a computational method to address the shock wave phenomenon. Most of its content is published in (Mavaleix-Marchessoux et al., 2020).

We do not study coupled FSI problems in this chapter, this matter being deferred to Chapter 3, but rather focus on the fluid part of the shock wave phenomenon, namely large-scale 3D rapid transient wave problems. To do so, it is useful to first recall the motivation and industrial constraints, as they drive the choice of the numerical method.

2.1 Motivation and industrial constraints

The overall purpose of this work is to design, implement and eventually validate a robust, accurate, fast numerical method to appreciate fluid-structure interactions for rapid dynamic problems (shock wave) and slower potential flows (oscillating bubble). This objective is subject to practical industrial constraints which highly influence the design of the numerical methods.

Analysing the effect of explosions on naval structures is one of the important topics of Naval Group Research. Since the work of Cole (Cole, 1948), it has been extensively studied both in Naval Group (recently: Leblond, 2007; Longère et al., 2013) and the Direction Générale de l'Armement (DGA; English: Directorate General of Armaments) (recently: Barras, 2012; Brochard, 2018). One goal of this work is to benefit from the previous studies and already available procedures, and enhance them to better simulate the phenomenon. In particular, an important industrial requirement was to use a FEM procedure to model the structure behaviour, implemented with the industrial code Abaqus®. In other words, for the structure part, we must comply with previous choices of modelling platforms, that are nonetheless relevant. At this point, it is important to stress that Abaqus® is not an open source software, with all the limitations this implies.

A key purpose of this thesis is to be able to deal with 3D rapid transient acoustic perturbations in water (shock wave) that impact large structures. Typically, the procedure must be able to model the effects of an incident field with a frequency content up to $f \sim 3$ kHz, on a submarine-like structure of length $L = 140$ m and diameter $D = 13$ m. It is instructive to evaluate some orders of magnitude, as they underscore the computational

challenges to address.

Consider a long cylinder closed by two half-spheres, with length $L = 140$ m and diameter $D = 13$ m. The total area of the structure is

$$A = \pi D(L - D) + \pi D^2 \approx 5700 \text{ m}^2.$$

The wavelength associated to a frequency of $f \sim 3$ kHz in water is

$$\lambda = c_f / f \approx 0.5 \text{ m}.$$

In order to meet the conventional rule of ten points per wavelength, the linear mesh size for the fluid part should be $h \approx 0.05$ m. Assume the fluid mechanics problem in the unbounded domain surrounding the structure is solved with a method that requires only the discretisation of the fluid-structure interface (like the BEM), for instance using a triangular mesh with one degree of freedom (DOF) per node. The typical area of a triangle is then $A_{\text{tri}} \sim h^2/2$, so the typical number of triangles needed to mesh the structure is $n \sim 2A/h^2 \sim 4.6\ 10^6$. This results in approximately $N \sim 2.3\ 10^6$ DOFs. Such a high number of DOFs is beyond the capabilities of standard BEMs, but nevertheless within reach of current fast BEMs.

Now, let assume the fluid part is rather solved with a volume method (like the FEM). A fluid volume mesh that surrounds the cylinder has to be generated. Consider as a minimal example a water layer of 2 m all around the structure. The exterior boundary of the 3D mesh is then a cylinder closed by two half-spheres, with length $l = 144$ m and diameter $d = 17$ m. Assume that the water layer is thick enough and the absorbing boundary conditions on the exterior surface are efficient enough so that the problem does not suffer from unphysical reflections. In this case, the main limitation of this domain-based approach would be the number of DOFs needed for the fluid part. To estimate the number of elements of such a mesh, the total volume of the mesh

$$V_{\text{tot}} = V_{\text{ext}} - V_{\text{int}} = \pi(d/2)^2(l - d) + \frac{4}{3}\pi(d/2)^3 - \left(\pi(D/2)^2(L - D) + \frac{4}{3}\pi(D/2)^3\right)$$

is to be divided by the typical volume of a hexahedron mesh cell. Using the previous computed value of $h \approx 0.05$ m, it holds

$$N \approx V_{\text{tot}}/h^3 \sim 10^8\,,$$

which appears to be quite a huge number considering the transient nature of the problem (the time discretisation must also be considered). In that case, the cubic dependence of N on the geometry dimensions stands as a significant limitation. This simple analysis of order of magnitudes appears to favour surface-based discretisation methods. Hence, we adopt a boundary integral equation (BIE) approach for solving the (linear acoustic) fluid problem associated with the shock wave.

This chapter presents the theories and concepts applied to address the solution of transient 3D acoustic problems using BIEs. It begins with a general introduction to BIEs for 3D acoustics (Lenoir, 2016; Sayas, 2016; Nédélec, 2001) in Section 2.2. Then, in Section 2.3, we introduce a numerical method, thereafter named $\mathcal{Z}$-BEM, that permits a reformulation of the time-domain BIE in terms of a set of frequency-domain BIEs. The numerical counterpart of BIE, the Boundary Element Method (BEM) (Bonnet, 1999; Dominguez, 1993; Banerjee, 1994; Shaw, 1966) is presented in Section 2.4, in the frequency domain. In particular, the Fast Multipole BEM (FM-BEM) (Chaillat, 2008; Ying, 2012), an

accelerated BEM, is presented in Section 2.4.2. Section 2.5 is dedicated to the improvement of the $\mathcal{Z}$-BEM procedure for rapid transient problems. Finally, in Sections 2.6 and 2.7, we present examples of applications to illustrate the efficiency of the procedure in the case of fluid-structure interaction.

2.2 Boundary Integral Equations for 3D acoustics

Boundary Integral Equations (BIEs) were initially introduced at the end of the nineteenth century; Kirchhoff's integral theorem (Kirchhoff, 1883) was for instance formulated in 1882. In this section, we introduce the theory for linear 3D acoustics.

2.2.1 Transient wave propagation problems

Theoretical formulation in an exterior domain, of the form $\mathbb{R}^3 \setminus \overline{\Omega_s}$

We consider transient linear wave propagation problems in an exterior acoustic domain of the form $\Omega_f = \mathbb{R}^3 \setminus \overline{\Omega_s}$, where Ω_s denotes a bounded Lipschitz (Sayas, 2016, Appendix D) domain with boundary Γ (see Figure 2.1).

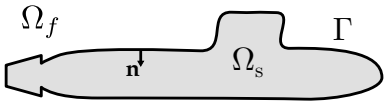

Figure 2.1: Acoustic unbounded domain $\Omega_f = \mathbb{R}^3 \setminus \overline{\Omega_s}$.

Both the velocity potential and the pressure satisfy the wave equation, so that ψ may refer to either physical quantity in what follows. Assuming the fluid to be at initial rest, the problems of interest have the form:

$$\text{Find } \psi \text{ such that } \begin{cases} \Delta\psi - \dfrac{1}{c^2}\dfrac{\partial^2\psi}{\partial t^2} = 0 & (\mathbf{x},t) \in \Omega_f \times [0,T]\,, \\ \psi(\mathbf{x},0) = 0 & \mathbf{x} \in \Omega_f\,, \\ \dfrac{\partial\psi}{\partial t}(\mathbf{x},0) = 0 & \mathbf{x} \in \Omega_f\,, \\ \text{Boundary condition} & \mathbf{x} \in \Gamma, \end{cases} \tag{2.1}$$

where $T > 0$ is the considered finite duration, and $c \equiv c_f$ is the fluid sound velocity. If $T = +\infty$, or in the frequency domain, the solution of (2.1) must also satisfy some radiation conditions to ensure the uniqueness of ψ and implies that it corresponds to outward waves. For finite T, which we assume in the following, there is no need to specify such decay conditions because the propagation takes place in a finite domain, due to the finite speed c, and so the support of $\psi(\cdot,t)$ is a bounded region of Ω_f for all $t \in [0,T]$. Therefore, in the following, $\Omega \subset \Omega_f$ refers to a (large enough) bounded domain such that any wave emitted from a point of Γ, or a possible fixed point source in the fluid domain (e.g., the locus of an underwater blast), cannot reach the exterior boundary of Ω due to causality. The spatial boundary conditions in (2.1) involve ψ or $\frac{\partial\psi}{\partial n} \equiv \nabla\psi \cdot \mathbf{n}$ on the surface, where $\mathbf{n}$ denotes the **outward normal to Ω_f** (**inward normal to Ω_s**). Examples are given later in Section 2.5.1.

All the derivatives written in (2.1) have to be understood as derivative of distributions, and ψ, treated as a function of time in this case, having values in some space E of functions

defined in Ω:

$$\begin{array}{ccc} [0,T] & \longrightarrow & E \\ t & \longmapsto & \psi(t,\cdot)\,, \end{array}$$

is expected to have enough regularity to make the variational form of (2.1) meaningful. For instance, with Dirichlet boundary condition $\psi = 0$ on Γ in (2.1), introducing the standard function spaces

$$L^2(\Omega) \equiv \left\{ f \,\middle/ \int_\Omega f^2 < \infty \right\}, \quad H_0^1(\Omega) \equiv \left\{ f \,\middle/ f \in L^2(\Omega), \nabla f \in \left(L^2(\Omega)\right)^3, f = 0 \text{ on } \partial\Omega \right\},$$

ψ is then usually sought in $\mathcal{E} \equiv \mathcal{C}^0([0,T]; H_0^1(\Omega)) \cap \mathcal{C}^1([0,T]; L^2(\Omega))$ (Allaire, 2012).

Solution to a point source. To solve (2.1), the problem related to a point source is first studied. Consider a fixed point $\mathbf{y} \in \Omega$. A point source is applied at $\mathbf{y}$, with a time modulated intensity $f(t)$, assumed to be twice continuously differentiable and such that $f(t) = \dot{f}(t) = 0, \forall t \leq 0$. In that case, (2.1) is transformed into:

$$\text{Find } G \text{ such that } \begin{cases} \Delta G - \dfrac{1}{c^2}\dfrac{\partial^2 G}{\partial t^2} + \delta(\mathbf{y}-\mathbf{x}) f(t) = 0 & \forall (\mathbf{x},t) \in \Omega \times [0,T]\,, \\ G(\mathbf{x},0) = 0 & \forall \mathbf{x} \in \Omega\,, \\ \dfrac{\partial G}{\partial t}(\mathbf{x},0) = 0 & \forall \mathbf{x} \in \Omega\,, \\ \text{Boundary condition} & \mathbf{x} \in \Gamma. \end{cases} \tag{2.2}$$

The solution to (2.2), if it exists, depends on the boundary conditions on Γ.

Free space fundamental solution. In the case where $\Omega_s = \varnothing$, the solution to (2.2) is called *free space fundamental solution* and is given by:

$$G(\mathbf{y},t,\mathbf{x}|f) \equiv G(\mathbf{y}-\mathbf{x},t|f) = \frac{f(t-r/c)}{4\pi r}, \quad r \equiv \|\mathbf{y}-\mathbf{x}\|\,, \tag{2.3}$$

$$\frac{\partial G}{\partial x^j}(\mathbf{y},t,\mathbf{x}|f) = -\frac{1}{4\pi r^2}\frac{\partial r}{\partial x^j}\left(f(t-r/c) + \frac{r}{c}\dot{f}(t-r/c) \right),$$

where x^j is the j-component of the field point $\mathbf{x}$ and $\dot{f}(u)$ denotes the derivative of f with respect to its argument, evaluated at u.
Note that $G(\mathbf{y},t,\mathbf{x}|f) = G(\mathbf{x},t,\mathbf{y}|f)$ and $\dfrac{\partial G}{\partial x^j}(\mathbf{y},t,\mathbf{x}|f) = -\dfrac{\partial G}{\partial y^j}(\mathbf{y},t,\mathbf{x}|f)$.

Impulsive fundamental solution. Consider the special case of an impulsive source, that is when $f(t) = \delta(t)$ in (2.2). The impulsive fundamental solution

$$G(\mathbf{y},t,\mathbf{x}) \equiv G(\mathbf{y},t,\mathbf{x}|\delta) = \frac{\delta(t-r/c)}{4\pi r}\,, \tag{2.4}$$

satisfies

$$G(\mathbf{y},0,\mathbf{x}) = \frac{\partial G}{\partial t}(\mathbf{y},0,\mathbf{x}) = 0\,, \quad \forall \mathbf{x} \neq \mathbf{y}\,,$$

$$G(\mathbf{y},t,\mathbf{x}|f) = G(\mathbf{y},t,\mathbf{x}) \star f\,, \tag{2.5}$$

where $\star$ denotes the time convolution product, defined for causal functions as

$$(u \star v)(t) = \int_0^t u(t-\tau)v(\tau)\,\mathrm{d}\tau = \int_0^t v(t-\tau)u(\tau)\,\mathrm{d}\tau = (v \star u)(t)\,, \quad \forall t \geq 0\,.$$

The relation (2.5) is obtained noting that

$$\frac{\partial(u \star v)}{\partial t} = \frac{\partial u}{\partial t} \star v = u \star \frac{\partial v}{\partial t}\,, \tag{2.6}$$

and using the property of δ

$$f(t) = \int_0^t f(t-\tau)\delta(\tau)\,\mathrm{d}\tau = (f \star \delta)(t)\,,$$

where "$\int_0^t f(t-\tau)\delta(\tau)\mathrm{d}\tau$" is an abuse of notation for the application of the Dirac distribution on the function f.

2.2.2 Integral representation formula for the interior problem

The problem (2.1) is termed at *initial rest* because of its initial conditions. Note also that no known body source $\mathcal{F}$ appears in its first equation. The general case, with $\mathcal{F} \neq 0$ and generic initial conditions is presented in (Bonnet, 1999).

To establish the boundary integral equation linked to the problem (2.1), it is convenient to first deal with a bounded domain $\Omega \subset \mathbb{R}^3$ without shell within (see Figure 2.2). In the following, the representation formula is derived for this bounded domain Ω; the corresponding problem (2.1) is then termed *interior problem*.

Consider a fixed point $\mathbf{y} \in \Omega$. We apply the time convolution between the equation satisfied by the impulsive fundamental solution G and the solution $\psi(\mathbf{x},t)$ to (2.1):

$$\left(\Delta_{\mathbf{x}} G(\mathbf{y},\cdot,\mathbf{x}) \star \psi(\mathbf{x},\cdot)\right)(t) - \left(\frac{1}{c^2}\frac{\partial^2 G}{\partial t^2}(\mathbf{y},\cdot,\mathbf{x}) \star \psi(\mathbf{x},\cdot)\right)(t) + \delta(\mathbf{y}-\mathbf{x})\psi(\mathbf{x},t) = 0. \tag{2.7}$$

Using (2.6) and the wave equation satisfied by ψ, (2.7) becomes

$$\left(\Delta_{\mathbf{x}} G(\mathbf{y},\cdot,\mathbf{x}) \star \psi(\mathbf{x},\cdot)\right)(t) - \left(G(\mathbf{y},\cdot,\mathbf{x}) \star \Delta_{\mathbf{x}}\psi(\mathbf{x},\cdot)\right)(t) + \delta(\mathbf{y}-\mathbf{x})\psi(\mathbf{x},t) = 0. \tag{2.8}$$

To obtain the sought integral representation, we cannot integrate (2.8) over Ω and use the Green's second identity

$$\forall u \in H^1(\Omega;\Delta), v \in H^1(\Omega;\Delta), \int_\Omega \Delta u\, v - \Delta v\, u\,\mathrm{d}V = \int_{\partial\Omega} \frac{\partial u}{\partial n} v - \frac{\partial v}{\partial n} u\,\mathrm{d}\Gamma\,,$$

because G and δ are distributions. Instead, the problem must be studied in a punctured domain $\Omega_\varepsilon = \Omega \setminus B(\mathbf{y},\varepsilon)$ obtained by removing a ball of radius ε and centre $\mathbf{y}$. The integral representation is then obtained through a limiting process when $\varepsilon \to 0$ (McLean, 2000) and holds as

$$\int_{\mathbf{x}\in\partial\Omega} \left(\frac{\partial G}{\partial n_{\mathbf{x}}}(\mathbf{y},\cdot,\mathbf{x}) \star \psi(\mathbf{x},\cdot)\right)(t) - \left(G(\mathbf{y},\cdot,\mathbf{x}) \star \frac{\partial \psi}{\partial n_{\mathbf{x}}}(\mathbf{x},\cdot)\right)(t)\,\mathrm{d}\Gamma_x + \psi(\mathbf{y},t) = 0\,. \tag{2.9}$$

(2.9) is easily generalised to $\mathbb{R}^3 \setminus \partial\Omega$: $\forall t \geq 0$, $\forall \mathbf{y} \in \mathbb{R}^3 \setminus \partial\Omega$,

$$\boxed{\kappa_{\mathbf{y}}\,\psi(\mathbf{y},t) = \int_{\partial\Omega} \left(\frac{\partial \psi}{\partial n}(\mathbf{x},t) \star G(\mathbf{y},t,\mathbf{x}) - \frac{\partial G}{\partial n}(\mathbf{y},t,\mathbf{x}) \star \psi(\mathbf{x},t)\right)\mathrm{d}\Gamma_x} \tag{2.10}$$

where $\kappa_{\mathbf{y}} = 1$ if $\mathbf{y} \in \Omega$, $\kappa_{\mathbf{y}} = 0$ if $\mathbf{y} \in \mathbb{R}^3 \setminus \overline{\Omega}$, and $\mathbf{n}$ denotes the **outward normal to** Ω. (2.10) is termed boundary integral representation formula because it expresses $\psi(\mathbf{y}, t)$ in terms of the variables on the boundary.

(2.10) holds for $\mathbf{y} \in \mathbb{R}^3 \setminus \partial\Omega$. The next step is to obtain the counterpart of (2.10) for $\mathbf{y} \in \partial\Omega$. This is the tricky part, because of the singular behaviour of the fundamental solution (2.4) when $\mathbf{x} = \mathbf{y}$. All the details are not presented here, only the general steps are depicted in the next section (see Bonnet, 1999, for a more comprehensive study).

2.2.3 Time domain Boundary Integral Equations

Boundary integral equation for the interior problem. In this subsection, $\Omega \subset \mathbb{R}^3$ still denotes a bounded domain. To formulate the counterpart of (2.10) for $\mathbf{y} \in \partial\Omega$, a punctured domain $\Omega_\varepsilon \equiv \Omega \setminus v_\varepsilon(\mathbf{y})$ is created by removing a neighbourhood $v_\varepsilon(\mathbf{y}) = \Omega \cap \overline{B(\mathbf{y}, \varepsilon)}$ of $\mathbf{y}$ included in a sphere of diameter ε (see Figure 2.2).
Therefore, $\partial\Omega_\varepsilon = \partial\Omega - (\partial\Omega \cap v_\varepsilon) + (\Omega \setminus \partial\Omega) \cap \partial v_\varepsilon$.

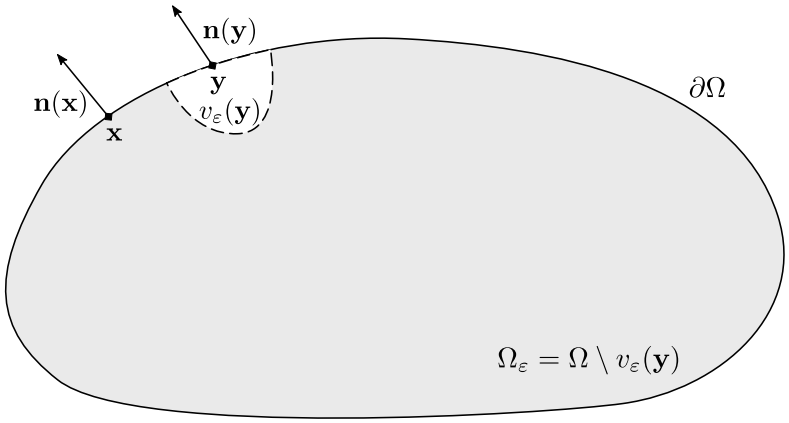

Figure 2.2: Geometrical notations used for the derivation of the boundary integral equation for the interior problem.

The boundary integral equation is obtained as the limiting form of (2.10) applied to Ω_ε

$$0 = \int_{\partial\Omega_\varepsilon} \left(\frac{\partial\psi}{\partial n}(\mathbf{x}, t) \star G(\mathbf{y}, t, \mathbf{x}) - \frac{\partial G}{\partial n}(\mathbf{y}, t, \mathbf{x}) \star \psi(\mathbf{x}, t) \right) \mathrm{d}\Gamma_x \tag{2.11}$$

when $\varepsilon \to 0$. To do so, (2.11) is cut into two integrals: one running over $\partial\Omega_\varepsilon \setminus \partial v_\varepsilon$, and the other one over $\partial\Omega_\varepsilon \cap \partial v_\varepsilon$. It is shown in (Bonnet, 1999) that the integral over $\partial\Omega_\varepsilon \cap \partial v_\varepsilon$ converges when $\varepsilon \to 0$, and provides the opposite of the *free term* $\kappa(\mathbf{y}) = \alpha/(4\pi)$, where α is the solid angle. For a regular boundary, $\kappa(\mathbf{y}) = 1/2$. Hence, the boundary integral equation is obtained for the interior problem: $\forall \mathbf{y} \in \partial\Omega$,

$$\kappa(\mathbf{y})\psi(\mathbf{y}, t) = \int_{\partial\Omega} \left(\frac{\partial\psi}{\partial n}(\mathbf{x}, t) \star G(\mathbf{y}, t, \mathbf{x}) - \frac{\partial G}{\partial n}(\mathbf{y}, t, \mathbf{x}) \star \psi(\mathbf{x}, t) \right) \mathrm{d}\Gamma_x \,. \tag{2.12}$$

Boundary integral equation for the exterior problem

The purpose is now to obtain the boundary integral equation for the problem (2.1), for an exterior domain $\Omega \subset \Omega_f = \mathbb{R}^3 \setminus \overline{\Omega_s}$. Let for instance choose a domain $\Omega \equiv \Omega_R$ bounded by a sphere S_R of centre a point within Ω_s and large enough radius R (to ensure the solution is zero on S_R), as illustrated in Figure 2.3.

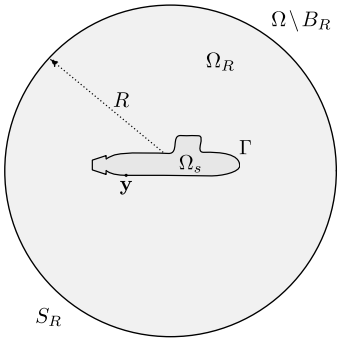

Figure 2.3: Geometrical notations used for the derivation of the boundary integral equation for the exterior problem.

Let $\mathbf{y}$ be a fixed point on $\partial\Omega_s$. For Ω_R, (2.12) provides

$$\kappa(\mathbf{y})\psi(\mathbf{y},t) = \int_{\partial\Omega_R} \left(\frac{\partial\psi}{\partial n}(\mathbf{x},t) \star G(\mathbf{y},t,\mathbf{x}) - \frac{\partial G}{\partial n}(\mathbf{y},t,\mathbf{x}) \star \psi(\mathbf{x},t) \right) \mathrm{d}\Gamma_x \,.$$

Using $\partial\Omega_R = \partial\Omega_s + S_R$, it comes

$$\begin{aligned}\kappa(\mathbf{y})\psi(\mathbf{y},t) = &\int_{\partial\Omega_s} \left(\frac{\partial\psi}{\partial n_s}(\mathbf{x},t) \star G(\mathbf{y},t,\mathbf{x}) - \frac{\partial G}{\partial n_s}(\mathbf{y},t,\mathbf{x}) \star \psi(\mathbf{x},t) \right) \mathrm{d}\Gamma_x \\ &+ \int_{S_R} \left(\frac{\partial\psi}{\partial n_R}(\mathbf{x},t) \star G(\mathbf{y},t,\mathbf{x}) - \frac{\partial G}{\partial n_R}(\mathbf{y},t,\mathbf{x}) \star \psi(\mathbf{x},t) \right) \mathrm{d}\Gamma_x \,.\end{aligned}$$

For a sufficiently large R (typically $R = O(cT)$) causality implies that

$$\int_{S_R} \left(\frac{\partial\psi}{\partial n_R}(\mathbf{x},t) \star G(\mathbf{y},t,\mathbf{x}) - \frac{\partial G}{\partial n_R}(\mathbf{y},t,\mathbf{x}) \star \psi(\mathbf{x},t) \right) \mathrm{d}\Gamma_x = 0 \,. \tag{2.13}$$

Then, the boundary integral equation is obtained for the exterior problem by using (2.13) and redefining the normal $\mathbf{n}$ as the **outward normal to** Ω_s:

$$\boxed{\varepsilon(\mathbf{y})\psi(\mathbf{y},t) = -\int_\Gamma \left(\frac{\partial\psi}{\partial n}(\mathbf{x},t) \star G(\mathbf{y},t,\mathbf{x}) - \frac{\partial G}{\partial n}(\mathbf{y},t,\mathbf{x}) \star \psi(\mathbf{x},t) \right) \mathrm{d}\Gamma_x \,, \mathbf{y} \in \mathbb{R}^3} \tag{2.14}$$

where $4\pi\varepsilon$ is the solid angle: $\varepsilon(P) = 1$ if $P \in \mathbb{R}^3 \setminus \overline{\Omega_s} = \Omega_f$, $\varepsilon(P) = 1/2$ if $P \in \Gamma$ where Γ is regular, $\varepsilon(P) = 0$ if $P \in \Omega_s$. Equation (2.14) is the generic form of boundary integral equations for an exterior domain set in the time domain. It may be rewritten as

$$\psi(\mathbf{y},t) = \mathcal{H}\{\psi\}(\mathbf{y},t) - \mathcal{G}\Big\{ \frac{\partial\psi}{\partial n} \Big\}(\mathbf{y},t) \qquad \mathbf{y} \in \Omega_f,\, t \in [0,T]$$

in terms of its Dirichlet and Neumann traces on Γ, where $\mathcal{G}\{f\}$ and $\mathcal{H}\{g\}$ are the single-layer and double-layer retarded potentials with densities f, g, defined for $\mathbf{y} \in \mathbb{R}^3 \setminus \Gamma$ by

$$\mathcal{G}\{f\}(\mathbf{y},t) = \int_\Gamma G(\mathbf{x}-\mathbf{y},t) \star f(\mathbf{x},t)\, \mathrm{d}\Gamma_x, \qquad \mathcal{H}\{g\}(\mathbf{y},t) = \int_\Gamma \frac{\partial G}{\partial n}(\mathbf{x}-\mathbf{y},t) \star g(\mathbf{x},t)\, \mathrm{d}\Gamma_x. \tag{2.15}$$

On a regular boundary Γ, it holds

$$\tfrac{1}{2}\psi(\mathbf{y},t) - \mathcal{H}\{\psi\}(\mathbf{y},t) + \mathcal{G}\Big\{ \frac{\partial\psi}{\partial n} \Big\}(\mathbf{y},t) = 0 \qquad \mathbf{y} \in \Gamma,\, t \in [0,T], \tag{2.16}$$

where $\mathcal{G}$ and $\mathcal{H}$ are the (weakly singular) boundary integral operators defined by formulas (2.15) with $\mathbf{y} \in \Gamma$. Substituting the relevant boundary condition into (2.16) finally produces a BIE governing the remaining unknown (see examples in Section 2.5.1).

Remark 4 *The boundary integral equation (2.14) can be equivalently recast*[1] *in the form of the Kirchhoff retarded potential formula, expressed for the velocity potential ϕ as*

$$4\pi\varepsilon(P)\phi(P,t) = -\int_\Gamma \left\{ \frac{1}{r}\frac{\partial\phi}{\partial n}(Q,t_r) + \frac{1}{r^2}\frac{\partial r}{\partial n}\phi(Q,t_r) + \frac{1}{cr}\frac{\partial r}{\partial n}\dot{\phi}(Q,t_r) \right\} \mathrm{d}S_Q\,, \tag{2.17}$$

where $\dot{\phi}(Q,\cdot)$ denotes the derivative of $\phi(Q,\cdot)$ with respect to its variable, r denotes the distance between P and $Q \in \Gamma$, $t_r \equiv t - r/c$ is the retarded time, $\mathbf{n}$ is the outward normal to the surface, going into the fluid, and ε is that previously introduced.

2.3 Time-domain BIE using the $\mathcal{Z}$-transform, $\mathcal{Z}$-BEM

The classical approach for the numerical solution of BIEs in the time domain, known as retarded potential BEM, exploits a direct space-time discretisation (Dominguez, 1993; Gwinner and Stephan, 2018; Antes, 1985; Ha-Duong, 2003; Abboud et al., 2001; Aimi et al., 2009; Costabel, 2004). It is delicate to implement because the fundamental solutions (2.3) couple the space and time variables through the retarded time, making the accurate evaluation of space-time element integrals quite technical and intricate. Moreover, retarded potential BEMs may experience numerical instabilities related to the choice of the time step. These difficulties can be sidestepped by resorting to the more-recently developed approach based on the convolution quadrature method (CQM) (Lubich, 1988a,b), which deals with transient problems by exploiting the time convolution structure of time-domain BIEs and combining suitably defined BEM solutions obtained in the complex frequency domain (Banjai and Sauter, 2009; Betcke et al., 2017; Nieto Ferro, 2013; Sayas, 2016; Falletta et al., 2012; Banjai et al., 2012; Labarca et al., 2019). CQM-based solution algorithms, which are becoming the mainstream approach for solving time domain BIEs, can therefore rely on the relative simplicity of frequency-domain BEMs and the availability of existing robust and efficient BEM codes. Most importantly, applications underlying this work need accelerated BEMs, which for frequency-domain BIEs have been extensively studied and allow to efficiently deal with large-scale time-harmonic problems, even at high frequencies (Chaillat et al., 2017a; Darbas et al., 2013; Darve, 2000; Fong and Darve, 2009; Bremer et al., 2013). Hence, adopting the CQM framework allows to take direct advantage of fast frequency-domain BEMs in dealing with transient rapid problems. Fast BEMs for retarded potential BEMs (Ergin et al., 1998; Takahashi et al., 2004) are comparatively harder to formulate, and thus less widespread (although they do exist).

2.3.1 $\mathcal{Z}$-transform of a causal time convolution

CQM-based approaches work by reformulating the time-domain BIE (2.16) in terms of BIEs in the (complex) frequency domain. They can conveniently be presented by focusing on the evaluation of the single-layer integral operator $G\{f\}$ for a given causal density f. This task in turn rests on the evaluation of time convolutions of the form

$$q(t) \equiv (G \star f)(t) = \int_0^t G(t-\tau)f(\tau)\,\mathrm{d}\tau = \int_0^t f(t-\tau)G(\tau)\,\mathrm{d}\tau = (f \star G)(t)\,, \quad \forall t \geq 0\,.$$

[1] The computation is detailed in Appendix C.3.

The quantity $G(t-\tau)$ may be expressed by inverting the Laplace transform $\bar{G}$ of G (assuming $\bar{G}$ to be well-defined, see Section 2.3.2 for details), so that

$$q(t) = \int_0^t \left(\frac{1}{2\pi i} \int_{\gamma - i\cdot\infty}^{\gamma + i\cdot\infty} \bar{G}(s) e^{s(t-\tau)} \, \mathrm{d}s \right) f(\tau) \, \mathrm{d}\tau \, .$$

Assuming applicability of Fubini's theorem, we obtain

$$q(t) = \frac{1}{2\pi i} \int_{\gamma - i\cdot\infty}^{\gamma + i\cdot\infty} \bar{G}(s) h(t;s) \mathrm{d}s, \qquad \text{with} \quad h(t;s) \equiv \int_0^t e^{s(t-\tau)} f(\tau) \, \mathrm{d}\tau \, . \tag{2.18}$$

Considering a sequence of discrete time instants $t_n = n\Delta t \, , n \in \mathbb{N}$, where Δt is the constant time step, the CQM is developed as a means to evaluate the sequence $(q_n)_{n\geq 0}$ of convolution values $q_n \equiv q(t_n)$, over a finite discrete time interval $\{0, \Delta t, 2\Delta t, \ldots, T = M\Delta t\}$, given the sequence $(f_n) \equiv \big(f(t_n)\big)_{n\geq 0}$ and the function G. The key departure point of the CQM consists in remarking that the function $t \mapsto h(t;s)$ introduced in (2.18) satisfies the initial-value problem

$$\begin{cases} \dfrac{\mathrm{d}h}{\mathrm{d}t}(t;s) = s\, h(t;s) + f(t) \, , \\ h(t \leq 0; s) = 0 \, . \end{cases} \tag{2.19}$$

The ordinary differential equation (2.19) is numerically solved for the time-discrete approximation $h_n(s) \equiv h(t_n; s)$ of $h(t;s)$ (with fixed s). By applying a linear k-step method (such as the backward Euler method) to (2.19), the sequence $\big(h_n(s)\big)$ solves

$$\begin{cases} \dfrac{\mathrm{d}h_n(s)}{\mathrm{d}t} \simeq \dfrac{1}{\Delta t} \displaystyle\sum_{j=0}^{k} \alpha_j h_{n+j-k}(s) \quad = \sum_{j=0}^{k} \beta_j (s h_{n+j-k}(s) + f_{n+j-k}) \, , & \forall n \in \mathbb{N} \, , \\ h_{-p}(s) = f_{-p} = 0 \, , & \forall p \in [\![1, k]\!] \, , \end{cases} \tag{2.20}$$

where the coefficients α_j and β_j are the constants of the multistep method (for instance, $k = 1$, $\alpha_0 = -1$, $\alpha_1 = 1$, $\beta_0 = 0$, $\beta_1 = 1$ for the backward Euler method); see e.g., (Quarteroni et al., 2007, Secs. 11.5 and 11.6).

The next step consists in reformulating equations (2.20), which relate the sequences $\big(h_n(s)\big)$ and (f_n), in terms of the $\mathcal{Z}$-transforms of those sequences. We recall (Jury, 1973) that the $\mathcal{Z}$-transform $\mathcal{Z}[(x_n)](\xi)$ of a discrete-time signal (x_n) is defined by

$$\mathcal{Z} : (x_n) = \{x_0, x_1, \ldots\} \longmapsto \mathcal{Z}[(x_n)](\xi) = \sum_{n=0}^{\infty} x_n \xi^n \equiv X(\xi) \, , \quad \xi \in \mathbb{C} \, .$$

The above value $X(\xi)$ of the $\mathcal{Z}$-transform is well defined for $|\xi|$ smaller than the radius of convergence ϱ of the above series. Multiplying the first equation of (2.20) by $\Delta t \, \xi^n$ for some $\xi \in \mathbb{C}$ and summing over n from 0 to ∞, we obtain

$$\left(\sum_{j=0}^{k} \alpha_j \, \xi^{k-j} \right) H(\xi; s) = \Delta t \left(\sum_{j=0}^{k} \beta_j \, \xi^{k-j} \right) (s H(\xi; s) + F(\xi)) \, ,$$

where $\xi \mapsto H(\xi; s)$ and $\xi \mapsto F(\xi)$ are the $\mathcal{Z}$-transforms of the sequences $\big(h_n(s)\big)$ and $\big(f_n\big)$. Letting $p(\xi)$ denote the ratio

$$p(\xi) = \frac{\sum_{j=0}^{k} \alpha_j \, \xi^{k-j}}{\sum_{j=0}^{k} \beta_j \, \xi^{k-j}} \, ,$$

we then have

$$H(\xi;s) = (p(\xi)/\Delta t - s)^{-1} F(\xi). \tag{2.21}$$

The $\mathcal{Z}$-transform $Q(\xi) \equiv \mathcal{Z}[(q_n)](\xi)$ is readily found, from the expression (2.18) of $q(t)$ evaluated at instants $t = t_n$, to be given by

$$Q(\xi) = \frac{1}{2\pi \mathrm{i}} \int_{\gamma - \mathrm{i}\cdot\infty}^{\gamma + \mathrm{i}\cdot\infty} \bar{G}(s) H(\xi;s)\, \mathrm{d}s.$$

Using (2.21) and Cauchy's residue theorem, $Q(\xi)$ is finally found to be related to $F(\xi)$ through

$$Q(\xi) = \frac{1}{2\pi i} \int_{\gamma - i\cdot\infty}^{\gamma + i\cdot\infty} \bar{G}(s) \left(\frac{p(\xi)}{\Delta t} - s \right)^{-1} F(\xi)\, \mathrm{d}s = \bar{G}\left(\frac{p(\xi)}{\Delta t} \right) F(\xi)\,. \tag{2.22}$$

2.3.2 Reformulation of the time-domain BIE

Since potentials and integral operators involve time convolutions of a causal fundamental solution and a causal density, the developments of Section 2.3.1 are directly applicable to the integral equation formulation of the transient scattering problems, with the help of (2.22) with $\bar{G}$ taken as the Laplace transform of a fundamental solution. Since the latter is a distribution, we first recall a few facts about the Laplace transform in time before proceeding further.

Let $f \in L^1_{loc}(\mathbb{R})$ be a locally integrable function with support in $\mathbb{R}^+$ (i.e., f is causal), and for which there exists a real number ξ_0 such that $e^{-\xi t} f(t) \in L^1(\mathbb{R})$ for any $\xi \geq \xi_0$ (possibly $\xi_0 = -\infty$). The Laplace transform $\mathcal{L}(f)(s)$ of f is then defined for any $s \in \mathbb{C}$, $\mathrm{Re}(s) > \xi_0$, by

$$\mathcal{L}(f)(s) \equiv \bar{f}(s) = \int_0^{+\infty} f(t) e^{-st} \mathrm{d}t\,,$$

where s is the frequency parameter. More generally, for any causal tempered distribution f, the Laplace transform is defined as (Sayas, 2016)

$$\mathcal{L}(f)(s) \equiv \bar{f}(s) = \langle f, \exp(-s\,\cdot\,) \rangle, \tag{2.23}$$

where $\langle f, \varphi \rangle$ denotes the value of the linear functional f applied to the (causal, smooth) test function φ. In particular, the Laplace transform of the fundamental solution $G(\mathbf{r}, t)$ defined in (2.4) is obtained, using (2.23), as

$$\bar{G}(\mathbf{r}, s) = \frac{e^{-sr/c}}{4\pi r}, \qquad r \equiv \|\mathbf{r}\|\,. \tag{2.24}$$

The inverse Laplace transform may be expressed by the Bromwich integral (or Mellin's inverse formula)

$$\mathcal{L}^{-1}\left(\bar{f}\right)(t) = f(t) = \frac{1}{2\pi i} \int_{\gamma - i\cdot\infty}^{\gamma + i\cdot\infty} \bar{f}(s) e^{+st} \mathrm{d}s\,, \quad \forall t \geq 0\,,$$

where γ is a real number such that $\gamma > r$, where r is such that $\bar{f}(s)$ is analytical in the region $\{s | \mathrm{Re}(s) > r\}$ and of polynomial growth at the most.

We begin by applying a collocation method for the time variable to the relevant BIE, enforcing its verification at the discrete time instants t_n, and seek the values $\psi_n \equiv \psi(\cdot, t_n)$ of the unknown at the same time instants. The collocation in time translates into setting

to zero the $\mathcal{Z}$-transform of the time-discrete BIE residuals. This is done by applying (2.22) to the $\mathcal{Z}$-transform of (2.16), and results in the one-parameter family of BIEs

$$\frac{1}{2}\Psi(\mathbf{y},\xi) - \int_\Gamma \frac{\partial \bar{G}}{\partial n}(\mathbf{x}-\mathbf{y},s)\Psi(\mathbf{x},\xi)\,\mathrm{d}\Gamma_x + \int_\Gamma \bar{G}(\mathbf{x}-\mathbf{y},s)\frac{\partial \Psi}{\partial n}(\mathbf{x},\xi)\,\mathrm{d}\Gamma_x = 0, \quad \mathbf{y}\in\Gamma,\ \xi\in\mathbb{C},\ s = p(\xi)/\Delta t, \tag{2.25}$$

linking the $\mathcal{Z}$-transforms of the Dirichlet and Neumann traces of solutions ψ to the original problem (2.1).

Remark 5 *The integral operators featured in the BIE (2.25) are the Laplace transforms of the time-domain operators (2.15), evaluated at values $s = p(\xi)/\Delta t$ of the complex frequency s. The BIE (2.25) governs the $\mathcal{Z}$-transform (not the Laplace transform) of the boundary unknown associated with the original propagation problem (2.1).*

Remark 6 *When a boundary quantity involves a time derivative (such as in the relationship $p = -\rho\dot{\phi}$ between pressure and velocity potential), we use*

$$\mathcal{Z}[d(x_n)](\xi) = \frac{D(\xi)}{\Delta t}\mathcal{Z}[(x_n)](\xi)$$

in the $\mathcal{Z}$ domain, where $D(\xi) \equiv \sum_{j=0}^{k} \alpha_j \xi^{k-j}$ is the symbol of the discrete (time) differentiation operator d embedded in the linear k-step method. When $D(\xi) = p(\xi)$, which is the case e.g., for the backward Euler and BDF2 schemes, the above rule coincides with the differentiation rule of the Laplace transform evaluated at $s = p(\xi)/\Delta t$.

Remark 7 *CQM-based solution methods for time-domain BIEs may be introduced and presented in several ways. A common approach is to first introduce the CQM (Lubich, 1988a,b), whereby a convolution $f \star G$ is expressed with a quadrature whose weights depend on $\bar{G}$, then apply it to the boundary integral equation (2.16), and finally take the $\mathcal{Z}$-transform of the obtained equation (Sayas, 2016). One alternatively can, following (Betcke et al., 2017), discretise in time the wave equation (2.1) (recast in first-order form) using a multistep scheme; the resulting PDE governing the $\mathcal{Z}$-transform $\Psi(\cdot,\xi)$ features the wave operator in the Laplace domain with $s = p(\xi)/\Delta t$, and can therefore be reformulated as the BIE (2.25). This derivation of the $\mathcal{Z}$-BEM avoids having to go into details of the CQM (as in e.g., Banjai and Sauter, 2009), in particular because we do not explicitly use the arising weights, allowing a concise presentation of the formulation that stays within the BIE framework.*

2.3.3 Solution synthesis in the time domain

Considering for example a Neumann problem (for which ψ is unknown and $\partial_n\psi$ prescribed), the time-discrete physical unknowns $\psi(\cdot,t_n)$ are obtained by taking the inverse $\mathcal{Z}$-transform of $\Psi(\cdot,\xi)$, given by

$$\psi(\cdot,t_k) = \frac{1}{2i\pi}\int_{\mathcal{C}} \Psi(\cdot,\xi)\xi^{-k-1}\,d\xi\,, \quad \forall k\in\mathbb{N}\,, \tag{2.26}$$

where $\mathcal{C}$ is a counterclockwise closed path encircling the origin and entirely in the region of convergence of $\Psi(\cdot,\xi)$. The inversion formula (2.26) uses the fact that $\psi(\cdot,t_k)$ is the k-th

coefficient of the power series expansion of $\Psi(\cdot,\xi)$, by applying Cauchy's residue theorem to $\Psi(\cdot,\xi)$. To evaluate (2.26) in practice, $\mathcal{C}$ is taken as the circle of radius ρ and a trapezoidal rule approximation is considered whereby $\mathcal{C}$ is discretised by a set of L complex numbers $\xi_p = \rho e^{2i\pi p/L}$. This provides the approximate value

$$\psi(\cdot,t_k) \approx \frac{1}{L}\sum_{p=0}^{L-1} \Psi(\cdot,\xi_p)\xi_p^{-k}\,, \quad \forall k \in [\![0,M]\!]\,, \tag{2.27}$$

where M is the total number of time steps. The suitable choice of parameters L,ρ is discussed in (Lubich, 1988b), where it is shown that setting $L = 2M$ and ρ such that $\rho^L = \varepsilon$ is sufficient to achieve $O(\varepsilon)$ accuracy.
Due to the approximation (2.27), for $\xi = \xi_p = \rho e^{2i\pi p/L}$, the $\mathcal{Z}$-transforms $(X_p) \equiv (X(\xi_p))$, $X(\xi_p) = \sum_{n=0}^{M} x_n \rho^n e^{2i\pi pn/L}$ (resp. the inverse formula) are evaluated by applying the fast Fourier transform (resp. inverse FFT) to the finite sequence $(x_n\rho^n)_{n=0}^{M}$ $\Big($resp. $(X_p\rho^{-p})_{p=0}^{L-1}\Big)$. Thus, evaluating and inverting the $\mathcal{Z}$-transforms both entail a $O(L\log L) = O(M\log M)$ complexity.

The $2M$ $\mathcal{Z}$-transforms $\Psi(\cdot,\xi_p)$ with $\xi = \xi_p$ $(0 \le p \le 2M-1)$ needed in (2.27) are governed by the BIEs (2.25) with $s = p(\xi_p)/\Delta t$, knowing the values $\partial_n\Psi(\cdot,\xi_p)$ of the $\mathcal{Z}$-transform $\partial_n\Psi(\cdot,\xi)$ of the Neumann data. A priori, this entails solving the BIE (2.25) for all values $\xi = \xi_p$ $(0 \le p \le 2M-1)$ of the $\mathcal{Z}$-transform variable. However, it is easy to show using (2.25) that $\Psi(\cdot,\overline{\xi}) = \overline{\Psi(\cdot,\xi)}$; moreover we have $\xi_{2M-p} = \overline{\xi_p}$, for $1 \le p \le 2M-1$. As a consequence, the evaluation, using (2.27), of the complete time-discrete solution needs only $M+1$ BIE solutions, instead of the expected $2M$. In the sequel, references to the number of frequency BEM problems solved take into account this symmetry.

Remark 8 *For some discrete-time signal $(\psi_n) = (\psi(t_n))$, let $\Psi \equiv \mathcal{Z}[(\psi_n)]$ and $\Psi^{(k)} \equiv \mathcal{Z}[(\psi_n^{(k)})]$, respectively, be the $\mathcal{Z}$-transforms of (ψ_n) and its truncated version $(\psi_n^{(k)}) \equiv (\psi_0,\dots,\psi_k,0,\dots)$. Then, applying (2.26) to Ψ or $\Psi^{(k)}$ yields the same value for $\psi(t_k)$. In other words, (2.26) is consistent with causality, as the evaluation of $\psi(t_k)$ is unaffected by the contributions to $\mathcal{Z}[(\psi_n)]$ of the time-discrete signal at later times.*

2.3.4 Summary of the computational procedure

Considering again a Neumann problem for definiteness, the $\mathcal{Z}$-BEM proceeds as follows:

- For each $k \in [\![0,M]\!]$, find $\Psi(\cdot,\xi_k)$ by solving the BIE (2.25) with $\xi = \xi_k$ and $s = p(\xi_k)/\Delta t$, $\partial_n\Psi(\cdot,\xi_k)$ being given;
- For each $k \in [\![1,M-1]\!]$, set $\Psi(\cdot,\xi_{2M-k}) = \overline{\Psi(\cdot,\bar{\xi}_k)}$;
- Compute each term of the sequence $\psi(t_n)$ by the (approximate) inverse $\mathcal{Z}$-transform (2.27), wherein $L = 2M$.

Concluding, the $\mathcal{Z}$-BEM allows to solve the time-domain BIE (2.16) at discrete time instants $t = 0,\Delta t,2\Delta t,\dots,M\Delta t = T$, by solving $M+1$ Laplace-domain BIEs, whose input can be computed with $O(M\log M)$ complexity. The overall complexity of the $\mathcal{Z}$-BEM is mainly determined by the $M+1$ frequency BIEs, to be solved using a fast BEM solver.

2.4 Fast Boundary Element Method for frequency-domain BIEs

The foregoing $\mathcal{Z}$-BEM procedure crucially relies upon solving BIEs (2.25) in the (complex) frequency-domain that may involve large boundary element (BE) discretisations. This has the definite advantage of relying on well-established formulations, in particular existing fast BEM solvers for frequency-domain problems. We summarise next the fast BEM framework used in this work.

2.4.1 Overview of the main steps of the BEM

The BEM is based on the discretisation of boundary integral equations, thus avoiding the discretisation of the entire domain Ω. All available BEM discretisation methods are compatible with the $\mathcal{Z}$-transform framework. We use the collocation method, in which boundary integral equations are enforced at a finite number of points on the surface, called collocation points (Banerjee, 1994; Bonnet, 1999); other possibilities include the Galerkin method (Bielak and Maccamy, 1991; Bonnet et al., 1998; Aimi et al., 2009; Ha-Duong, 2003; Kallivokas et al., 2005).

Discretisation of the boundary Γ and reference element method

A boundary element representation of $\Gamma = \partial\Omega$ is based on the choice of a set of N_N points $\mathbf{y}^1, \ldots, \mathbf{y}^{N_N}$ located on Γ, termed *geometrical nodes*, that construct N_E elements $\Gamma_1, \ldots, \Gamma_{N_E}$ whose union forms the discretised representation Γ_d of Γ (see Figure 2.4).

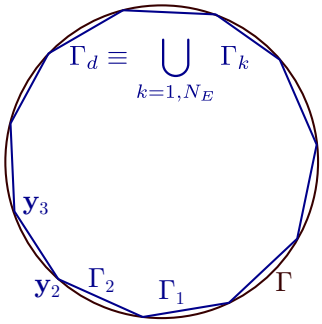

Figure 2.4: Example of discretisation of a circle.

For instance, for a 3D problem, Γ is a surface and the elements are usually triangles or quadrilaterals. For a 2D problem, Γ is a line and the elements are segments. Hence, the integration over Γ in (2.14) is approximated by an integration over Γ_d and so a sum of integration over Γ_k.

Integrations over Γ_k are commonly computed using a simple reference element Δ_e, to make the computation of the integrals easier. If Γ_k is one-dimensional, the integration domain is changed from Γ_k to $[-1, 1]$. If Γ_k is two-dimensional, the integration domain is changed from Γ_k to a unit square or a rectangle triangle whose catheti have unit length. Hence, a mapping of each element Γ_k onto Δ_e is considered:

$$\xi \in \Delta_e \longrightarrow \mathbf{y}(\xi) \in \Gamma_k\,, \quad k \in [\![1, N_e]\!]\,.$$

Interpolation of boundary variables and unknowns. Both the variables and the unknowns are interpolated using shape functions:

$$\mathbf{y}(\xi) = \sum_{i=1}^{N_{\text{sf}}} \mathbf{y}^i N_i(\xi) \quad \text{and} \quad \begin{cases} \psi(\xi) = \displaystyle\sum_{i=1}^{N_{\text{sf}}} \psi^i N_i(\xi)\,, \\ q(\xi) \equiv \dfrac{\partial \psi}{\partial n}(\xi) = \displaystyle\sum_{i=1}^{N_{\text{sf}}} q^i N_i(\xi)\,, \end{cases} \quad \text{where } \xi \in \Delta_e\,.$$

The number N_{sf} of shape functions depends on the chosen element type. Common shape functions are given in Table 2.1.

Linear element	Quadratic element	Cubic element
$N_1(\xi) = \dfrac{(1-\xi)}{2}$	$N_1(\xi) = \dfrac{\xi(\xi-1)}{2}$	$N_1(\xi) = \dfrac{9}{16}\left(\dfrac{1}{9} - \xi^2\right)(\xi - 1)$
	$N_2(\xi) = (1-\xi)(1+\xi)$	$N_2(\xi) = \dfrac{27}{16}\left(\dfrac{1}{3} - \xi\right)\left(1 - \xi^2\right)$
$N_2(\xi) = \dfrac{(1+\xi)}{2}$	$N_3(\xi) = \dfrac{\xi(\xi+1)}{2}$	$N_3(\xi) = \dfrac{27}{16}\left(\dfrac{1}{3} + \xi\right)\left(1 - \xi^2\right)$
		$N_4(\xi) = -\dfrac{9}{16}\left(\dfrac{1}{9} - \xi^2\right)(\xi + 1)$

Table 2.1: Usual shape functions used to interpolate the variables and the unknowns.

Once discretised with the collocation approach, a boundary integral equation set in the frequency domain, such as (2.25), leads to a system of generic form

$$[\mathbf{H}]\{\boldsymbol{\psi}\} = [\mathbf{G}]\{\mathbf{Q}\}\,, \tag{2.28}$$

where the N-vectors $\{\boldsymbol{\psi}\}$ and $\{\mathbf{Q}\}$ are the discretised traces of ψ and $-\partial_n\psi$ on the discretised boundary, and $[\mathbf{G}]$, $[\mathbf{H}]$ are $N \times N$ matrix discretisations of operators $\mathcal{G}$ and $\mathcal{I}/2 - \mathcal{H}$, respectively (see definition (2.15)).

Solving the system of BEM equations, limitations of standard BEM. Invoking the boundary conditions of the problem being solved, the generic equation (2.28) is rewritten as:

$$[\mathbf{K}]\{\mathbf{v}\} = \{\mathbf{f}\}\,, \tag{2.29}$$

where the $N \times N$ influence matrix $[\mathbf{K}]$ is related to $[\mathbf{G}]$ or $[\mathbf{H}]$, and $\{\mathbf{v}\}$, $\{\mathbf{f}\}$ are N-vectors collecting the DOFs that remain unknown and quantities known from the boundary conditions, respectively. For instance, for a Neumann problem where $\partial_n\psi$ is prescribed on Γ, $[\mathbf{K}] = [\mathbf{H}]$, $\{\mathbf{v}\} = \{\boldsymbol{\psi}\}$ and $\{\mathbf{f}\} = [\mathbf{G}]\{\mathbf{Q}\}$. By contrast with the FEM (see e.g., Hughes, 1987), the matrices $[\mathbf{H}]$, $[\mathbf{G}]$ and $[\mathbf{K}]$ are fully populated and (for the collocation approach adopted here) non-symmetric (Dominguez, 1993; Banerjee, 1994). Applying direct solvers to the system (2.29) entails a $O(N^3)$ complexity, which is unacceptable for large-scale problems.

One of the most efficient techniques to deal with large BEM problems is to solve (2.28) with an iterative algorithm, like the Generalised Minimal RESidual method (GMRES) (Saad and Schultz, 1986) for instance. The idea of the method is to iteratively find a vector

$\{\tilde{\mathbf{v}}\}$ such that $\|[\mathbf{K}]\{\tilde{\mathbf{v}}\} - \{\mathbf{f}\}\|$ is less than a given tolerance $\varepsilon_{\text{GMRES}}$. The procedure is based on the construction of Krylov subspaces that are expanded at each new iteration. When using this approach, the major time-consuming task becomes the evaluation of a matrix-vector product $[\mathbf{K}]\{\mathbf{v}\}$ at each GMRES iteration. The complexity of the matrix-vector product is of order $O(N^2)$ if either the matrix is stored or if it is re-evaluated at each GMRES iteration using standard BEMs, because the integrals that run over the discretised surface (so N points) must be computed for each of the N collocation points.

In that respect, the goal of accelerated BEMs naturally arises: to accelerate each evaluation of $[\mathbf{K}]\{\mathbf{v}\}$ without actually forming the full matrix $[\mathbf{K}]$. Available BEM acceleration methods include the Fast Multipole Method (FMM), which has proved very efficient and flexible for wave propagation problems (Chaillat, 2008; Darbas et al., 2013; Darve, 2000; Nishimura, 2002). On the other hand, hierarchical matrix ($\mathcal{H}$-matrix) based solvers, which use low-rank approximations of recursively defined off-diagonal matrix blocks (Hackbusch, 1999; Chaillat et al., 2017b), are very appropriate for problems involving multiple right-hand sides. In this chapter, the BEM is accelerated using the multi-level FMM, implemented in the in-house FM-BEM solver COFFEE (2020). The computational complexity of each matrix-vector product is then $O(N \log N)$, instead of $O(N^2)$.

2.4.2 Fast Multipole accelerated Boundary Element Method

To present the FMM concept, it is instructive to go back to its original application, namely the N-body problem in physics (Greengard, 1988; Greengard and Rokhlin, 1987). Consider a set of many particles in mutual interaction through a cohesive force whose potential is inversely proportional to the inter-particle distance (denoted r thereafter). This notably describes the interaction of stars through the gravitational potential, or the interaction of charged particles through the Coulomb's potential. The idea is as follows (Greengard, 1988; Greengard and Rokhlin, 1987; Ying, 2012): due to the spatial decay of the potential, the interaction between two well-separated sets $\{\mathbf{x}_i\}$ and $\{\mathbf{y}_j\}$ of particles can be roughly approximated by the interaction between the set centres $\mathbf{x}_g, \mathbf{y}_g$ carrying the net charges (see Figure 2.5), acting as monopoles. This approximation (and its refinements involving multipoles) in particular separates the variables $\mathbf{x}, \mathbf{y}$.

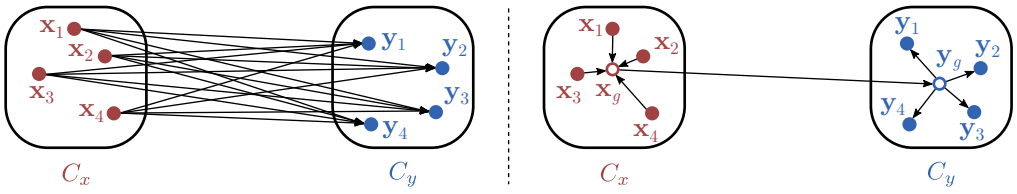

Figure 2.5: Illustration of the FMM concept, actions of the particles in a cell C_x (centre $\mathbf{x}_g$) on the particles in a cell C_y (centre $\mathbf{y}_g$). Left: without FMM, right: with FMM.

For wave propagation, the fundamental solution has to be reformulated in such a way that the $\mathbf{x}$ and $\mathbf{y}$ variables ($r = \|\mathbf{x} - \mathbf{y}\|$) become separated. Using the notations of Figure 2.5, the position vector $\mathbf{r}$ is expressed as $\mathbf{r} = \mathbf{r}_g + (\mathbf{y} - \mathbf{y}_g) - (\mathbf{x} - \mathbf{x}_g)$, where $\mathbf{r}_g = \mathbf{y}_g - \mathbf{x}_g$. Then, the fundamental solution (2.24) admits the decomposition (Darve, 2000; Epton and Dembart, 1995):

$$\bar{G}(r,s) = \lim_{L\to+\infty} \int_{\hat{\alpha}\in\mathcal{S}} e^{s\,\hat{\alpha}\cdot(\mathbf{x}-\mathbf{x}_g)/c} \mathcal{G}_L(\hat{\alpha}; \mathbf{r}_g; s) e^{-s\,\hat{\alpha}\cdot(\mathbf{y}-\mathbf{y}_g)/c}\, \mathrm{d}\hat{\alpha}\,, \tag{2.30}$$

where $\mathcal{S}$ denotes the unit sphere of $\mathbb{R}^3$, and $\mathcal{G}_L$ is a transfer function defined in terms of the modified spherical Bessel functions k_p (Olver et al., 2010, Chap. 10) and the Legendre polynomials P_p (Olver et al., 2010, Chap. 18) by

$$\mathcal{G}_L(\hat{\alpha}; \mathbf{r}_g; s) = \frac{s}{16\pi^2 c} \sum_{0 \le p \le L} (2p+1) i^p \mathsf{k}_p(s r_g / c) P_p(\cos(\hat{\alpha}, \mathbf{r}_g)) \,.$$

The decomposition (2.30) achieves the desired separation between the variables $\mathbf{x}$ and $\mathbf{y}$. When inserted into a boundary integral equation like (2.25), it allows to approximate the integral. However, it is valid only for well separated sets of points $\mathbf{x}, \mathbf{y}$. The resulted procedure is termed FM-BEM for Fast Multipole BEM, and some specific optimised FM-BEM procedures achieve a complexity $O(N \log(N))$ (Chaillat et al., 2008).

Now that the principle of the method has been presented, its implementation can be explained in detail. First, the single-level FMM is presented. Then, the principle is enhanced by recursive applications of the single-level FMM, leading to the multi-level FMM.

Single-level FMM. Consider a structure of boundary Γ. In order to apply the FMM, it is necessary to define a grid composed of cells embedding the boundary Γ (see Figure 2.6 for a 2D depiction). For a chosen point $\mathbf{y} \in \Gamma$, let C_y denote the cell to which $\mathbf{y}$ belongs. The adjacent cell set $\mathcal{A}(C_y)$ comprises those cells sharing at least a common vertex with C_y that intersect Γ. Any cell C not belonging to $\mathcal{A}(C_y)$ is well-separated from C_y. This single-level algorithm solves (2.28) iteratively, with evaluations of $[\mathbf{K}]\{\mathbf{v}\}$ combining adjacent and far contributions. The latter are computed using the decomposition (2.30), while the former use standard matrix-vector products.

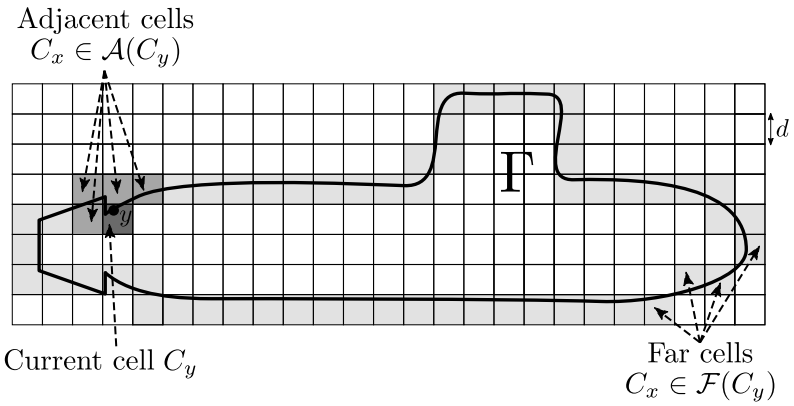

Figure 2.6: Two-dimensional grid embedding the boundary Γ. Definition of adjacent and far cells.

An important parameter of the method is the size cell d. This size depends on the considered problem, and notably the value of the involved frequencies (the higher the frequency, the smaller d is).

Actually, a single-level FMM does not offer the optimal complexity $O(N \log(N))$, but rather evaluates $[\mathbf{K}]\{\mathbf{v}\}$ with a $O(N^{3/2})$, sub-optimal, complexity. Though it is more efficient than the standard BEM, a multi-level FMM has to be introduced in order to achieve optimally-low complexity.

Principle of the multi-level FMM. The idea of the multi-level FMM is to reduce the complexity of the single-level FMM by increasing the size of far cells whenever possible,

while reducing the near-interaction part of the evaluation. The multi-level FMM is driven by a recursive *octree*, constructed using large cells that are hierarchically subdivided into $2 \times 2 \times 2 = 8$ children cubic cells for 3D problems. The octree is constructed such that:

- The largest cubic cell contains Γ; it defines the *tree root* (level $\ell = 0$) of the octree.
- Level $\ell = 1$: it is composed of the 8 children cells of the tree root, the latter being their *parent cell*. The level-1 cells are all adjacent, so the FMM cannot yet be applied.
- Level ℓ is composed of at most 8^ℓ cells (cells that do not intersect Γ being discarded).
- The last level $\bar{\ell}$, implicitly defined by a preset subdivision-stopping criterion, is made of *leaf cells*.

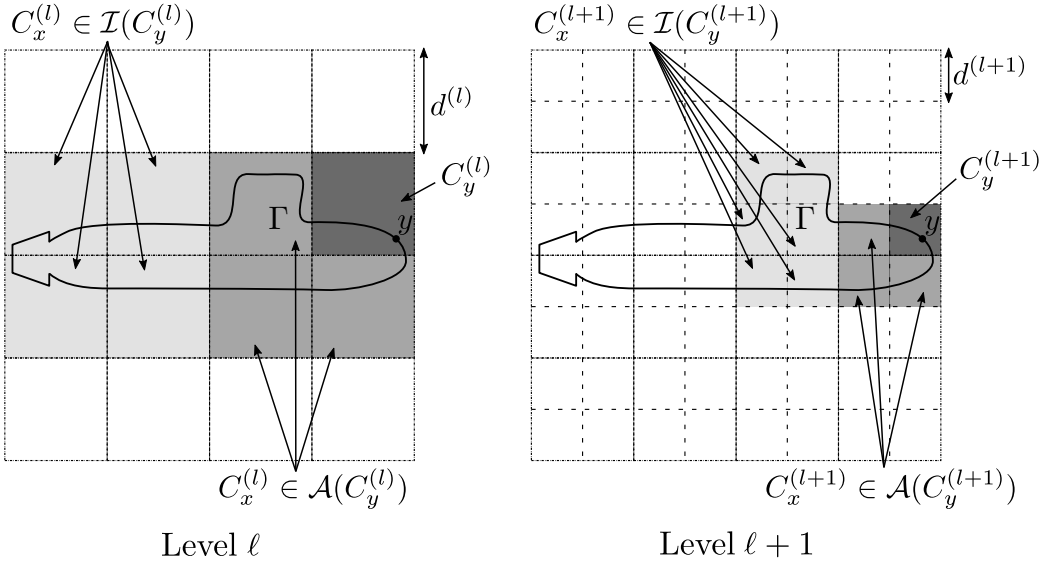

Figure 2.7: Illustration of the multi-level FMM in 2D. Both the interaction lists and the adjacent regions reduce in size as the level number increases.

The speed-up process is applied at each level from level $\ell = 2$ to level $\ell = \bar{\ell}$. It works by using clusters that are largest (i.e., of smallest level ℓ) whenever possible, to derive the maximum possible benefit from the decomposition (2.30). To this purpose, the notion of interaction list is defined. Consider a point $\mathbf{y}$ on Γ (see Figure 2.7). This point belongs to a level-2 cell denoted $C_y^{(2)}$. The speed-up process is then applied to the interactions between $C_y^{(2)}$ and all the non-adjacent level-2 cells, the latter constituting the interaction list $\mathcal{I}(C_y^{(2)})$ of $C_y^{(2)}$. At level 3, $\mathbf{y}$ belongs to a child cell $C_y^{(3)}$ of $C_y^{(2)}$. The interaction list $\mathcal{I}(C_y^{(3)})$ contains the level-3 cells not adjacent to $C_y^{(3)}$ whose parent cell belongs to $\mathcal{A}(C_y^{(2)})$. Thus, interactions are carried out level by level, until interactions between leaf cells are reached; those are computed using standard boundary element techniques. This process ensures that all contributions to $[\mathbf{K}]\{\mathbf{v}\}$ are accounted for, while taking maximum advantage from the decomposition (2.30).

Remark 9 *In practice, the multi-level FMM is more complex than what is presented in this section, but the basic principle remains the same. In particular, a notion of downward and upward passes are introduced for an efficient computation of the interactions between the cells. A detailed exposition of the method and its implementation can be found in (Chaillat, 2008).*

In this thesis, we use an already-developed (COFFEE, 2020) FMM procedure for solving acoustic boundary integral equations. This procedure was dealing with equations set in the frequency domain, and one contribution of this work was to set up a solving-process in the time domain, designing the $\mathcal{Z}$-BEM procedure presented in Section 2.3. In particular, some improvements have been made so that the $\mathcal{Z}$-BEM efficiently solves rapid transient problems.

2.5 Improvements of the $\mathcal{Z}$-BEM procedure for rapid transient problems

The $\mathcal{Z}$-BEM procedure presented in Section 2.3 still lacks efficiency when dealing with rapid transient problems involving large numbers of small time steps, even with the required frequency-domain BIEs solved using the FM-BEM, because BIEs (2.25) need to be solved for a large number of high complex frequencies ($s(\xi) = p(\xi)/\Delta t$ becoming large for small time steps). In this section, we present proposed improvements to the $\mathcal{Z}$-BEM procedure that specifically address this concern and are applicable to all rapid transient problems, such as those arising in our target FSI analyses. To this end, we first introduce two types of wave propagation problems arising in the course of solving FSI problems, namely radiation and scattering problems.

2.5.1 Radiation and scattering problems for FSI applications

As already mentioned in this dissertation, our work is motivated by eventual applications to FSI problems, which involve a deformable structure (or a set thereof) occupying the bounded region Ω_s and facing incoming waves in the surrounding acoustic fluid. In this context, it is convenient to decompose the total pressure field p^{tot} in Ω into a sum of three components: $p^{\text{tot}} = p^{\text{inc}} + p^{\text{ref}} + p^{\text{rad}}$ (Junger and Feit, 1986). The incident field p^{inc} defines the acoustic field in the absence of the structure. The reflected field p^{ref} is the pressure perturbation that would arise were the structure motionless. It is a non-physical quantity, as it has to compensate for the incident field that does not see the obstacle. The radiated field p^{rad} is then the correction to the fluid state due to the motion of the structure, which radiates an acoustic wave into the fluid (see Figure 2.8).

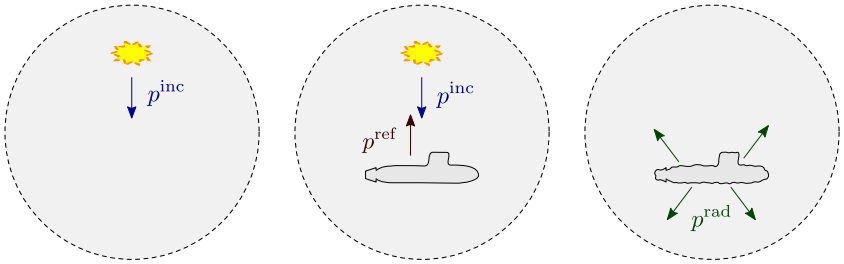

Figure 2.8: Decomposition of the fluid variables into incident, reflected and radiated parts.

When considering coupled FSI problems under the assumption of small deformations (small strains and and small displacements), the decomposition concentrates the coupled part of the problem in the radiated contribution, as the reflected one is obtained for a motionless structure. This leads us to focus in this chapter on the cases of (i) wave scattering by a motionless geometry, and (ii) radiation of a wave by a given structure motion. Both cases are formulated by invoking the kinematic boundary condition $\nabla\phi \cdot \mathbf{n} = \mathbf{v} \cdot \mathbf{n} \equiv u$ on

Γ (where $\nabla\phi$ and $\mathbf{v}$ are respectively the fluid and solid velocities on Γ). The respective pressure fields p^{ref} and p^{rad} thus solve (2.1) together with the Neumann boundary condition

$$\begin{aligned} \partial_n p^{\text{rad}} &= -\rho\,\dot{u} && \text{case (i)},\\ \partial_n p^{\text{ref}} &= -\partial_n p^{\text{inc}} && \text{case (ii)}. \end{aligned} \tag{2.31}$$

Substituting these in (2.16) and using the notations introduced in Section 2.2.3, the radiated pressure field p^{rad} for case (i) solves the boundary integral equation

$$\tfrac{1}{2}p^{\text{rad}}(\mathbf{y},t) - \mathcal{H}\{p^{\text{rad}}\}(\mathbf{y},t) = \mathcal{G}\{\,\rho\dot{u}\,\}(\mathbf{y},t) \qquad \mathbf{y}\in\Gamma,\ t\in[0,T].$$

Similarly, the reflected pressure p^{ref} for case (ii) satisfies the BIE

$$\tfrac{1}{2}p^{\text{ref}}(\mathbf{y},t) - \mathcal{H}\{p^{\text{ref}}\}(\mathbf{y},t) = \mathcal{G}\{\,\partial_n p^{\text{inc}}\,\}(\mathbf{y},t) \qquad \mathbf{y}\in\Gamma,\ t\in[0,T]. \tag{2.32}$$

For case (ii), another formulation, using $p^{\text{Ref}} \equiv p^{\text{inc}} + p^{\text{ref}}$ as unknown, is obtained by taking advantage of the fact that the incident field p^{inc} satisfies the interior BIE

$$\tfrac{1}{2}p^{\text{inc}}(\mathbf{y},t) + \mathcal{H}\{p^{\text{inc}}\}(\mathbf{y},t) - \mathcal{G}\{\partial_n p^{\text{inc}}\}(\mathbf{y},t) = 0 \qquad \mathbf{y}\in\Gamma,\ t\in[0,T]. \tag{2.33}$$

Then, the difference (2.32) - (2.33) leads to

$$\tfrac{1}{2}p^{\text{Ref}}(\mathbf{y},t) - \mathcal{H}\{p^{\text{Ref}}\}(\mathbf{y},t) = p^{\text{inc}}(\mathbf{y},t) \qquad \mathbf{y}\in\Gamma,\ t\in[0,T]. \tag{2.34}$$

The two formulations (2.32) or (2.34) provide similar results, but (2.34) is preferred in the following, because it does not require the computation of $\mathcal{G}$ nor the one of $\partial_n p^{\text{inc}}$ (in UNDEX analyses, p^{inc} is the input, as explained in Chapter 1).

The respective discretised BEM systems for the $\mathcal{Z}$-transforms of the total field $\mathbf{P}^{\text{Ref}}$ in the reflected case or $\mathbf{P}^{\text{rad}}$ in the radiation case therefore have the form

$$\left.\begin{aligned} \mathbf{H}(s)\{\mathbf{P}^{\text{rad}}(\xi)\} &= s\rho\,\mathbf{G}(s)\{\mathbf{U}(\xi)\} && \text{case (i)}\\ \mathbf{H}(s)\{\mathbf{P}^{\text{Ref}}(\xi)\} &= \mathbf{P}^{\text{inc}}(\xi) && \text{case (ii)} \end{aligned}\right\} \qquad s = p(\xi)/\Delta t\,. \tag{2.35}$$

Remark 10 *Although we focus in this work on exterior Neumann problems, the methods proposed are easily transposable to other types of exterior boundary-value problems (e.g., involving Dirichlet or Robin boundary conditions).*

2.5.2 Reducing the number of BEM problems through a high-frequency approximation

Using small time steps Δt in either BEM system (2.35) means that most of the complex frequencies $s(\xi)$ are high. It is therefore useful to exploit any available results pertaining to high-frequency approximations of dynamical problems. For deformable solids, the high-frequency range is defined as *the frequency band for which there is a uniform high modal density* (Ohayon and Soize, 1998). For wave scattering problems, a frequency may be considered as high if the ratio κ/λ between the local radius of curvature κ and the characteristic wavelength λ is large.

Here, we propose to improve our $\mathcal{Z}$-BEM treatment by relying on the assumed availability of an asymptotic high-frequency approximation (HFA) of solutions to (2.25) which can be invoked whenever $|s(\xi_k)| = |p(\xi_k)|/\Delta t > f_{\text{HFA}}$ for some threshold frequency f_{HFA}. Then, BEM problems (2.28) are actually solved when $|s(\xi_k)| \le f_{\text{HFA}}$ whereas a (faster to evaluate) HFA approximation is used instead when $|s(\xi_k)| > f_{\text{HFA}}$. The main issue then is whether and how a HFA and a threshold f_{HFA} can be satisfactorily defined. For the present study (and its intended applications), the answer differs according to whether a radiation or a scattering problem is being solved.

2.5.3 HFA for wave radiation problems

We first consider the case of waves radiated into a fluid by a moving structure (case (i) in (2.31)). For such problems, a simple HFA consists in setting $p \approx \rho c u$. The physical interpretation of this HFA lies in the fact that, if the surface Γ is smooth and vibrates at a high frequency, the radiated pressure at $\mathbf{y} \in \Gamma$ is determined by interactions with points close to $\mathbf{y}$ (due to causality), which approximately lie on the tangent plane to Γ at $\mathbf{y}$. Then, the radiated pressure locally resembles that of a vibrating infinite plate, which is known to be given by $p = \rho c u$ (Leblond, 2007). This approximation may also be retrieved in some reference configurations, e.g., the breathing sphere problem (see Appendix C.4). In this case, where an explicit HFA is available, the procedure relies on the evaluation of relative differences

$$\delta_{\mathrm{HFA}}(s) \equiv \frac{\|\psi_{\mathrm{BEM}}(s) - \psi_{\mathrm{HFA}}(s)\|_{L^2(\Gamma)}}{\|\psi_{\mathrm{BEM}}(s)\|_{L^2(\Gamma)}}, \tag{2.36}$$

and the choice of a preset tolerance $\mathrm{tol}_{\mathrm{HFA}}$. The steps are then the following:

- Solve BEM problems (2.28) for frequencies $s(\xi_k) = p(\xi_k)/\Delta t$ of increasing modulus;
- After each solution, compare the BEM and HFA solutions, for instance in terms of δ_{HFA};
- Set the cut-off frequency f_{HFA} to that value of $|s(\xi_k)|$ for which $\delta_{\mathrm{HFA}} \leq \mathrm{tol}_{\mathrm{HFA}}$;
- Use the HFA to approximate the solution of all BEM problems with $|s(\xi_k)| > f_{\mathrm{HFA}}$ (i.e., do not solve (2.28) in those cases).

The efficiency of the procedure relies on the number M_B of frequency-domain BEMs to be actually solved, which depends on several parameters, such as the tolerance tol, but more importantly on the high-frequency nature of the considered problem. This approach is exemplified in Section 2.6.1, where numerical results are presented in the simple case of a breathing sphere.

2.5.4 HFA for wave scattering problems

The foregoing approach may be applied whenever an explicit HFA is known. This is not the case for scattering problems (case (ii) in (2.31)), for which in particular f_{HFA} can no longer simply be set against a preset tolerance. We propose instead an *ad hoc* treatment.

The starting point for finding approximate solutions to this class of problems is the Kirchhoff HFA (Baker and Copson, 1950). This idea is also used in the high-frequency BEM literature (Abboud et al., 1994; Bruno et al., 2004; Chandler-Wilde and Langdon, 2007). Let $\mathbf{s} \in \Omega$ denote a source point emitting spherical waves. Then, $\mathbf{d}(\mathbf{y}) \equiv (\mathbf{y} - \mathbf{s})/\|\mathbf{y} - \mathbf{s}\|$ is the propagation direction of the incident wave at $\mathbf{y} \in \Gamma$. The Kirchhoff HFA for the total pressure p^{ref} on Γ is ($p^{\mathrm{Ref}} \equiv p$)

$$p_{\mathrm{HFA}}(\mathbf{y}, t) = 0 \qquad \text{if } \mathbf{d}(\mathbf{y}) \cdot \mathbf{n}(\mathbf{y}) > 0\,, \tag{2.37a}$$

$$p_{\mathrm{HFA}}(\mathbf{y}, t) = 2p^{\mathrm{inc}}(\mathbf{y}, t) \qquad \text{if } \mathbf{d}(\mathbf{y}) \cdot \mathbf{n}(\mathbf{y}) < 0\,. \tag{2.37b}$$

This simple HFA is known to provide accurate results in the regions of Γ where $|\mathbf{d}(\mathbf{y}) \cdot \mathbf{n}(\mathbf{y})| \simeq 1$. On the other hand, in the region where $|\mathbf{d}(\mathbf{y}) \cdot \mathbf{n}(\mathbf{y})| \simeq 0$, this HFA is discontinuous and hence imprecise.

Our purpose is to heuristically define an improved approximation of the same type, ensuring a similarly low computation time. The idea is to find a coefficient $C = C(\mathbf{y})$, depending on the evaluation point $\mathbf{y} \in \Gamma$, relating the $\mathcal{Z}$-transforms through $P_{\mathrm{HFA}} = C(\mathbf{y})P^{\mathrm{inc}}$.

To describe our HFA, we study a HF example problem involving a long cylinder facing a spherical wave (see details in Section 2.6.2, see Figure 2.11). BEM problems (2.28) are solved for complex frequencies s of increasing modulus. For a point $\mathbf{y} \in \Gamma$, we introduce the complex ratio

$$\mathcal{R}(\mathbf{y}, s) \equiv P(\mathbf{y}, s)/P^{\text{inc}}(\mathbf{y}, s)\,. \tag{2.38}$$

If the obstacle is convex, it can be shown (Abboud et al., 1994; Bruno et al., 2004; Chandler-Wilde and Langdon, 2007) that for any point $\mathbf{y} \in \Gamma$, $s \mapsto \mathcal{R}(\mathbf{y}, s)$ becomes approximately constant (with $\text{Im}(\mathcal{R})$ small relative to $\text{Re}(\mathcal{R})$) as $|s|$ becomes large (see Figure 2.13). On the basis of these observations, we propose the following, empirical, HFA construction:

- Choose a cut-off frequency f_{HFA} until which all problems (2.28) are solved; f_{HFA} then is the highest frequency modulus for which the BIE (2.25) is solved using the $\mathcal{Z}$-BEM procedure;
- Assume $\mathcal{R}(\mathbf{y}, s)$ to remain constant for $|s| > f_{\text{HFA}}$, and define the HFA approximation of $P(\cdot, s)$ for any $|s| > f_{\text{HFA}}$ by $P_{\text{HFA}}(\mathbf{y}, s) = \mathcal{R}(\mathbf{y})P^{\text{inc}}(\mathbf{y}, s)$, with $\mathcal{R}(\mathbf{y}) \equiv \mathcal{R}(\mathbf{y}, f_{\text{HFA}})$.

Of course, the numerical gain lies in approximating the solution of a given frequency-domain scattering problem by means of a simple multiplication, instead of solving a costly BEM problem. The required number of BEM solutions in this framework depends on the high-frequency nature of the original problem (see Section 2.6). We also tried the HFA variant $P_{\text{HFA}}(\mathbf{y}, s) = \text{Re}(\mathcal{R}(\mathbf{y}))P^{\text{inc}}(\mathbf{y}, s)$, which produced similar results.

The best value of f_{HFA} is impossible to determine *a priori*. In practice, one may choose between two alternative methods: (a) set f_{HFA} to the highest possible value for which the BEM problem can practically be solved by means of the available computer resources (given that increasing $|s|$, and especially increasing $\text{Im}(s)$, entails refining the BE mesh), or (b) set an arbitrary initial guess for f_{HFA}, then gradually increase its value until the results in the time domain are deemed satisfactory (the errors induced by a too-low value of f_{HFA} are easily recognisable). Numerical experiments for this approach will be discussed in Section 2.6.2 and Section 2.6.3.

2.5.5 HFA yields $O(1)$ complexity in time

The spatial complexity of the FM-BEM is $O(N \log N)$. Asymptotically, the time complexity of our procedure is given by the complexity of the $\mathcal{Z}$-transform, computed with an FFT, so $O(M \log M)$. However, performing the FFT is much faster than solving a BEM problem. Then, in practice, for reasonable values of M (we tried up to $M = 10^5$), the time complexity of the procedure depends on the number M_B of frequency-domain BEM problems actually solved. Without recourse to a HFA, we have $M_B = M + 1$, see Section 2.3.4. By contrast, the availability of a HFA, such that BEM problems are solved only when $|p(\xi)|/\Delta t \leq f_{\text{HFA}}$ for some threshold f_{HFA}, has the remarkable consequence of making the overall complexity in time constant (instead of linear). More precisely:

Proposition 1 *Assume that all zeros of $p(\xi)$, except $\xi = 1$, have modulus strictly greater than 1. Let $\xi_k = \rho e^{\mathrm{i}k\pi/M}$ $(0 \leq k \leq 2M-1)$ with ρ such that $\rho^M = \varepsilon$, in accordance with the synthesis formula (2.27) used for discrete times $t_n = n\Delta t$ $(0 \leq n \leq M)$. Let $M_0 \in \mathbb{N}$. For a given threshold f_{HFA} and any $M \geq M_0$, there exists $K \in \mathbb{N}$ depending only on f_{HFA}, M_0 and the chosen multistep method (in particular, K does not depend on Δt) such that we have*

$$\frac{|p(\xi_k)|}{\Delta t} \geq f_{HFA} \qquad \textit{for all} \quad k \in [\![K, 2M-K]\!].$$

In other words, for any large enough M, the number of complex frequencies with modulus smaller than a chosen HFA threshold is at most $2K-1$, and independent of Δt.

Proof Let B denote the closed unit disk in the complex plane. We begin by observing that the consistency requirement for the linear multistep method dictates that $\xi = 1$ be a single root of the symbol $p(\xi)$ (Quarteroni et al., 2007, Secs. 11.5 and 11.6); we can then write $p(\xi) = (1-\xi)q(\xi)$, with $q(1) \neq 0$. Having assumed that all other zeros of p have modulus strictly greater than 1, there exists $q_0 > 0$ such that $|q(\xi)| \geq q_0$ for all $\xi \in B$, and we have $|p(\xi)| \geq q_0|1-\xi|$.

Then, for the values $\xi_k = \rho e^{\mathrm{i}k\pi/M}$ $(0 \leq k \leq 2M-1)$ of interest, we have

$$|1-\xi_k|^2 = (1-\rho)^2 + 2\rho\big(1-\cos\big((k\pi/M)\big)\big). \tag{2.39}$$

Moreover, letting ρ_0 be defined by $\rho_0^{M_0} = \varepsilon$, we have $1 \geq \rho \geq \rho_0$ for any $M \geq M_0$.

Case 1: $\cos(k\pi/M) \geq 0$. For this case, observing in addition that $(1-\rho)^2 \geq 0$ and $1-\cos u \geq (4/\pi^2)u^2$ for any $u \in [-\pi/2, \pi/2]$, we get

$$|p(\xi_k)|^2 \geq q_0^2|1-\xi_k|^2 \geq \frac{8}{\pi^2}q_0^2\rho_0\Big(\frac{k\pi}{M}\Big)^2.$$

This implies that

$$\frac{|p(\xi_k)|^2}{\Delta t^2} = \frac{M^2|p(\xi_k)|^2}{T^2} \geq f_{\mathrm{HFA}}^2 \qquad \text{for any } \ k,\ K \leq |k| \leq \frac{M}{2}, \qquad \text{with } \ K \equiv \Big\lfloor \frac{f_{\mathrm{HFA}}T}{q_0\sqrt{8\rho_0}} \Big\rfloor,$$

where $\lfloor x \rfloor$ denotes the integral part of $x \in \mathbb{R}$. Consequently, the inequality $|p(\xi)|/\Delta t \leq f_{\mathrm{HFA}}$ of main interest can possibly be verified only by $\xi = \xi_k$ with $1-K \leq k \leq K-1$, i.e., has at most $2K-1$ solutions such that $\cos(k\pi/M) \geq 0$.

Case 2: $\cos(k\pi/M) \leq 0$. In that case, (2.39) implies that $|p(\xi)|^2 \geq 2\rho_0 q_0^2$, while $\Delta t \leq T/M_0$, so the target inequality $|p(\xi)|/\Delta t \leq f_{\mathrm{HFA}}$ implies

$$q_0 M_0\sqrt{2\rho_0} = \sqrt{2}q_0 M_0 \varepsilon^{1/2M_0} \leq f_{\mathrm{HFA}}T,$$

with the equality resulting from the definition of ρ_0. Since $M_0\varepsilon^{1/2M_0} \to \infty$ as $M_0 \to \infty$, M_0 can be selected such that

$$q_0 M_0\sqrt{2\rho_0} \geq f_{\mathrm{HFA}}T$$

in which case any ξ_k such that $\cos(k\pi/M) \leq 0$ violates the target inequality $|p(\xi)|/\Delta t \leq f_{\mathrm{HFA}}$.
On combining the outcomes of cases 1 and 2, the proof is complete.

Proposition 1 and its proof mean that, after taking advantage of both the HFA and the symmetry under conjugation of ξ_k mentioned in Section 2.3.3, the expected number of actually required BEM solutions satisfies the estimate

$$M_B \leq 1 + \Big\lfloor \frac{f_{\mathrm{HFA}}T}{q_0\sqrt{8\rho_0}} \Big\rfloor, \tag{2.40}$$

which depends only very mildly in M_0 (we have e.g., $\sqrt{\rho_0} \approx 0.75, 0.97, 0.997$ for $M_0 = 10, 100, 1000$).

Remark 11 *The assumption made on the zeros of $p(\xi)$ in Prop 1, which is verified e.g., by the backward Euler and BDF2 schemes, is equivalent to assuming that all zeros of the characteristic polynomial of the numerical differentiation operator underlying the multistep scheme, except $\xi = 1$, lie outside the closed unit disk of $\mathbb{C}$, i.e., that the multistep scheme is strongly stable (see e.g., Quarteroni et al. (2007, Secs. 11.5 and 11.6) for an overview of the properties of multistep methods).*

For multistep schemes that are only zero-stable, $p(\xi)$ has other zeros (of multiplicity 1) on the unit circle, which would provide additional clusters of points ξ_k satisfying $|p(\xi_k)|/\Delta t \leq f_{HFA}$.

Remark 12 *We indicate that another interesting approach having a $O(1)$ time complexity has recently been proposed (Anderson et al., 2020; Anderson, 2020). However, its computational gain is based on a band-limited representation of long time signals, a premise which does not readily fit our target industrial studies featuring discontinuous incident waves.*

2.5.6 Adapting the mesh refinement to the complex frequency

For a given wave propagation problem, the BEM problems (2.28) are solved with a fast FM-BEM solver. This solver is efficient with a fixed number of nodes per wavelength (typically 10 or so) (Chaillat, 2008). This implies that using the same mesh for all frequencies is not efficient. On the other hand, generating a mesh for each frequency is impractical. To strike a balance, about 10 meshes of Γ are created, with uniform and decreasing mesh size. For a given frequency $s(\xi_k)$, the associated BEM problem is solved using the least refined mesh that has at least 8 points per wavelength, and the BEM solutions obtained on that mesh are interpolated to a master mesh (chosen for post-processing, or in the future for fluid-structure coupling) using the software feflo.a (Loseille, 2017).

2.6 Numerical validation of the HFA-enhanced $\mathcal{Z}$-BEM

In view of the industrial context of our study, we choose to validate the fast $\mathcal{Z}$-BEM method described in Section 2.3 and Section 2.5 on simple configurations that are representative of the interaction between an underwater explosion and a submarine. The resulting blast is a spherical wave that propagates in an unbounded acoustic medium at speed c, before interacting with a shell whose surface is known. Two academic problems are accordingly considered in this section to demonstrate the efficiency of the $\mathcal{Z}$-BEM: a breathing sphere, and the scattering of a spherical wave by a rigid infinite cylinder. Reference solutions are available for both problems, see Appendices C.4 and C.5. Results on a more-complex configuration evocative of the industrial problem will then be presented in Section 2.7.

All numerical results of this section have been obtained under the following conditions:

- The accuracy ε of the discrete inverse $\mathcal{Z}$-transform (2.27) is set to 10^{-5};
- The number of frequencies L is set to twice the number of time steps: $L = 2M$;
- The value of ρ is set according to ε, such that $\rho^L = \varepsilon$;
- The backward differentiation formula of order 2 (BDF2) is used: $p(\xi) = (3-4\xi+\xi^2)/2$;
- The GMRES tolerance for the FM-BEM frequency-domain solver is set to 10^{-5};
- The fluid velocity and mass density are $c = 1500\,\mathrm{m/s}$ and $\rho = 1000\,\mathrm{kg/m^3}$, respectively.

The two possible sources of errors when using the $\mathcal{Z}$-BEM procedure are (i) the FM-BEM procedure, and (ii) the CQM-HFA procedure. The FM-BEM procedure used here

has already been validated (Chaillat, 2008; Chaillat et al., 2008), in terms of both its convergence and its complexity. We will thereafter evaluate solution errors against a reference solution p_{ex}, which reflect the cumulative effect of sources (i) and (ii), expecting factor (ii) to be dominant.

2.6.1 First validation case: breathing sphere

Consider a spherical shell of radius a, submerged in an infinite fluid domain Ω, with mass density ρ and sound velocity c. The shell and fluid are both at initial rest. At time $t = 0$, the shell starts pulsating, or breathing, with a radially-symmetric normal velocity $u = \mathbf{u} \cdot \mathbf{n}$; this creates a radiated field in the surrounding fluid. We look for the induced acoustic pressure in the fluid domain, and more specifically on the sphere surface $\Gamma = \{r = a\}$. This radiation problem consists in solving (2.1) for $\psi = \phi$ with the boundary condition

$$\partial_n \phi(\mathbf{y}, t) = u(t)\,, \quad \mathbf{y} \in \Gamma = \{r = a\},$$

expressing the prescribed normal wall velocity u. The results presented in this section are obtained with $a = 1$ m and u set to

$$u(t) = u(t;\omega) = u_0 \sum_{i=1}^{5} u_i \sin(2\pi f_i t)\,, \tag{2.41}$$

where $u_1 = 1$, $u_2 = 1.2$, $u_3 = 0.7$, $u_4 = 2.8$, $u_5 = 1.4$, and the frequencies are set to $f_1 \equiv \omega/(2\pi) = f_{\max}$, $f_2 = f_{\max}/1.7$, $f_3 = f_{\max}/2.4$, $f_4 = f_{\max}/7.6$, $f_5 = f_{\max}/25.4$. The angular frequency parameter ω is fixed[2]. The amplitude u_0 is assumed to be small enough for the linear acoustic fluid model to be correct. This problem has a closed-form analytical solution p_{ex}, derived in Appendix C.4.

Figure 2.9 shows that the pressure p^{rad} on Γ computed using our fast $\mathcal{Z}$-BEM procedure agrees very well with the analytical solution p_{ex}, with relative errors (see (2.42)) $\delta(\Gamma) = 1.7\%$ and $\delta(\Gamma) = 1.3\%$ for the two considered values $f_{\max} = 5\ 10^2$ Hz and $f_{\max} = 4\ 10^3$ Hz of the prescribed frequency. The latter are typical of situations where a submarine faces a remote underwater explosion, where T is of the order of a few milliseconds.

We now examine the influence of the HFA ($P^{\text{rad}} = \rho c U$ in this case, see Section 2.5.3) on both solution accuracy and computational efficiency. The BEM problems are solved for the requisite frequencies $s(\xi_k) = p(\xi_k)/\Delta t$, taken in order of increasing modulus. Each BEM solution is compared to its HFA approximation by way of the relative difference δ_{HFA} (see (2.36)), with $\delta_{\text{HFA}}(s(\xi_k))$ expected to decrease as $|s(\xi_k)|$ increases. For a certain frequency $s = s_{\text{HF}}$, $\delta_{\text{HFA}}(s)$ becomes smaller than a preset tolerance tol_{HFA} (typically 5 %). Then, the high-frequency limit f_{HFA} is set to $|s_{\text{HF}}|$, and BEM solutions for $|s(\xi_k)| > f_{\text{HFA}}$ are evaluated using the HFA.
Table 2.2 illustrates the influence of f_{HFA} on the accuracy of the transient solution, employing the two previously-considered values of $f_{\max}$ in (2.41). It also shows the corresponding number M_B of frequency-domain BEM solutions computed, the relative BEM-HFA difference δ_{HFA} at frequency f_{HFA} (see (2.36)) and the overall solution error

$$\delta(\Gamma) \equiv \frac{\|p - p_{\text{ex}}\|_{L^2([0,T];L^2(\Gamma))}}{\|p_{\text{ex}}\|_{L^2([0,T];L^2(\Gamma))}}. \tag{2.42}$$

As expected, $\delta(\Gamma)$ decreases when f_{HFA} is increased, while the overall solution error steadily reduces until reaching a limiting value that is the best accuracy achievable with the considered mesh. Therefore, the procedure appears to be both consistent and accurate.

[2]This is **not** a time-harmonic problem, since the sphere **starts** breathing at $t = 0$, a time-harmonic steady state being reached only in the infinite-time limit.

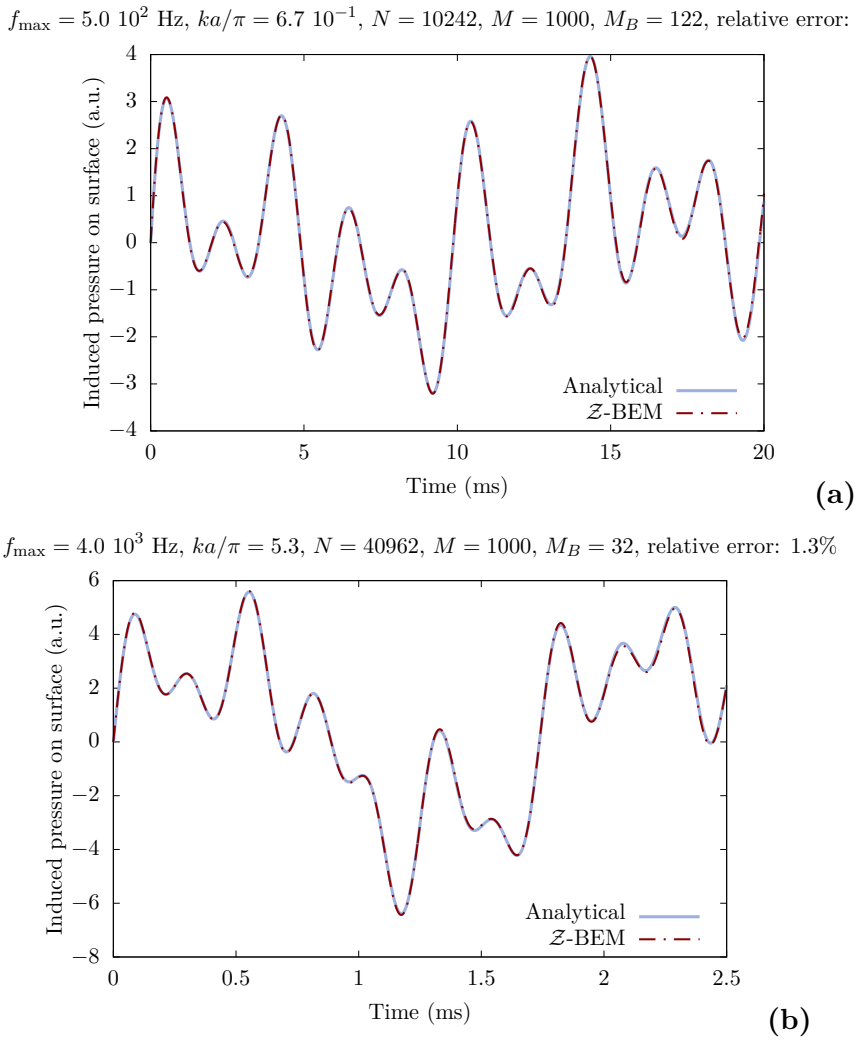

Figure 2.9: Breathing sphere: pressure induced on the surface (with $k = \omega/c$).

The fast $\mathcal{Z}$-BEM procedure is seen to accurately solve rapid acoustic radiation problems in the time domain at the cost of only a moderate number M_B of frequency BEM solutions, thanks to a HFA. The gain of the method lies in the number of frequency BEM problems solved: as shown in Proposition 1, for a given physical problem, M_B is asymptotically independent of the time step Δt. Indeed, selecting an overly small time step should not artificially increase the number of BEM problems, as this does not *per se* mean that the considered physical problem is a high frequency one. On the other hand, M_B decreases as the intrinsic high-frequency character of the problem increases, as more information on the solution is then provided by the HFA. Case (b) of Table 2.2 clearly illustrates the efficiency of the procedure: only $M_B = 32$ BEM solutions are needed (the $M+1-M_B = 969$ missing frequency-domain solutions being provided by the HFA) to achieve an accuracy of 1.3%, that is nearly the same as that obtained without HFA (at the cost of $M + 1$ =1001 BEM solutions). Moreover, these M_B solutions can be computed concurrently (see Section 2.7.1). Going to the other extreme of solving case (b) using only the HFA (no BEM solution), the obtained solution is expected to be accurate only for the first time steps, and this is corroborated by Figure 2.10. The best compromise between accuracy and efficiency then clearly has to combine BEM and HFA solutions.

$f_{\max}$ (kHz)	f_{HFA} (kHz)	$k_{\mathrm{HFA}}a/\pi$	M_B	$\delta_{\mathrm{HFA}}(f_{\mathrm{HFA}})$ (%)	$\delta(\Gamma)$ (%)
(a) 0.5	6.6	8.9	43	22.2	4.7
	8.0	10.6	51	19.5	3.2
	9.9	13.3	63	12.9	2.1
	13.3	17.7	83	12.5	1.9
	19.9	26.6	122	6.5	1.7
	39.8	53.1	224	3.6	1.7
(b) 4.0	17.7	23.6	15	8.4	4.6
	26.6	35.4	22	5.8	4.1
	39.8	53.1	32	3.7	1.3
	79.7	106.3	63	1.9	1.2

Table 2.2: Breathing sphere: influence of the choice of f_{HFA} on time-domain solution accuracy (with $k_{\mathrm{HFA}} = 2\pi f_{\mathrm{HFA}}/c$). Relative difference indicators δ_{HFA} and $\delta(\Gamma)$ are defined by (2.36) and (2.42).

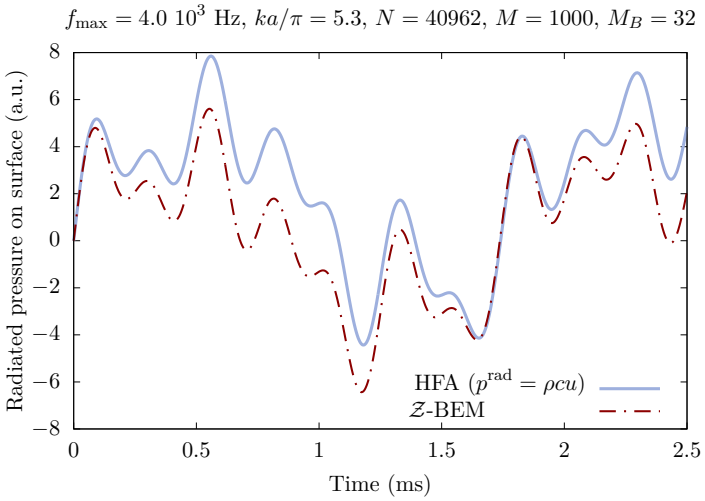

Figure 2.10: Breathing sphere: $\mathcal{Z}$-BEM solution and HFA for the radiated pressure p^{rad} on Γ.

2.6.2 Second validation case: rigid infinite cylinder facing a spherical wave

We now consider the scattering of a wave by an infinite cylinder, a configuration more representative of our intended applications, which allows comparisons to a semi-analytical reference solution. The incident wave results from the explosion of $W = 100\,\mathrm{kg}$ of TNT at a point $\mathbf{s}$ whose distance to the cylinder axis is $d_0 = 100\,\mathrm{m}$ (see Figure 2.11). As explained in Section 1.2, the explosion generates an abrupt acoustic wave whose pressure field is empirically expressed as (Cole, 1948)

$$p^{\mathrm{inc}}(\mathbf{y},t) = p_m(r)\exp\left(-\frac{t-r/c}{\tau(r)}\right)H(t-r/c), \qquad r = \|\mathbf{y}-\mathbf{s}\|, \tag{2.43}$$

where

- H is the Heaviside step function,

- $p_m(r) = K_1 \left(\dfrac{W^{1/3}}{r} \right)^{a_1}$ is the magnitude of the initial pressure jump,
- $\tau(r) = K_2 W^{1/3} \left(\dfrac{W^{1/3}}{r} \right)^{a_2}$ characterises the pressure decay in time.

K_1, K_2, a_1, a_2 are parameters that depend on the kind of explosive material; the values

$$K_1 = 5.24\ 10^7\ \text{SI},\ a_1 = 1.13, \qquad K_2 = 8.4\ 10^5\ \text{SI},\ a_2 = -0.23,$$

were used to obtain the results presented thereafter (Swisdak, 1978). A sum of two exponentials (Geers and Hunter, 2002) could equally well be considered in (2.43) (see Section 1.2) without affecting our procedure, which is independent of the form of the input pressure (as long as it is a HF solicitation).

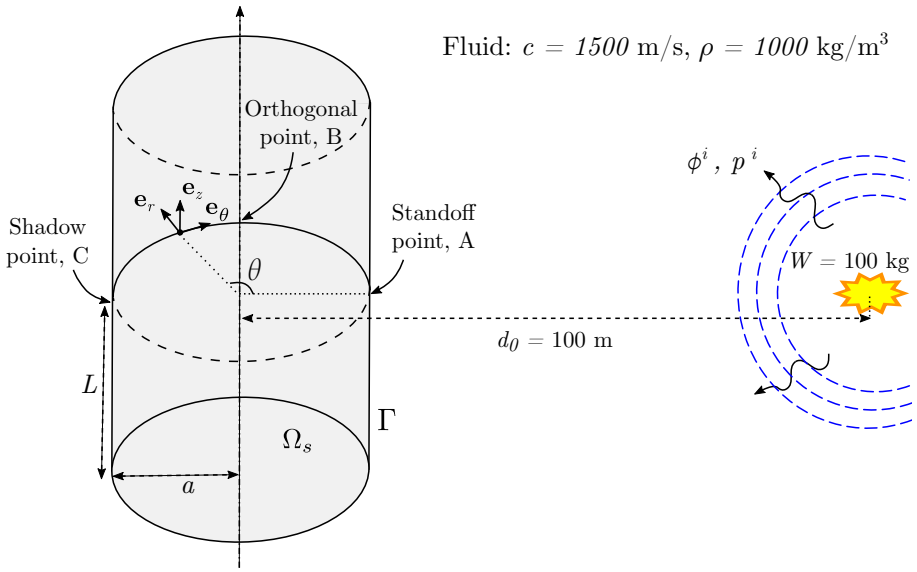

Figure 2.11: Infinite cylinder facing an underwater explosion.

Numerical results yielded by our fast $\mathcal{Z}$-BEM, incorporating all improvements presented in Section 2.5, are compared to those provided by an in-house implementation of the semi-analytical approach given in Appendix C.5. The $\mathcal{Z}$-BEM procedure is in particular used with the mesh interpolation presented in Section 2.5.6, carried out with 8 meshes with uniform decreasing mesh size. For the $\mathcal{Z}$-BEM computations, a finite cylinder is considered, axially long enough to ensure that the results obtained for the considered duration T coincide (due to causality) to those for an infinite cylinder. The following parameters were used for the $\mathcal{Z}$-BEM computations: $T = 5\,\text{ms}$ (with results only shown for $T = 3\,\text{ms}$ to ensure their insensitivity to the finite cylinder length), $f_{\text{HFA}} = 45\ 10^3\,\text{Hz}$, $k_{\text{HFA}}a/\pi = 30$ ($a = 0.5\,\text{m}$), $k_{\text{HFA}}L/\pi = 300$ ($L = 5$ m), $h = 0.0056\,\text{m}$ (mesh size of the most refined mesh), $N \approx 10^6$ DOFs, $M = 10^4$. The parameters for the semi-analytical approximation (Appendix C.5) are $M = 2048$, $N^\theta_{\text{modes}} = 90$ and $N^z_{\text{modes}} = 200$. The master mesh chosen for plots and post-processing (on which all the frequency-domain solutions are interpolated) has $7\ 10^4$ DOFs and a mesh size $h = 0.022\,\text{m}$. The choice of the master mesh has very little influence on the result quality.

Figure 2.12 shows the total pressure p^{Ref} at three points of the cylinder surface: the standoff point A facing the explosion ($\theta = 0$, $z = 0$ with the notations of Figure 2.11), the shadow point C ($\theta = \pi$, $z = 0$) opposite to A, and the orthogonal point B ($\theta = \pi/2$, $z = 0$).

f_{HFA} (kHz)	$k_{\mathrm{HFA}}a/\pi$	$k_{\mathrm{HFA}}L/\pi$	M_B	$\delta(\mathbf{x})$ (%) $\mathbf{x}=A$	$\mathbf{x}=B$	$\mathbf{x}=C$
20.0	13.3	133	32	4.9	3.6	9.4
25.0	16.7	167	40	4.8	3.4	8.3
30.0	20.0	200	48	4.7	3.4	8.0
35.0	23.3	233	56	4.7	3.3	7.6
40.0	26.7	267	64	4.7	3.3	7.5
45.0	30.0	300	72	4.7	3.3	7.4

Table 2.3: Scattering by a small cylinder ($a = 0.5\,\mathrm{m}$, $L = 5\,\mathrm{m}$): influence of f_{HFA} on time-domain solution accuracy (with $k_{\mathrm{HFA}} = 2\pi f_{\mathrm{HFA}}/c$). The pointwise relative difference indicator δ is defined by (2.44).

To avoid Gibbs phenomena associated to discontinuous inputs, the time variation of the incident pressure is modified so as to vary smoothly from zero to its maximum during a small time interval (typically set to $\tau/20$ or $\tau/10$, where τ refers to the exponential time constant related to the explosion), a customary treatment in underwater explosion analysis. In particular, this implies that the input is regular enough to formulate the BEM problems for the pressure (see discussions in Section 1.2.3). The fast $\mathcal{Z}$-BEM and the semi-analytical method are seen in Figure 2.12 to provide very similar results (with the $\mathcal{Z}$-BEM solution at the shadow point C exhibiting small non-physical perturbations that slightly affect the overall solution).

Table 2.3 illustrates the influence of f_{HFA} on the accuracy in the time domain of the solution at the standoff, orthogonal and shadow points, in terms of the relative pointwise solution error

$$\delta(\mathbf{x}) \equiv \frac{\|p(\mathbf{x},\cdot) - p_{\mathrm{ex}}(\mathbf{x},\cdot)\|_{L^2([0,T])}}{\|p_{\mathrm{ex}}(\mathbf{x},\cdot)\|_{L^2([0,T])}} \tag{2.44}$$

for the acoustic time-dependent pressure response $p(\mathbf{x},\cdot)$ evaluated at a point $\mathbf{x} \in \Gamma$. The trends are similar to those observed for the pulsating sphere example (see Table 2.2); in particular, the solution errors decrease as f_{HFA} increases. This indicates that the enhanced HFA we designed for the scattering case is efficient for cylindrical geometries. Note that the solution accuracy is estimated with p_{ex} taken as the semi-analytical solution, which also only approximates the exact solution due to various factors such as series truncations. The time-domain solution $t \mapsto p^{\mathrm{Ref}}(A,t)$ at the standoff point is almost optimal with $M_B = 32$ BEM solutions, as adding more BEM solutions only slightly reduces the solution error. The same observation holds for $t \mapsto p^{\mathrm{Ref}}(B,t)$. The solution appears to be most accurate in this region ($\theta \approx \pi/2$), which makes our HFA attractive because this is precisely the case where the classical Kirchhoff approximation is least accurate (see Section 2.5.4). At the shadow point, non-physical oscillations appear once p^{inc} reaches that point. The magnitude of these oscillations reduces as f_{HFA} increases, which makes sense since they are caused by insufficient accuracy when using the HFA at frequencies not high enough.

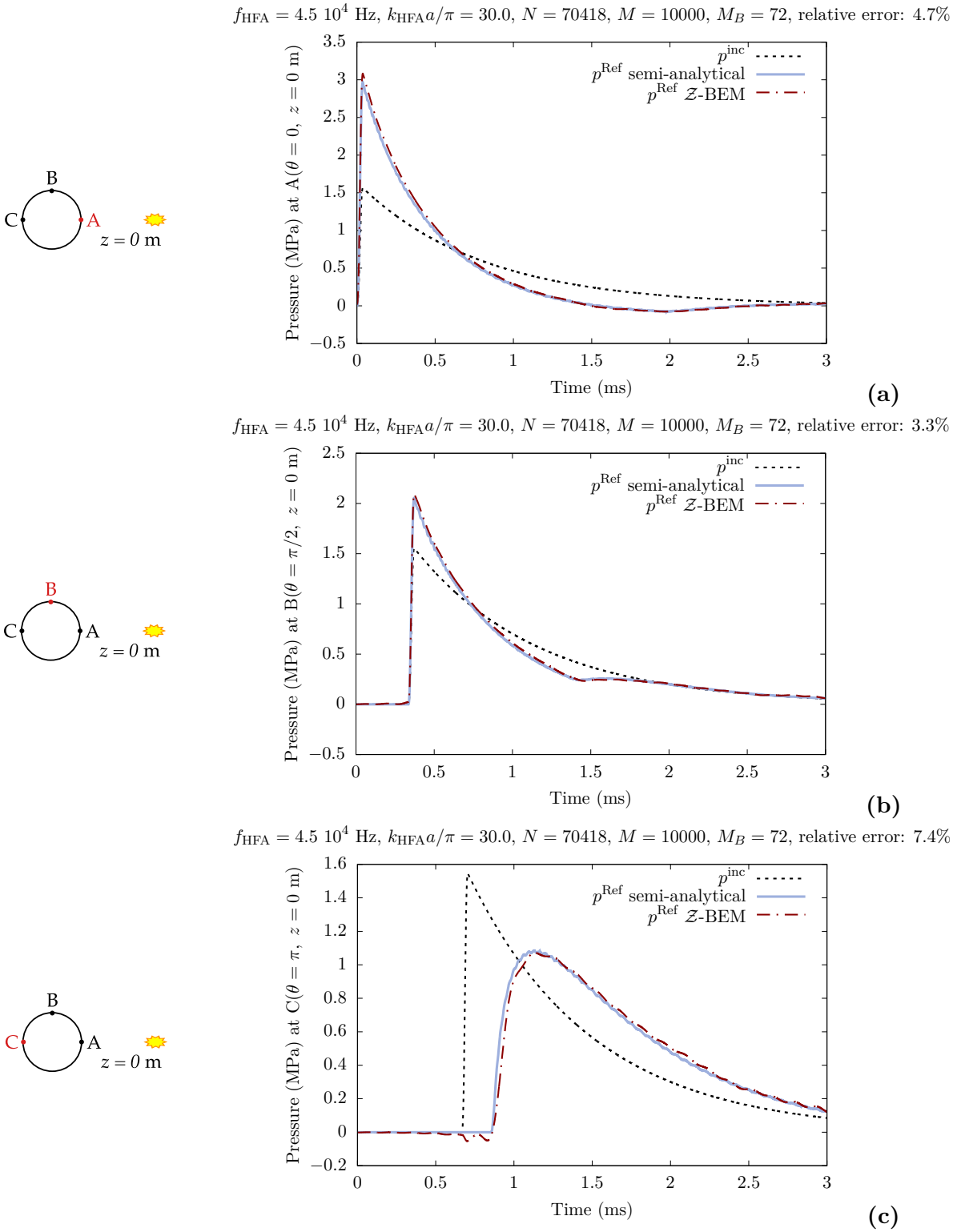

Figure 2.12: Scattering by a small cylinder ($a = 0.5\,\mathrm{m}$, $L = 5\,\mathrm{m}$, see Figure 2.11): comparison between the $\mathcal{Z}$-BEM and semi-analytical solutions for the total field p^{Ref} on the $z = 0$ plane, at the standoff (a), orthogonal (b) and shadow (c) points. The incident field at those points is also shown.

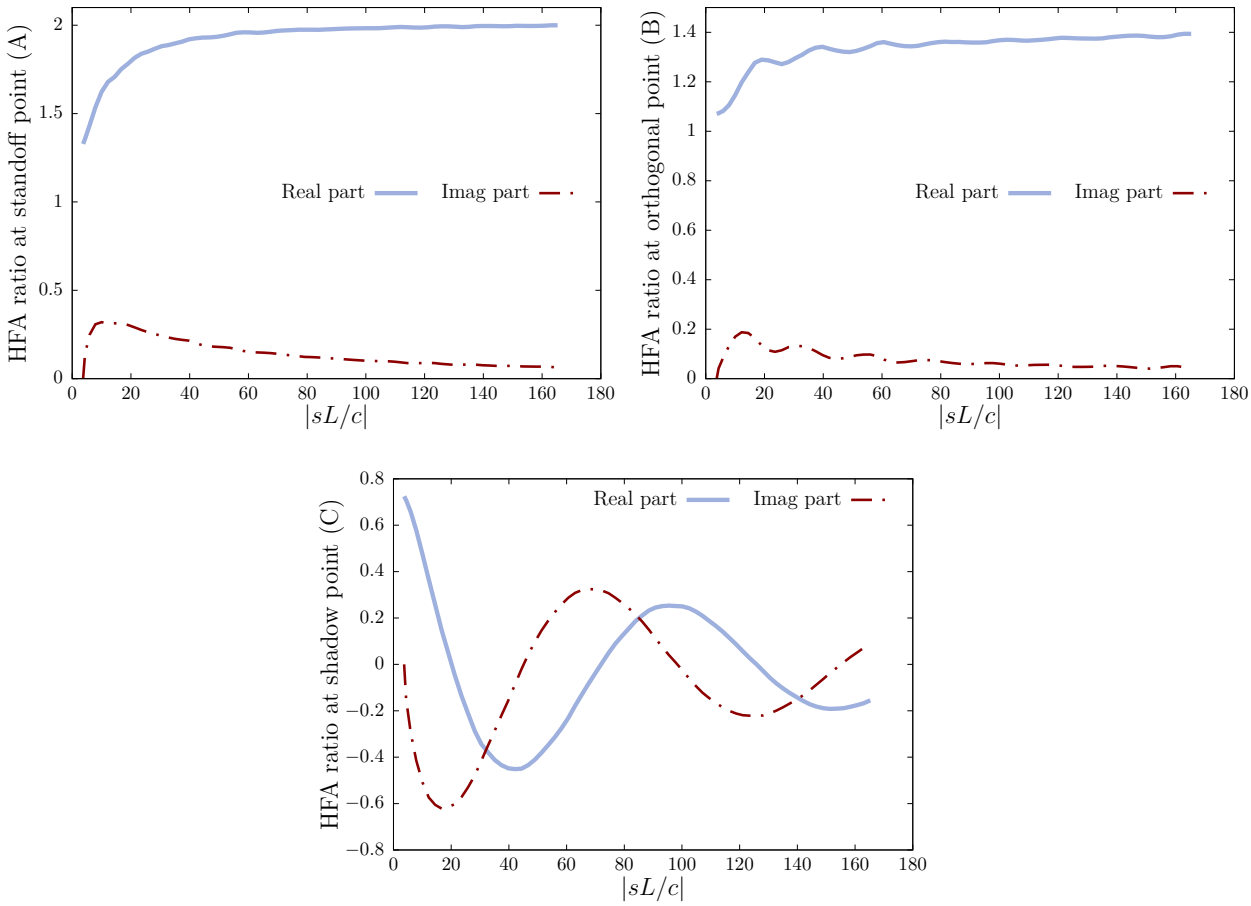

Figure 2.13: Scattering by a small cylinder ($a = 0.5$ m, $L = 5$ m, see Figure 2.11): HFA ratio $\mathcal{R}(\mathbf{y}, s)$ at standoff (A), orthogonal (B) and shadow (C) points.

By contrast with Section 2.6.1, differences between BEM and HFA solutions are not provided in Table 2.3, since they are zero by construction for $|s| = f_{\text{HFA}}$ (see Section 2.5.4). The HFA quality in the scattering case depends on whether the ratio (2.38) is stable as $|s|$ increases. This behaviour varies according to the location on the surface, as illustrated on Figure 2.13, and appears, from a comparison with Table 2.3, to be correlated with the overall time-domain solution accuracy.

The results of this section, for a small cylinder facing an underwater explosion, validate sufficient accuracy of the proposed HFA-enhanced $\mathcal{Z}$-BEM. They also show its efficiency, since for this case only 72 BEM solutions are needed to get satisfactory results (by comparison, $O(M)$ BEM problems are needed for either a time-domain BEM or the $\mathcal{Z}$-BEM without HFA).

2.6.3 Example involving premature onset of HFA

So far, we considered cases for which computational resources allowed to solve BEM problems at any frequency below a physically reasonable HFA threshold. However, for applications such as modelling a submarine facing an underwater explosion, the size and complexity of the structure would make solving all the BEM problems failing a preset tolerance tol_{HFA} of (say) 5% too expensive. In such cases, the number of practically solvable BEM problems results from computational constraints rather than a sensible HFA threshold. Therefore, in practice, f_{HFA} is set to the highest frequency that can be dealt

with by the BEM, and all problems (2.25) for which $|s(\xi)| \geq f_{\mathrm{HFA}}$ are solved using a HFA, even though some of those HFA solutions will have low accuracy.

This makes it important to evaluate how a forced premature recourse to a HFA affects the accuracy of the time-domain solution. To this end, we consider a variant of the configuration studied in Section 2.6.2 involving a larger cylinder, and use the following parameters: $T = 20\,\mathrm{ms}$, $f_{\mathrm{HFA}} = 4.5\ 10^3\,\mathrm{Hz}$, $k_{\mathrm{HFA}}a/\pi = 30$ ($a = 5\,\mathrm{m}$), $k_{\mathrm{HFA}}L/\pi = 300$ ($L = 50$ m), $h = 0.056\,\mathrm{m}$ (mesh size of the most refined mesh), $N \approx 10^6$ DOFs, $M = 10^4$. The parameters for the semi-analytical approximation (Appendix C.5) are, as before, $M = 2048$, $N^{\theta}_{\mathrm{modes}} = 90$ and $N^{z}_{\mathrm{modes}} = 200$. Again, we use the mesh interpolation, the master mesh used for plots and post-processing having $7\ 10^4$ DOFs and a $h = 0.22\,\mathrm{m}$ mesh size.

The total pressure p^{Ref} on Γ for this non-optimal set of parameters is presented in Figure 2.14 and Figure 2.15. The too-small value of f_{HFA} used results in stronger non-physical oscillations in the shadow region, yet the overall result remains satisfactory in view of the challenging problem dimensions considered since

- the overall trend of the solution is correct;
- in the shadow zone, the non-physical oscillations occur about a mean value that corresponds to the correct solution.

The advantage of our method is then to obtain an accurate enough solution under challenging conditions that might prevent other numerical methods to perform. The loss of accuracy induced by forced premature recourse to HFA depends on the limitation of computational resources. The influence of f_{HFA} is in addition quantitatively illustrated in Table 2.4, corroborating the above-mentioned trends. The $O(1)$ complexity in time afforded by the HFA (see Section 2.5.5) is demonstrated for this example in Table 2.5, which shows the evolution of M_B in the cylindrical cases presented in this article, obtained using the backward differential formula of order 2.

Figure 2.16 illustrates the HFA ratio in the case of the large cylinder, it shows similar behaviour as in the small cylinder case (see Figure 2.13).

f_{HFA} (kHz)	$k_{\mathrm{HFA}}a/\pi$	$k_{\mathrm{HFA}}L/\pi$	M_B	δ(x) (%)					
				x = A	x = B	x = C	x = D	x = E	x = F
2.0	13.3	133	13	18.7	4.9	38.6	11.9	4.1	36.8
2.5	16.7	167	16	13.8	4.1	23.1	9.6	3.5	22.8
3.0	20.0	200	20	9.8	3.5	22.5	7.4	3.2	21.2
3.5	23.3	233	23	7.8	3.2	18.3	6.5	3.1	16.8
4.0	26.7	267	26	6.8	3.3	15.2	5.6	3.1	14.3
4.5	30.0	300	29	6.1	3.4	13.7	5.3	3.1	12.3

Table 2.4: Scattering by a large cylinder ($a = 5\,\mathrm{m}$, $L = 50\,\mathrm{m}$): influence of f_{HFA} on time-domain solution accuracy (with $k_{\mathrm{HFA}} = 2\pi f_{\mathrm{HFA}}/c$). The pointwise relative difference indicator δ is defined by (2.44).

Cyl diameter (m)	$f_{\mathbf{HFA}}$ **(kHz)**	T **(ms)**	M	M_B	**Estimate** (2.40)
1.0	45.0	5.0	10^2	52	80
			10^3	76	
			10^4	77	
			10^5	77	
10.0	4.5	20.0	10^2	25	32
			10^3	29	
			10^4	29	
			10^5	29	

Table 2.5: Scattering by a large cylinder ($a = 5\,\mathrm{m}$, $L = 50\,\mathrm{m}$, see Figure 2.11): demonstration of the $O(1)$ time complexity of the procedure.

To conclude, since the computational complexity of our procedure is $O(N \log N)$ with regards to the number of spatial DOFs N, and $O(1)$ with regards to the number of time steps M, future improvements in computing resources will benefit our procedure more than other procedures with higher complexity.

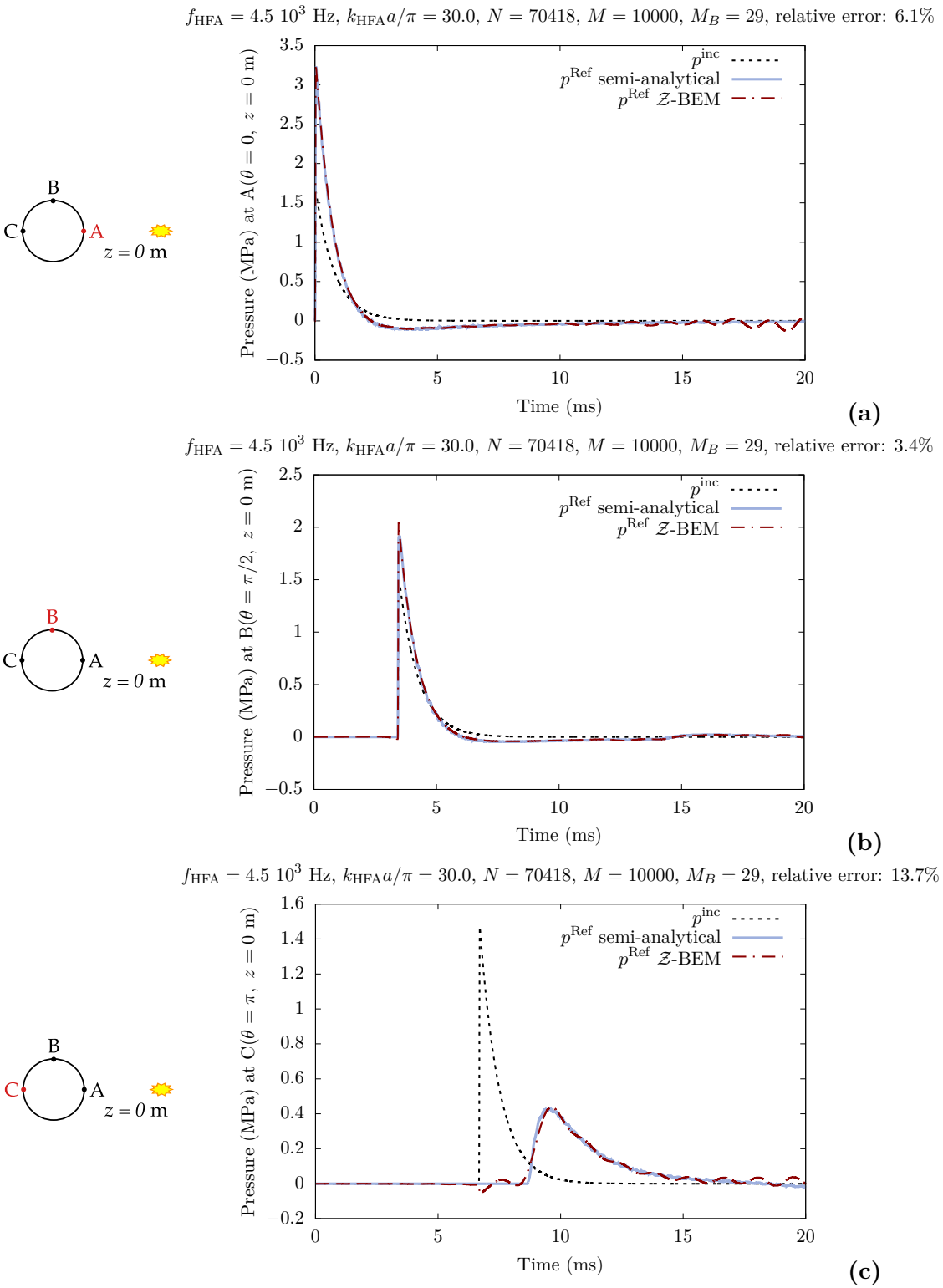

Figure 2.14: Scattering by a large cylinder ($a = 5\,\mathrm{m}$, $L = 50\,\mathrm{m}$, see Figure 2.11): comparison between the $\mathcal{Z}$-BEM and semi-analytical solutions for the total field p^{Ref} on the $z = 0$ plane, at the standoff (a), orthogonal (b) and shadow (c) points. The incident field at those points is also shown.

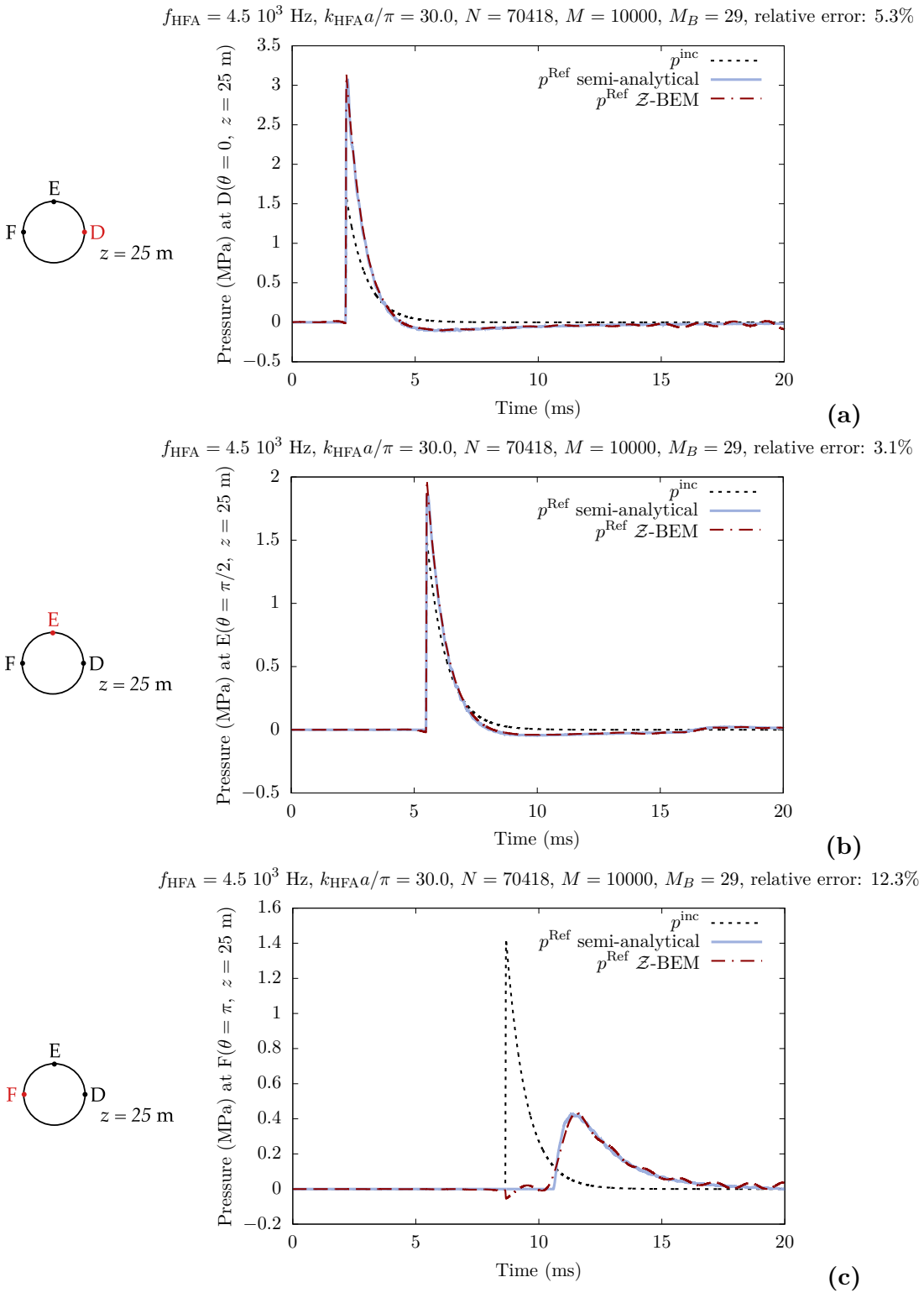

Figure 2.15: Scattering by a large cylinder ($a = 5\,\mathrm{m}$, $L = 50\,\mathrm{m}$, see Figure 2.11): comparison between the $\mathcal{Z}$-BEM and semi-analytical solutions for the total field p^{Ref} on the $z = 25\,\mathrm{m}$ plane, at the equivalent of the standoff (a), orthogonal (b) and shadow (c) points. The incident field at those points is also shown.

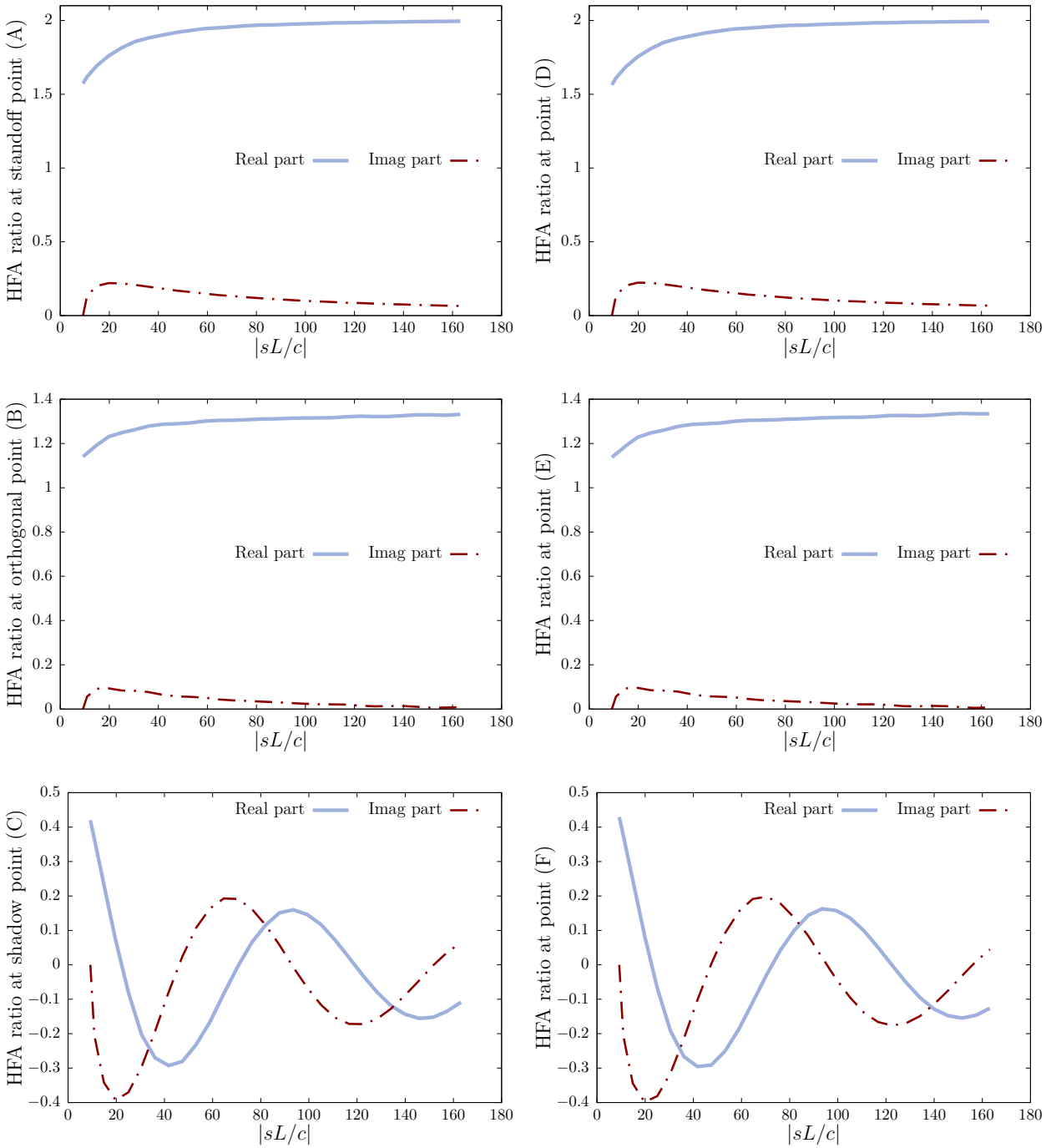

Figure 2.16: Scattering by a large cylinder ($a = 5\,\mathrm{m}$, $L = 50\,\mathrm{m}$, see Figure 2.11): HFA ratio.

2.7 Scattering of a spherical wave by a rigid motionless complex structure

This final section demonstrates the efficiency of the fast $\mathcal{Z}$-BEM procedure for the three-dimensional scattering of a spherical wave by a complex submarine-shaped structure, referred to as BB2. Its geometry, provided in (Overpelt et al., 2015), corresponds to a realistic submarine of length 70.2 m and height 16.4 m. It is composed of three main parts: the beam (cylindrical hull), the sail, and the planes (2 sail planes, 4 back planes). The propeller has been removed from the geometry and is not modelled.

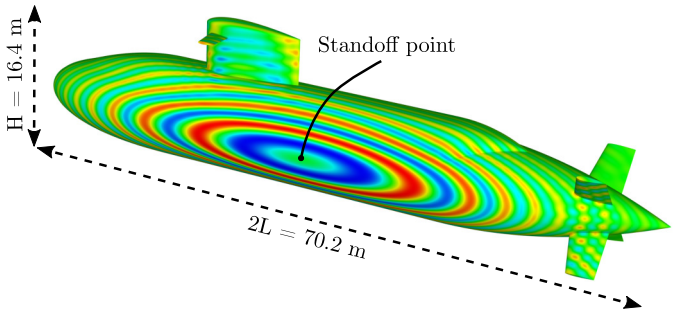

Figure 2.17: Scattering by a rigid motionless submarine: $\mathcal{Z}$-transform of the total pressure $P^{\mathrm{Ref}}(s)$ on the submarine surface, with $sL/c \approx 6.01 + 166\mathrm{i}$.

The BB2 is assumed to be motionless, and faces an explosion of $W = 100$ kg of TNT located 100 m away from the submarine centre. The standoff point is located on the beam; it is at the centre of the concentric ellipses in Figure 2.17. The main goal is to compute the total pressure field p^{Ref} on the submarine surface Γ. As before, the $\mathcal{Z}$-BEM procedure entails the solution of a large number of frequency-domain problems, using either the FM-BEM or a HFA. For the FM-BEM, 7 meshes are defined, with regular decreasing mesh size. The master mesh, used for interpolation, has $N \approx 3\ 10^5$ DOFs, corresponding to a mesh size of $h = 0.1$ m. The most refined mesh has $N \approx 3\ 10^6$ DOFs, corresponding to a mesh size of $h = 0.03$ m. Since N is large, f_{HFA} and M_B are set as explained in Section 2.6.3. For a given frequency $s(\xi_k)$, the associated BEM problem is solved using the least refined mesh that has at least 8 points per wavelength, except for the finest mesh, which is used with at least 6 points per wavelength. The latter restriction results in $f_{\mathrm{HFA}} = 8.667$ kHz (i.e., $k_{\mathrm{HFA}}L/\pi = 417$) and $M_B = 56$.

2.7.1 Frequency-domain BEM performance

The characteristics of a sample of the 56 BEM solution evaluations are provided in Table 2.6. As $|s|$ increases, the iterative BEM procedure behaves as expected on several respects. In particular, the number of FMM levels slowly increases (up to 8), while the GMRES iteration count also increases with N and $|s|$. The latter however remains moderate for all used frequencies, despite the geometrical complexity; this is due to the use of complex frequencies, which implies a spatially-decaying factor $e^{-\mathrm{Re}(s)r/c}$ in the fundamental solution, thereby reducing the effect of far contributions and improving the condition number of the BEM matrices. For GMRES, we avoided using initial guesses that depend on previously-obtained solutions (at lower frequencies), as this allows all BEM solutions to be computed concurrently, i.e., full parallelism for this part of the process. The elapsed time for the whole transient analysis thus depends directly on the number of

N	Im (sL/c)	# of levels	GMRES iters.	Pts per λ
155 083	26.43	5	20	9.0
530 021	56.63	6	28	8.8
1 048 115	64.18	7	29	11.1
	86.83	7	30	8.2
2 787 749	109.49	8	31	11.4
	139.70	8	32	8.9
	154.80	8	33	8.1
	177.47	8	34	7.0
	185.02	8	35	6.8
	192.57	8	36	6.5
	200.12	8	37	6.2
	207.68	8	38	6.0

Table 2.6: Scattering by a rigid motionless submarine: characteristics of some of the frequency-domain BEM solution evaluations (Re$(sL/c) = 6.0$).

computers (nodes) available. Here, the computations were run on a single machine with a 3.5GHz Intel XEON E5-2637 v3 processor, 8 cores, 2 chips, 4 cores/chip, 2 threads/core, and 768 GB of RAM.

2.7.2 HFA, time-domain results

We now assess the HFA proposed in Section 2.5.4 on this example, which features a complex geometry; in particular, Γ is not convex, implying that Kirchhoff-type approximations no longer have theoretical justification. Figure 2.18 shows the HFA ratio $\mathcal{R}(\mathbf{y}, s)$ (see (2.38)) at various points $\mathbf{y}$ as a function of $|s|$. On the cylindrical hull of the submarine, the ratio is stable (like for the cylinder case). In regions with more-complex local geometry, typically near the submarine planes or between two plates (where waves are trapped), $s \mapsto \mathcal{R}(\mathbf{y}, s)$ is oscillatory. This observation is reinforced by Figure 2.19, which reveals the regions of the submarine surface where $s \mapsto \mathcal{R}(\mathbf{y}, s)$ is not stable by plotting the relative oscillation $\mathbf{y} \mapsto \Delta_{\text{HFA}}(\mathbf{y})$ over the last third of the set of M_B BEM frequencies, defined by

$$\Delta_{\text{HFA}}(\mathbf{y}) = \frac{1}{2} \frac{\max\limits_{k\in J} \left(\mathcal{R}(\mathbf{y}, s_k)\right) - \min\limits_{k\in J} \left(\mathcal{R}(\mathbf{y}, s_k)\right)}{\max\limits_{k\in I} |\operatorname{Re}(\mathcal{R}(\mathbf{y}, s_k))| + \max\limits_{k\in I} |\operatorname{Im}(\mathcal{R}(\mathbf{y}, s_k))|} \tag{2.45}$$

with $I \equiv [\![1, M_B]\!]$, $J \equiv [\![2M_B/3, M_B]\!]$ and where $\max(z) \equiv \max(\operatorname{Re}(z)) + \mathrm{i}\max(\operatorname{Im}(z))$ (and similarly for $\min(z)$) for $z \in \mathbb{C}$. By construction, $0 \leq \Delta_{\text{HFA}} \leq 1$. Low values of Δ_{HFA} (showing at most moderate relative variations of $s \mapsto \mathcal{R}(\mathbf{y}, s)$) occur mainly on the smooth, locally convex, parts of Γ, larger values (showing significant relative variations of $s \mapsto \mathcal{R}(\mathbf{y}, s)$) being by contrast observed near the sail and back regions, where the surface has features with smaller length scales.

Importantly, this observed behaviour of $\mathcal{R}(\mathbf{y}, s)$ is consistent with the expectation that HFAs of Kirchhoff type are valid in locally convex regions where the radius of curvature is moreover large relative to the characteristic wavelength. The validity of HFAs in regions of complex geometry would entail values of f_{HFA} well beyond the current capabilities of the frequency-domain BEMs for this configuration. We nonetheless tried our heuristic approach to HFA on the submarine surface, to observe its effect on the overall result.

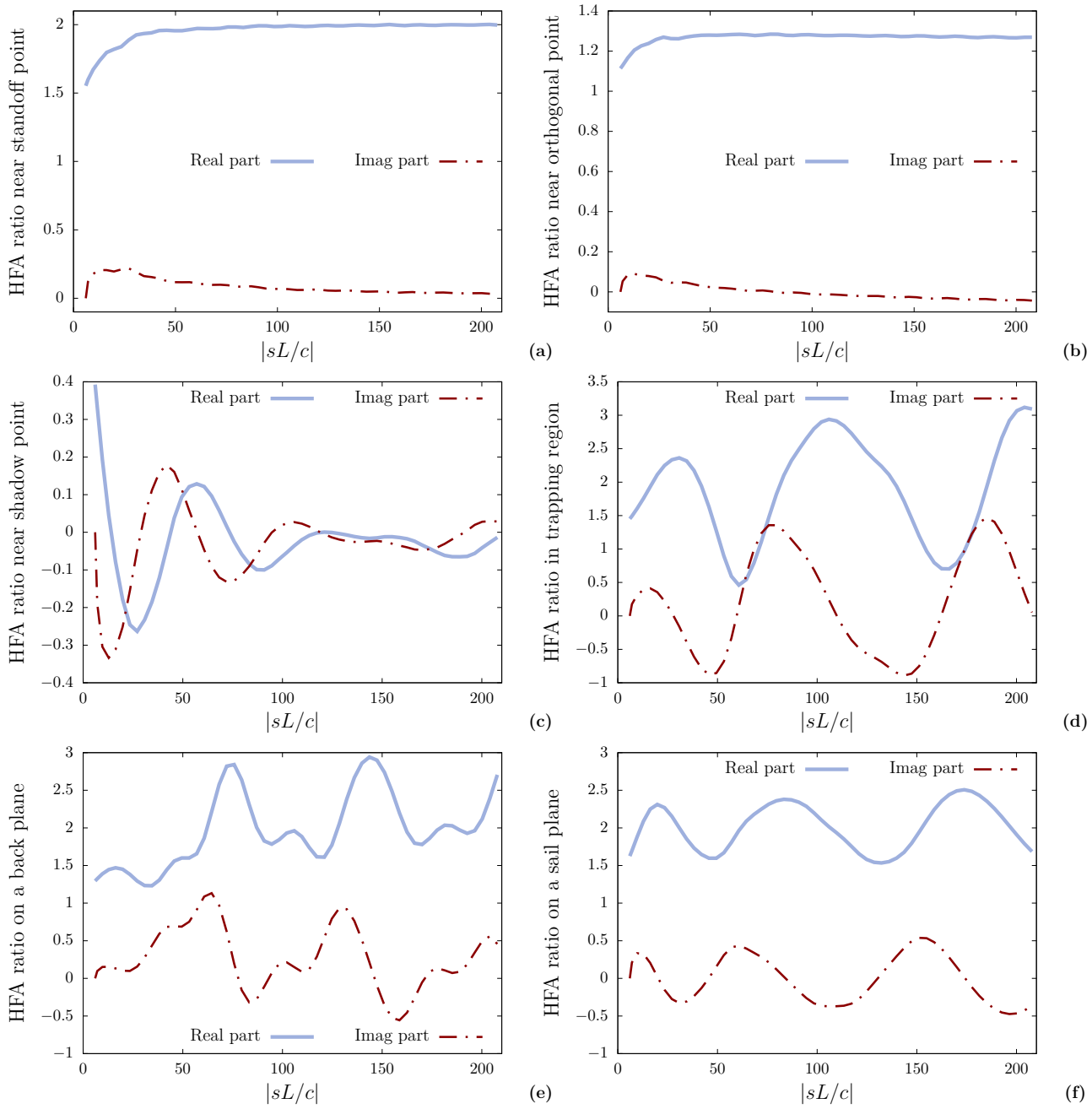

Figure 2.18: Scattering by a rigid motionless submarine: behaviour of the HFA ratio.

The number $M_B = 56$ of frequency-domain BEMs to be solved is very small compared to the $M + 1 = 10001$ frequency-domain BEMs that would be solved without using a HFA. Figure 2.20 shows how the frequencies for which a BEM problem is solved are concentrated near the origin in the complex s-plane. The real part of these frequencies (attenuation part) is almost constant ($\mathrm{Re}(s) \approx 6.0$), whereas their imaginary part (oscillatory part) grows from 0 to the limit fixed by f_{HFA}.

Figure 2.21 shows the computed surface pressure field 5.4 milliseconds after the incident wave first hits the submarine. The quality of the computation is illustrated by the smooth wave front, propagating on the beam. In the shadow zone, the causality of the wave is respected (the total field needs more time than the incident field to reach points in

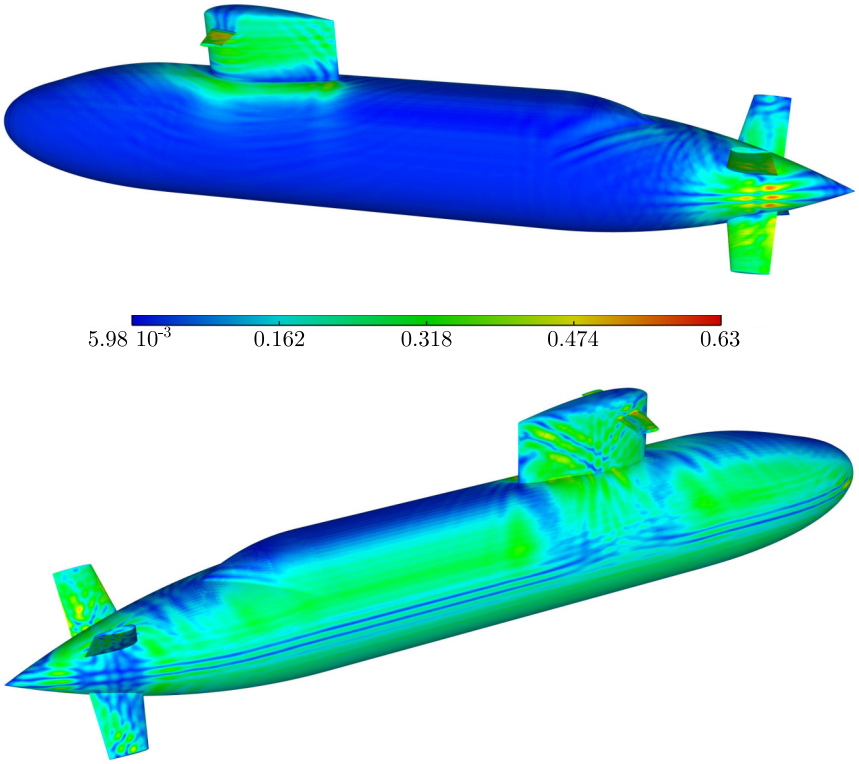

Figure 2.19: Scattering by a rigid motionless submarine: relative oscillation $\boldsymbol{\Delta_{\mathrm{HFA}}(y)}$ of $\mathbf{y \mapsto \Delta_{HFA}(y)}$ plotted as a function of $\mathbf{y \in \Gamma}$. BEM solutions for $\boldsymbol{M_B = 56}$ complex frequencies were computed.

the shadow zone). In the back region of the submarine, planes trap waves and multiple reflexions are accordingly observed. The quality of the computed wave front is somewhat reduced in the trapping region, as two small unphysical spots appear, presumably as a result of applying a HFA in a region whose complexity makes it invalid at the frequencies used, as previously observed in cases (d,e,f) of Figure 2.18.

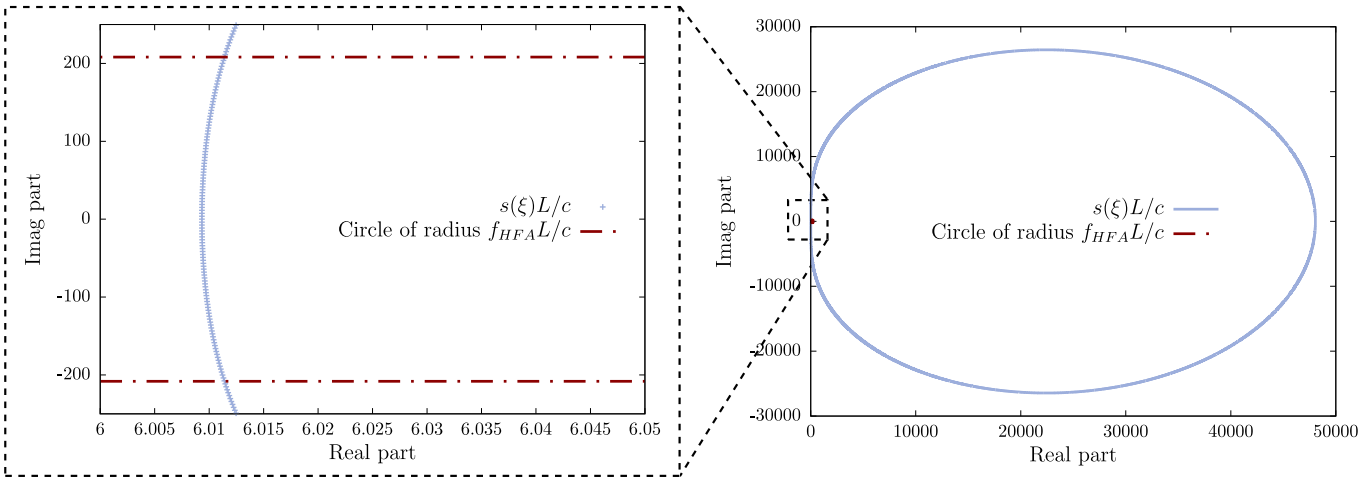

Figure 2.20: Scattering by a rigid motionless submarine: complex frequencies $\boldsymbol{sL/c}$ used by the $\mathcal{Z}$-BEM. The frequencies for which a BEM problem is solved are concentrated near the origin.

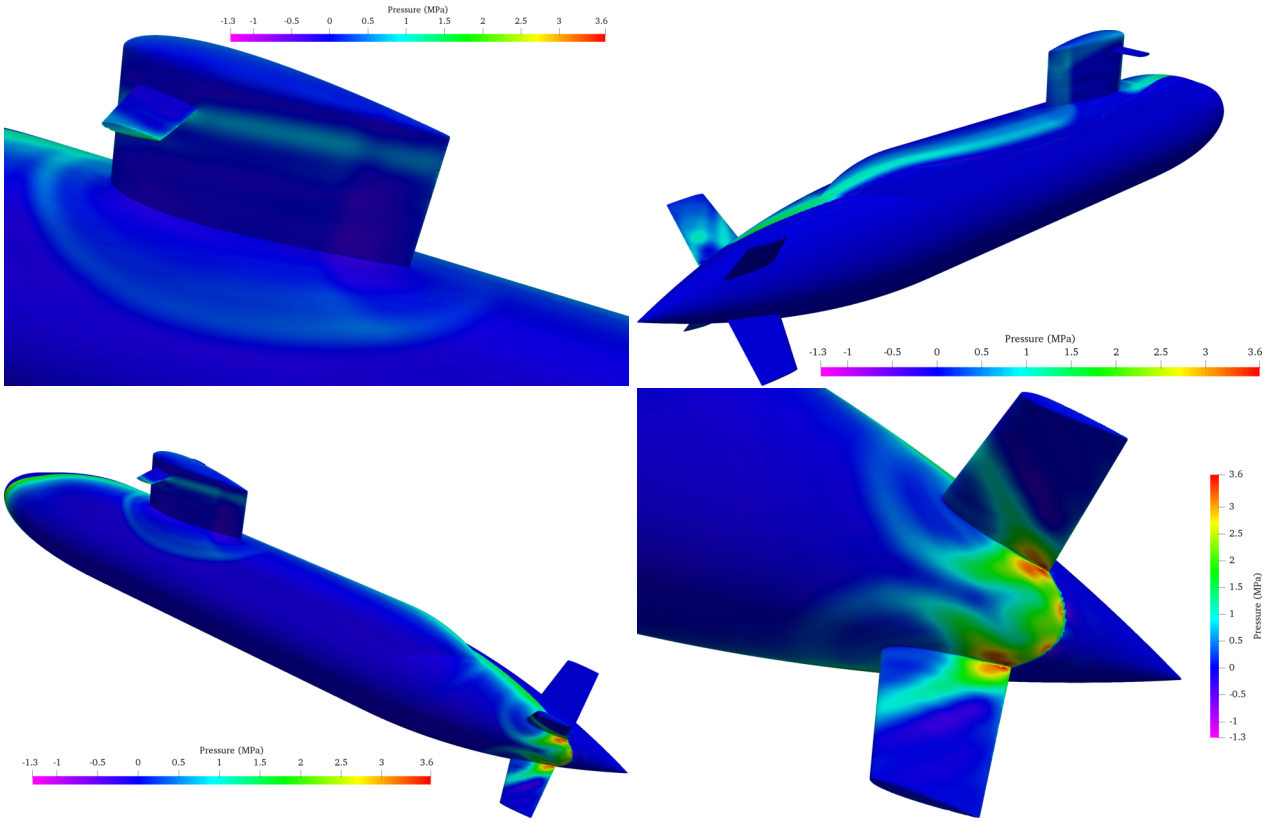

Figure 2.21: Scattering by a rigid motionless submarine: total pressure field on the surface, 5.4 milliseconds after the incident wave first hits the submarine.

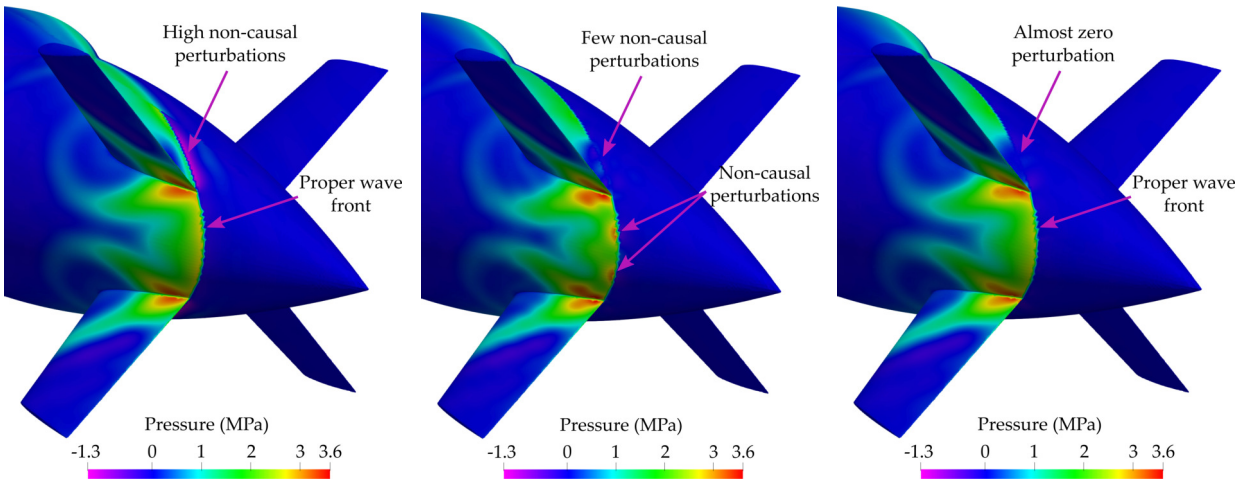

Figure 2.22: Scattering by a rigid motionless submarine: total pressure field on the surface, 5.4 milliseconds after the incident wave first hits the submarine. Close-up on the back part for three variants of the HFA, based on the Kirchhoff approximation (left), $\mathcal{R}(\mathbf{y}, s_{\mathbf{HFA}})$ (middle) or an average of $\mathcal{R}(\mathbf{y}, \cdot)$ (right).

There is obviously much room for improvement in, and deeper investigation into, the design and justification of more elaborate and accurate HFAs, with expected benefits to solution accuracy reachable within moderate M_B. For now, we tried a simple modification where $\mathcal{R}(\mathbf{y}, s_{\text{HFA}})$ is replaced by its mean value over s, for $|s| \in [0, f_{\text{HFA}}]$, when $\Delta_{\text{HFA}}(\mathbf{y}) > 0.1$ (see (2.45) and Figure 2.19); i.e., for the points where $\mathcal{R}(\mathbf{y}, s)$ is not constant yet. We compare in Figure 2.22 the pressure field obtained in the back region of the submarine using three versions of the HFA, based on (i) the Kirchhoff approximation (2.37), (ii) $\mathcal{R}(\mathbf{y}, s_{\text{HFA}})$, and (iii) a frequency-averaged value of $\mathcal{R}(\mathbf{y}, \cdot)$. For version (i), the total pressure field is well represented in the trapping region, where $\mathcal{R}(\mathbf{y}, s) = 2$ defines a suitable approximation. However, it leads to non-physical perturbations behind back planes, with pressure showing negative and positive peaks whereas it should vanish by causality. If used for subsequent FSI analyses, this pressure input may deteriorate overall FSI solutions in regions with complex geometry, due to induced non-physical deformations. With version (ii), the pressure solution in the region behind the back plane is improved. However, perturbations appear at the wave front in the trapping region, as two non-physical (non-causal) spots appear; they are due to a value of f_{HFA} that is locally too low, see cases (d,e,f) of Figure 2.18. Finally, using version (iii) in the geometrically complex regions identified in Figure 2.19 produces a correct wave front in the trapping region (its peak value being however lower than that obtained using the Kirchhoff HFA) and removes non-physical pressure jumps behind the back plane.

2.8 Conclusion

The main purpose of this chapter was to design and implement a BEM-based numerical procedure that can solve large-scale 3D rapid transient acoustic problems. After an introduction to the theory of BIEs, in Section 2.2, we presented a straightforward way to reformulate a transient wave propagation problem into a set of frequency-domain BIEs, by resort to the $\mathcal{Z}$-transform, in Section 2.3. Then, the BEM, and one of its acceleration method, the FMM, were briefly presented in Section 2.4. Thereafter, we enhanced the $\mathcal{Z}$-BEM procedure so that it efficiently solves rapid large-scale problems, thanks to a HFA, in Section 2.5. We first illustrated the efficiency of our $\mathcal{Z}$-BEM procedure, based on the $\mathcal{Z}$-transform and the use of a HFA, in the case of rapid transient radiation problems, in Section 2.6.1. Then, we addressed the scattering case, where an *ad hoc* HFA was designed, in Section 2.6.2. This empirically constructed HFA was shown in Section 2.7 to remain effective for dealing with large complex geometries. Finally, since the complexity of the $\mathcal{Z}$-BEM procedure is $O(1)$ in regards to the time discretisation and $O(N \log N)$ for the spatial discretisation, it ranks among the most competitive available methods.

The goal of Chapter 3 is now to develop a coupled FEM/BEM approach for the complete fluid-structure interaction (FSI) problem, a natural approach when the surrounding medium can, as here, be considered as unbounded.

Chapter 3

Fluid-structure interaction coupling for the shock wave

The purpose of this chapter is now to solve the coupled FSI problem for the shock wave phenomenon. The BEM is the appropriate tool to deal with the fluid part of the problem (see Section 2.1). For that reason, we have created a BEM numerical procedure to deal with rapid transient 3D large-scale uncoupled FSI problems in Chapter 2. On the other hand, the possibly complex model for the structure part is better modelled using the FEM. Hence, we design a FEM/BEM coupling procedure to solve the overall FSI problem.

This chapter is organised as follows. In Section 3.1, we introduce monolithic and iterative procedures, and explain the constraints in the specific case we consider. Then, in Section 3.2, we present an adapted procedure to the physics, but which we cannot implement because of some practical constraints related to the industrial context. To solve the FSI problem given these constraints, we therefore introduce a hybrid FEM/BEM method in Section 3.3. Then, we review some common fluid-structure coupling strategies, in Section 3.4, for a specific reference case of UNDEX FSI. Finally, we assess the efficiency of our hybrid FEM/BEM procedure by comparison to other FSI procedures on this reference case, in Section 3.5.

3.1 Step-by-step FEM/BEM procedures for fluid-structure interaction

Fluid-structure interaction is widely studied in the literature. A FSI problem is termed *weak* when only the action of the fluid on the structure or the structure on the fluid is considered. In contrast, a FSI problem is termed *strong* when both the action of the fluid on the structure and the retro-action of the structure on the fluid are considered. We focus on strategies designed for strong FSI problems, as *weak* interactions are easier to solve. In particular, we seek a procedure compatible with FEM/BEM coupling.

FEM/BEM coupling is probably the most appropriate method when modelling the interaction between a very large (infinite) medium and a bounded structure whose part or all of its surface is in contact with the very large medium. Indeed, it is widely used in soil-structure interaction (Clouteau et al., 2013), with applications in earthquake engineering (Nieto Ferro, 2013; Adnani, 2018) or in civil engineering with the calculation of the response of a structure to traffic induced vibrations (François et al., 2005). Furthermore, BEM/FEM coupling is of great use in fluid-structure interaction (Soares Jr. and Mansur, 2005; Véron, 2016), and has for example been applied to the study of dams behaviour (Von Estorff, 1991;

Seghir et al., 2009) or the analysis of the interaction between a shell and an underwater explosion (Felippa et al., 2001; Zhang and Yao, 2008). FEM/BEM coupling is also used for applications in electromagnetism (Kurz et al., 1996; Alouges et al., 2018) and other areas.

3.1.1 Monolithic versus partitioned iterative procedures

A FSI problem is governed by a set of equations describing (i) the fluid evolution in $\Omega \equiv \Omega_f$, (ii) the structure dynamics in Ω_s, (iii) the interface conditions on the fluid-structure boundary Γ. A possible generic form is

$$\begin{cases} (\mathcal{S}) : \text{structure evolution equations, set in } \Omega_s, \\ (\mathcal{F}) : \text{fluid evolution equations, set in } \Omega_f, \\ (\mathcal{KC}) : \text{kinematic transmission condition, set on } \Gamma, \\ (\mathcal{DC}) : \text{dynamic transmission condition, set on } \Gamma. \end{cases} \tag{3.1}$$

The set $(\mathcal{S})$ determines the structure behaviour, it results from a chosen model for the structure, such as the thin shell theory in our case. The set $(\mathcal{F})$ determines the fluid behaviour, it also results from a chosen model for the fluid, such as the linear acoustic theory in our case. $(\mathcal{KC})$ expresses the continuity of a certain kinematic quantity at the fluid-structure interface Γ. In our case, the structure cannot be penetrated, so it expresses the continuity of the normal velocity on the external structure surface Γ. Similarly, $(\mathcal{DC})$ expresses the continuity of a certain dynamic quantity, such as the continuity of normal stress at the interface Γ.

A natural way to solve (3.1) is to solve all the equations as a unified set. It consists in deriving a variational formulation from (3.1), governing the full fluid-structure interaction problem. This approach is termed monolithic and is widely used in the field of fluid-structure interaction (Tallec and Mouro, 2001; Sigrist, 2015; Morand and Ohayon, 1995). Another approach, termed partitioned or staggered, consists in splitting (3.1) into two sets of equations that are related through the equality of some mutual physical quantities (velocity, stress,...). For instance, the fluid and the structure equations are alternately solved and the interface continuity conditions relate the solutions (Felippa et al., 2001; Véron, 2016). A recent comparison between monolithic and partitioned methods for fluid-structure interaction may be found in e.g., (Ha et al., 2017).

A significant part of this work is devoted to the study of partitioned procedures because they are well adapted to the coupling between two different software in a *black-box* way (Zorrilla et al., 2020). Therefore, they appear to be attractive when the fluid and structure parts are modelled by means of a BEM and a FEM codes, respectively. However, separately solving the inherently coupled fluid and structure equations implies the recourse to successive problem-solving, to ensure the (separately) obtained solutions in the fluid and the structure parts correspond to the solution of the coupled fluid-structure problem. Typically, at a fixed time step, the fluid and structure equations are alternately solved, until a fluid-structure solution that simultaneously satisfies both sets of equations is found, before advancing to the next time step. These procedures are termed *step-by-step*. Alternatively, some algorithms perform the successive problem-solving on the entire time interval, rather than at each time step. In both cases, convergence issues may be encountered during the successive problem-solving process. These numerical issues constitute the main limitation of partitioned procedures, compared to monolithic ones. An example of partitioned procedures is presented in the next Section 3.1.2.

3.1.2 A transient step-by-step FEM/BEM iterative coupling procedure

The use of a partitioned FEM/BEM procedure in the context of UNDEX is not a novel idea. Nowadays, a reference procedure used by industry to evaluate the effects of an UNDEX on a submarine is an iterative step-by-step procedure that couples two codes, both belonging to Livermore Software Technology Corp.: LS-DYNA® (FEM, structure) and USA (BEM, fluid). The overall procedure is depicted in (Felippa et al., 2001) and corresponds to an iterative step-by-step FEM/BEM coupling, in which the BEM(-fluid) and FEM(-structure) equations are alternately solved at each time step, as illustrated in Figure 3.1. USA (for Underwater Shock Analysis) solves an approximation of the 3D wave equation called *Doubly Asymptotic Approximation (DAA)* (Geers and Toothaker, 2000; Lee et al., 2009; Geers and Felippa, 1983; Geers, 1978), that relates the normal fluid-particle velocity, the surface pressure and their temporal derivatives. It is obtained from asymptotic analysis arguments and approximation of Kirchhoff's retarded potential formula (2.17), and aims at providing a good order of magnitude of the solution, that is expected to be precise right after the explosion hits the hull (small times, large frequencies) and during the slower bubble process (long times, small frequencies), for cylindrical and spherical geometries.

The main limitations of the coupling procedure are due to USA. Developed in the years 1980 – 2000, USA relies on a standard BEM, with complexity in $O(N^2)$ (N denotes the number of interfacial DOFs), when today's fast BEMs, like the one we use in the $\mathcal{Z}$-BEM (COFFEE, 2020; Chaillat, 2008), achieve $O(N \log N)$ complexity. Moreover, USA relies on the DAA, a necessary approximation at the time the software was developed, because it allows the BEM operators to be independent of time (frequency), and so re-usable at each time step. We believe this approximation is no longer necessary, in view of recent progress in fast BEMs (Chaillat, 2008; Darbas et al., 2013; Darve, 2000; Nishimura, 2002; Hackbusch, 1999; Chaillat et al., 2017b). On the other hand, a definite advantage of this FEM/BEM procedure is that it does not need a volume fluid mesh, as both the reflected and the radiated parts (see Figure 2.8) are dealt with the BEM.

3.1.3 Why not using a step-by-step procedure?

Designing a procedure on the same model as USA, but with a more efficient BEM part, is one of the path studied in this work. The scheme is as illustrated on Figure 3.1: at each time step, a BEM procedure solves the fluid part of the problem, then a FEM procedure solves the structure part, the two procedures exchanging information at the interface Γ. Some sub-iterations are usually necessary to ensure convergence to the coupled fluid-structure solution before advancing to the next time step. A procedure of this type requires at least M (M being the number of time steps) BEM solutions, and then is efficient only if each BEM solution is cheap. This is not the case for the shock wave phenomenon, as it seems unrealistic, with current numerical resources, to perform M (typically $M \sim 10^4$) BEM problem-solving with $N \sim 10^6$ spatial DOFs each (see Section 2.7). Therefore, a step-by-step procedure is inadequate and a new strategy must be found.

Remark 13 *The key assumption performed in USA that permits a step-by-step coupling is the use of the DAA, as it provides re-usable BEM operators at each time step. We wish to design a numerical procedure without relying on this strong assumption.*

Remark 14 *In the case of potential incompressible flow, step-by-step partitioned procedures show great performance, notably because the BE mesh needs less refinement than for high frequency acoustic perturbations (Véron, 2016; Le Mestre et al., 2019). Therefore, the*

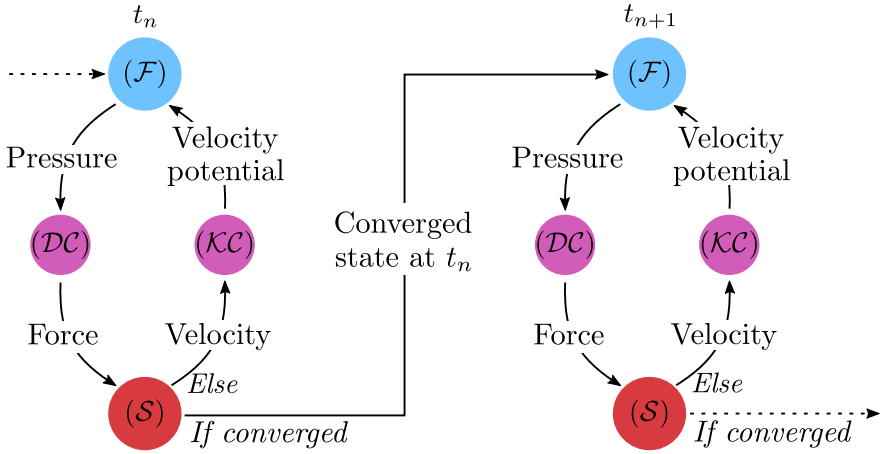

Figure 3.1: Schematic illustration of step-by-step FSI partitioned procedures.

step-by-step partitioned procedure appears to be a relevant approach for the oscillating bubble part of the UNDEX analysis, as will be shown in Chapter 4.

3.2 FEM/BEM procedures iterating over the full time interval

Our interest in partitioned procedures that alternate problem-solving for the entire time interval emerges from two ingredients: (i) step-by-step iterative procedures seem inadequate, and (ii) the $\mathcal{Z}$-BEM procedure we designed in Chapter 2 is best used in this scope. Indeed, to preserve its attractive $O(1)$ complexity with respect to the time discretisation, the $\mathcal{Z}$-BEM needs to solve problems on the entire time interval. The concept then consists in performing successive transient analyses over the entire time interval, rather than enforcing the coupling between the two solvers at each time step.

Domain decomposition methods (DDMs) (Dolean et al., 2015; Toselli and Widlund, 2006) achieve this purpose. They aim to solve a problem like (3.1) by splitting it into boundary value problems on subdomains, and iterating between them to match the solutions on the subdomain interface (the fluid-structure interface Γ in our case). Recent works on DDMs may be found in, e.g., Bouajaji et al., 2015; Vion and Geuzaine, 2018; Modave et al., 2020b; Lieu et al., 2020; Parolin, 2020. Common domain decomposition in space consists in solving, in parallel, problems at each time step, and exchange information through the interface Γ. Space-time domain decomposition (Gander et al., 2003) consists in solving time-dependent problems in the subdomains, in parallel, and exchange information through the space-time interface $\Gamma \times [0, T]$. One of the advantages of space-time DDMs is that it allows different time steps in each subdomain, according to its physical properties (Halpern et al., 2012; Hoang et al., 2013).

The FSI problem (3.1) is embedded with physical Neumann boundary conditions, in our case of the form

$$\frac{\partial \phi}{\partial n} = u_S \qquad \text{on } \Gamma \times [0, T], \tag{3.2a}$$

$$\sigma \cdot \mathbf{n} = -p_F \, \mathbf{n} \qquad \text{on } \Gamma \times [0, T], \tag{3.2b}$$

where ϕ is the fluid velocity potential, u_S the structure normal velocity, σ the structure stress tensor and p_F the fluid pressure. Neumann boundary conditions are known to lead to

convergence issues (Lecouvez, 2015; Caudron, 2018). Instead, Robin boundary conditions

$$p_F + \alpha_1 \frac{\partial \phi}{\partial n} = (-\sigma \cdot \mathbf{n}) \cdot \mathbf{n} + \alpha_1 u_S \qquad \text{on } \Gamma \times [0,T], \tag{3.3a}$$

$$\sigma \cdot \mathbf{n} + \alpha_2 u_S \, \mathbf{n} = -p_F \, \mathbf{n} + \alpha_2 \frac{\partial \phi}{\partial n} \mathbf{n} \qquad \text{on } \Gamma \times [0,T], \tag{3.3b}$$

where α_1 and α_2 are algorithmic parameters, are extensively used and studied in the context of domain decomposition (Hassan et al., 2018; Japhet et al., 2014). In particular, there exist cases for which Robin conditions provide a convergent algorithm (whereas common Neumann conditions lead to a non-convergent algorithm) e.g., the Schwarz algorithm (Lions, 1990; Després, 1991).

3.2.1 FEM/BEM coupling with Robin boundary conditions

To introduce Robin boundary conditions and their related coefficients α_i, we derive an example of procedure performing successive problem-solving for the entire time interval, inspired from both space-time DDMs and the LArge Time INcrement (LATIN) method (Néron, 2004), which we present for our specific case of fluid-structure interaction. Consider the set of equations (3.1)

$$\begin{cases} (\mathcal{S}) : \text{structure evolution equations, set in } \Omega_s, \\ (\mathcal{F}) : \text{fluid evolution equations, set in } \Omega_f, \\ (\mathcal{KC}) : \text{kinematic transmission condition, set on } \Gamma, \\ (\mathcal{DC}) : \text{dynamic transmission condition, set on } \Gamma. \end{cases}$$

The LATIN is an iterative method that is based on successive solutions of two subsets of equations from (3.1), for large time intervals (or the full time interval $[0,T]$) (Ladevèze et al., 2010).

Separation into two subsets. The first principle of the LATIN method is to separate the solutions of the equations in (3.1) into two subsets $\mathcal{E}$ and $\mathcal{C}$

$$\mathcal{E} : \text{ set of solutions to the evolution field equations } (\mathcal{S}) \text{ and } (\mathcal{F}); \tag{3.4a}$$

$$\mathcal{C} : \text{ set of solutions to the continuity conditions } (\mathcal{KC}) \text{ and } (\mathcal{DC}). \tag{3.4b}$$

$\mathcal{E}$ is composed of the solutions that satisfy the fluid and (possibly non-linear) structure equations. In our case, these solutions are typically represented by four quantities: field kinematic and dynamic quantities for the structure (v^+, f^+) and the fluid (v^-, f^-). The set $\mathcal{C}$ gathers the solutions to the linear continuity equations, with kinematical and dynamical quantities (V^+, F^+, V^-, F^-) defined on the interface Γ, related to the traces on Γ of (v^+, f^+, v^-, f^-). A typical way to define $\mathcal{E}$ and $\mathcal{C}$ is

$$\mathcal{E} = \left\{ s \equiv (v^+, f^+, v^-, f^-) \mid \mathcal{S}(v^+, f^+) = 0,\ \mathcal{F}(v^-, f^-) = 0 \right\}, \tag{3.5a}$$

$$\mathcal{C} = \left\{ S \equiv (V^+, F^+, V^-, F^-) \mid V^+ = V^-,\ F^+ + F^- = 0 \right\}. \tag{3.5b}$$

Then, the solution s_e of the fluid-structure problem (3.1) is such that $s_e \in \mathcal{E}$ and $S_e \in \mathcal{C}$.

In the following, we consider the specific case of fluid-structure interaction for the shock wave part of the problem. As explained in Section 2.5.1, the fluid unknown $p^{\mathrm{sc}} \equiv p^{\mathrm{tot}} - p^{\mathrm{inc}}$ may be decomposed into two components: the reflected one, independent of the structure motion, and the radiated one. Then, the uncoupled part of the problem, the reflected

pressure, is obtained at any point and any time through a $\mathcal{Z}$-BEM pre-computation, and so the dynamic variable for the fluid part of the FSI problem reduces to p^{rad}. Therefore, (v^+, f^+, v^-, f^-) is set to $(\mathbf{v}, \mathbf{t}, u, p)$, where $\mathbf{v}$ is the structure velocity, $\mathbf{t} = \sigma \cdot \mathbf{n}$ the traction vector, $u = \partial_n \phi$ the normal fluid velocity, p is the **radiated** pressure, and $\mathbf{n}$ is the outward normal to the structure. Let $h \equiv -(p^{\text{inc}} + p^{\text{ref}})$, the set $\mathcal{C}$ holds as

$$\mathcal{C} = \{S \equiv (\mathbf{v}\cdot\mathbf{n}, \mathbf{t}, u, p\mathbf{n}) \mid \mathbf{v}\cdot\mathbf{n} = u \text{ on } \Gamma,\ \mathbf{t} + p\mathbf{n} = h\mathbf{n} \text{ on } \Gamma\}\,. \tag{3.6}$$

Introduction of Robin boundary conditions. Like most iterative methods, the LATIN needs an *initial guess*. Let consider for instance that the initial (0) iteration consists in finding a solution in $\mathcal{E}$. To solve the associated equations, two continuity equations must be specified/guessed. The simplest (non-optimal) choice is to set $u_0 = 0$ (and so $p_0 = 0$) on Γ for the fluid and $\mathbf{t} = h\mathbf{n}$ on Γ for the structure. Then, two uncoupled problem-solving are performed, and lead to a solution $s_0 = (\mathbf{v}_0, \mathbf{t}_0, u_0, p_0) \in \mathcal{E}$.

The idea of the LATIN is to build a solution $s_{1/2} \in \mathcal{C}$ from $s_0 \in \mathcal{E}$ by setting (on Γ) two relations of the form

$$\Big(\mathbf{t}_{1/2} - \mathbf{t}_0\Big) - k\Big(\mathbf{v}_{1/2} - \mathbf{v}_0\Big) = 0\,, \tag{3.7a}$$

$$\Big(p_{1/2} - p_0\Big) - k\Big(u_{1/2} - u_0\Big) = 0\,, \tag{3.7b}$$

where $k > 0$ is an algorithmic parameter with appropriate physical units. Since $s_{1/2} \in \mathcal{C}$, it holds

$$\mathbf{v}_{1/2}\cdot\mathbf{n} = u_{1/2}\,, \tag{3.8a}$$

$$\mathbf{t}_{1/2} + p_{1/2}\mathbf{n} = h\mathbf{n}\,. \tag{3.8b}$$

The relations (3.7) and (3.8) form a system of 8 scalar equations with 8 scalar unknowns. Its solution holds as

$$p_{1/2} = \frac{1}{2}\left(p_0 - \mathbf{t}_0\cdot\mathbf{n} + h - k(u_0 - \mathbf{v}_0\cdot\mathbf{n})\right)\,, \tag{3.9a}$$

$$u_{1/2} = -\frac{1}{2k}\left(p_0 + \mathbf{t}_0\cdot\mathbf{n} - h - k(u_0 + \mathbf{v}_0\cdot\mathbf{n})\right)\,, \tag{3.9b}$$

$$\mathbf{t}_{1/2} = h\mathbf{n} - \frac{1}{2}\left(p_0 - \mathbf{t}_0\cdot\mathbf{n} + h - k(u_0 - \mathbf{v}_0\cdot\mathbf{n})\right)\mathbf{n}\,, \tag{3.9c}$$

$$\mathbf{v}_{1/2} = \mathbf{v}_0 + \frac{1}{k}(h\mathbf{n} - \mathbf{t}_0) - \frac{1}{2k}\left(p_0 - \mathbf{t}_0\cdot\mathbf{n} + h - k(u_0 - \mathbf{v}_0\cdot\mathbf{n})\right)\mathbf{n}\,. \tag{3.9d}$$

Note that $s_{1/2} \in \mathcal{C}$ is obtained from $s_0 \in \mathcal{E}$ via explicit formulas, without needing costly problem-solving. Now that $s_{1/2} \in \mathcal{C}$ is known, we seek s_1 by setting

$$\Big(\mathbf{t}_1 - \mathbf{t}_{1/2}\Big) + k\Big(\mathbf{v}_1 - \mathbf{v}_{1/2}\Big) = 0\,, \tag{3.10a}$$

$$\Big(p_1 - p_{1/2}\Big) + k\Big(u_1 - u_{1/2}\Big) = 0\,. \tag{3.10b}$$

Gathering all the unknowns in the left hand-side, (3.10) becomes

$$\mathbf{t}_1 + k\mathbf{v}_1 = \mathbf{t}_{1/2} + k\mathbf{v}_{1/2}\,, \tag{3.11a}$$

$$p_1 + ku_1 = p_{1/2} + ku_{1/2}\,, \tag{3.11b}$$

which corresponds to two Robin boundary conditions that are used to solve the fluid and structure problems, to obtain $s_1 \in \mathcal{E}$. It is possible to relate s_1 to s_0, using (3.9),

$$\mathbf{t}_1 + k\mathbf{v}_1 = (\mathbf{t}_0 \cdot \mathbf{n})\mathbf{n} - \mathbf{t}_0 - k((\mathbf{v}_0 \cdot \mathbf{n})\mathbf{n} - \mathbf{v}_0) - p_0\mathbf{n} + ku_0\mathbf{n} + h\mathbf{n}\,, \tag{3.12a}$$

$$p_1 + ku_1 = h - \mathbf{t}_0 \cdot \mathbf{n} + k(\mathbf{v}_0 \cdot \mathbf{n})\,. \tag{3.12b}$$

Introducing the projection operator $\mathcal{P} := \mathcal{I} - \mathbf{n} \otimes \mathbf{n}$, (3.12) becomes

$$\mathbf{t}_1 + k\mathbf{v}_1 = h\mathbf{n} - \mathcal{P}(\mathbf{t}_0 - k\mathbf{v}_0) - p_0\mathbf{n} + ku_0\mathbf{n}\,, \tag{3.13a}$$

$$p_1 + ku_1 = h - \mathbf{t}_0 \cdot \mathbf{n} + k(\mathbf{v}_0 \cdot \mathbf{n})\,. \tag{3.13b}$$

The method then reduces to successive problem-solving of the evolution equations with Robin boundary conditions (3.13), until convergence using a stagnation criterion of the form $\|s_k - s_{k+1}\| \leq \varepsilon_{\text{LATIN}}$, for a fixed tolerance $\varepsilon_{\text{LATIN}}$. To check whether the method provides the correct solution to the FSI problem, the converged solution s must satisfy the initial problem (3.1). The evolution equations are naturally satisfied, as s is a member of $\mathcal{E}$. Because s is the converged solution by stagnation, it satisfies (3.13) with $s_0 = s_1 = s$:

$$\mathbf{t} + k\mathbf{v} = h\mathbf{n} - \mathcal{P}(\mathbf{t} - k\mathbf{v}) - p\mathbf{n} + ku\mathbf{n}\,, \tag{3.14a}$$

$$p + ku = h - \mathbf{t} \cdot \mathbf{n} + k(\mathbf{v} \cdot \mathbf{n})\,. \tag{3.14b}$$

Combining (3.14b)-(3.14a)$\cdot\mathbf{n}$ provides the kinematic boundary condition $u = \mathbf{v} \cdot \mathbf{n}$ for $k \neq 0$. Using $u = \mathbf{v} \cdot \mathbf{n}$, (3.14a) becomes

$$2\mathbf{t} = h\mathbf{n} + (\mathbf{t} \cdot \mathbf{n})\mathbf{n} - p\mathbf{n}. \tag{3.15}$$

To obtain the sought dynamic boundary condition, we observe that (3.15) implies $\mathcal{P}(\mathbf{t}) = 0$, i.e., $\mathbf{t} = (\mathbf{t} \cdot \mathbf{n})\mathbf{n}$, and then $\mathbf{t} = h\mathbf{n} - p\mathbf{n}$.

The efficiency of the method heavily relies on the choice of k, that is, in view of (3.11), interpreted as a positive artificial added damping. In the case of rapid dynamic problems, it seems reasonable to set k according to the high frequency approximation $p^{\text{rad}} - \rho c u \simeq 0$, so $k = \rho c$.

3.2.2 Limitations of Neumann boundary conditions

As stated previously, Robin boundary conditions, like (3.13), are often used in the context of interactions between several domains. The main advantage of Robin conditions is well illustrated in (3.13a): the coupling nature of the problem manifests itself in the fact that $\mathbf{t}_1$ and $\mathbf{v}_1$ are obtained from the fluid data u_0 and p_0, but also from the tangential part of the structure data $\mathbf{t}_0$ and $\mathbf{v}_0$. On the contrary, Neumann boundary conditions (3.6) relate $\mathbf{t}_1$ to p_0 and $\mathbf{v}_1$ to u_0. Such conditions do not couple enough the variables, in particular because a quantity at step (1) depends only on quantities at initial step (0).

In this work, we must comply with an industrial choice that is the use of Abaqus® for the structure FEM part. Though this choice is fully justified given the industrial context, this has the regrettable disadvantage that only the usual Neumann boundary conditions (3.6) are accessible. In particular, we did not (nor did the Abaqus® hotline) find a simple way to practically enforce Robin boundary conditions[1], like (3.13). This considerably limits the design of a procedure that alternates problem-solving on the entire time interval, like space-time DDMs or their LATIN variant.

[1] It is possible for analyses performed with Abaqus® on a stand-alone basis, but not yet with the procedure that couples Abaqus® to another, external, solver.

We tried to implement some naive coupling procedures using Neumann boundary conditions in each domain, but they all failed to converge. Indeed, solving the structure part, for the whole interval $[0, T]$, with a Neumann boundary condition means getting $\mathbf{t}_1$ and $\mathbf{v}_1$ from the fluid data p_0. In that case, the Neumann datum does not depend on quantities of the current (1) iteration, but only on a quantity of the previous (0) iteration. The solving process then evolves as illustrated on Figure 3.2. During the first time steps, the procedure seems fine, as $\mathbf{v}_0$ and $\mathbf{v}_1$ have similar trends at the beginning. After a while, $\mathbf{v}_1$ smoothly deviates from $\mathbf{v}_0$, and at a certain time instant $\mathbf{v}_1$ and $\mathbf{v}_0$ have opposite signs. The radiated pressure p_0 is related to a restoring force $\mathbf{f}_0$ that moderates the structure motion of iteration (0). However, as $\mathbf{v}_1$ and $\mathbf{v}_0$ are opposite, $\mathbf{f}_0$ accentuates the structure motion at iteration (1), instead of moderating it. Then, for the case illustrated in Figure 3.2, the value of $\mathbf{v}_1$ increases at each iteration, and the procedure diverges (in other cases, the procedure may attenuate more and more the solution until the pressure tends to zero). To prevent this phenomenon, we tried, at a time instant t_n, to replace the pressure $p_0(t_n)$ by a combination between $p_0(t_n)$ and $\rho_f c_f \mathbf{v}_1(t_{n-1}) \cdot \mathbf{n}$, to add a contribution that is related to the current (1) iteration, and so always opposite to the motion. This helped the procedure convergence, but not enough.

We believe the use of Robin conditions, like (3.13), would avoid the convergence issues we faced, as the quantities at iteration (1) are related to both quantities of iteration (0) and (1). We are currently investigating a means to implement a convergent procedure based on Robin boundary conditions, that would allow a full $\mathcal{Z}$-BEM/FEM coupling, with successive problem-solving on the entire time interval, which we hope to present in future work. Meanwhile, as we had to solve the problem given the practical constraints, we decided to go back to the study of monolithic FEM/FEM approaches.

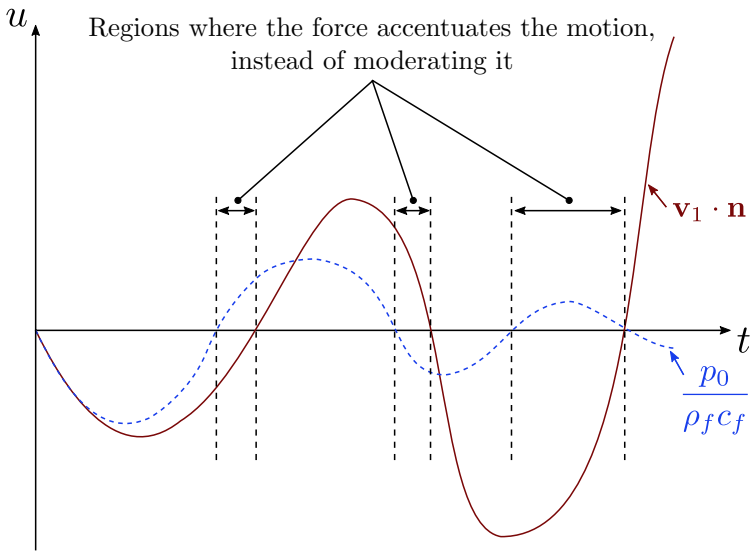

Figure 3.2: Illustration of the divergence observed when performing successive fluid and structure problem-solving on the entire time interval using Neumann boundary conditions.

3.3 Hybrid $\mathcal{Z}$-BEM/FEM/FEM approach

So far, only partitioned procedures have been described. One of the main advantages of monolithic approaches lies in the direct solving of the entire set of equations (3.1), therefore avoiding convergence issues encountered in partitioned procedures. However, common monolithic FEM/FEM approaches require the 3D discretisation of the fluid domain. As explained in Section 2.1, in case of rapid transient large-scale problems, it would be too expensive to obtain a refined enough mesh for the large-scale fluid domain. Some treatments can nonetheless help to overcome the difficulties of the FEM, by drastically restricting the fluid domain using non-reflecting boundary conditions for instance (Graham et al., 2017). The purpose of those conditions is to absorb the waves at the artificial boundary Γ_∞ that truncates the fluid domain. Generally, those absorbing conditions are not ideal, in the sense that they lead to some unwanted reflections at Γ_∞. The challenge is then to find and use, for the specific problem considered, the best possible absorbing condition (Modave et al., 2020a; Bécache et al., 2010; Givoli, 1991).

To design an efficient procedure within the afore mentioned practical constraints, the starting point is the fluid decomposition into reflected and radiated fields, $p^{\text{tot}} = p^{\text{inc}} + p^{\text{ref}} + p^{\text{rad}}$ (see Figure 2.8). The reflected field does not involve a fluid-structure coupling, as the structure is motionless for this problem. In that sense, obtaining the reflected part is easier than the radiated part. The BEM is perfectly adapted to the reflected part, because the FEM would require a very refined mesh in a large volume of fluid, to accurately compute (i) the incident field propagation, if it is not imposed on the surface through a boundary condition (Khoun, 2021), (ii) the multi-reflections on the surface, for instance in the back region of a submarine (see Section 2.7, Figure 2.22). On the other hand, the radiated pressure is a more local phenomenon: locally, the structure vibrates and radiates waves. The decomposition then allows to perform a FEM/FEM coupling for the radiated part only, and the obtention of p^{rad} at the fluid-structure interface requires only a fine mesh near the interface Γ. Of course, a volume mesh not refined far from Γ deteriorates the solution (so p^{rad}) in these remote regions. For some FSI problems, e.g., the study of the acoustic signature of a submarine, where the computation of the pressure far from the submarine must be accurate, refining the fluid mesh only near the structure would not suffice. However, this raises no issue in our case, as the quantity of interest for the fluid part is only the pressure at the fluid-structure interface Γ, required to compute the structure behaviour.

From this analysis emerges a procedure, which we label $\mathcal{Z}$-BEM/FEM/FEM: for a given problem (structure and input), the reflected pressure in the fluid is computed using the $\mathcal{Z}$-BEM, whereas the fluid-structure coupling, that couples the radiated pressure to the structure motion, is solved with a common FEM/FEM procedure, using a volume 3D mesh for the fluid that is refined only near the fluid-structure interface (see Figure 3.3). This hybrid procedure satisfies the practical constraints (related to the industrial context), since the BEM fluid and the FEM structure solvers may be used in a *black-box* manner. We use Abaqus® for the FEM part, and the coupling is ensured through an interface provided by the so-called Coupling Simulation Engine (CSE) (Dassault Systèmes SIMULIA, 2017; Véron, 2016). The steps of the $\mathcal{Z}$-BEM/FEM/FEM procedure are the following (see Figure 3.3):

- Compute the reflected pressure using the $\mathcal{Z}$-BEM procedure (see Chapter 2);
- Compute the nodal forces $\mathbf{f}$ associated to the pressure $p^{\text{inc}} + p^{\text{ref}}$, on each point of the mesh, for each time step of the whole interval $[0, T]$;
- For the FEM part, apply $\mathbf{f}$ on the interface Γ through ($\mathcal{DC}$) in (3.1), and solve the

FEM/FEM FSI problem between the structure (its whole complex model) and a truncated 3D volume mesh for the exterior water, that is refined only near the FSI interface.

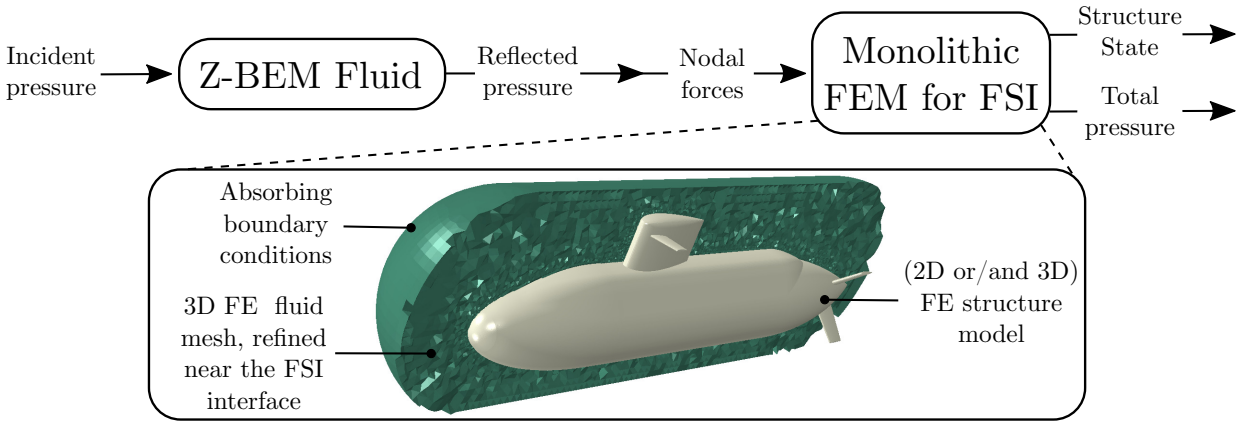

Figure 3.3: Main steps of the hybrid $\mathcal{Z}$-BEM/FEM/FEM procedure.

The coupling is then all performed in the FEM part, but remains more efficient than a volume FEM for both p^{ref} and p^{rad}, the latter being more costly to achieve the same precision, as it is shown on a typical UNDEX FSI problem in Sections 3.4 and 3.5. In the rest of this chapter, the hybrid $\mathcal{Z}$-BEM/FEM/FEM procedure is labelled $\mathcal{Z}$-BEM/FEM, for convenience.

3.4 Definition of a comparative study of FSI strategies

This section is dedicated to a comparative study between some FSI strategies in the context of UNDEX. Given the industrial context, we choose the reference case of a steel cylindrical hull submerged in water, facing a remote underwater explosion (see Figure 3.4). The purpose is to compare numerical methods based on the FEM, the BEM, or semi-analytical approaches, to show their strengths and weaknesses. Also, the goal is to validate our $\mathcal{Z}$-BEM/FEM procedure.

3.4.1 Test problem: remote explosion on long cylindrical shell

We study the FSI problem between a submerged long cylindrical shell and a remote underwater explosion. The physical problem parameters are provided in Figure 3.4. The cylinder is closed by two hemispheres and the total length is $2L = 53.7$ m. We study this FSI problem in a time interval $[0, T]$, where T is chosen such that the strains (i.e., the deformation that is not a rigid motion) in the cross-section $(\mathcal{P})$ containing the explosion are not influenced by the hull spherical extremities (due to causality). Also, we consider a relatively far explosion, $W = 1000$ kg of TNT at $d_0 = 100$ m from the cylinder centre, so that the wave front hitting the hull is roughly planar (spherical with a large radius of curvature).

The configuration is similar to Section 2.6.2, though now the cylinder is deformable. In particular, we use again the single-exponential fit (2.43) with the same explosive material parameters:

$$K_1 = 5.24\ 10^7\,\text{SI},\ a_1 = 1.13, \qquad K_2 = 8.4\ 10^5\,\text{SI},\ a_2 = -0.23. \tag{3.16}$$

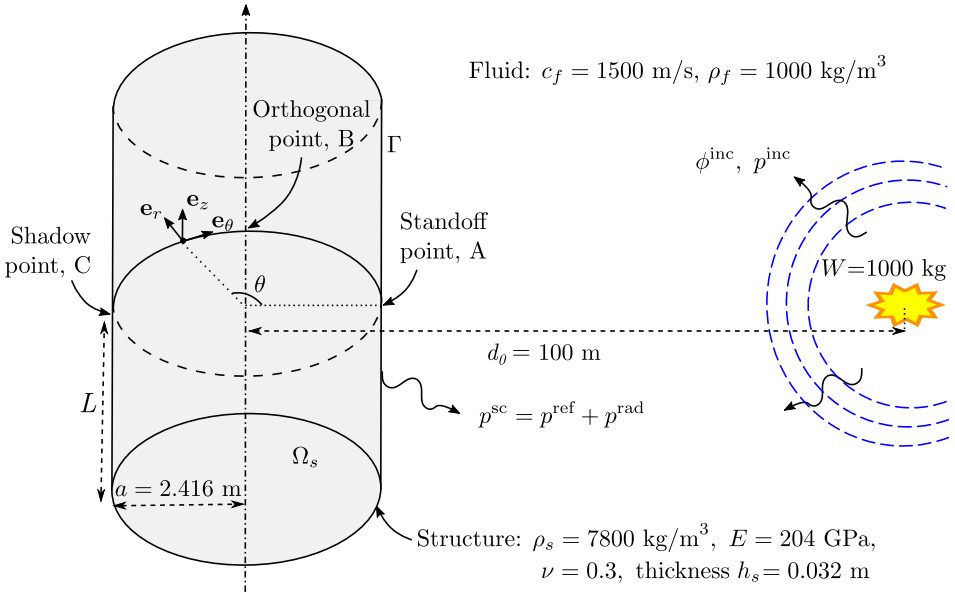

Figure 3.4: Cylinder of radius $a = 2.416$ facing a remote UNDEX, notations and physical parameters.

Finally, the configuration has been chosen so that the assumption of small linear deformations is relevant, the shock factor (1.2) being rather small: $K \simeq 0.32$.

3.4.2 FSI solution methods considered

A semi-analytical solution for infinite cylinders. In UNDEX analysis, semi-analytical approaches have historically been very useful. Indeed, before computer resources allowed an efficient use of discretisation methods, the interaction between a spherical wave and a cylinder (or a circle in 2D) was studied using (semi-)analytical methods (Cole, 1948). They mainly consist in solving an equation (e.g., the wave equation) by decomposing the solution upon an infinite base of solutions (e.g., Bessel's functions). Then, solving the equation satisfied by each coefficient, the solution is approximated through a truncated reconstruction. In the FSI context, and more specifically for UNDEX analysis, the details may be found in e.g., (Junger and Feit, 1986; Brochard, 2018; Leblond, 2007).

An in-house code of Naval Group allows to solve the FSI problem with a semi-analytical approach. It relies on a spatial modal decomposition, to solve the 2D wave equation and the 2D Love-Kirchhoff shell equations mode by mode, before summing modal contributions over a (truncated) basis. The details may be found in (Leblond et al., 2009; Sigrist and Leblond, 2008). Recent, yet unpublished, improvements of the code allow to use the $\mathcal{Z}$-transform, rather than the Laplace transform, to go to the frequency domain, which reduces Gibbs phenomenon due to the discontinuous incident pressure (Rakotomalala et al., 2021).

This 2D procedure provides results comparable to the 3D solution in the cross-section ($\mathcal{P}$) only subject to strong assumptions: (i) the cylinder must be long enough to be treatable as infinite, and (ii) the remote UNDEX must be far enough to allow treating the wave front as flat or cylindrical. As most semi-analytical modal approaches, the procedure is efficient only if few modes are sufficient to well represent the solution. Actually, since the 2D procedure is quite fast, we were able to check the influence of the number of spatial modes, and noticed that setting it to $N^\theta = 65$ is enough regarding the target accuracy in

the industrial context.

A monolithic FEM/FEM approach. A monolithic FEM/FEM approach is implemented in the French software code_aster® (Code_Aster Open Source, 2020). The FEM structure model is a code_aster® shell, and the volume mesh for the exterior fluid is refined only near the interface Γ, for the computational reasons explained previously. BGT1 absorbing conditions are used to artificially truncate the exterior fluid domain (Bayliss et al., 1982; Leblond and Sigrist, 2016). Only implicit time schemes are considered for this procedure.

The procedure relies on the assumption of small deformations (small strains and small rigid displacement), so that the FEM matrices may be computed once at the first time step, and re-used afterwards. Contrary to the $\mathcal{Z}$-BEM/FEM procedure, the fluid unknown gathers both the radiated and the reflected parts. As explained in Section 3.3, the reflected part in not as local as the radiated part, so it requires a volume finite element (FE) mesh refined in a larger portion of fluid, at least when dealing with complex geometries. This FEM/FEM procedure, developed in the context of another Naval Group PhD thesis (Khoun, 2021), cannot yet deal with large structures, which is the reason we consider small hull dimensions (compare to a submarine) for the reference case considered.

The hybrid $\mathcal{Z}$-BEM/FEM procedure with Abaqus®. The first step of the $\mathcal{Z}$-BEM/FEM procedure consists in getting the reflected pressure, for each node of the mesh, for each time step, with the $\mathcal{Z}$-BEM, using the software COFFEE (2020) (see Chapter 2). Then, the nodal forces $\mathbf{f}$ are obtained from the nodal values of $p^{\text{Ref}} = p^{\text{inc}} + p^{\text{ref}}$, using linear shape functions, and serve as input to solve the FEM/FEM coupling in Abaqus®. Details on how to perform a coupling between Abaqus® and another, external, code may be found in (Véron, 2016; Dassault Systèmes SIMULIA, 2017). For the FEM part, the FEM structure model is an Abaqus® shell, and the volume mesh for the exterior fluid is refined only near the interface Γ (see Figure 3.5), to reduce the number of elements to a quadratic function of the structure dimensions, instead of a cubic function. In particular, this is necessary to deal with rapid transient problems involving large structures, with reasonable computation times. Abaqus® absorbing conditions (cylindrical and spherical acoustic impedances) are used to artificially truncate the exterior fluid domain. At the interface Γ, the fluid and structure meshes do not have to be compatible, the `*TIE` functionality of Abaqus® is used to enforce the two geometric surfaces to coincide. Under the assumption of small linear deformations, the problem may be solved using either Abaqus® explicit or Abaqus® implicit within reasonable computation times, so the two cases will be presented in Section 3.5.

During the computation of p^{ref}, the structure is considered motionless. The obtained results are then valid only under the hypotheses of (i) small strains, to ensure the shape of the structure is well approximated by the initial shape, (ii) small rigid displacement, to ensure the computed value of $p^{\text{inc}}(P,t)$ with a motionless structure remains close to the value of $p^{\text{inc}}(P(t),t)$ when the geometry moves ($P(0) = P$). The latter hypothesis is easily verified for remote UNDEX because (i) p^{inc} evolves as $1/r$, and (ii) the rigid displacement is marginal in the considered time interval. The $\mathcal{Z}$-BEM/FEM procedure has the advantage of needing very few hypotheses, compared to the other procedures (see details in Tables D.1 and D.2).

3.5 Comparative study: validation of our coupling procedure

The goal of this section is to compare our $\mathcal{Z}$-BEM/FEM procedure to the other procedures introduced in Section 3.4, on the cylindrical shell configuration presented Section 3.4.1. In addition to validating our procedure (checking that the results are correct), it permits to (i) assess its efficiency, and (ii) identify the scope of application of each procedure. We present the results of four procedures: the code_aster® FEM/FEM, the semi-analytical method, the $\mathcal{Z}$-BEM/FEM with an explicit scheme for the structure, and the $\mathcal{Z}$-BEM/FEM with an implicit scheme for the structure. The comparison between the procedures is summarised in Appendix D, Tables D.1 to D.4. The numerical parameters of each procedure are provided in Tables D.5 and D.6. Apart from the semi-analytical approach, the meshes of each procedure have been chosen such that the computation runtime is about 5 days. For instance, for the $\mathcal{Z}$-BEM/explicit FEM procedure, it leads to around 10^7 tetrahedral linear elements for the fluid FE mesh, and the structure shell has around 3 10^5 nodes (with 5 DOFs per node). To improve the results, the fluid and structure FE meshes have been refined near the standoff point. A snapshot of the used meshes (Figure 3.5) illustrates these refinements.

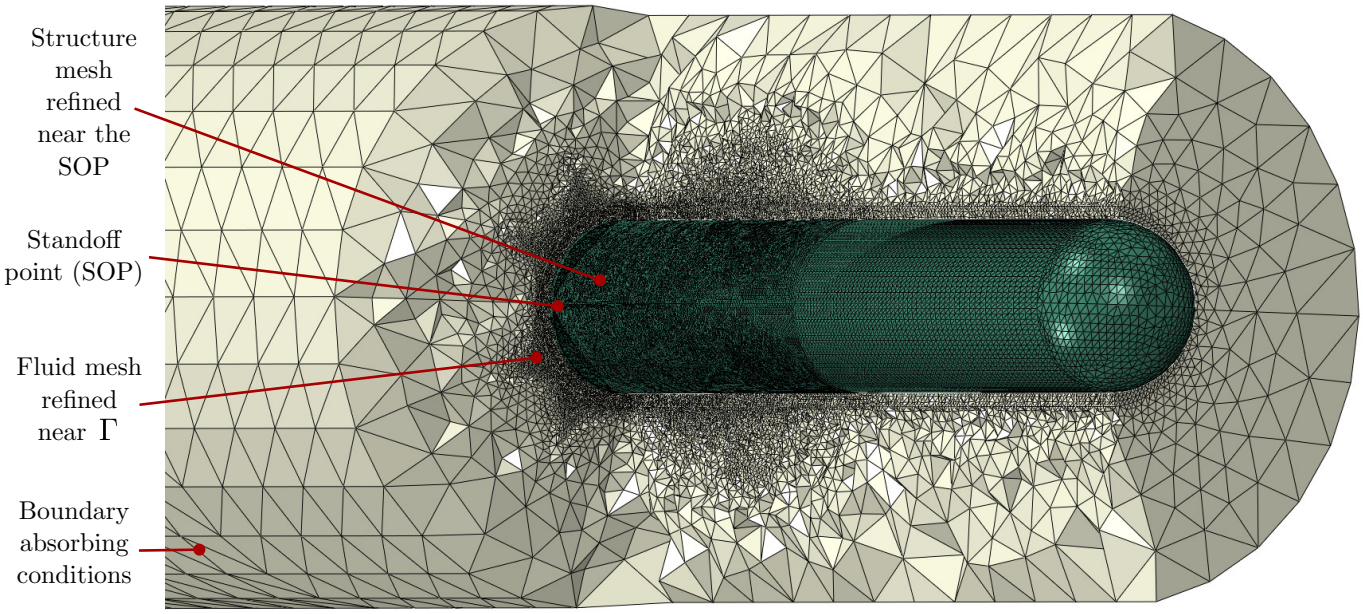

Figure 3.5: 3D view of the meshes used for the FEM part in the $\mathcal{Z}$-BEM/explicit FEM procedure. Both the 3D fluid and 2D structure meshes are refined near the standoff point.

Remark 15 *It would be interesting to include the results of the LS-DYNA® FEM/USA BEM procedure presented in Section 3.1.2. However, due to practical issues, we do not currently have access to these codes. The comparison will be performed in a future work, once access is restored. We nonetheless include the procedure in the comparison tables provided in Appendix D, as the reader could be interested to compare its characteristics to those of the procedures we actually ran.*

3.5.1 Kinematic response of structure

We first compare the procedure results based on the kinematic response of the structure. We report results in two forms. Firstly, line plots of the solutions (displacements, velocities, accelerations) at the three points (A,B,C) defined in Figure 3.4 are shown in Figures 3.6 to 3.8. Secondly, snapshots of these solutions on the hull are shown in Figures 3.9 to 3.11. For the $\mathcal{Z}$-BEM/implicit FEM procedure, the computation is performed only for the first 5 ms, because of a too-large computational time. The line plots are used to compare the four procedures, whereas the snapshots play a more illustrative role, by showing the quality of the solutions for the $\mathcal{Z}$-BEM/explicit FEM procedure.

Remark 16 *In the line plots, the time instant $t = 0$ is set shortly before the shock wave hits the hull, so that the acceleration discontinuity at the standoff point is well observed (and not disturbed by the figure axes). However, in the subsequent comments, notably concerning the maximum acceleration, we keep the convention that $t = 0$ corresponds to the instant the shock wave hits the hull.*

Remark 17 *In the line plots, the radial and orthoradial components are respectively carried by basis vectors e_r and e_θ, as defined in Figure 3.4.*

Figures 3.6 to 3.8 illustrate the structure dynamics at the three reference points in the cross-section ($\mathcal{P}$). A part of the observed differences on the displacements is probably due to the rigid motion, which is more and more important as time elapses. We are not interested in the rigid motion in this analysis, notably because we did not adapt the mass of the structure to the mass of the corresponding volume of water (in practice, the submarine mass is equal to the mass of the same volume of water, in order to remain still at a given depth underwater). Some tricks allow to numerically modify the global mass of the hull, typically by adding a surface mass all over the finite element mesh, but none were used in the benchmark.

We now focus on the accelerations, as it is the most difficult quantity to obtain without numerical instabilities. For the standoff point (A), all the procedures are in good agreement. Some oscillations are noticeable for all the procedures except the semi-analytical method. The typical frequency of these oscillations is a few kHz, so is not a priori high enough to be confidently explainable by numerical perturbations. However, three facts support this assumption:

- The oscillations vary according to the procedure used;
- They depend on numerical parameters such as the mesh size, the time scheme,...
- The mean responses provided by all procedures coincide.

At the orthogonal (B) and shadow (C) points, high oscillations deteriorate the results of both implicit methods ($\mathcal{Z}$-BEM/implicit FEM and FEM/FEM). These oscillations are more significant for the accelerations (Figure 3.6) than for the velocities and displacements. This is a commonly observed phenomenon: the more derivatives a quantity involves, the more disturbed it becomes. Indeed, for a perturbation of the acceleration of the form $\sin(\omega t)$, with a large ω, the perturbation on the velocity becomes $\cos(\omega t)/\omega$, and so is reduced of a factor $1/\omega$. To reduce these oscillations, some numerical damping could be introduced, as it will be explained in Section 3.5.2, but too much numerical damping also leads to other unwanted effects, which will be commented on in Section 3.5.3.

Remark 18 *The mesh used in the computation has been refined in the standoff region, but still has a satisfactory mesh size everywhere (see Figure 3.5). This affects the result*

quality only moderately, except for the accelerations (Figure 3.9), where a loss of quality is noticeable at the horizontal extremities of the picture obtained one millisecond after the explosion hits the cylinder.

Remark 19 *For the semi-analytical method, the orthoradial acceleration at point (B) is a bit perturbed by oscillations. Increasing the number N^θ of modes (set to 65) does not significantly improve the results of orthoradial accelerations. Instead, the results could be filtered.*

The computed kinematic response of the structure shows a rather good agreement between the four procedures. Some differences are nonetheless noticeable for the accelerations. The remainder of this section is dedicated to the study of the numerical perturbations observed in the accelerations, and their consequences in the context of industrial studies.

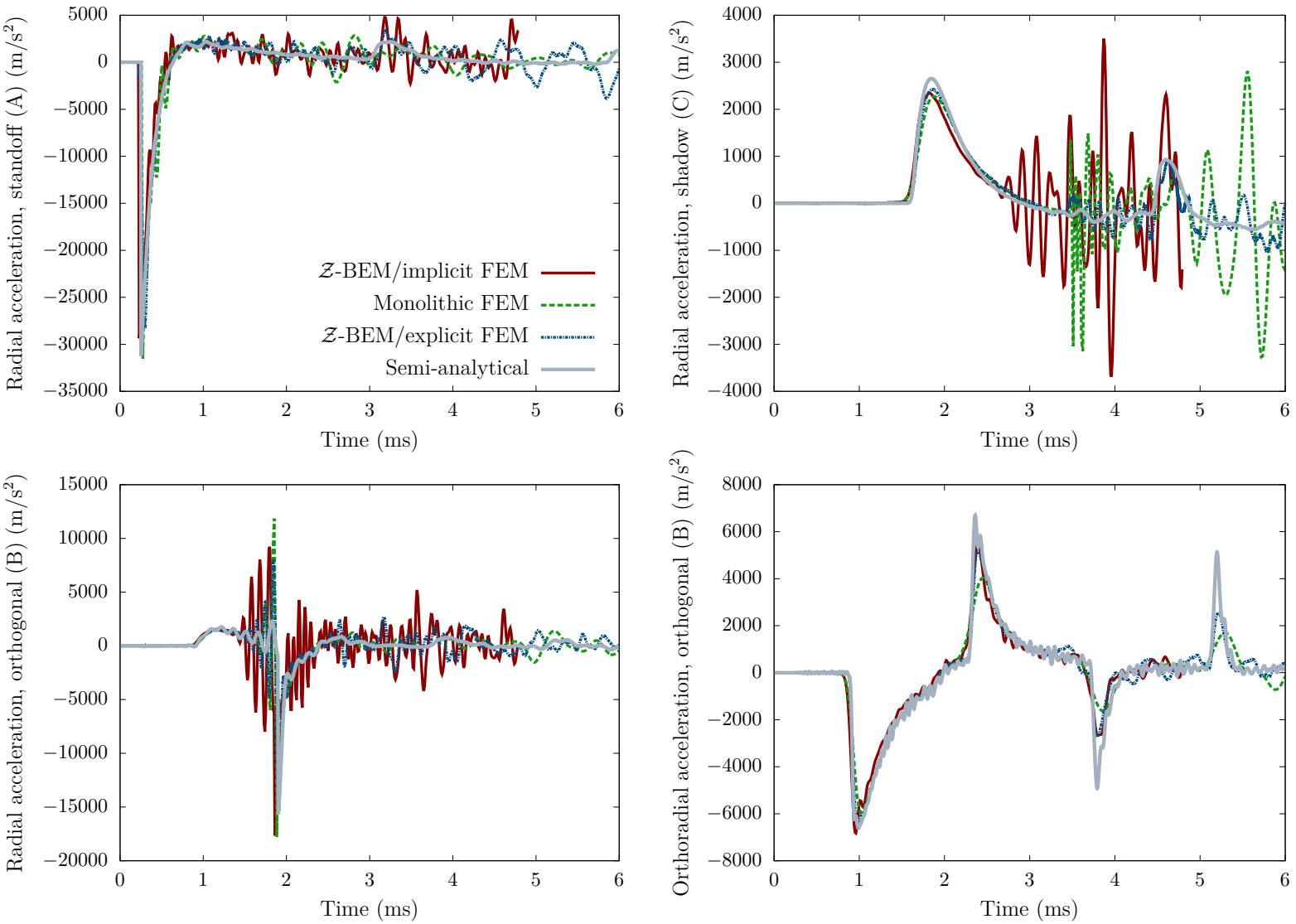

Figure 3.6: Accelerations at the standoff (A), orthogonal (B) and shadow (C) points, defined as in Figure 3.4.

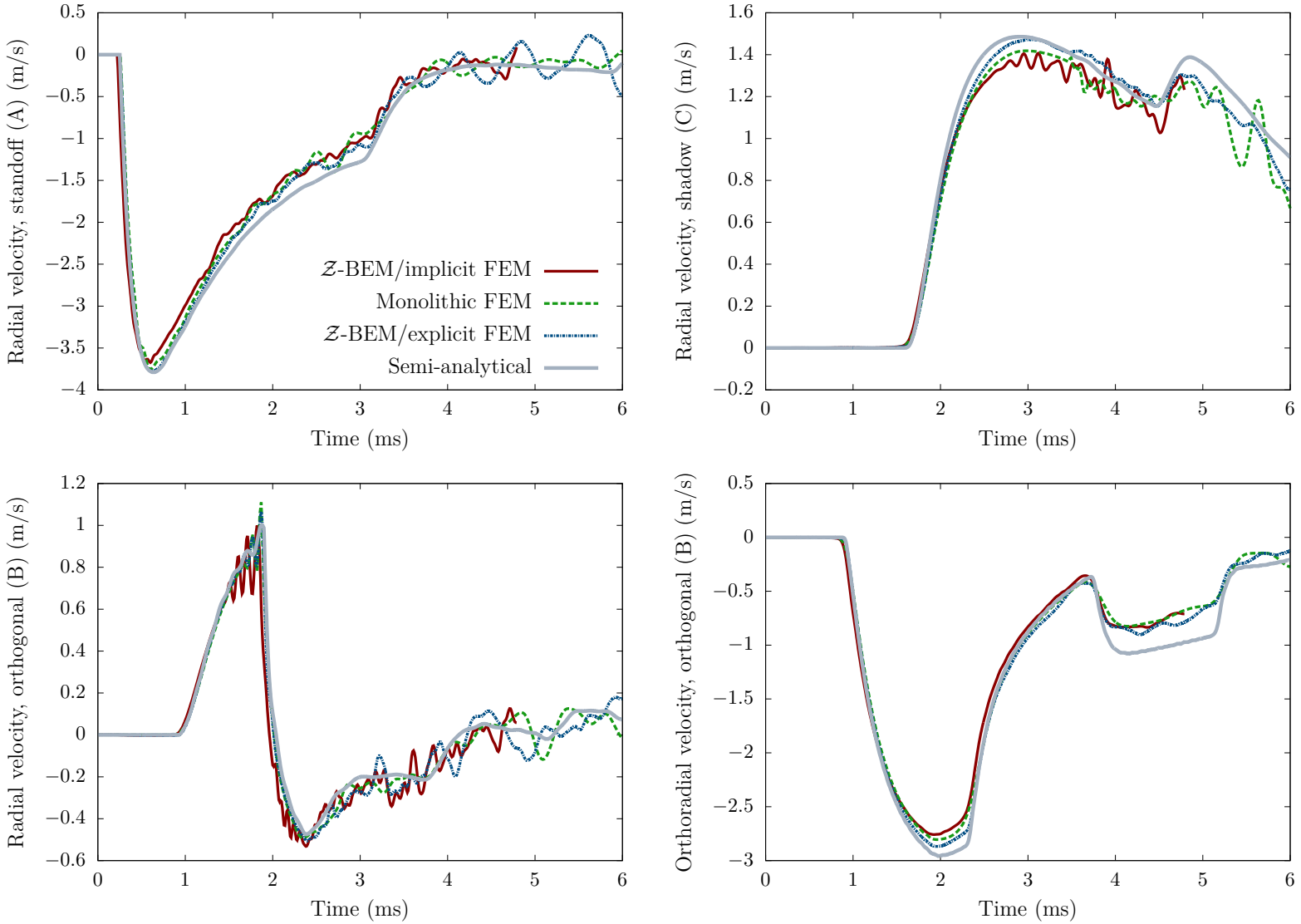

Figure 3.7: Velocities the standoff (A), orthogonal (B) and shadow (C) points, defined as in Figure 3.4.

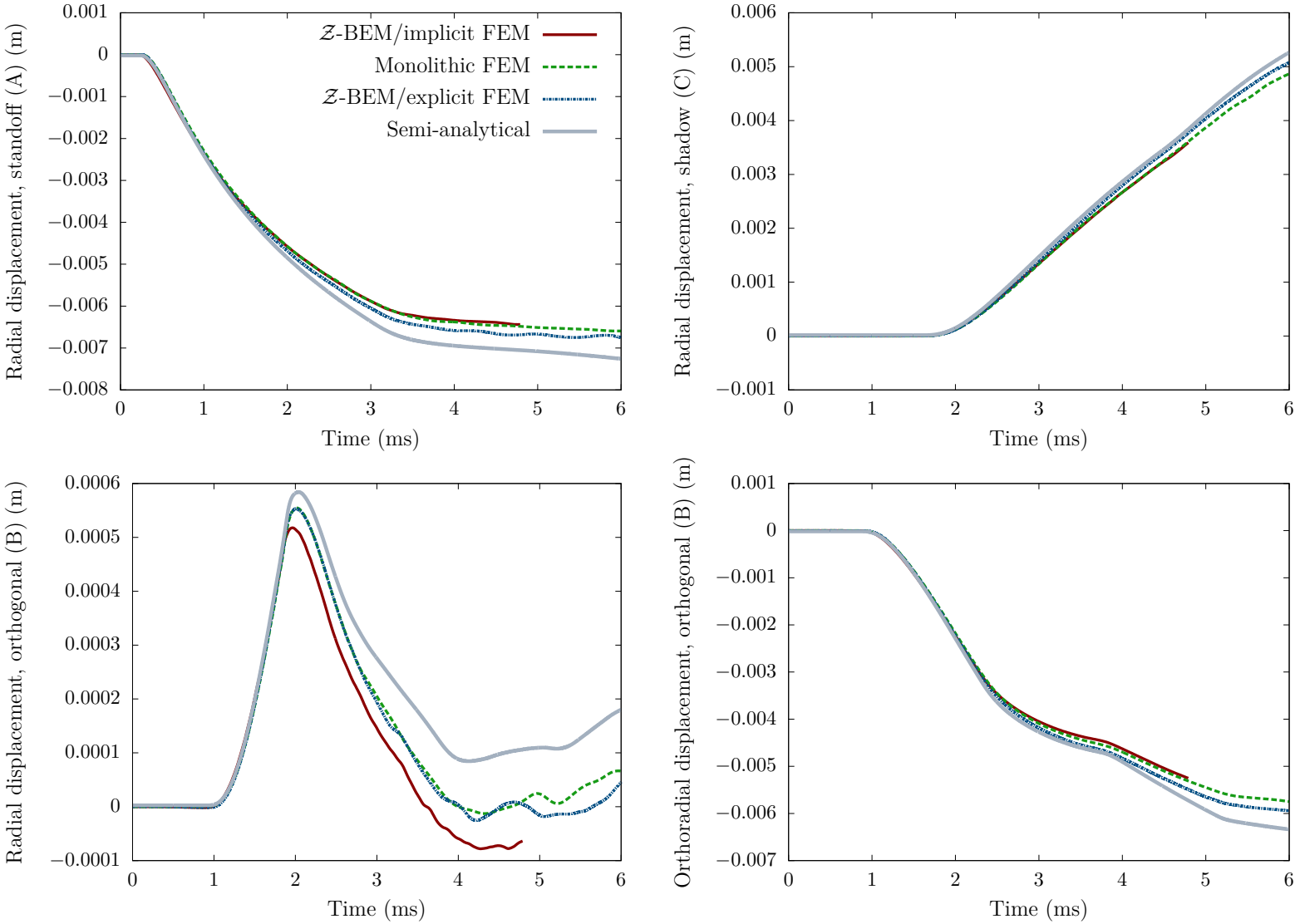

Figure 3.8: Displacements at the standoff (A), orthogonal (B) and shadow (C) points, defined as in Figure 3.4.

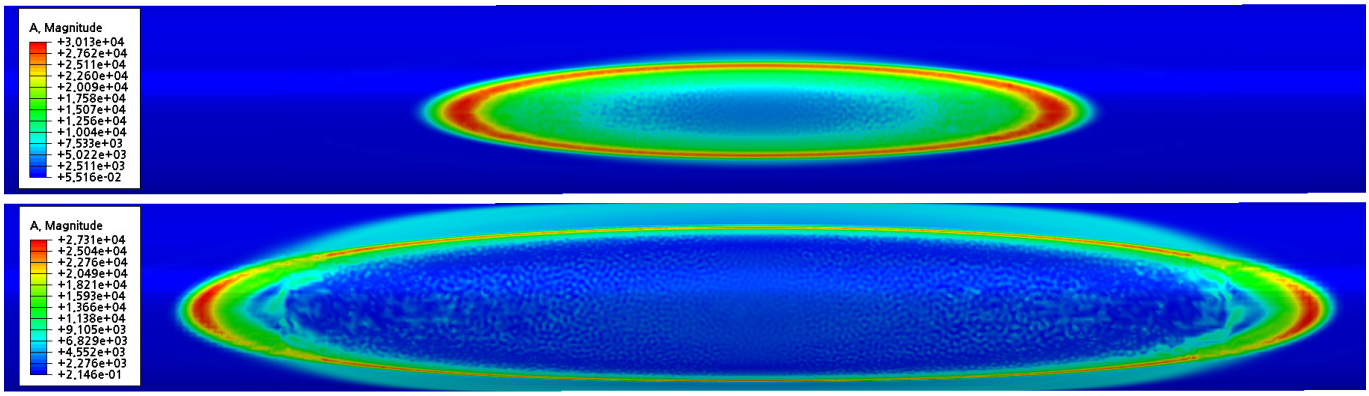

Figure 3.9: Snapshots of the acceleration magnitude on the hull, expressed in $\mathrm{m/s^2}$, at $t = 0.5$ ms (top) and $t = 1$ ms (bottom). Results of the $\mathcal{Z}$-BEM/explicit FEM procedure.

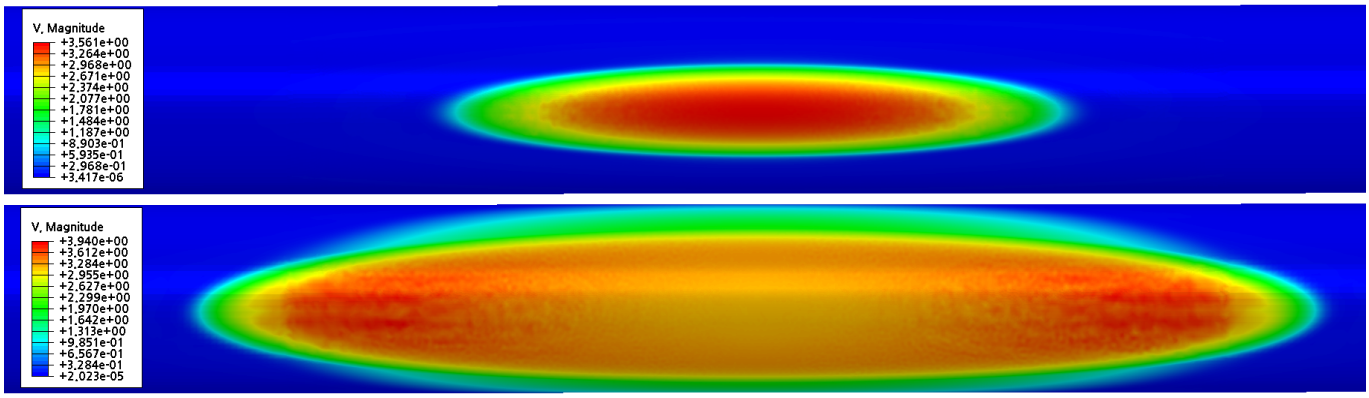

Figure 3.10: Snapshots of the velocity magnitude on the hull, expressed in m/s, at $t = 0.5$ ms (top) and $t = 1$ ms (bottom). Results of the $\mathcal{Z}$-BEM/explicit FEM procedure.

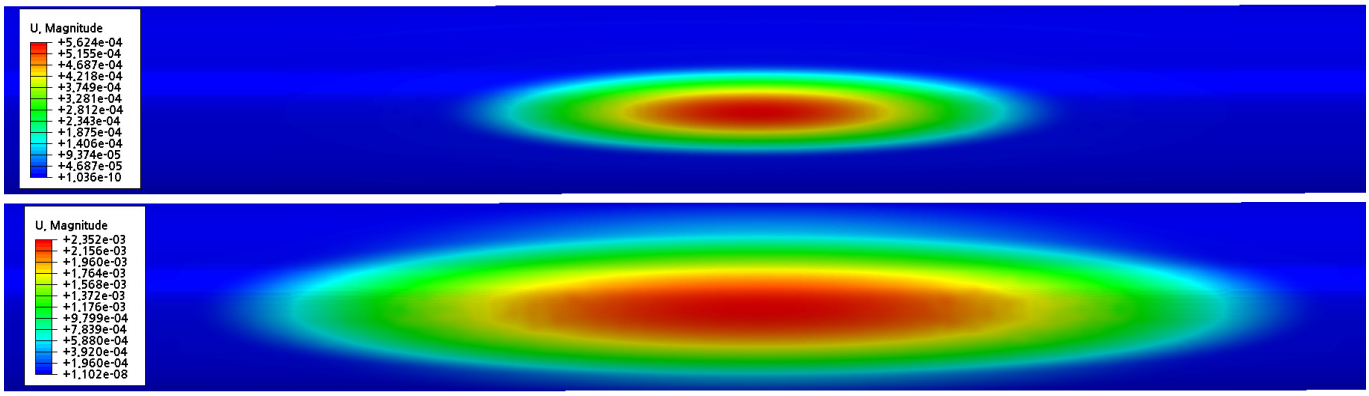

Figure 3.11: Snapshots of the displacement magnitude on the hull, expressed in m, at $t = 0.5$ ms (top) and $t = 1$ ms (bottom). Results of the $\mathcal{Z}$-BEM/explicit FEM procedure.

3.5.2 Handling high frequencies in the incident field

As explained in Section 1.2, for a fixed point P in the fluid, the incident pressure $p^{\text{inc}}(P,\cdot)$ is modelled as a discontinuous function of time. In the frequency domain, such an excitation involves arbitrary large frequencies. Usual BEMs and FEMs require the use of a mesh approximating a given geometry with elementary geometrical entities. Consider for instance a uniform triangle 2D-mesh of the interface Γ with mesh size h and $P1$ Lagrange boundary elements. Such a mesh cannot accurately solve problems involving variables that *oscillate within an element*, since the solution is represented by linear shape functions. The common rule of n_λ *points per wavelength* suggests that the highest frequency that can accurately be dealt with, for wave propagation problems with sound speed c, satisfies $f_{\max} = c/(n_\lambda\, h)$, where typically $n_\lambda \in [6, 10]$ depending of the target accuracy, in an industrial context.

We first tried to solve our FSI problem without filtering the incident pressure, other than the natural filtering arising from the use of a discrete time interval (i.e., the excitation involves very high frequencies related to the sampling frequency f_s of the time interval $[0, T]$, which is typically $f_s \sim 1$ MHz). In that case, the obtained results are numerically disturbed by highly oscillating perturbations, especially for the acceleration (with similar shape to those observed in Figure 3.6). These oscillations are due to the use of meshes that are not fine enough for the given excitation; they are well known in the context of UNDEX (Dassault Systèmes SIMULIA, 2009, Section 8.1.4). Since it would not be reasonable to use meshes that can handle frequencies up to 1 MHz, for the large geometries we consider, we need a way to attenuate these high frequencies. There are many ways to do so:

- Explicitly modify the expression of p^{inc}, for instance by smoothing the wave front. This is a common procedure in UNDEX analysis, where the wave front is being smoothed during a time of typically $\tau/10$, where τ is the time constant of the exponential decay, defined in (2.43).
- Use a dissipative time integration scheme, such as the Hilber-Hugues-Taylor (HHT) scheme, that attenuates high frequencies and introduce numerical damping (Géradin and Rixen, 1997; Hughes, 1987).
- Explicitly rely on a numerical filter, e.g., the Butterworth filter (Butterworth, 1930) (other choices are also relevant), to smooth the excitation before solving.

Each of the above methods has advantages and drawbacks. The first one is easy to implement and is probably the most famous in the field of UNDEX, because it is the one historically used, in particular in the reference code USA (Section 3.1.2). Its main drawback is that it does not specify *a priori* a cut-off frequency until which the results are not affected. In fact, we numerically noticed that this smoothing process is quite harsh, because it affects medium frequencies (some KHz). This process, however, seems consistent with the implementation means at the time the code USA was developed. In view of current major advancements in numerical simulation, we believe we no longer need to resort to this smoothing process.

Using dissipative time integration schemes to introduce numerical damping stands as an attractive method, notably because it does not require the explicit use of a filter. However, it usually relies on the choice of some parameters, that control the damping. Then, it is important to well analyse the influence of these parameters on the overall solution, to strike a balance between (i) preserving a satisfying solution that is not too much attenuated, and (ii) removing unphysical perturbations arising from the use of a discontinuous input.

The explicit recourse to a numerical filter to smooth the excitation presents the advantage of allowing to choose the cut-off frequency f_c. In particular, it permits to guarantee the validity of the obtained solution in a certain frequency range. However, the

use of an explicit filter requires that it be well mastered, especially concerning the order of the filter. These concerns have been extensively studied in the literature, and we refer e.g., to (Bianchi and Sorrentino, 2007).

Remark 20 *We recall that a Butterworth filter is designed such that its gain $G(\omega)$ (magnitude of the transfer function $H(i\omega)$) be provided by*

$$G(\omega) = \frac{G_0}{\sqrt{1 + (\omega/\omega_c)^{2n}}},$$

where G_0 is the gain at zero frequency, n the filter order, $\omega_c = 2\pi f_c$, and f_c is the cut-off frequency. The filter is then approximately flat in the pass band ($f < f_c$), reduced of 3 dB at the cut-off frequency f_c, and reduced of $20n$ dB per decade in the stop band ($f > f_c$).

For the results presented in this section, the input of the $\mathcal{Z}$-BEM/explicit FEM procedure was filtered using a Butterworth of order 5, with $f_c = 10$ kHz, whereas the implicit methods introduced small numerical damping through their time-stepping schemes (see Table D.6). No smoothing was performed for the semi-analytical procedure.

3.5.3 Unwanted effects of smoothing processes, shock response spectrum

Shock response spectrum. To assess the procedure results, and in particular the three smoothing methods mentioned in Section 3.5.2, it is instructive to go back to our industrial aim. One of our goals is to make sure that the equipment within the submarine remain functional after the explosion. The equipment are linked to the hull through mechanical systems acting like damped spring-mass systems, precisely to reduce the effects of underwater explosions (Lalanne, 2010; Wang et al., 2019). These systems act like filters, with a cut-off frequency that notably depends on the mass of the equipment. Based on the knowledge of the onboard equipment, the engineers identify a frequency range of interest for a given submarine. Then, our purpose is to accurately solve the hull behaviour in this frequency range, and in particular the acceleration of the hull, which is coupled to the equipment.

Therefore, we evaluate the smoothing procedures regarding their ability to accurately infer the equipment response to the UNDEX. To do so, a first approximation is to uncouple the hull dynamics from the equipment[2], i.e., to solve the dynamics of the hull in the absence of the equipment, and then use the acceleration of the hull (at the point where the equipment is fixed) as input to infer the equipment dynamics. Doing so, we solve a basic damped spring-mass system equation

$$\ddot{x} + 2\,\xi\,\omega\,\dot{x} + \omega^2 x = s \tag{3.17}$$

for a given source excitation s, where $\dot{x}$ denotes the time derivative of the system length variation x, ξ is the damping coefficient, $\omega = \sqrt{k/m}$ is the natural pulsation, k is the spring constant, and m is the system mass. The obtained results are called *Shock Response Spectrum (SRS)*.

The SRS for the pseudo-acceleration $\omega^2 x$ at the standoff (A) and shadow (C) points are provided in Figure 3.12, for $\xi = 0.05$. At each natural frequency $\omega = 2\pi f$, the equation

[2]This approximation is more relevant for lighter equipment.

(3.17) is solved, with $s = a/m$ obtained from the hull acceleration a. Then, the SRS is the function

$$g : \begin{array}{ccc} [f_{\min}, f_{\max}] & \longrightarrow & \mathbb{R} \\ f & \longmapsto & (2\pi f)^2 \max\limits_{t\in[0,T]} x(t;f) \end{array} .$$

The goal of Figure 3.12 is to know, for a given frequency f (so a specific on-board equipment), the order of magnitude of the maximum acceleration experienced by the equipment, and so to know whether it would still be operational after the explosion.

In the range [100 Hz,600 Hz], the four procedures have very similar results at the standoff point. For the $\mathcal{Z}$-BEM/implicit FEM procedure, the computation is performed only for the first 5 ms, and therefore the SRS are obtained for a reduced range (long time corresponds to low frequencies). At very high frequencies, the four procedures present noticeable differences. The solution obtained with Abaqus® explicit may be considered as accurate up to around 7 kHz, instead of 10 kHz, because the Butterworth filter used, with a cut-off frequency of 10 kHz, is not a perfect filter. For the two implicit methods, the numerical damping introduced by the time-stepping scheme is expected to affect the solution at high frequencies, but the value up which the solution is correct is not provided a priori, contrary to when using a Butterworth filter.

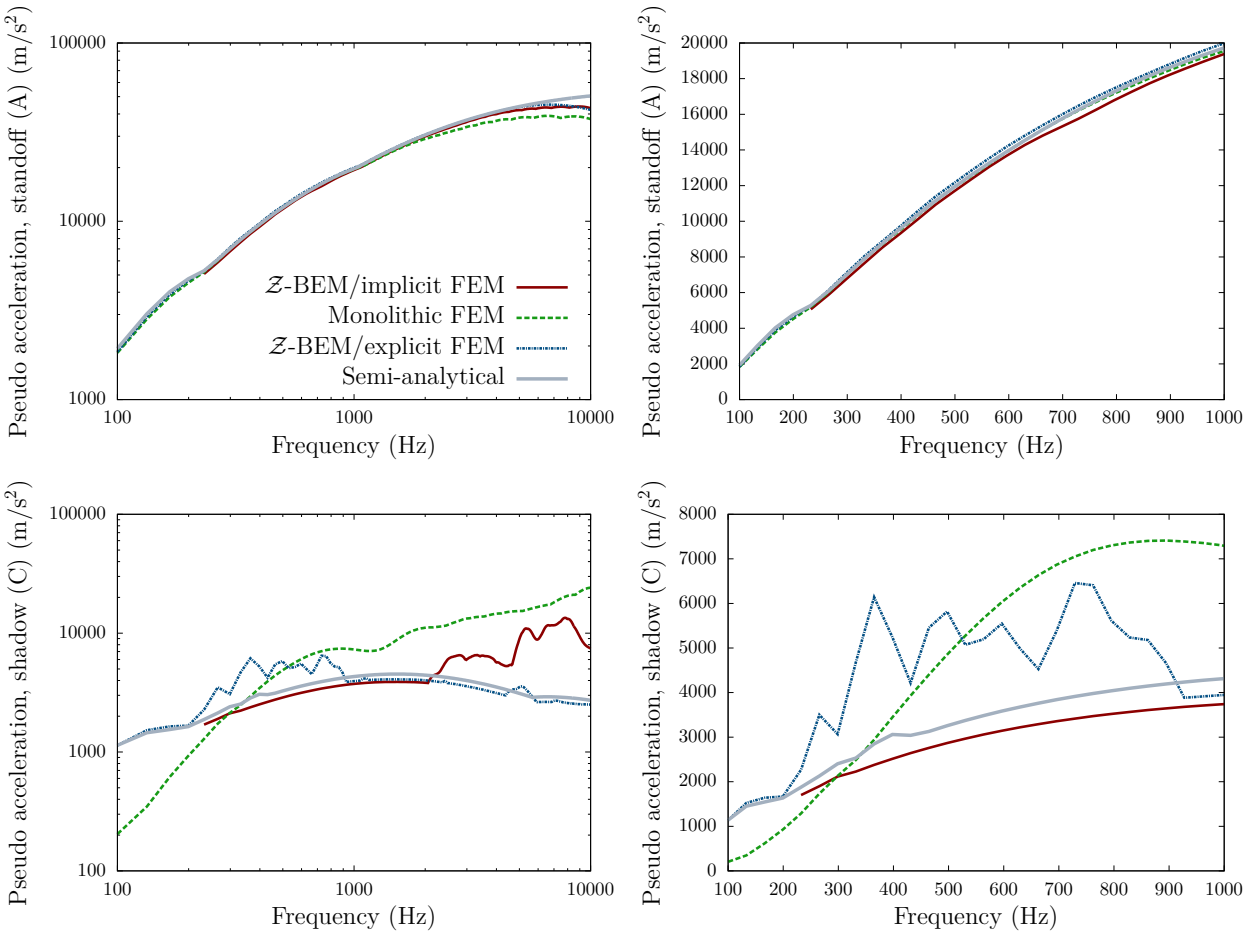

Figure 3.12: Shock response spectrum for the pseudo-acceleration at the standoff (A) and shadow (C) points.

The SRS at the shadow point is also provided. It shows the difficulty to get proper results at this point, as the four procedures do not provide similar results on the whole

frequency range. Instead, the Abaqus® explicit method corresponds to the semi-analytical one at high frequencies, whereas the Abaqus® implicit is close to the semi-analytical solution at lower frequencies.

In view of the results, we advise the use of a numerical filter, because it permits to control the frequency range affected, and allows less disturbed results for the accelerations, as shown in Figure 3.6.

Consequences of a common smoothing process. We now study the influence of the most common smoothing process in the context of UNDEX: modify the form (2.43) of the incident pressure so that it linearly grows to its maximum during a time of $\tau/10$, where τ is the time constant of the exponential decline, defined in (2.43). In the following we refer to this process as the $\tau/10$ *smoothing procedure*.

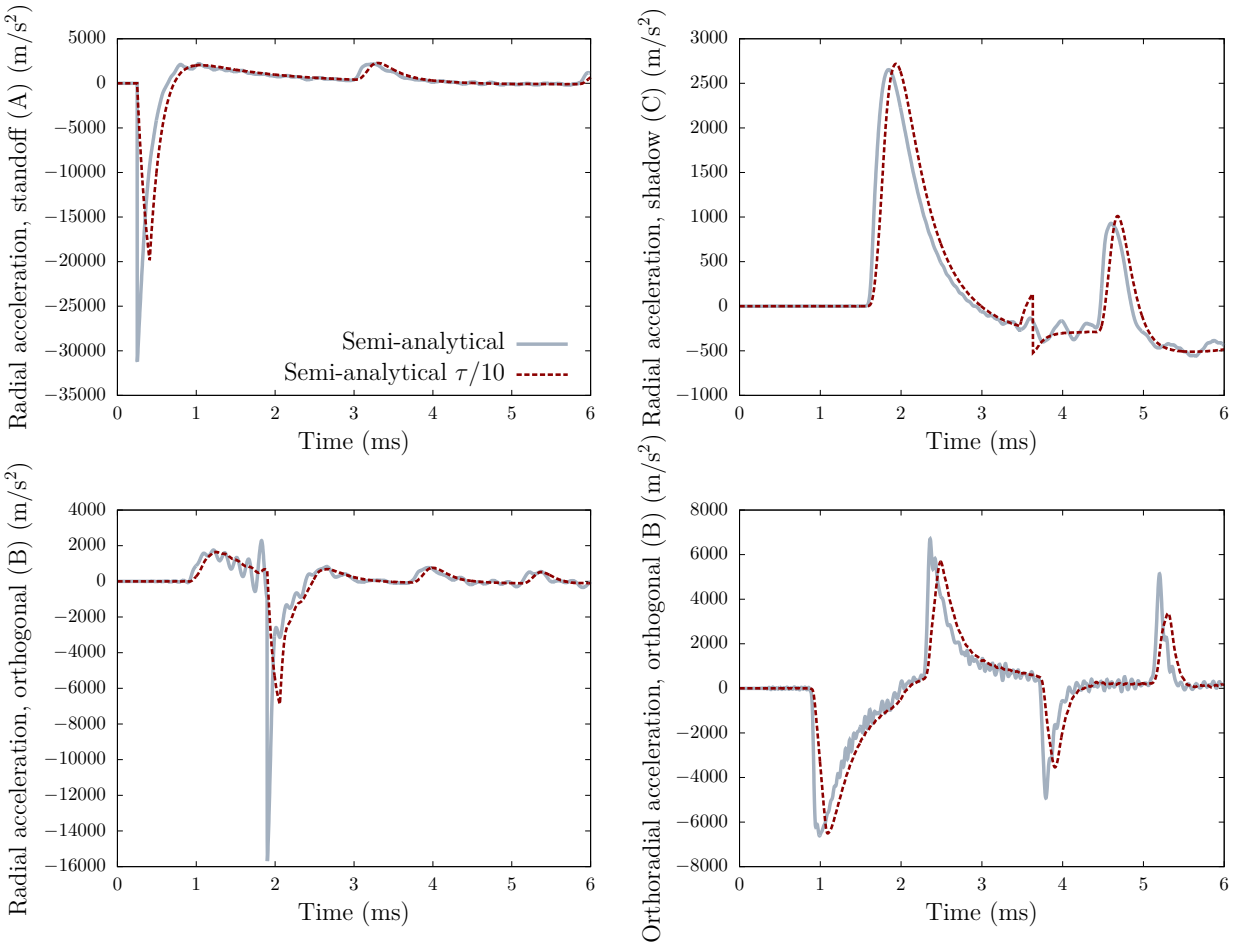

Figure 3.13: Accelerations at the standoff (A), orthogonal (B) and shadow (C) points, comparison between the results obtained with and without the $\tau/10$ smoothing process, for the semi-analytical procedure.

We compare the accelerations obtained with and without the smoothing process, for the semi-analytical procedure, shown in Figure 3.13. The influence of the $\tau/10$ smoothing procedure is noticeable whenever the acceleration should be discontinuous. Instead, the acceleration jump is smoothed, and the acceleration maximum is reduced. Also, at the shadow point C, the smoothing process introduces an unphysical jump when the incident pressure reaches the point (but the total pressure front has not yet reached the shadow point, because it has to go around the obstacle), at $t \simeq 3.5$ ms. We believe this jump is a

consequence of the too harsh smoothing process, which affects the wave character of the incident pressure (i.e., it is no longer a wave), and therefore the reflected pressure (which is supposed to compensate for the incident pressure) struggles to match the exact opposite form of the incident pressure. The smoothing process has little influence on the velocities and displacements, which are therefore not shown. The two SRS displayed on Figure 3.14 show the influence of the smoothing procedure: it considerably underestimates the results at the standoff point for frequencies higher than 2 kHz. In view of the good agreement observed in Figure 3.12, compared to the results of the $\tau/10$ smoothing procedure, we recommend not to use the $\tau/10$ smoothing procedure when dealing with deformable structures, though it has little influence on the pressure field for rigid cases (scattering problems such as those presented in Chapter 2, see e.g., Figure 2.12).

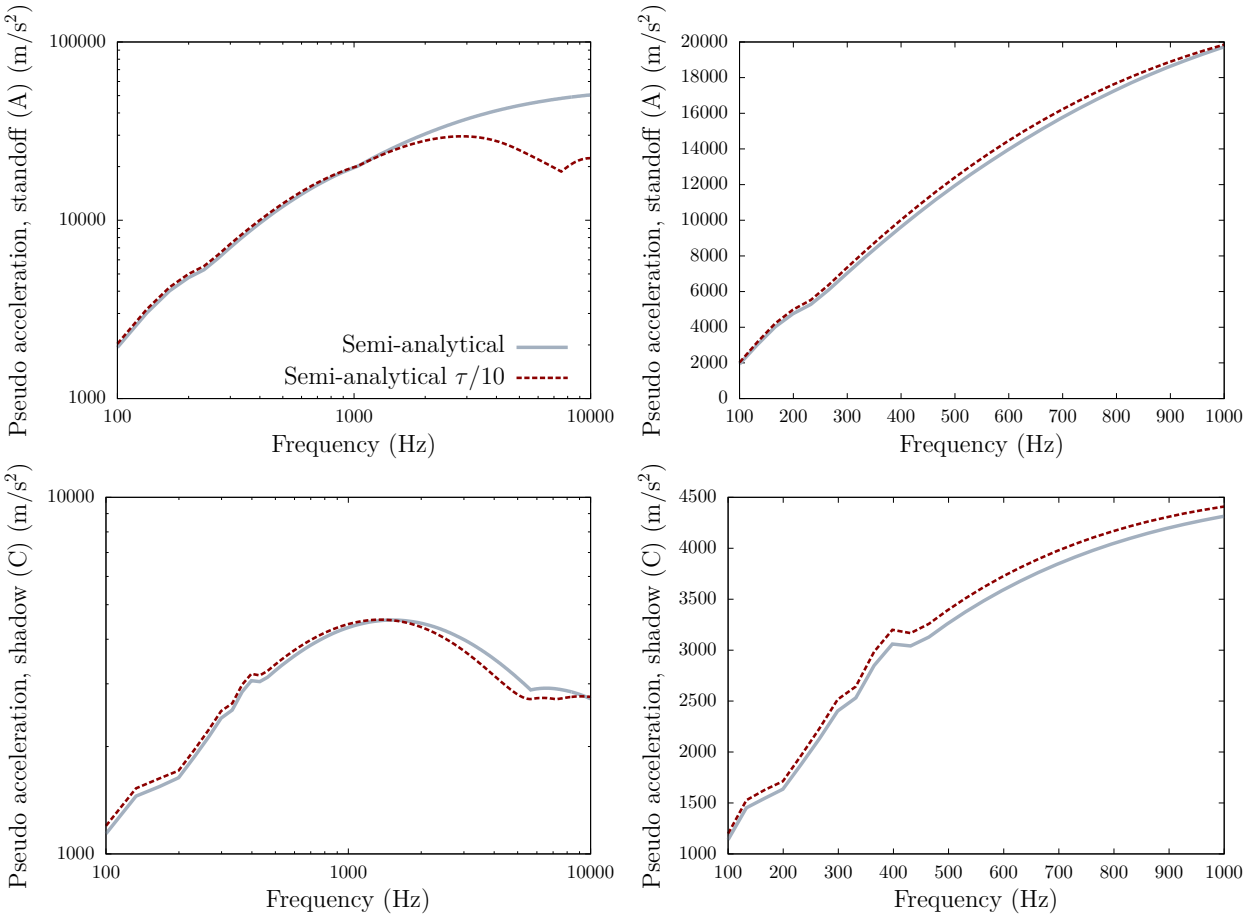

Figure 3.14: Shock response spectrum for the pseudo-acceleration at the standoff (A) and shadow (C) points. Comparison between the results obtained with and without the $\tau/10$ smoothing process, for the semi-analytical procedure.

Which procedure best matches the maximum acceleration? We now assess the procedure ability to accurately match the maximum acceleration. Though less important than the SRS, this remains an interesting performance indicator, notably because it permits to check that the smoothing processes used are not too harsh.

When the standoff region is a regular boundary, like in our case, the maximum acceleration at the standoff point is provided by that of an infinite Taylor plate submitted to a plane wave front. The justification relies on two ingredients: (i) there exists an

arbitrary small time T such that, in $[0,T]$, the region of Γ in which the solution (both fluid and structure quantities) is not zero is arbitrary small, around the standoff point, because of causality (for both the waves propagating in the fluid and in the structure), and (ii) the regular boundary may be arbitrary close to its tangent plane, and the spherical wave front to a plane wave front, when considering a sufficiently small area. Then, for any arbitrary small ε, there exists T_ε such that, in $[0,T_\varepsilon]$, the acceleration at the standoff point of our cylindrical shell corresponds to that of an infinite plate. The acceleration of the plate is obtained by applying the Newton law, after division by an elementary surface (Leblond, 2007):

$$\rho_s h_s \, a(t) = p^{\text{tot}}(t) \, ,$$

and so, at $t = 0$,

$$a(0) = \frac{2\, p_m}{\rho_s h_s} \, ,$$

where p_m is the maximum pressure defined in (2.43), and the factor 2 comes from $p^{\text{ref}}(0) = p^{\text{inc}}(0)$ and $p^{\text{rad}}(0) = \rho_f c_f u(0) = 0$. Using

$$p_m(r) = K_1 \left(\frac{W^{1/3}}{r} \right)^{a_1} \tag{3.18}$$

and the coefficient values provided in (3.16), the maximum acceleration, obtained at $t = 0$, is

$$a_{\max} \simeq 3.2 \ 10^4 \ \text{m/s}^2.$$

Figure 3.6 shows that the FEM/FEM procedure is the one reaching the closest maximum acceleration (apart from the semi-analytical one). The $\mathcal{Z}$-BEM/explicit FEM procedure leads to the smallest value, with $a_{\max} \simeq 2.8 \ 10^4$ m/s^2. This makes sense, as it is the most filtered one. The implicit methods, that are smoothed only because of some numerical damping in the implicit scheme used (see Table D.6), produce better values of $a_{\max}$ but are more sensitive to oscillatory perturbations, as discussed previously. Then, when using filters, the user must strike a balance between a too-disturbed solution and a too-smoothed (and so too low maximum value) of the acceleration.

3.5.4 Summary: strengths and weaknesses of each procedure

In this section, we solved a FSI test problem using different numerical methods. The comparison performed assesses the efficiency of a monolithic FEM/FEM procedure, a semi-analytical approach, and the hybrid $\mathcal{Z}$-BEM/FEM procedure.

First of all, the comparison performed in this benchmark validates the correct functioning of our $\mathcal{Z}$-BEM/FEM procedure for this almost realistic configuration (the cylinder radius is a bit small compared to the industrial purpose). Secondly, it shows the key role of filters and/or numerical damping to obtain a correct solution when dealing with a discontinuous input (very large frequency content), using a discrete mesh (with a not arbitrary small mesh size, limited by computer resources). To well understand the influence of the smoothing processes, the shock response spectrum is the appropriate tool, given the industrial purpose. In particular, we showed the limitations of the commonly used smoothing process named "$\tau/10$", which we advise not to use, but rather prefer ordinary filters, such as, e.g., a Butterworth filter. Another important conclusion concerns the *choice* of a procedure. The four we studied have advantages and drawbacks, and the choice of one of them depends on the specific configuration considered. Moreover, other procedures are potentially feasible,

in particular based on BEM/FEM coupling, provided the FEM code used for the structure allows Robin conditions (see Section 3.2).

The semi-analytical procedure is relevant if (i) the geometry is a cylinder, (ii) only the results in the 2D cross-section ($\mathcal{P}$) are of interest, or more specifically at the standoff point, (iii) the explosion is sufficiently far away to approximate the spherical wave front by a plan or cylindrical wave front, and (iv) the study takes place in a sufficiently small time interval so that, given the cylinder dimensions, the results in ($\mathcal{P}$) are not affected by the cylinder extremities. The case study in this section is a good example of applications of the semi-analytical procedure, where we advise to use it, because it is much faster than the other procedures, except if you desire the 3D solution on the hull, like provided in Figures 3.9 to 3.11.

The FEM/FEM procedure is relevant if (i) a rather small geometry (compared to a submarine) is considered, for which a refined enough volume FE mesh may be used, or (ii) the geometry is simple, and without trap regions in which multiple reflections appear (if it the case, a refined volume mesh must be used in these regions, to well represent the reflected pressure). Also, in its current form, the code_aster® FEM/FEM procedure cannot yet deal with high deformations, and allows only implicit schemes, but these limitations are only practical, and will probably be removed in future work.

The hybrid $\mathcal{Z}$-BEM/implicit FEM procedure is relevant if (i) implicit schemes are preferred, to avoid the risk of error accumulation encountered with explicit schemes, and (ii) the explosion is not too big, so that the deformations remain small and elastic (otherwise, the computation becomes a bit costly). In all other cases, and especially when dealing with complex large geometries, we advise the $\mathcal{Z}$-BEM/explicit FEM procedure. The $\mathcal{Z}$-BEM/FEM procedure can deal with all kind of problems, as it relies on few hypotheses, but it stands less efficient for small geometries than FEM/FEM procedures. This is explained by two factors: (i) the volume mesh limitations affecting FEM/FEM procedures decrease as the geometry dimensions reduce, and (ii) the $\mathcal{Z}$-BEM procedure introduced in Chapter 2 does not benefit that much from small geometry dimensions. This latter remark needs some explanations.

Consider the two cases studied in Section 2.6.2 and Section 2.6.3, that is a small (radius $a = 0.5$ m) and a big (radius $a = 5$ m) cylinders facing a remote UNDEX. For both problems, the most refined mesh has $N \sim 10^6$ DOFs. Of course, it results in a mesh size ten times smaller for the small cylinder, but it also implies that the frequencies considered high for the small cylinder are higher than that of the big cylinder. More precisely, as explained in Section 2.5.2, a frequency may be considered as high if the ratio κ/λ between the local radius of curvature κ and the characteristic wavelength λ is large. In our case, the radius of curvature (so the radius) is ten times smaller for the small cylinder, and so it compels the procedure to actually solve, with the FM-BEM, frequency problems for higher frequencies than in the case of the big cylinder, where the recourse to a high frequency approximation is possible for smaller frequencies. This explains the relatively similar result quality for the two problems, illustrated in Figure 2.12 and Figure 2.14, whereas a FEM procedure would provide much better results in the case of the small cylinder than the big one, for a similar number of DOFs.

3.6 Conclusion and future work

This chapter was devoted to the design, implementation and validation of a fluid-structure coupling procedure for the FSI problem of a submarine facing a remote UNDEX. After reviewing some coupling strategies available in the literature, we explained why a $\mathcal{Z}$-BEM-

fluid/FEM-structure coupling procedure would be an appropriate choice. However, because of some practical constraints, this solution could not be implemented during this PhD work. Instead, we designed a hybrid $\mathcal{Z}$-BEM/FEM/FEM procedure, in which the reflected part of the fluid is computed using the $\mathcal{Z}$-BEM, and the coupled part of the FSI problem is solved with a common monolithic FEM/FEM approach. Even though the reflected part is solved using the BEM, and therefore the volume fluid mesh can be refined only near the fluid-structure interface, the FEM/FEM coupling presents some drawbacks compared to a full FEM-structure/BEM-fluid coupling:

- A non-uniform 3D volume mesh has to be generated, with a geometrically complex internal boundary (submarine surface);
- The volume mesh must be truncated (approximation of the radiation condition), which may entail unwanted reflections.

Because of these limitations, we are still investigating the $\mathcal{Z}$-BEM/FEM procedure, with Robin boundary conditions.

The cross-validation performed in Section 3.5 validates the hybrid $\mathcal{Z}$-BEM/FEM/FEM procedure in the case of a long cylinder. Despite its limitations, the $\mathcal{Z}$-BEM/explicit FEM procedure appears to be the most appropriate to deal with a realistic industrial case, which will be done in Chapter 5. Before that, the procedure designed to deal with the FSI problem associated to the gas bubble phenomenon is presented in Chapter 4.

Chapter 4

Fluid-structure interaction for the oscillating gas bubble

Benefitting from the analyses of Chapter 1, the goal of this fourth chapter is to design a computational method to address the fluid-structure interaction (FSI) problem of a ship facing a gas bubble. We first recall the fluid model in Section 4.1. Then, in Section 4.2, we formulate the coupled FSI problem, and present the step-by-step FEM/BEM coupling procedure we choose to solve it. To speed up the fluid solving process, we study the time-independence property of the BEM operators and introduce the $\mathcal{H}$-matrices in Section 4.3. We summarise our numerical methodology in Section 4.4, and validate it on the simple problem of a sphere in a uniform flow in Section 4.5, before solving the FSI problem of a gas bubble impacting a stiffened submarine hull in Section 4.6.

4.1 Reminders: the bubble phenomenon

In this section, we recall the conclusions of Chapter 1 and stress some differences between the bubble and shock wave phenomena, notably concerning the non-linear aspects of the bubble fluid response.

4.1.1 Hypotheses and modelling

We assume the fluid to be incompressible and potential. Under these hypotheses, the velocity potential satisfies the Laplace equation (1.26), and the pressure is inferred from the latter through the generalised Bernoulli equation (1.29) (see Section 1.3). We choose the Hicks model (Hicks, 1970; Leblond, 2007) to describe the bubble dynamics in the absence of the ship. Similarly to the bubble model presented in Section 1.3.2, the Hicks model provides the bubble motion: evolution of the bubble radius R and the depth Z over time, under some specified hypotheses. Then the velocity potential is related to $R(t)$ and $Z(t)$ through the relation (1.27). We recall that the bubble model is purposely treated as an independent part of the overall procedure. This means that any bubble model (consistent with the assumption of incompressible and potential flow) may be used in the procedure we design, the latter taking as input the velocity potential induced by the bubble in the fluid in the absence of the structure.

Like for the shock wave phenomenon (Chapters 2 and 3) we choose the boundary element method (BEM) to model the fluid part of the FSI problem, whereas the finite element method (FEM) is best suited for the structure (it easily allows combination of various theories, e.g., shell and beam theories, constitutive non-linearity such as plasticity,

complex interior of the submarine,...). Our purpose is then to design a FEM/BEM coupling to solve the coupled FSI problem, for far-field explosions.

4.1.2 Time dependence of the geometric domains

Like in the shock wave part, the FSI problem admits the generic form (3.1)

$$\begin{cases} (\mathcal{S}) : \text{structure evolution equations, set in } \Omega_s, \\ (\mathcal{F}) : \text{fluid evolution equations, set in } \Omega_f, \\ (\mathcal{KC}) : \text{kinematic transmission condition, set on } \Gamma, \\ (\mathcal{DC}) : \text{dynamic transmission condition, set on } \Gamma. \end{cases}$$

The main difference between the two problems lies in the fluid equations ($\mathcal{F}$). For the bubble phenomenon, the Laplace equation (1.26) for the total velocity potential

$$\Delta\phi = 0 \tag{4.1}$$

is time-independent, contrary to the wave equation (1.20). This reflects an important assumption of the incompressible model: the time scales involved are high enough so that the propagation time of the information may be neglected. In other words, the perturbations appear to propagate at an infinite speed. In that sense, the Laplace equation (4.1) may be seen as the limit of the wave equation (1.20) when the fluid velocity c tends to infinity. However, the solution of an acoustic problem, e.g., the breathing sphere presented in Section 2.6.1, is in general quite different from that of the analogous problem with the Laplace equation (named pulsating sphere in this case). Consider for instance a sphere pulsating in an incompressible fluid, with a time-dependent prescribed normal wall velocity u provided by (2.41)

$$u(t) = u(t;\omega) = u_0 \sum_{i=1}^{5} u_i \sin(2\pi f_i t)\,. \tag{4.2}$$

The limit of the acoustic solution[1] when c tends to infinity does not provide the solution to the pulsating sphere in an incompressible fluid. Instead, it rather gives the linear part of the latter. This is a key difference between the two modelling: in acoustics, a breathing sphere sees its surface oscillating with a sufficiently low magnitude, so that the approximation $\Gamma(t) \simeq \Gamma(0)$ remains valid. A pulsating sphere in an incompressible flow oscillates more slowly, but possibly with a larger amplitude, and then, at a time instant $t > 0$, $\Gamma(t)$ is different from $\Gamma(0)$, and this adds a non-linear term (with respect to the solicitation, so the prescribed normal wall velocity u) in the fluid velocity potential.

To conclude, the time-dependence of the incompressible fluid problem, analogous to (2.1), manifests itself in the boundary condition and the time-dependent geometric domains. With Neumann boundary conditions, the fluid problem exhibits the form

$$\text{For } t \in [0,T], \text{ find } \phi \text{ such that } \begin{cases} \Delta\phi(\mathbf{x};t) = 0 & \mathbf{x} \in \Omega_f(t), \\ \dfrac{\partial\phi}{\partial n}(\mathbf{x};t) = h(\mathbf{x};t) & \mathbf{x} \in \Gamma(t), \end{cases} \tag{4.3}$$

where h is a given Neumann datum. (4.3) shows the fluid problem reduces to the solving, at each time step, of a quasi-static problem with an updated boundary $\Gamma(t)$.

[1] The solution to a breathing sphere in an acoustic fluid with the same prescribed velocity (4.2).

4.1.3 Fluid decomposition

In the acoustic case, the fluid velocity potential is decomposed into an incident, a reflected and a radiated part (see Section 2.5.1), leading to two distinct problems, with different boundary conditions (see (2.31)). Since the Laplace equation (4.1) is linear, a similar decomposition is possible, into an ambient part ϕ^{amb} (analogous to the incident part), that describes the flow in the absence of the structure; a rigid part ϕ^{rig} (analogous to the reflected part), that would be the perturbation induced by a rigid (mobile) structure; and a deformable part ϕ^{def}, defined as $\phi^{\text{def}} = \phi^{\text{tot}} - \phi^{\text{rig}} - \phi^{\text{amb}}$. In the acoustic case, the decomposition holds true for the pressure, because of the linear relation $p = -\rho_f \partial_t \phi$ between the pressure and the velocity potential, that permits to define $p^{\text{tot}} = p^{\text{inc}} + p^{\text{ref}} + p^{\text{rad}}$. However, for the oscillating bubble, the pressure is related to the velocity potential through the generalised Bernoulli equation (1.29)

$$\frac{\partial \phi}{\partial t} + \frac{1}{2} \nabla\phi \cdot \nabla\phi + \frac{1}{\rho_f} p - g\, \xi_P = 0\,, \tag{4.4}$$

that contains non-linear terms, so the pressure does not inherit the velocity potential decomposition. Also, contrary to the acoustic case, the contribution ϕ^{rig} cannot be computed during a pre-calculation in which the structure is supposed motionless in $[0, T]$, because $\Gamma(t)$ is time-dependent, and so $\phi^{\text{rig}}(t)$ must be deduced from $\phi^{\text{amb}}(t)$ on $\Gamma(t)$. Therefore, the classical decomposition $\phi^{\text{tot}} \equiv \phi = \phi^{\text{amb}} + \phi^{\text{per}}$ is preferred for incompressible flows, where ϕ^{per} is the perturbation due to the structure, so the unknown in our case, since ϕ^{amb} is given (for a remote UNDEX, the bubble dynamics is not affected by the presence of the structure).

4.2 FEM/BEM coupling for the FSI problem

Under the assumptions specified above in Section 4.1, we formulate the coupled FSI problem using Neumann physical boundary conditions:
Find $(\mathbf{u}, \sigma, \phi, p)$ such that

$$(\mathcal{S}) \begin{cases} \rho_s \ddot{\mathbf{u}}(\mathbf{x}, t) - \operatorname{div} \sigma(\mathbf{u})(\mathbf{x}, t) = \mathbf{f}_v(\mathbf{x}, t) & \forall t \in [0, T], \forall \mathbf{x} \in \Omega_s(t), \\ \sigma(\mathbf{u})(\mathbf{x}, t) \cdot \mathbf{n} = \mathbf{f}_s(\mathbf{x}, t) = -p(\mathbf{x}, t)\mathbf{n} & \forall t \in [0, T], \forall \mathbf{x} \in \Gamma(t), \\ \text{Constitutive equation: relation between } \sigma \text{ and } \mathbf{u}, \end{cases} \tag{4.5a}$$

$$(\mathcal{F}) \begin{cases} \Delta \phi^{\text{per}}(\mathbf{x}, t) = 0 & \forall t \in [0, T], \forall \mathbf{x} \in \Omega_f(t), \\ \dfrac{\partial \phi^{\text{per}}}{\partial n}(\mathbf{x}, t) = -\dfrac{\partial \phi^{\text{amb}}}{\partial n}(\mathbf{x}, t) + \dot{\mathbf{u}}(\mathbf{x}, t) \cdot \mathbf{n} & \forall t \in [0, T], \forall \mathbf{x} \in \Gamma(t), \\ \dfrac{\partial \phi}{\partial t}(\mathbf{x}, t) + \dfrac{|\nabla \phi(\mathbf{x}, t)|^2}{2} + \dfrac{1}{\rho_f} p(\mathbf{x}, t) - g\, \xi_P = C(t) & \forall t \in [0, T], \forall \mathbf{x} \in \Omega_f(t), \end{cases} \tag{4.5b}$$

where $\mathbf{u}$ is the structure displacement, $\mathbf{n}$ the outward normal to the structure, ρ_s the structure mass density, σ the Cauchy stress tensor, $\mathbf{f}_v$ gathers the external volume force, and $\mathbf{f}_s$ is a given Neumann datum (surface force exerted by the fluid), obtained through the dynamic condition of continuity:

$$\mathbf{f}_s = -p\,\mathbf{n} \qquad \text{on } \Gamma, \tag{4.6}$$

where p is the fluid pressure. In the fluid, ϕ denotes the total velocity potential, $\mathbf{g}$ is the gravity, ξ_P is the water depth at the considered point P, and the space-independent function C is obtained when integrating the Bernoulli equation (see Appendix C.2.5).

4.2.1 Boundary element method for the Laplace equation

We choose to use the BEM to solve the fluid part of the problem. In Section 2.2, we presented the theory of boundary integral equations (BIEs) for 3D acoustics. The boundary integral equation for the Laplace equation is obtained following similar steps, except they are a bit simpler because the equation is time-independent. In the end, the integral equation for the velocity potential ϕ, on the regular boundary Γ, analogous to (2.16), for a fixed time $t \in [0, T]$, holds as (Banerjee, 1994; Bonnet, 1999)

$$\tfrac{1}{2}\phi(\mathbf{y}, t) - \mathcal{H}_0\{\phi(t)\}(\mathbf{y}) + \mathcal{G}_0\Big\{\frac{\partial \phi(t)}{\partial n}\Big\}(\mathbf{y}) = 0 \qquad \mathbf{y} \in \Gamma\,, \tag{4.7}$$

in terms of its Dirichlet and Neumann traces on Γ, where $\mathcal{G}_0\{f\}$ and $\mathcal{H}_0\{g\}$ are the single-layer and double-layer potentials with densities f, g, analogous to (2.15),

$$\mathcal{G}_0\{f\}(\mathbf{y}) = \int_\Gamma G_0(\mathbf{x}-\mathbf{y}) f(\mathbf{x})\, \mathrm{d}\Gamma_x, \qquad \mathcal{H}_0\{g\}(\mathbf{y}) = \int_\Gamma \frac{\partial G_0}{\partial n}(\mathbf{x}-\mathbf{y}) g(\mathbf{x})\, \mathrm{d}\Gamma_x.$$

In the above definitions, G_0 is the *free space fundamental solution* of the Laplace equation, given by

$$G_0(\mathbf{x}-\mathbf{y}) = \frac{1}{4\pi r}\,, \qquad r := \|\mathbf{x}-\mathbf{y}\|.$$

The BEM presented in Section 2.4.1 is compatible with the Laplace equation, and (4.7) leads to a system of generic form (2.28)

$$[\mathbf{H_0}]\{\boldsymbol{\phi}\} = [\mathbf{G_0}]\{\mathbf{Q}\}\,, \tag{4.8}$$

where the N-vectors $\{\boldsymbol{\phi}\}$ and $\{\mathbf{Q}\}$ are the discretised traces of ϕ and $-\partial_n\phi$ on the discretised boundary, and $[\mathbf{G_0}]$, $[\mathbf{H_0}]$ are $N \times N$ matrix discretisations of $\mathcal{G}_0$ and $\mathcal{I}/2 - \mathcal{H}_0$, respectively. For discrete time instants $\{0, \Delta t, \dots T = M\Delta t\}$, the fluid part of the problem then reduces to M BEM problems (4.8), the dependence in time manifesting itself through the evolving value of the Neumann datum.

4.2.2 Step-by-step FEM/BEM coupling procedure

To solve the FSI problem (4.5), we choose[2] a rather common procedure: a FEM/BEM step-by-step coupling. As briefly explained in Section 3.1.2, the set of coupled equations (4.5) is divided into two sets of equations: the structure part (4.5a) and the fluid part (4.5b). The procedure consists in solving, at each time step t_n, the fluid and structure equations in an uncoupled way. The fluid ($s^0_{\mathcal{F}}(t_n)$) and structure ($s^0_{\mathcal{S}}(t_n)$) solutions obtained do not *a priori* correspond to the solution of the coupled FSI problem ($s_{\mathcal{F}}(t_n), s_{\mathcal{S}}(t_n)$). To find the correct coupled FSI solution, we resort to an iterative process termed *sub-cycling*.

Sub-cycling. The fluid quantities at a time instant t_n depend on the structure ones at t_n, and *vice versa*. Therefore, independently solving structure and fluid equations requires cycling at each time step (Felippa et al., 2001; Véron, 2016). This notion is described on Figure 4.1. It begins with an initial guess (based on the values at the previous time instants) for the velocity at t_n, denoted $\mathbf{v}^0_n$. Solving the fluid equations (4.5b) provides p^0_n, which, through the dynamic condition of continuity ($\mathcal{DC}$), is used to solve the structure equations

[2] Our choice is motivated by the coupling flexibility: it easily permits to couple a BEM solver dealing with the fluid part to any industrial FEM solver for the structure part (we use Abaqus® in this thesis, see Section 2.1).

(4.5a). This provides a new value of the velocity, denoted $\mathbf{v}_n^1$, that may differ from $\mathbf{v}_n^0$. The procedure consists in cycling, i.e., alternately solve fluid and structure equations, at the same time instant, until a stagnation convergence criterion is satisfied, e.g., until a relative error between the accelerations $\mathbf{a}_n^k$ and $\mathbf{a}_n^{k+1}$ is below a pre-fixed tolerance ε_{sc}.

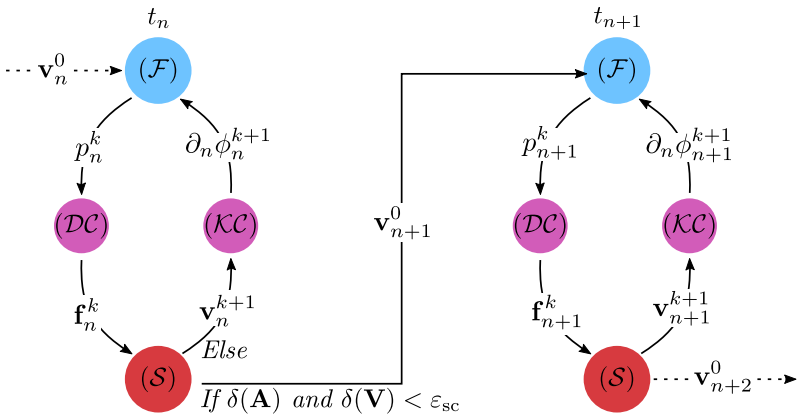

Figure 4.1: Sub-cycling scheme used for the iterative procedure to solve the FSI problem.

The initial guess $\mathbf{v}_n^0$ is of great importance, because a good guess can drastically reduce the number of sub-cycles, denoted N_{sc}, and so the computation time of the procedure.

This sub-cycling at each time step is the key part of step-by-step procedures: the gain obtained both in terms of algorithmic complexity and ease of implementation, compared to monolithic procedures, may be spoiled because of a difficult, perhaps impossible, sub-convergence at each time step. Also, given the large amount $M\,N_{\text{sc}}$ of fluid and structure problem to be solved, the algorithm is viable only if each solution is cheap. For the fluid part, this, in general, requires an acceleration technique.

4.3 Accelerating the fluid BEM solving

When dealing with incompressible flows, the BE mesh representing the fluid-structure interface Γ does not need to be as refined as in the shock wave case. Indeed, in acoustics, the characteristic element size must be small relative to the typical wavelength of the problem, whereas in the framework of incompressible flow, where information is transmitted instantaneously, the mesh size is not subject to such constraints. Its only requirement is to be small enough to well represent the structure geometry (and the structure dynamic response in the FSI context). In our context, with a submarine facing a gas bubble, the typical order of magnitude of the number of fluid DOFs is $N \sim 10^4$ to 10^5, and $M \sim 10^3$ to 10^4. Solving 10^3 BEM problems with 10^5 DOFs each is not so easy however, and is indeed very costly if the BEM operators have to be re-computed at each time step. Hence, it is important to avoid re-computation of BEM operators at each time step.

4.3.1 Re-using BEM operators

The purpose of this section is to explain to what extent the BEM operators may be re-used at each time step. Let $\Gamma \equiv \Gamma(t)$ and $\Gamma_0 \equiv \Gamma(0)$ respectively denote the current and initial configurations of the fluid-structure interface, and let $\boldsymbol{\Phi}$ be the deformation taking Γ_0 to Γ (see Figure 4.2). Using a Lagrangian description and omitting the time variable t, the

current position $\mathbf{x}$ on Γ of a material point is related to its initial position $\hat{\mathbf{x}}$ on Γ_0 through

$$\mathbf{x} = \boldsymbol{\Phi}(\hat{\mathbf{x}}) \qquad (\hat{\mathbf{x}} \in \Gamma_0,\ \mathbf{x} \in \Gamma).$$

In practice, $\boldsymbol{\Phi}$ is (approximately) known by sequentially updating the interface, using the converged kinematic response of the structure at each time step.

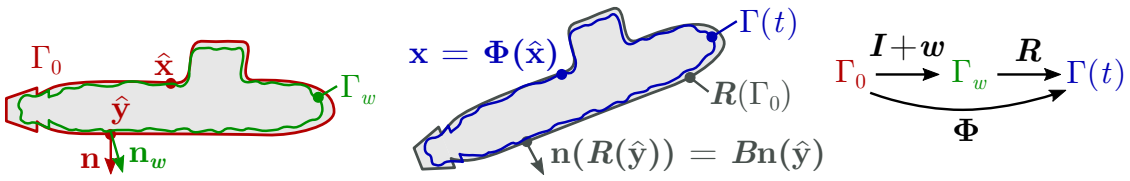

Figure 4.2: Decomposition of the displacement into rigid and deformation (strain) motions, notations.

To cater for a potentially significant rigid-body contribution to the interface deformation, $\boldsymbol{\Phi}$ is assumed to have the form

$$\boldsymbol{\Phi} = \boldsymbol{R} \circ (\boldsymbol{I} + \boldsymbol{w}), \quad \text{i.e.,} \quad \mathbf{x} = \boldsymbol{R}(\hat{\mathbf{x}} + \boldsymbol{w}(\hat{\mathbf{x}})) \qquad (\hat{\mathbf{x}} \in \Gamma_0, \mathbf{x} \in \Gamma), \tag{4.9}$$

where $\boldsymbol{w}$ is a displacement field while $\boldsymbol{R}$ describes a rigid-body motion. Any rigid-body motion is given by

$$\boldsymbol{R}(\mathbf{x}) = \boldsymbol{R}[\boldsymbol{c}, \boldsymbol{B}](\mathbf{x}) = \boldsymbol{c} + \boldsymbol{B}\mathbf{x}$$

in terms of a translation vector $\boldsymbol{c} \in \mathbb{R}^3$ and a rotation matrix $\boldsymbol{B} \in \mathbb{R}^{3\times 3}$ satisfying $\boldsymbol{B}^{\mathrm{T}}\boldsymbol{B} = \boldsymbol{B}\boldsymbol{B}^{\mathrm{T}} = \boldsymbol{I}$ and $\mathrm{Det}(\boldsymbol{B}) = 1$, and is thus determined by 6 scalar parameters.

The decomposition (4.9) can be defined with $\boldsymbol{R}$ chosen arbitrarily, without particular relation to the motion $\boldsymbol{\Phi}$. A sensible choice for $\boldsymbol{R}$, for a given motion $\boldsymbol{\Phi}$, may be defined by the minimisation problem

$$\min_{\boldsymbol{c},\boldsymbol{B}} \int_{\Gamma_0} \|\boldsymbol{\Phi}(\mathbf{x}) - \boldsymbol{R}[\boldsymbol{c}, \boldsymbol{B}](\mathbf{x})\|^2 \,\mathrm{d}S\,,$$

which (since $\|\boldsymbol{\Phi}(\mathbf{x}) - \boldsymbol{R}(\mathbf{x})\| = \|\boldsymbol{w}(\mathbf{x})\|$) aims at making the non-rigid displacement $\boldsymbol{w}$ smallest (in the $L^2(\Gamma_0)$ norm sense).

The current velocity potential $\phi = \phi(\cdot, t)$ is governed by the BIE (4.7) written on the current surface Γ. To ascertain the effect of the interface motion on the BIE, we reformulate it on the fixed (initial) surface Γ_0 by setting $\mathbf{x} = (\boldsymbol{R} \circ (\boldsymbol{I} + \boldsymbol{w}))(\hat{\mathbf{x}})$ and introducing the convected versions on Γ_0 of the Neumann datum and unknown potential, respectively given by $\hat{h} := h \circ \boldsymbol{\Phi}$ and $\hat{\phi} := \phi \circ \boldsymbol{\Phi}$. This reformulation relies on the key observations that we have

$$\mathbf{n}(\boldsymbol{R}(\hat{\mathbf{y}})) = \boldsymbol{B}\mathbf{n}(\hat{\mathbf{y}}), \qquad \mathrm{d}S(\boldsymbol{R}(\hat{\mathbf{y}})) = \mathrm{d}S(\hat{\mathbf{y}})$$

and, by virtue of the isotropy and translational invariance of the kernel G_0,

$$G_0(\boldsymbol{R}(\hat{\mathbf{y}}) - \boldsymbol{R}(\hat{\mathbf{x}})) = G_0(\hat{\mathbf{y}} - \hat{\mathbf{x}}), \qquad \mathbf{n}(\boldsymbol{R}(\hat{\mathbf{y}})) \cdot \nabla_{\boldsymbol{R}} G_0(\boldsymbol{R}(\hat{\mathbf{y}}) - \boldsymbol{R}(\hat{\mathbf{x}})) = \mathbf{n}(\hat{\mathbf{y}}) \cdot \nabla G_0(\hat{\mathbf{y}} - \hat{\mathbf{x}})$$

for any rigid-body motion $\boldsymbol{R}$. As a result, the BIE (4.7) is recast as

$$\begin{aligned} \frac{1}{2}\hat{\phi}(\hat{\mathbf{x}}) - \int_{\Gamma_0} \mathbf{n}_w(\hat{\mathbf{y}}) \cdot \nabla G_0\big(\hat{\mathbf{y}} - \hat{\mathbf{x}} + \boldsymbol{w}(\hat{\mathbf{y}}) - \boldsymbol{w}(\hat{\mathbf{x}})\big)\, \hat{\phi}(\hat{\mathbf{y}}) J(\hat{\mathbf{y}})\, \mathrm{d}S(\hat{\mathbf{y}}) \\ = \int_{\Gamma_0} G_0\big(\hat{\mathbf{y}} - \hat{\mathbf{x}} + \boldsymbol{w}(\hat{\mathbf{y}}) - \boldsymbol{w}(\hat{\mathbf{x}})\big)\, \hat{h}(\hat{\mathbf{y}}) J(\hat{\mathbf{y}})\, \mathrm{d}S(\hat{\mathbf{y}}), \end{aligned} \tag{4.10}$$

wherein $J := \|(\boldsymbol{I}+\nabla\boldsymbol{w})^{-\mathrm{T}}\mathbf{n}\|\,\mathrm{Det}(\boldsymbol{I}+\nabla\boldsymbol{w})$ is the surface Jacobian of the mapping $\boldsymbol{I}+\boldsymbol{w}$ taking Γ_0 to Γ_w (Henrot and Pierre, 2018, Def. 5.4.2) and $\mathbf{n}_w := (\boldsymbol{I}+\nabla\boldsymbol{w})^{-\mathrm{T}}\mathbf{n} \,/\, \|(\boldsymbol{I}+\nabla\boldsymbol{w})^{-\mathrm{T}}\mathbf{n}\|$ is the unit normal on Γ_w (Henrot and Pierre, 2018, Prop. 5.4.14). Equation (4.10) is readily seen to be the BIE formulation of the potential flow problem in the domain Ω_w exterior to the deformed surface Γ_w defined by

$$\Delta\hat{\phi}_w = 0 \;\text{ in } \Omega_w, \qquad \partial_n\hat{\phi}_w = \hat{h}_w \;\text{ on } \Gamma_w, \qquad |\hat{\phi}_w(\mathbf{x})| = O(|\mathbf{x}|^{-2}) \;\text{ at infinity,} \tag{4.11}$$

where $\hat{\phi}_w := \hat{\phi}\circ(\boldsymbol{I}+\boldsymbol{w})^{-1} = \phi\circ\boldsymbol{R}$ and $\hat{h}_w := \hat{h}\circ(\boldsymbol{I}+\boldsymbol{w})^{-1} = h\circ\boldsymbol{R}$ are the convected versions on Γ_w of $\hat{\phi}$ and $\hat{h}$. In other words, solving the BIE (4.7) is equivalent to solving the BIE (4.10) or the exterior boundary-value problem (4.11), with $\boldsymbol{R}$ and $\boldsymbol{w}$ determined from $\boldsymbol{\Phi}$ on the basis of (4.9).

In practice, to allow re-usability of integral operators while Γ evolves under the time-stepping procedure, we solve problem (4.7) approximately by setting $\boldsymbol{w} = \mathbf{0}$ in (4.10), seeking $\hat{\phi}_0$ which satisfies

$$\frac{1}{2}\hat{\phi}_0(\hat{\mathbf{x}}) - \int_{\Gamma_0}\mathbf{n}(\hat{\mathbf{y}})\cdot\nabla G_0(\hat{\mathbf{y}}-\hat{\mathbf{x}})\,\hat{\phi}_0(\hat{\mathbf{y}})\,\mathrm{d}S(\hat{\mathbf{y}}) = \int_{\Gamma_0} G_0(\hat{\mathbf{y}}-\hat{\mathbf{x}})\,\hat{h}(\hat{\mathbf{y}})\,\mathrm{d}S(\hat{\mathbf{y}}),$$

and setting $\phi_0 := \hat{\phi}_0\circ\boldsymbol{\Phi}$ as the approximate solution of (4.7), i.e., $\phi_0 \approx \phi$. The potential $\hat{\phi}_0$ equivalently solves the exterior boundary-value problem (4.11) with $\boldsymbol{w} = \mathbf{0}$.

The issue of estimating the difference $\hat{\phi}_w - \hat{\phi}_0$, i.e., the approximation error $\phi - \phi_0$ incurred by re-using the integral operators defined on Γ_0, is addressed by the theory of shape differentiation of boundary-value problems (Henrot and Pierre, 2018). Under sufficient regularity of Γ_0 and h, solutions $\hat{\phi}_w$ of interior boundary value problems similar to (4.11) are shown to be differentiable with respect to $\boldsymbol{w}$ in a neighbourhood of $\boldsymbol{w} = \mathbf{0}$ (at which the approximation $\hat{\phi}_0$ is evaluated), the relevant norm for $\boldsymbol{w}$ being the $W^{1,\infty}$ norm defined (on extensions to $\mathbb{R}^3$ of $\boldsymbol{w}$) by

$$\|\boldsymbol{w}\|_{1,\infty} := \sup_{\mathbf{x},\mathbf{y}\in\mathbb{R}^3,\,\mathbf{y}\neq\mathbf{x}}\left(|\boldsymbol{w}(\mathbf{y})| + \frac{|\boldsymbol{w}(\mathbf{y})-\boldsymbol{w}(\mathbf{x})|}{|\mathbf{y}-\mathbf{x}|}\right).$$

This implies an approximation error that is linear in $\|\boldsymbol{w}\|_{1,\infty}$, an acceptable approximation when the non-rigid part $\boldsymbol{w}$ of the interface displacement and its strain are small.

To conclude, under the assumptions that the non-rigid displacement and its strain are small (but no assumption on the rigid motion), the BEM operators computed at the initial time step can be re-used to obtain the solution at the following time steps. In our context, according to UNDEX experts, the local deformation is expected to be small (Liu et al., 2018). However, it is known that a submarine facing an UNDEX bubble shows bending deformation (Zhang et al., 2011). This bending could compel us to update the BE mesh. Then, we could for instance choose to update the latter whenever the deformation (or its strain) is greater than a user-specified tolerance. Hopefully, the mesh updates will not occur at each time step.

Remark 21 *In future work, if the free water surface or/and the sea bed are considered, the derivation performed in this section is no longer valid for a generic rigid motion $\boldsymbol{R}$, and so the BEM operators should a priori be re-computed at each time step. Some specific rigid motions (typically if the submarine translates parallel to the water surface) may all the same allow to re-use the BEM operators.*

4.3.2 Appropriate BEM acceleration techniques

The Fast Multipole Method (FMM), introduced in Section 2.4.2, is a very efficient technique in the context of the Helmholtz equation (linear acoustics). The $\mathcal{Z}$-BEM procedure we designed in Chapter 2 to deal with the shock wave phenomenon requires about 50-100 BEM solutions in practice. In this context, each BEM problem, involving different BEM operators because the latter are frequency-dependent, can be efficiently solved using the Fast Multipole BEM (FM-BEM). For the gas bubble phenomenon, a quite larger number of BEM problems must be solved, but the BEM operators are time-independent. Under the assumptions specified above in Section 4.3.1, using the same BEM operators for all BEM problems is a reasonable approximation. The fluid part of the FSI problem then consists in solving a set of problems $[\mathbf{H_0}]\{\boldsymbol{\phi}(t)\} = [\mathbf{G_0}]\{\mathbf{Q}(t)\}$ with fixed BEM matrices $[\mathbf{H_0}]$ and $[\mathbf{G_0}]$. Such problems are termed multiple right-hand side (Simoncini and Gallopoulos, 1995), as only the right-hand side (and of course the solution) differs from one problem to another. An efficient way to deal with multiple right-hand side problems is to compute and store the BEM operators once and for all when solving the first BEM system. Then, these operators may be re-used for each problem, to compute the matrix-vector product required in the GMRES method (we use again GMRES (Saad and Schultz, 1986) for the oscillating bubble phenomenon). The FM-BEM is not well suited for dealing with multiple right-hand sides, because it does not store/assemble the matrices, implying that matrix-vector product sequences must be computed anew for each BEM problem. Standard BEMs do compute and store the matrices, so they could be used in the context of multiple right-hand side problems, but at prohibitive computing and memory costs. An acceleration technique alternative to the FMM, namely the $\mathcal{H}$-matrix method, turns out to be much better suited to multiple right-hand sides.

4.3.3 $\mathcal{H}$-matrix based accelerated Boundary Element Method

As just explained, the use of an $\mathcal{H}$-matrix BEM solver is motivated by the time-independence of the BEM operators. This section, largely inspired from (Chaillat et al., 2017b), briefly presents the concept of hierarchical matrices ($\mathcal{H}$-matrices) and the adaptive cross approximation (ACA). One of the main advantage of the $\mathcal{H}$-matrices, compared to the FMM, is that a compressed representation of the BEM matrices can actually be stored. This compressed form can notably be used for preconditioning strategies (Amlani et al., 2019; Kpadonou et al., 2020), and also re-used when dealing with multiple systems with the same BEM operator (Bebendorf, 2008).

In the following, the numerical rank of a matrix $\mathbb{A} \in \mathbb{R}^{N\times N}$ is defined as

$$r(\varepsilon) := \min_{0\leq r\leq N} \{\|\mathbb{A} - \mathbb{A}_r\| \leq \varepsilon \|A\|\},$$

where $\mathbb{A}_r$ denotes the truncated singular value decomposition (SVD) of $\mathbb{A}$ where only the singular vectors associated to the r largest singular values are kept, and $\varepsilon > 0$ is a given tolerance.

$\mathcal{H}$-matrix representation. Originally introduced by Hackbush (Hackbusch, 1999), $\mathcal{H}$-matrices aim at computing a data-sparse representation of some special dense matrices (e.g., those resulting from discretisation of non-local operators). The principle is to (i) partition a fully-populated matrix into blocks and (ii) perform low-rank approximations on those *a priori* known (using an admissibility criterion) to be well suited for such decompositions. Typically, the off-diagonal blocks produced by the partition process are expected to undergo

compression (see Figure 4.3). The low-rank representations of those blocks reduce both memory requirements and CPU times of a matrix-vector product, making the $\mathcal{H}$-matrix method a powerful tool for fast iterative solvers, where the time-consuming step is precisely the matrix-vector product. Also, $\mathcal{H}$-matrix arithmetic allows to derive fast direct solvers.

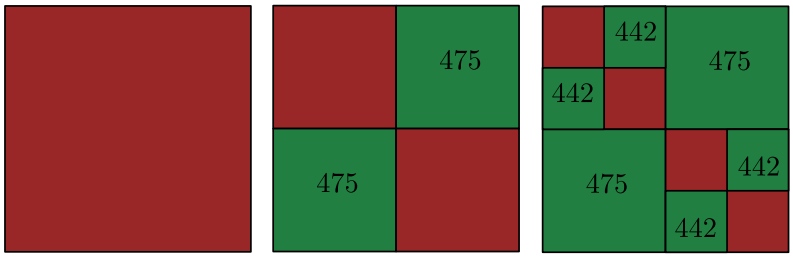

Figure 4.3: Example of computed numerical ranks of each block of the Green's tensor of the Navier equation, to achieve an accuracy of 10^{-4}, i.e., if singular values smaller than 10^{-4} are neglected in the singular value decomposition. The number in a green block is its numerical rank. From (Chaillat et al., 2017b).

Clustering of the unknowns. A prior step to the partition of the matrix (denoted $\mathbb{A}$ in the following) is a re-arrangement of its row and column indices, to reflect the physical distance in the matrix (i.e., consecutive indices of $\mathbb{A}$ should correspond to close geometrical entities). To do so, a simple approach consists in building a binary cluster tree $\mathcal{T}_I$ of indices corresponding, at each level, to a geometric partition of the object (Hackbusch, 2015), as illustrated in Figure 4.4.

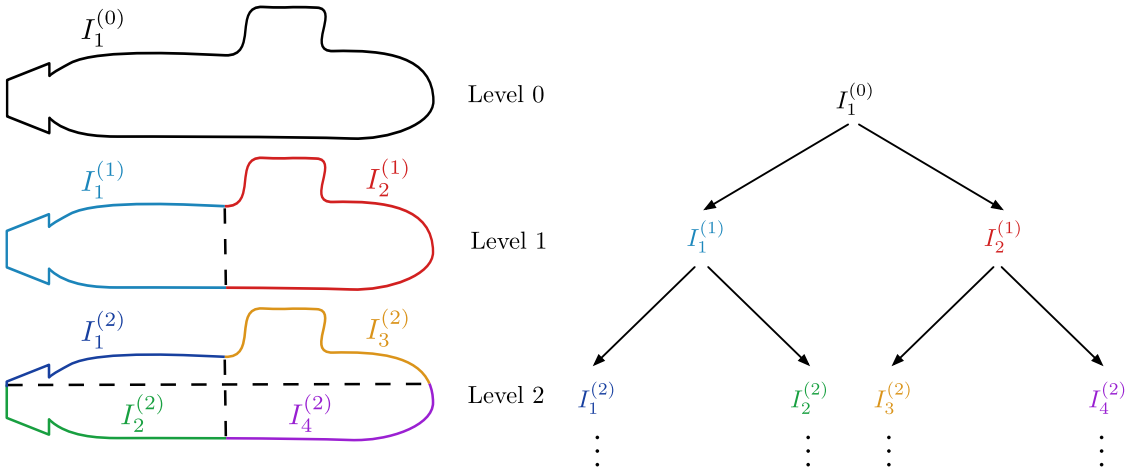

(a) Partition of the physical domain (b) Binary cluster tree $\mathcal{T}_I$

Figure 4.4: Illustration of the clustering of the degrees of freedom: (a) partition of the DOFs of a submarine, and (b) corresponding binary tree. After (Chaillat et al., 2017b).

Subdivision of the matrix. Following this clustering of the unknowns, a block cluster representation $\mathcal{T}_{I\times I}$ of the matrix $\mathbb{A}$ is defined by associating each set of indices $I_k^{(l)}$ of the

cluster tree $\mathcal{T}_I$ to the other set of indices. Hence, each node of $\mathcal{T}_{I\times I}$ is composed of a pair (σ,τ) of indices of $\mathcal{T}_I$, so of the form $\left(I_k^{(l)}, I_{k'}^{(l)}\right)$, and defines a block of $\mathbb{A}$ (see Figure 4.5).

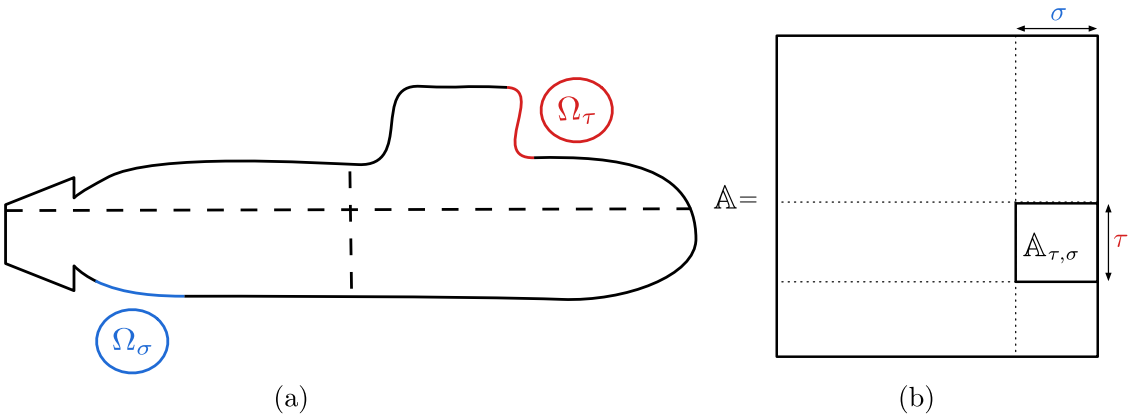

Figure 4.5: Illustration of the construction of the block cluster tree: (a) clustering of the unknowns on the geometry and (b) corresponding block clustering in the matrix. After (Chaillat et al., 2017b).

Considering only the leaf level L, i.e., only the nodes (σ,τ) of the form $\left(I_k^{(L)}, I_{k'}^{(L)}\right)$, provides a uniform partition $\mathcal{U} \subset \mathcal{T}_{I\times I}$ that defines a block structure of $\mathbb{A}$ with a full pattern of 4^{L-1} blocks (see Figure 4.6a). However, Figure 4.3 shows this partition is not optimal. Indeed, some parts of $\mathbb{A}$, and especially off-diagonal blocks, can accurately be approximated by a low-rank matrix at a non-leaf level (i.e., for larger clusters). Such blocks are said to be *admissible*. Then, a more appropriate hierarchical representation $\mathcal{P} \subset \mathcal{T}_{I\times I}$ may be obtained as follows: from the highest (0) level, and its unique node $\left(I_1^{(0)}, I_1^{(0)}\right)$ representing the full matrix, each block is recursively subdivided until it is either admissible or a node of the leaf level (see Figure 4.6b). For complex 3D geometries, an admissibility condition, based on the geometry and the interaction distance between the points, is used to determine *a priori* the admissible blocks.

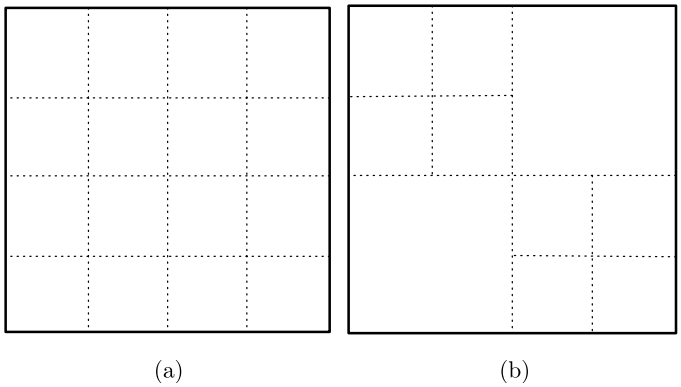

Figure 4.6: (a) Block cluster representation $\mathcal{T}_{I\times I}$ for the illustrative example (full structure); (b) hierarchical partition $\mathcal{P} \subset \mathcal{T}_{I\times I}$ of the same matrix based on the admissibility condition (sparse structure). From (Chaillat et al., 2017b).

A well-adapted method to the Laplace Green's function. $\mathcal{H}$-matrix representations do not result in efficient algorithms for all matrices. The crucial part is to know *a*

priori (i) if savings will be obtained when trying to approximate admissible blocks with a sum of rank-one matrices (tensor products of two vectors), and (ii) which blocks are admissible, without explicit computation of the rank of all the blocks, which would be too expensive. For asymptotically smooth kernels $G(\mathbf{x}, \mathbf{y})$, it is proved that, under some *a priori* conditions on the distance between $\mathbf{x}$ and $\mathbf{y}$, the kernel is a degenerate function (i.e., it is well approximated by a finite sum of functions with separated variables) (Chaillat et al., 2017b). This property leads, after discretisation, to the efficient approximation of blocks of the matrix by low-rank matrices. The Laplace Green's function, that we use in this chapter, is an example of asymptotically smooth kernel for which the $\mathcal{H}$-matrix method is very efficient.

Low-rank approximation algorithm. Various algorithms are available to compute the low-rank approximation of the admissible blocks previously identified. The truncated Singular Value Decomposition (SVD) (Golub and Van Loan, 1996) gives the best low-rank approximation (Eckart-Young theorem) for unitary invariant norms (e.g., Frobenius or spectral norms), in the sense that it produces an approximation with the smallest possible numerical rank for a given prescribed accuracy ε. However, the SVD requires the computation of all the entries of $\mathbb{A}$, and its complexity, of the order of $O(N^3)$ for a $N \times N$ matrix, hinders its use for large-scale problems.

On the other hand, the Adaptive Cross Approximation (ACA) (Bebendorf et al., 2015; Bebendorf and Rjasanow, 2003) provides a quasi-optimal low-rank approximation without the need to assemble the complete block. Based on the fact that a matrix of rank r is the sum of r matrices of rank 1, the ACA is an iterative algorithm that improves an approximation $\mathbb{B}_k$ of the matrix $\mathbb{A}$ by adding rank-1 matrices:

$$\mathbb{B}_k = \sum_{l=1}^{k} \mathbf{u}_l \mathbf{v}_l^* = \mathbb{U}_k \mathbb{V}_k^* , \qquad \mathbb{U}_k, \mathbb{V}_k \in \mathbb{C}^{N \times k}.$$

The purpose is to iteratively shift the information from the residual $\mathbb{R}_k = \mathbb{A} - \mathbb{B}_k$ to the next approximation $\mathbb{B}_{k+1}$. A stopping criterion is used to determine the appropriate numerical rank, for instance until

$$\|\mathbb{A} - \mathbb{B}_k\|_{\mathrm{F}} \leq \varepsilon_{\mathrm{ACA}} \|A\|_{\mathrm{F}} ,$$

where $\|\cdot\|_{\mathrm{F}}$ denotes the Frobenius norm, and $\varepsilon_{\mathrm{ACA}} > 0$ is a given parameter. We denote r_{ACA} the numerical rank obtained by the ACA for a required accuracy $\varepsilon_{\mathrm{ACA}}$. Various ACAs, that differ by the choice of the best pivot at each iteration, are available. The fully-pivoted ACA consists in choosing the pivot as the largest entry in the residual. Similarly to the SVD, it requires the computation of all the entries of $\mathbb{A}$, and is therefore not suitable for the practical construction of $\mathcal{H}$-matrices. On the other hand, the partially-pivoted ACA proposes an alternative approach that do not require the assembly of the complete matrix. The idea is to maximise alternately the residual for only one of the two indices, the other being kept fixed, so that only one row and one column are evaluated at each iteration. The details on the resulting algorithm may be found in (Chaillat et al., 2017b). The complexity of the partially-pivoted ACA is reduced to $O\left(r_{\mathrm{ACA}}^2 (m+n)\right)$ for a $m \times n$ matrix $\mathbb{A}$, whereas the complexity of the fully-pivoted one is $O\left(r_{\mathrm{ACA}} mn\right)$.

The BEM code COFFEE developed at POEMS, whose FMM accelerated part was introduced in Chapter 2, offers an $\mathcal{H}$-matrix accelerated BEM solver (Chaillat et al., 2017b; Kpadonou et al., 2020) that uses the partially-pivoted ACA, and iteratively solve the BEM problem with a GMRES algorithm.

4.4 Summary: numerical methodology

We now summarise the step-by-step FEM/BEM coupling procedure.

Initialisation. The initialisation of the method concerns the first sub-cycle ($k = 0$) of the first time step ($n = 0$). The procedure starts with the fluid part, setting the structure normal velocity on Γ according to the initial conditions, so $u_0^0 = 0$ for initial rest. The $\mathcal{H}$-BEM operators are computed and stored, then the coupling procedure starts.

Coupling procedure steps. At each time step t_n, at sub-cycling iteration k, the following steps are carried out:

- **Estimate the structure normal velocity** u_n^k based on previous values
$$\left\{u_n^{k-1}, u_n^{k-2}, \dots, u_{n-1}, u_{n-2}, \dots\right\}.$$
- **Evaluate the ambient flow and its normal derivative** on the updated surface Γ_n^k.
- **Compute the Neumann datum** for the fluid part, using the ambient flow and the structure normal velocity.
- **Check whether the strains are sufficiently low**, according to a pre-fixed tolerance ε_Γ, and either **update the fluid-structure interface and recompute the BEM operators**, or **re-use the already computed BEM operators**.
- **Solve the $\mathcal{H}$-BEM problem to get $\boldsymbol{\phi}^{\mathbf{per}}$** for a given GMRES tolerance $\varepsilon_{\text{GMRES}}$ and $\mathcal{H}$-matrix threshold $\varepsilon_{\mathcal{H}}$.
- **Evaluate $\nabla\boldsymbol{\phi}^{\mathbf{tot}}$**: compute the surface gradient $\nabla_s\phi^{\text{tot}}$ and add the already known value of $\partial_n\phi^{\text{tot}}$. For the tangential part of $\nabla\phi^{\text{tot}}$, the surface gradient is obtained through a common FEM procedure: ϕ^{tot} is reconstructed on the surface (from nodal values) using linear shape functions, then the tangential part $\nabla_s\phi^{\text{tot}}$ is obtained using the gradient of the shape functions (Schotté, 2001).
- **Compute $\boldsymbol{\partial_t\phi}^{\mathbf{tot}}$**: the numerical derivative is computed using the backward differentiation formula of order 4 (bdf4), except for the first time steps, where bdf1, bdf2 or bdf3 are used, whenever enough past values are available.
- **Compute $\boldsymbol{p}$** using the Bernoulli equation (4.4).
- **Compute the nodal forces $\mathbf{f}$**: the integration over the surface is performed using linear shape functions to reconstruct p on the surface from the nodal values (Véron, 2016).
- **Solve the structure equations** using the FEM.
- **Check the stagnation convergence criterion**, for a pre-fixed tolerance ε_{sc}. If it is converged, **advance to the next time step**. Else, **continue sub-cycling**, i.e., go back to the first step.

For the numerical examples presented in this chapter, we define the relative $L^2(\Gamma)$ error of a scalar function $f(\mathbf{x}, t)$ at a given time t by

$$\delta_{L^2}(f)(t) = \frac{\sqrt{\int_\Gamma (f_{\text{ref}}(\mathbf{x},t) - f_{\text{comp}}(\mathbf{x},t))^2 \mathrm{d}S}}{\sqrt{\int_\Gamma f_{\text{ref}}(\mathbf{x},t)^2 \mathrm{d}S}},$$

where f_{ref} is the reference value and f_{comp} is the numerically computed one. To a vector $\mathbf{v}(\mathbf{x}, t)$, we associate the matrix $\mathbf{V}$ of dimension $(M + 1) \times (L)$, with $L = 3N$ for a

three-dimensional vector, whose line n contains

$$[v_1(\mathbf{x}_1, t_n), v_2(\mathbf{x}_1, t_n), v_3(\mathbf{x}_1, t_n), v_1(\mathbf{x}_2, t_n), \ldots].$$

Then, we define the relative error $\delta(\mathbf{V})$ at discrete time t_n as

$$\delta(\mathbf{V})(t_n) = \frac{\sqrt{\sum_{p=1}^{L} (\mathbf{V}_{\text{ref}}[n,p] - \mathbf{V}_{\text{comp}}[n,p])^2}}{\sqrt{\sum_{p=1}^{L} \mathbf{V}_{\text{ref}}[n,p]^2}}. \tag{4.12}$$

When considering a uniform mesh and a scalar function f, $\delta_{L^2}(f)$ and $\delta(\mathbf{F})$ (with $L = N$) are numerically close. For the sub-cycling, we set the stagnation convergence criterion on both the acceleration and the velocity, using (4.12) as relative error to compare two successive solutions.

Before dealing with a concrete industrial case in Section 4.6, we validate the FSI BEM/FEM procedure on the problem of a rigid sphere in a uniform flow, a configuration for which analytical solutions are available.

4.5 Validation example: rigid sphere in a uniform flow

We consider the problem of a rigid sphere immersed in an infinite fluid domain, with ambient flow velocity $\nabla\phi^{\text{amb}} = U(t)\mathbf{e}_x$, for a given time-dependent velocity amplitude $U(t)$, $t \in [0, T]$. We validate first our $\mathcal{H}$-matrix based solver for the case of a motionless sphere (Section 4.5.1), and then the step-by-step coupling procedure on the case of a mobile sphere (Section 4.5.2).

4.5.1 Motionless sphere

We consider the potential flow around a motionless sphere Γ of centre O and radius a. Let $\mathcal{R}$ be a frame with origin O and x axis in the ambient flow direction (the other axes are arbitrary, see Figure 4.7). The ambient velocity potential is given at a point $P(x, y, z)$ by

$$\phi^{\text{amb}}(P, t) = U(t)x\,. \tag{4.13}$$

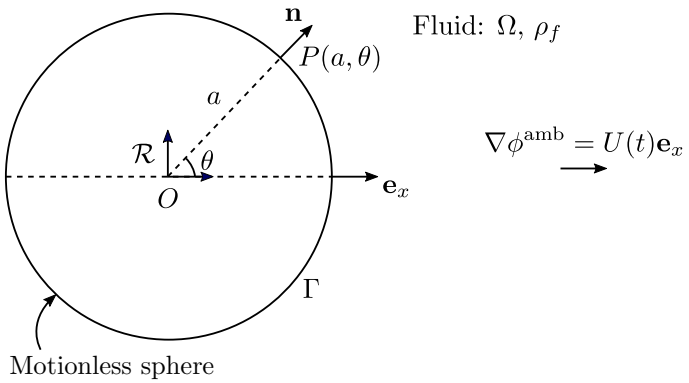

Figure 4.7: Rigid motionless sphere submerged in an infinite fluid domain, with ambient flow velocity $\nabla\phi^{\text{amb}} = U(t)\mathbf{e}_x$.

The perturbation of the flow induced by the presence of the sphere, $\phi^{\text{per}} = \phi^{\text{tot}} - \phi^{\text{amb}}$, solves the Laplace equation $\Delta\phi^{\text{per}} = 0$ with the boundary condition

$$\frac{\partial\phi^{\text{tot}}}{\partial n}(P, t) = 0 \Longrightarrow \frac{\partial\phi^{\text{per}}}{\partial n}(P, t) = -\frac{\partial\phi^{\text{amb}}}{\partial n}(P, t) = -U(t)\cos\theta\,, \quad \forall P \in \Gamma, \forall t \in [0, T]\,,$$

where θ denotes the angle between **OP** and the x axis, $\cos\theta = \mathbf{n}\cdot\mathbf{e}_x$ (see Figure 4.7).

Using the expression of the Laplacian in spherical coordinates (r,θ,φ), and looking for the solution in the form $\phi^{\text{per}}(r,\theta) = \phi_r^{\text{per}}(r)\phi_\theta^{\text{per}}(\theta)$, it comes:
$\forall (r,\theta)\in[a,+\infty[\times[0,2\pi[\,,\forall t\in[0,T]$,

$$\begin{aligned}
\phi^{\text{per}}(r,\theta,t) &= \frac{1}{2}U(t)\frac{a^2}{r^2}a\cos\theta\,, \\
\phi^{\text{tot}}(r,\theta,t) &= \frac{1}{2}U(t)\frac{a^2}{r^2}a\cos\theta + U(t)r\cos\theta\,, \\
\nabla\phi^{\text{tot}}(r,\theta,t) &= \left(1-\frac{a^3}{r^3}\right)U(t)\cos\theta\,\mathbf{e}_r - \left(1+\frac{a^3}{2r^3}\right)U(t)\sin\theta\,\mathbf{e}_\theta\,.
\end{aligned} \tag{4.14}$$

Remark 22 *The problem considered may appear "unphysical" in that the energy in the fluid is infinite. A problem quite similar, with a finite energy, is the study of the flow created by a sphere translating along the x axis with velocity $-U(t)$. In that case, ϕ^{tot} solves the Laplace equation with the boundary condition $\partial_n\phi^{tot} = -U(t)\cos\theta$ on Γ, and is therefore given by $\phi^{tot} = \phi^{per}$, i.e., (4.14) (Véron, 2016).*

If we omit the effects of gravity, the buoyant force and the hydrostatic pressure, the pressure created by the fluid on the sphere is provided by the Bernoulli equation

$$\frac{\partial\phi}{\partial t} + \frac{1}{2}|\nabla\phi|^2 + \frac{1}{\rho_f}p = C(t). \tag{4.15}$$

To compute the net force

$$\mathbf{f}(t) = f(t)\mathbf{e}_x = -\int_\Gamma p(Q,t)\mathbf{n}(Q)\mathrm{d}S_Q$$

applied on the sphere, the value of the constant $C(t)$ is irrelevant, because $\displaystyle\int_\Gamma C(t)n\,\mathrm{d}S = 0$. Then, redefining $p \equiv p - C(t)\rho_f$, it holds:
$\forall P(r=a,\theta,\varphi)\in\Gamma,\forall t\in[0,T]$,

$$\begin{aligned}
p(\theta,t) &= -\rho_f\left(\frac{3}{2}\dot{U}(t)a\cos\theta + \frac{9}{8}U(t)^2\sin(\theta)^2\right), \\
f(t) &= -\int_0^\pi p(\theta,t)\cos\theta\,2\pi a\sin\theta\mathrm{d}\theta = 2\pi\rho_f a^3\dot{U}(t).
\end{aligned}$$

Results. The following parameters are used for the numerical tests:

- $U(t) = U_0\cos(2\pi ft)$, with $U_0 = 15.0$ m/s and $f = 4$ Hz.
- $\rho_f = 1000$ kg/m^3, $a = 3$ m.
- $T = 0.5$ s, number of time steps $M = 200$ (100 time steps per period).
- For the BEM: $\varepsilon_{\text{GMRES}} = 10^{-4}$; we use $P1$ Lagrange boundary elements; the $\mathcal{H}$-matrix threshold is set to $\varepsilon_{\mathcal{H}} = 10^{-4}$. Blocks containing less than $n_{\text{leaf}} = 50$ points are considered as leaves, and therefore no longer subdivided.
- $N = 2562$ DOFs (no need to use a very refined mesh, as the only requirement is to well represent the geometry).

Figure 4.8 illustrates the fluid quantities and the net force for three different values of θ. The good agreement between analytical and computed solutions validate the procedure. Figure 4.9 allows a finer analysis of the errors, as it shows the relative error for each

quantity. The relative errors are quite low (less than 1%), except for $\partial_t \phi$ at the first time steps, because (i) the time derivative is not yet computed with the bdf4, since not enough past values are available, and (ii) the analytical value is close to zero, so the relative error is artificially high.

This simple example of a motionless sphere allows to validate the fluid part of our procedure. It shows the numerical approximations, and in particular the $\mathcal{H}$-matrix approximation with $\varepsilon_{\text{GMRES}} = 10^{-4}$ and $\varepsilon_{\mathcal{H}} = 10^{-4}$, permit errors below 1%, the latter being the target accuracy for our industrial purpose. The next step is to validate the procedure in the case of a mobile structure, allowing to test the FSI component of our procedure.

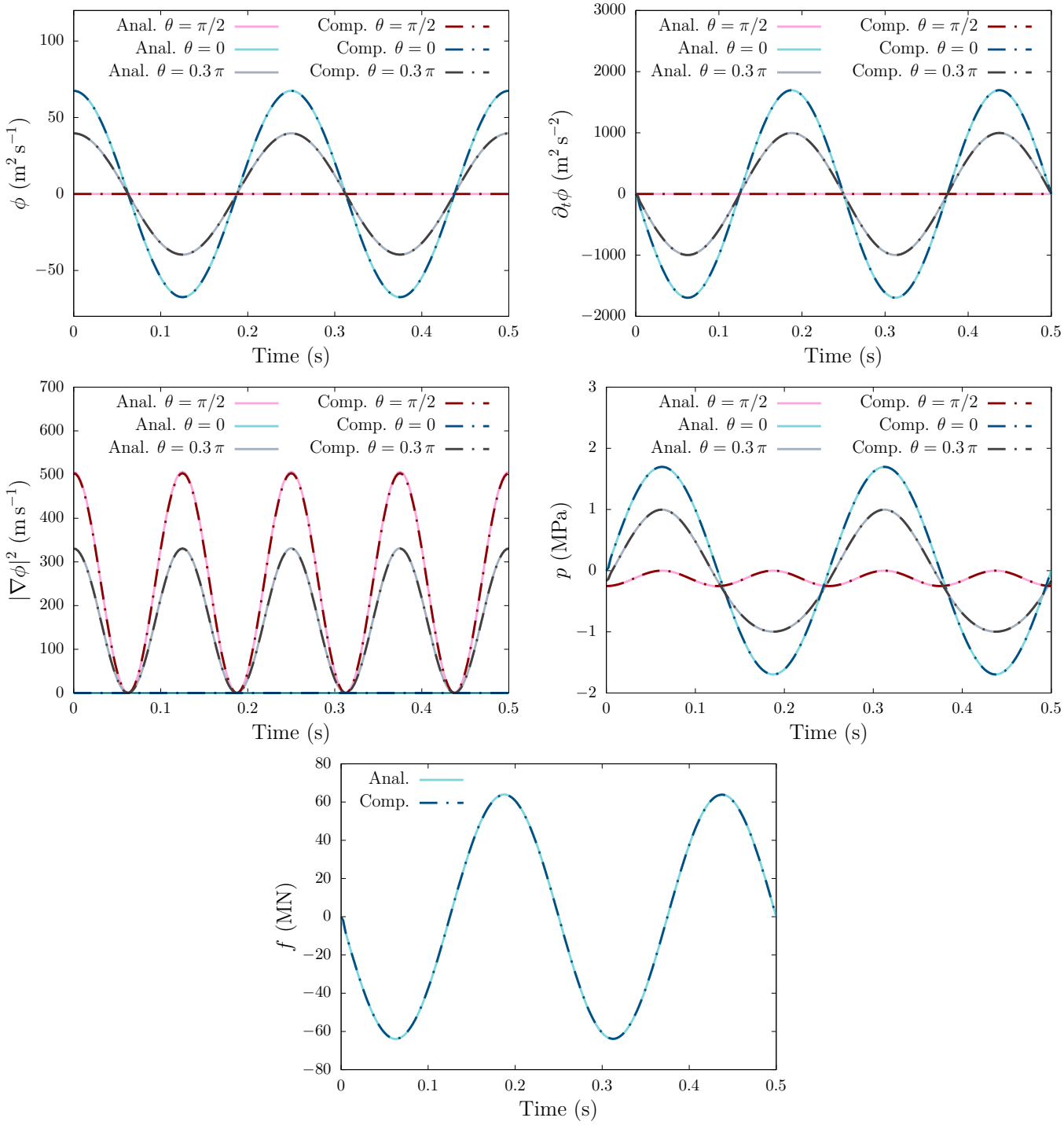

Figure 4.8: Motionless sphere: comparison between analytical and computed solutions for three different values of θ.

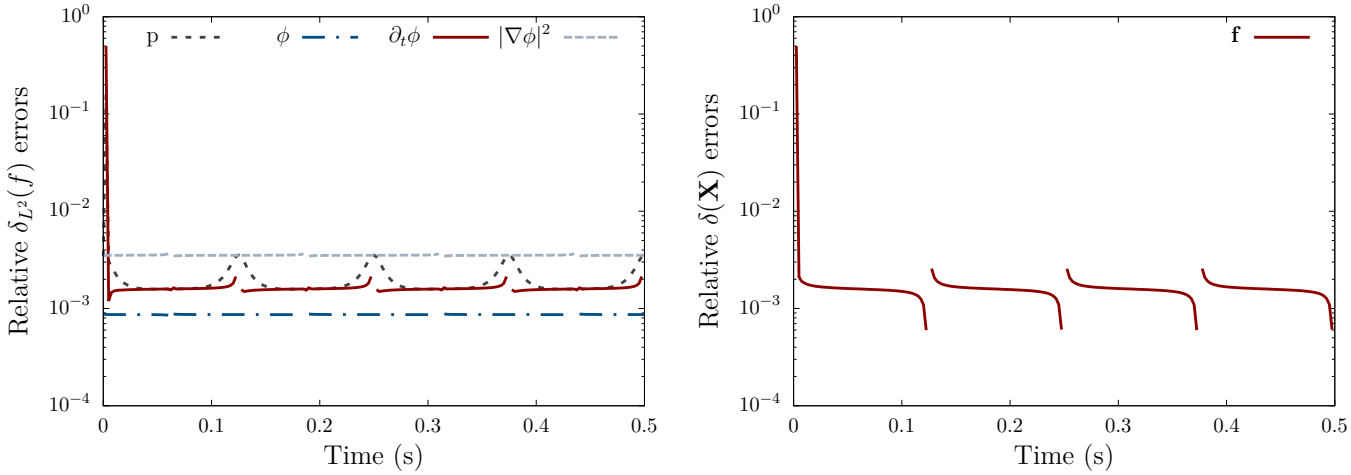

Figure 4.9: Motionless sphere: relative errors as functions of time. The relative error is not computed whenever the analytical quantity is 10^7 smaller than its maximum, to avoid division by zero.

4.5.2 Mobile rigid sphere

Our procedure must deal with strong fluid-structure interaction, i.e., when considering both the action of the fluid on the structure, and the retro-action of the latter on the fluid. Therefore, we now study the case where the rigid sphere is allowed to move (see Figure 4.10).

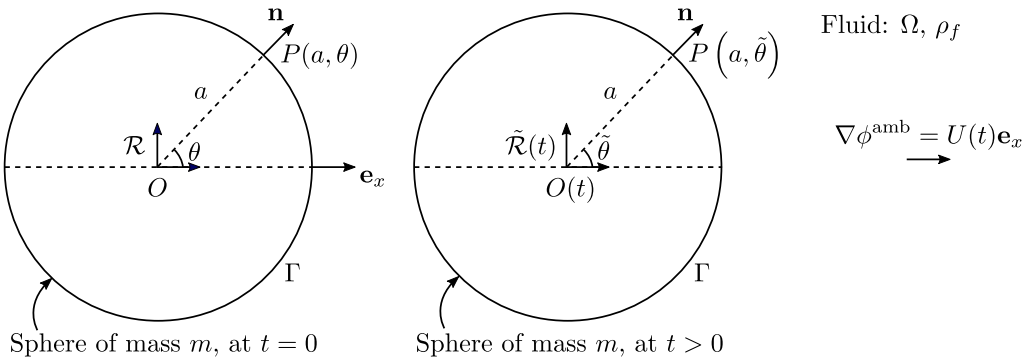

Figure 4.10: Rigid mobile sphere submerged in an infinite fluid domain, with ambient flow velocity $\boldsymbol{\nabla\phi^{\text{amb}} = U(t)\mathbf{e}_x}$.

Due to the uniaxial flow, it then moves along the x axis. In that case, we consider a moving frame $\tilde{\mathcal{R}}(t)$ with the origin following the sphere centre $O(t)$, and $\tilde{\mathcal{R}}(0) = \mathcal{R}$. The ambient velocity potential at a point $P(x,y,z)$ remains provided by (4.13). In the frame $\tilde{\mathcal{R}}(t)$, it is expressed, at the same point $P(\tilde{x},y,z)$, by

$$\phi^{\text{amb}}(x = \tilde{x} + d(t), t) = U(t)(\tilde{x} + d(t)) \equiv \psi^{\text{amb}}(\tilde{x}, t),$$

where $\mathbf{d}(t) = d(t)\mathbf{e}_x$ is the sphere displacement, $d(0) = 0$. The new variables ψ^{tot}, ψ^{per} and

ψ^{amb} are related to ϕ^{tot}, ϕ^{per} and ϕ^{amb} through

$$\begin{aligned}\psi(P,t) &= \phi(P,t)\,,\\ \frac{\partial\psi}{\partial t}(P,t) &= \frac{\partial\phi}{\partial t}(P,t) + \mathbf{v}(t)\cdot\nabla_{\mathcal{R}}\phi(P,t)\,,\\ \nabla_{\tilde{\mathcal{R}}(t)}\psi(P,t) = \nabla_{\mathcal{R}}\phi(P,t)\,,\ \Delta_{\tilde{\mathcal{R}}(t)}\psi(P,t) &= \Delta_{\mathcal{R}}\phi(P,t)\,,\end{aligned} \tag{4.16}$$

where $v(t) = \partial_t d(t)$ is the sphere axial velocity. Hence, ψ^{per} is solution to the Laplace equation with the boundary condition

$$\frac{\partial\psi^{\text{tot}}}{\partial n}(P,t) = \mathbf{v}(t)\cdot\mathbf{n} \Longrightarrow \frac{\partial\psi^{\text{per}}}{\partial n}(P,t) = (-U(t)+v(t))\cos\tilde{\theta}\,,\quad \forall P\in\Gamma, \forall t\in[0,T]\,,$$

where $\tilde{\theta}$ is the analogous of θ in the moving frame $\tilde{\mathcal{R}}(t)$ (see Figure 4.10). Following the same steps as in Section 4.5.1 (with any equation for ψ being set in the moving frame, where Γ is fixed), it comes

$$\begin{aligned}\psi^{\text{per}}(\tilde{r},\tilde{\theta},t) &= \frac{1}{2}(U(t)-v(t))\frac{a^2}{\tilde{r}^2}a\cos\tilde{\theta}\,,\\ \psi^{\text{tot}}(\tilde{r},\tilde{\theta},t) &= \frac{1}{2}(U(t)-v(t))\frac{a^2}{\tilde{r}^2}a\cos\tilde{\theta} + U(t)\left(\tilde{r}\cos\tilde{\theta}+d(t)\right),\\ \nabla\psi^{\text{tot}}(\tilde{r},\tilde{\theta},t) &= \left((v(t)-U(t))\frac{a^3}{\tilde{r}^3}\cos\tilde{\theta} + U(t)\cos\tilde{\theta}\right)\mathbf{e}_r\\ &\quad + \left(\frac{1}{2}(v(t)-U(t))\frac{a^3}{\tilde{r}^3}\sin\tilde{\theta} - U(t)\sin\tilde{\theta}\right)\mathbf{e}_\theta\,.\end{aligned} \tag{4.17}$$

Using (4.16), the Bernoulli equation (4.15) is rewritten for ψ:

$$\frac{\partial\psi}{\partial t} - \mathbf{v}\cdot\nabla\psi + \frac{1}{2}|\nabla\psi|^2 + \frac{1}{\rho_f}p = C(t), \tag{4.18}$$

where again $C(t)$ is without detriment set to zero. On the surface Γ, the pressure is found to be expressed by

$$\begin{aligned}-\frac{1}{\rho_f}p(\tilde{\theta},t) &= \dot{U}(t)\left(\frac{3}{2}a\cos\tilde{\theta}+d(t)\right) + \frac{9}{8}U(t)^2\sin(\tilde{\theta})^2\\ &\quad + v(t)^2\left(\frac{5}{8}-\frac{9}{8}\cos(\tilde{\theta})^2\right) + U(t)v(t)\left(-\frac{9}{4}\sin(\tilde{\theta})^2+1\right) - \frac{1}{2}\dot{v}(t)a\cos\tilde{\theta}\,,\end{aligned} \tag{4.19}$$

so that the corresponding net force is given by

$$f(t) = 2\pi\rho_f a^3\dot{U}(t) - \frac{2}{3}\pi\rho_f a^3\dot{v}(t)\,. \tag{4.20}$$

It is, as expected, composed of two terms: the force in the absence of motion, and the added mass term. The structure motion is governed by the second law of Newton:

$$m\dot{v}(t) = f(t) \Longleftrightarrow \dot{v}(t) = m_r\dot{U}(t)\,, \tag{4.21}$$

where the mass ratio $m_r = (2\pi\rho_f a^3)/(m+2\pi\rho_f a^3/3)$ is equal to 1 when the sphere mass corresponds to the mass of the same volume of water. (4.21) provides the solution of the structure quantities

$$v(t) = m_r(U(t)-U(0)) + v(0)\,, \tag{4.22}$$

$$d(t) = m_r(\mathcal{P}(U)(t) - U(0)t) + v(0)t\,, \tag{4.23}$$

where $\mathcal{P}(U)$ is the primitive of U such that $\mathcal{P}(U)(0)=0$. By inserting (4.22) and (4.23) into (4.17), (4.19) and (4.20), all the unknowns are expressed in terms of U, m_r and $v(0)$: the FSI problem is solved.

Time integration for the structure part. At a discrete time t_n, the acceleration $\mathbf{a}(t_n)$ is computed from the nodal forces $\mathbf{f}(t_n)$. Then, assuming a linear variation in time of the acceleration in $[t_{n-1}, t_n]$, the velocity and the displacement are obtained as

$$\begin{aligned}\mathbf{v}(t_n) =&(\mathbf{a}(t_n) + \mathbf{a}(t_{n-1}))\frac{\Delta t}{2} + \mathbf{v}(t_{n-1})\,,\\ \mathbf{d}(t_n) =&(\mathbf{a}(t_n) + 2\mathbf{a}(t_{n-1}))\frac{\Delta t^2}{6} + \mathbf{v}(t_{n-1})\Delta t + \mathbf{d}(t_{n-1})\,,\end{aligned}$$

where $\mathbf{a}(t_{-1}) = \mathbf{v}(t_{-1}) = \mathbf{d}(t_{-1}) = \mathbf{0}$.

Results. The numerical results are obtained with the same numerical parameters as for the motionless sphere (Section 4.5.1) except for the ambient velocity, which is here set to $U(t) = A\,t^4(T-t)^4$, with $T = 0.5$ s and $A = 15(0.25)^8$ SI (set such that $U_{\max} = 15$ m/s). Also, $v(0) = 0$, $m = 8/3\pi a^3\rho_f$, $m_r = 0.6$.

Figures 4.11 and 4.12 illustrate respectively the fluid and structure solutions for three different values of θ. The good correlation between analytical and computed solutions validate the procedure when dealing with a mobile rigid structure. The relative errors, displayed in Figure 4.13, are artificially high for the first and last time steps because the analytical values are close to zero.

The relative error for the acceleration is dictated by $\varepsilon_{\text{sc}} = 10^{-3}$. When $M = 200$, though the stagnation convergence criterion takes into account both the acceleration and the velocity, the latter does not exactly reach the desired precision ε_{sc}, especially close to time instants for which the velocity is zero. This is due to the numerical integration of the acceleration, needed to get the velocity, that introduces an error decreasing with Δt. Then, since $\mathbf{v}$ affects the value of ϕ, and so of all the fluid quantities, it deteriorates all the errors.

Figure 4.13 also shows the errors when $M = 1000$ time steps (all the other numerical parameters remain unchanged). The error introduced by the numerical integration is now reduced, and the target error level ε_{sc} can be reached, both for fluid and structure quantities. Note that the choice of ε_{sc} must be consistent with the other tolerances set in the procedure (notably $\varepsilon_{\text{GMRES}} = 10^{-4}$ and $\varepsilon_{\mathcal{H}} = 10^{-4}$), because it would be useless to drastically decrease one tolerance but not the others.

Figure 4.14 shows the number of sub-cycles N_{sc} needed at each time step to reach a fixed precision ε_{sc} for the acceleration and the velocity. For a fixed ε_{sc}, N_{sc} mainly depends on M and the quality of the initial guess used for the velocity. Indeed, the purpose is to iteratively guess the value of $\mathbf{v}_{n+1}$, or more precisely $\mathbf{v}_{n+1}\cdot\mathbf{n}$, so the choice of $\mathbf{v}^0_{n+1}$ is of great importance. A quite simple guess is to set $\mathbf{v}^0_{n+1} = \mathbf{v}_n$, but this leads to a too large number of sub-cycles when $M = 200$. Figure 4.14 compares the results between a linear guess, corresponding to the first-order Taylor expansion

$$\mathbf{v}^0_{n+1} = \mathbf{v}_n + \Delta t\,\mathbf{a}_n\,,$$

and a quadratic guess

$$\mathbf{v}^0_{n+1} = \mathbf{v}_n + \Delta t\,\mathbf{a}_n + \frac{\Delta t^2}{2}\,\dot{\mathbf{a}}_n\,,$$

where the numerical time derivative of the acceleration is performed with the bdf4. When $M = 200$ and $\varepsilon_{\text{sc}} = 10^{-2}$, the use of the quadratic guess drastically reduces N_{sc}, as the latter is almost always equal to 2, which is its minimal value. For a quadratic guess when $M = 200$ and $\varepsilon_{\text{sc}} = 10^{-3}$, the mean value of N_{sc} slightly increases, compared to $\varepsilon_{\text{sc}} = 10^{-2}$, and it is a bit higher when the acceleration is close to zero. This behaviour is still observed

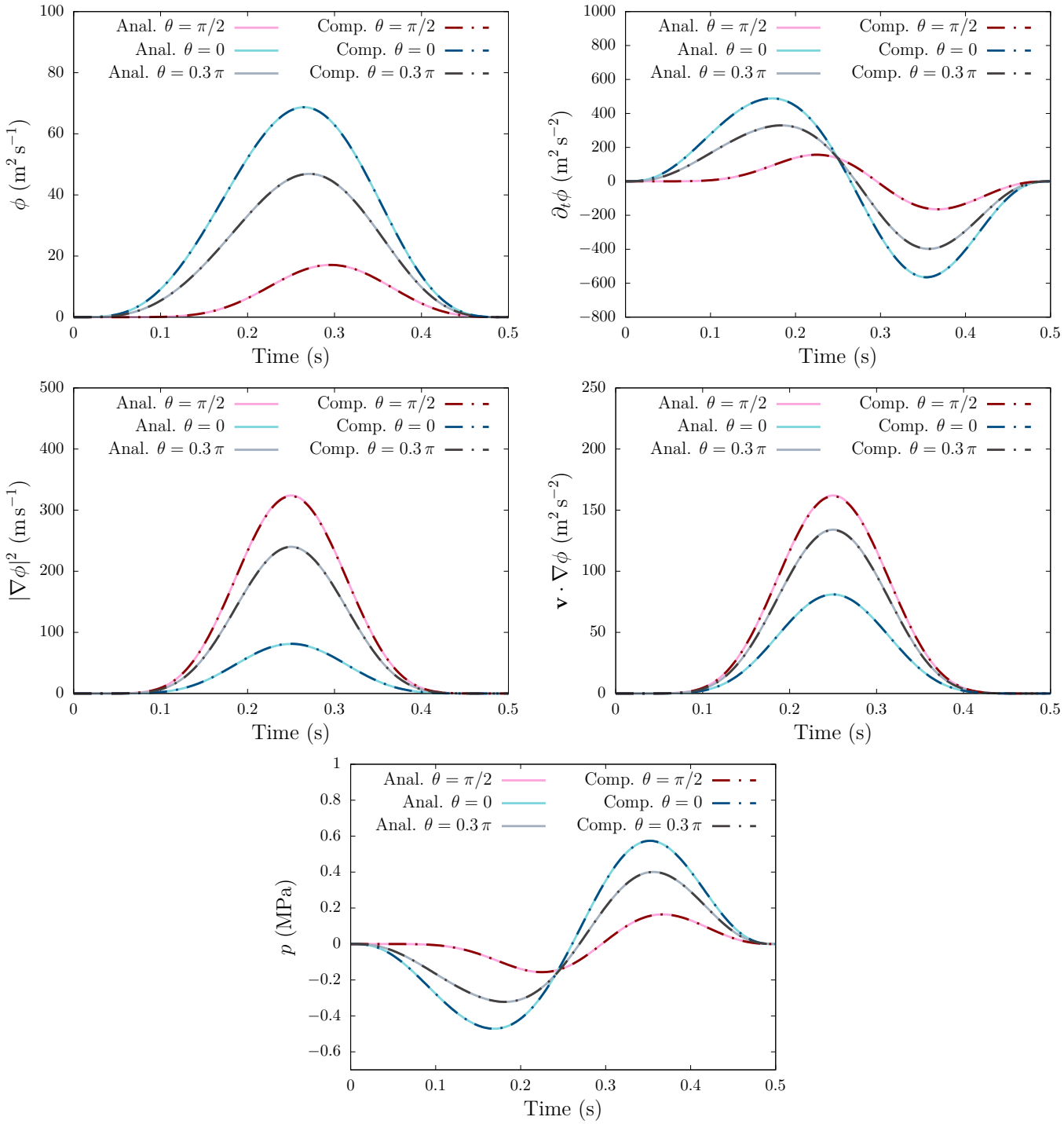

Figure 4.11: Mobile sphere: comparison between analytical and computed fluid solutions for three different values of θ. Obtained with quadratic guess for the velocity, $\varepsilon_{sc} = 10^{-3}$, $M = 200$.

as ε_{sc} decreases, as shown by the case $\varepsilon_{sc} = 10^{-4}$. When $M = 1000$, the use of a quadratic guess leads to $N_{sc} = 2$ whenever the acceleration is not close to zero, even for $\varepsilon_{sc} = 10^{-4}$. Finally, the use of the linear guess with $\varepsilon_{sc} = 10^{-3}$ implies $N_{sc} > 2$ even though $M = 1000$, which confirms the need for a quadratic guess.

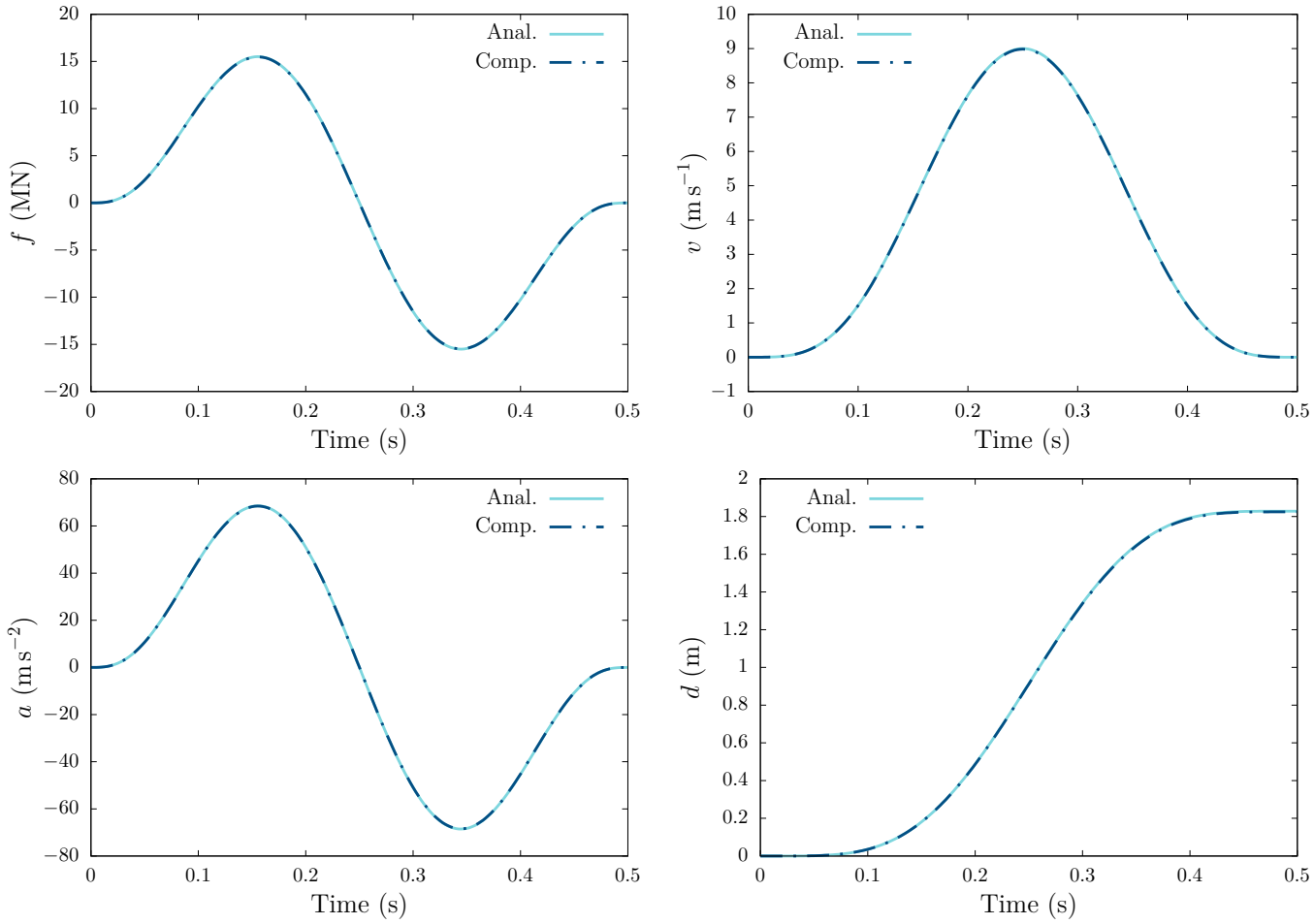

Figure 4.12: Mobile sphere: comparison between analytical and computed structure solutions for three different values of θ. Obtained with quadratic guess for the velocity, $\varepsilon_{\mathrm{sc}} = 10^{-3}$, $M = 200$.

Conclusion. The case of the rigid mobile sphere in an ambient flow of the form $\nabla\phi^{\mathrm{amb}} = U(t)\mathbf{e}_x$ allows to validate the FSI procedure developed. In particular, it shows the importance of using a good guess for the velocity in the sub-cycling, and stresses that numerical errors on the fluid quantities implies numerical errors on the structure quantities, and *vice versa*.

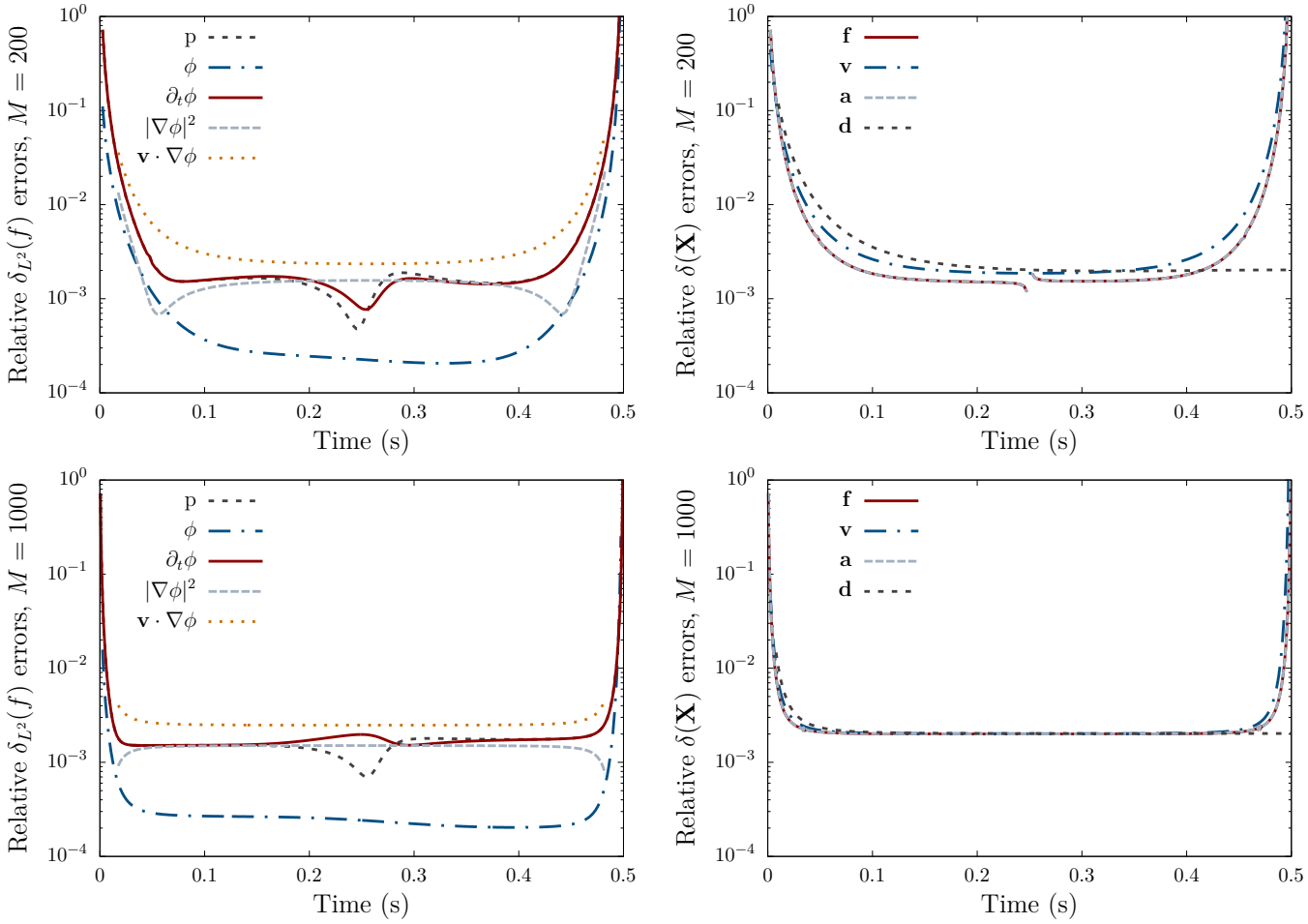

Figure 4.13: Mobile sphere: relative errors as functions of time. The relative error is not computed whenever the analytical quantity is 10^7 smaller than its maximum, to avoid division by zero. Obtained with quadratic guess for the velocity, $\varepsilon_{\mathbf{sc}} = 10^{-3}$.

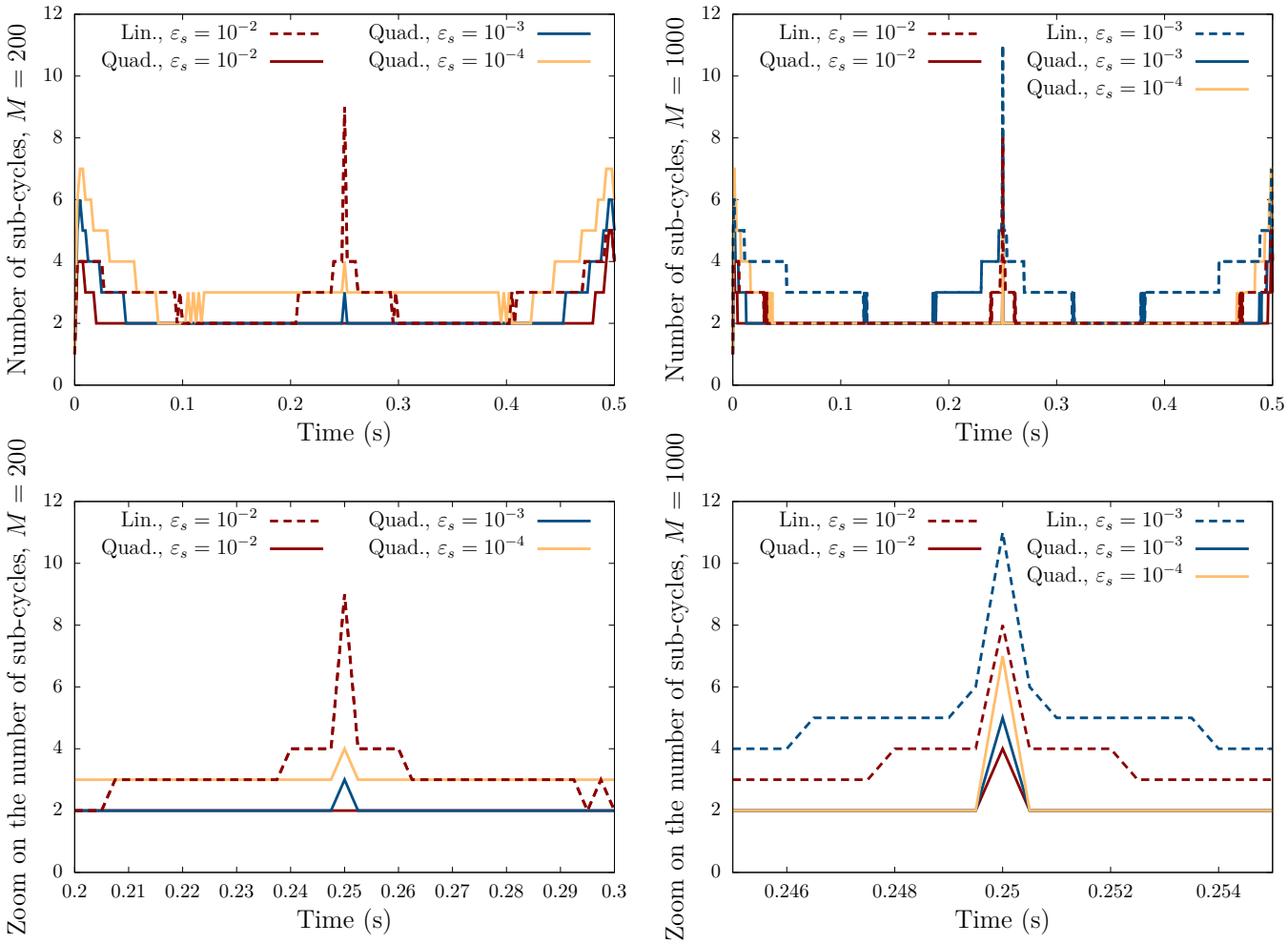

Figure 4.14: Mobile sphere: number of sub-cycles per time increment.

4.6 Fluid-structure interaction between a stiffened hull and a gas bubble

4.6.1 Problem definition, stiffening process

This example considers the effects of the gas bubble of an UNDEX of $W = 1000$ kg of TNT located at $d_0 = 50$ m from a stiffened hull. The FSI problem is treated by means of the procedure presented in Section 4.4: the fluid pressure is obtained from the ambient velocity potential (1.27) using the Bernoulli equation (4.18), and provides the Neumann datum for the structure part, through (4.6). The notations and physical parameters are provided in Figure 4.15.

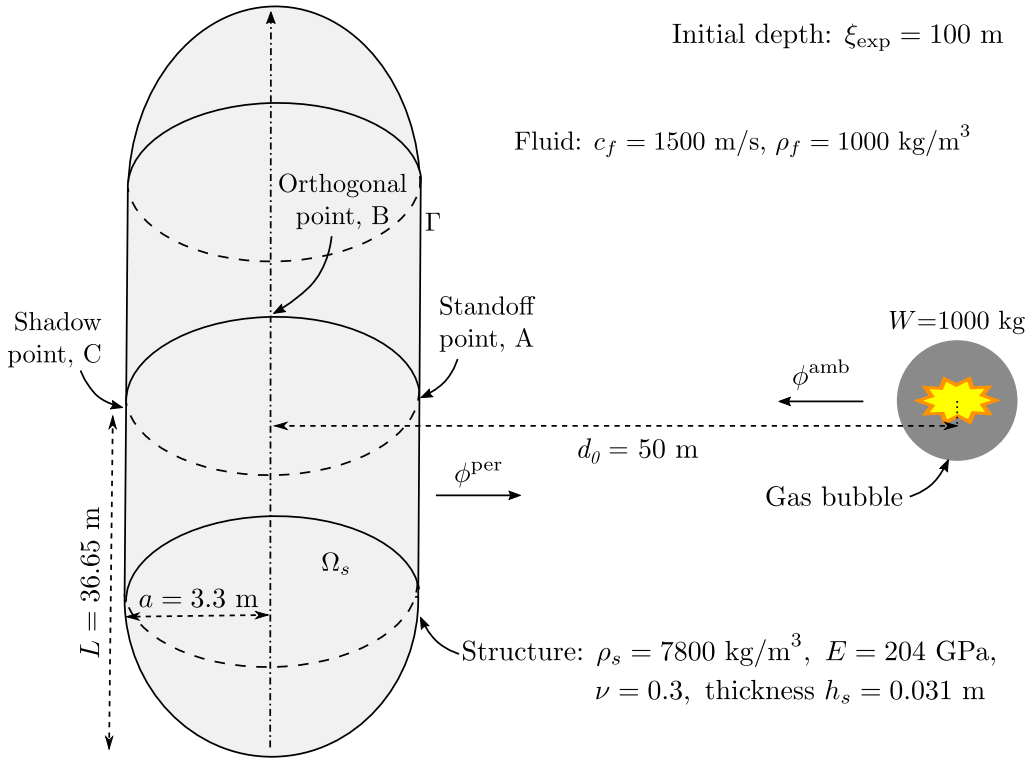

Figure 4.15: FSI between the stiffened hull and the gas bubble, notations and physical parameters.

We consider an explosion of 1000 kg of TNT at a water depth $\xi_{\text{exp}} = 100$ m, that generates a gas bubble of maximum radius and pseudo-period provided by (1.25) with $K_3 = 2.11$ SI and $K_4 = 3.50$ SI, so

$$T \simeq 0.42 \text{ s}, \quad R_{\max} \simeq 7.3 \text{ m}. \tag{4.24}$$

Structure numerical model: stiffened cylindrical hull. The part of interest of the submarine when studying the effects of UNDEX is the stiffened hull. Stiffening is a process that aims at improving the hull resistance while minimising the weight. For submarines, it consists in fixing T-shaped beams across (or along) the cylindrical shell, as illustrated in Figure 4.16. It then increases the robustness of the hull, that has to resist to the hydrostatic pressure and underwater explosions, while being lighter than a thicker hull having the same resistance.

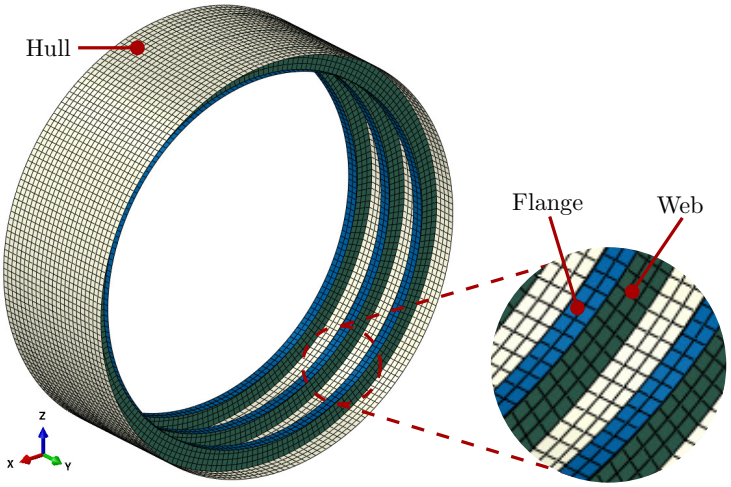

Figure 4.16: Portion of the stiffened cylindrical hull, notations.

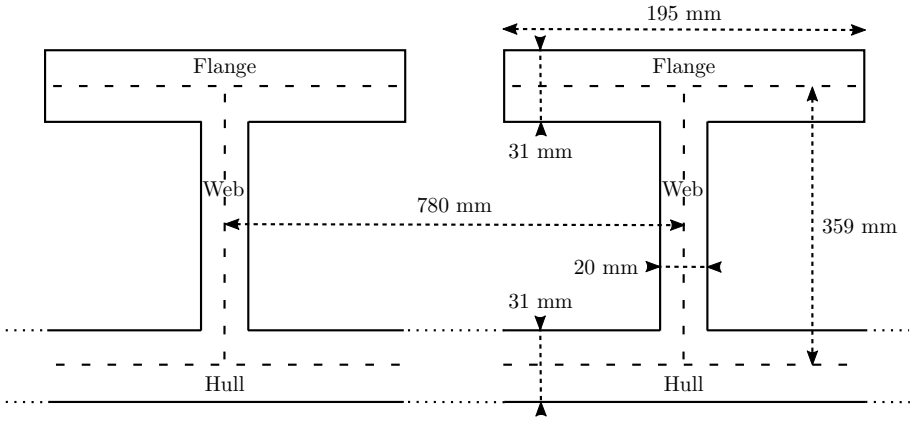

Figure 4.17: Stiffener dimensions.

The geometry considered is a cylinder closed by two hemispheres, whose characteristics are provided in Figure 4.15. The stiffener dimensions are given in Figure 4.17. The hull is stiffened with 85 regularly spaced stiffeners (this number is related to the distance between two stiffeners and the cylindrical part length), positioned on the cylindrical part (the semi-spherical closing parts are not stiffened). The whole model is made of Abaqus® shell elements (S4R). The mesh sizes are such that the flange is meshed with 2 elements, the web with 3 elements, and 6 elements lie between two stiffeners for the cylindrical part (see Figure 4.16). It leads to around 3 10^5 nodes for the structure part (5 DOFs per nodes), of which 10^5 are on the FSI interface Γ.

4.6.2 The gas bubble of an underwater explosion of 1000 kg

Before solving the coupled FSI problem, we first comment the bubble created by the explosion. The Hicks model we use provides the bubble radius and bubble depth variation, illustrated in Figure 4.18. The model leads to a slightly smaller value of $R_{\max}$ than expected (see (4.24)). Also, the model is known to introduce low energy losses, compared to experimental results, which manifests itself in Figure 4.18 with a smaller than expected decline of the maximum radius of each bubble expansion (Leblond, 2007, Section 1.4.1.3).

To study the bubble effects (notably the induced pressure), we consider the FSI problem

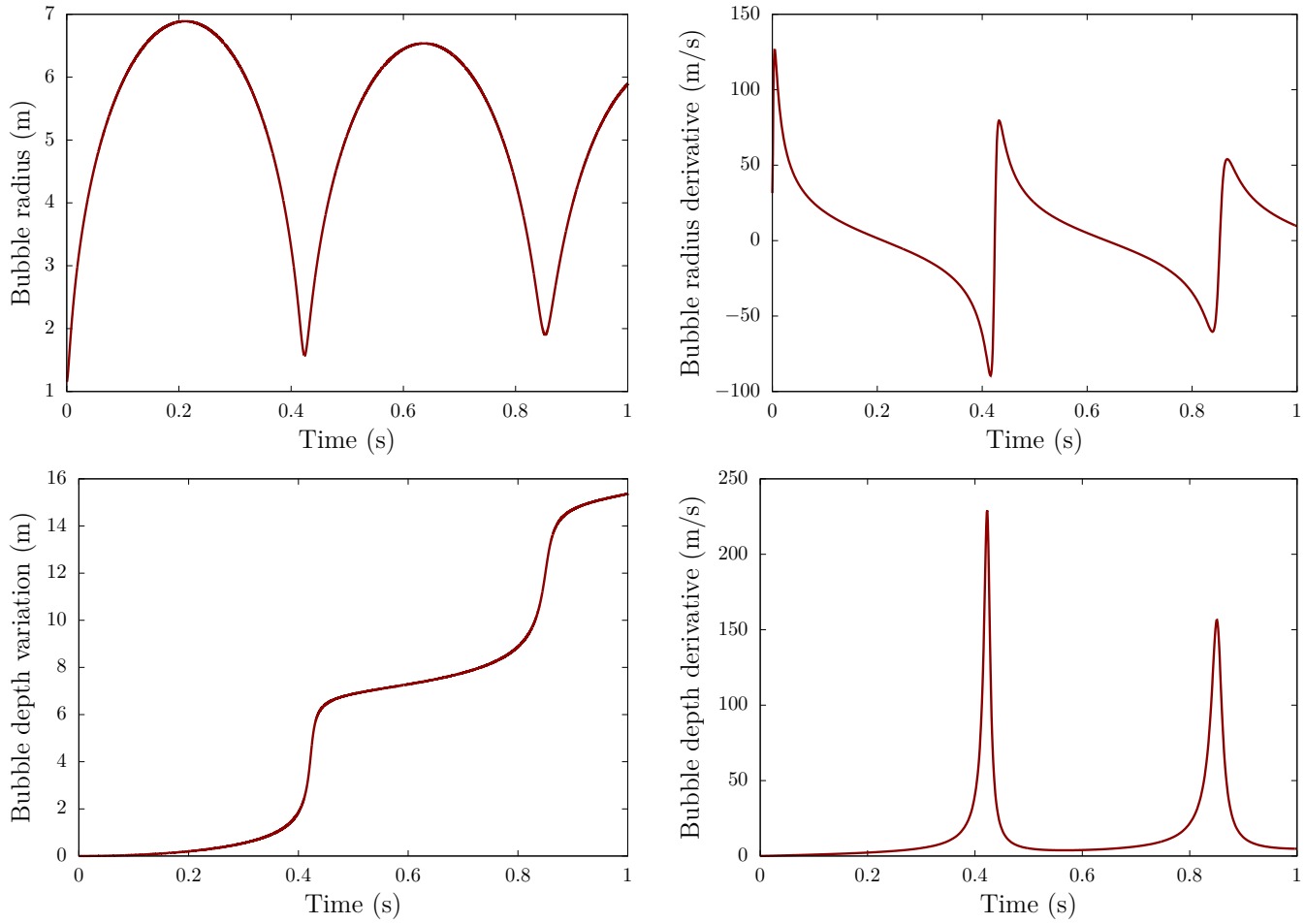

Figure 4.18: Bubble radius and depth variation obtained with the Hicks model, for an UNDEX of $W = 1000$ kg of TNT at water depth $\xi_{\text{exp}} = 100$ m.

presented Section 4.6.1 but with a rigid motionless structure. The bubble centre is initially located at a distance $d_0 = 50$ m from the structure centre (so the standoff distance is $d_s = 46.7$ m), see Figure 4.15. The considered explosion is powerful, as the shock factor (1.2) is quite large: $K \simeq 0.68$.

We compute the velocity potential and pressure on the obstacle surface Γ, like in Section 4.5.1. The ambient velocity potential is given by (1.27):

$$\phi^{\text{amb}}(r,\theta,t) = -\frac{R^2(t)\dot{R}(t)}{r} - \frac{R^3(t)\dot{Z}(t)}{2r^2}\cos\theta\,, \tag{4.25}$$

where θ is defined as in Figure 1.4. The obstacle is meshed with $N = 1890$ fluid DOFs, and $T_{\mathcal{B}} = 1$ s, $M = 1000$. We do not consider the effects of the weight, the buoyant force and the hydrostatic pressure.

The results at the standoff point are illustrated in Figure 4.19. The perturbation of the velocity potential due to the presence of the obstacle, ϕ^{per}, is quite small compared to the ambient potential ϕ^{amb}. This is explained by the moderate spatial variation of ϕ^{amb} along Γ: the remoter the explosion, the smallest the difference between two distances $r_P = \|\mathbf{OP}\|$ and $r_Q = \|\mathbf{OQ}\|$, P and Q being two different points on Γ, and O the bubble centre. In the limit case where ϕ^{amb} is constant along Γ, then $\phi^{\text{per}} = 0$, which, in our case, is reflected by the boundary integral equation (4.7), because $\phi^{\text{amb}} = C(t)$ implies

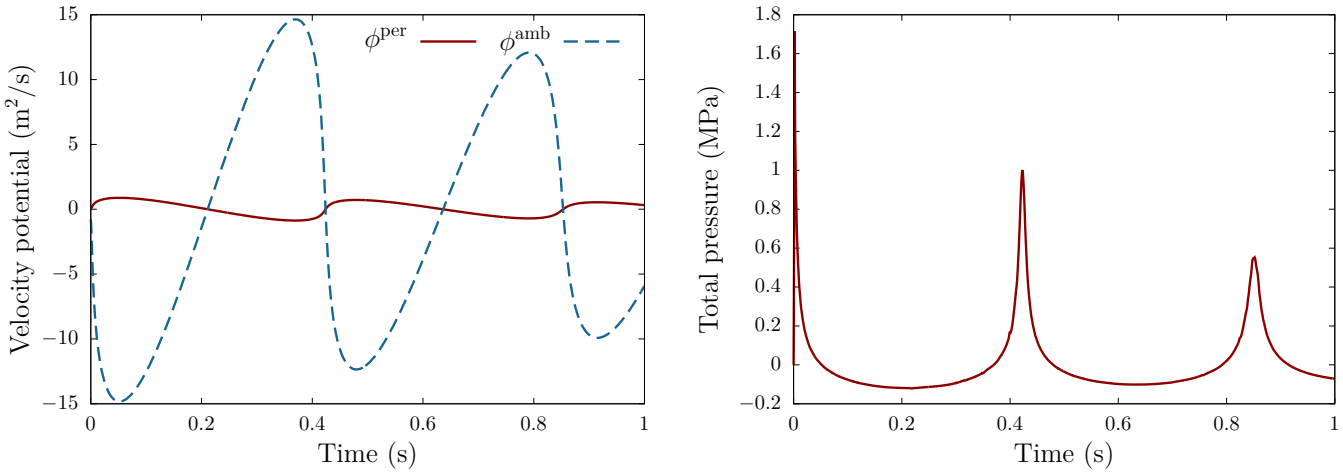

Figure 4.19: Velocity potentials and total pressure at the standoff point of the rigid structure.

$\partial\phi^{\text{per}}/\partial n = -\partial\phi^{\text{amb}}/\partial n = 0$, and then (4.7) implies $\phi^{\text{per}} = 0$.

The total pressure presents an initial (at $t = 0$) jump, due to the bubble radius discontinuity. We do not study the initial phase, because it is dealt with in the analysis of the shock wave phase, and rather focus on the time interval $[T_{\mathcal{W}}, T_{\mathcal{B}}]$, where $[0, T_{\mathcal{W}}]$ is the time interval of the shock wave phenomenon. Therefore, we re-define the simulation duration $T = T_{\mathcal{B}} - T_{\mathcal{W}}$ and set $t = 0$ as the time instant the bubble procedure starts, so after a duration $T_{\mathcal{W}}$ from the initial burst instant. Of course, the bubble dynamics has to be computed on the whole time interval $[0, T_{\mathcal{B}}]$, though it is used only in $[T_{\mathcal{W}}, T_{\mathcal{B}}]$.

We do not perform the junction between the two phenomena in this example. The structure initial state is then not provided by the output state of the shock wave phase. Instead, it is considered at initial rest. The junction between the shock wave and the gas bubble phenomena is discussed later in Chapter 5.

We set $T_{\mathcal{W}} = 50$ ms and use a smoothing procedure to enforce a zero pressure at $t = 0$, and then smoothly go back to the bubble pressure in a small time duration of $T_{\text{smooth}} = 10$ ms, using the smooth windowing function (Anderson et al., 2020)

$$\eta(u) = \exp\left(\frac{2e^{-1/u}}{u-1}\right), \quad u \in [0,1], \tag{4.26}$$

with $u = t/T_{\text{smooth}}$. This smoothing procedure is necessary in the context of fluid-structure interaction, otherwise the structure is submitted to an artificial pressure jump at the first time step, that disrupts the FSI coupling.

Figure 4.20 shows the pressure obtained on the redefined time interval $[0, T]$, as well as the contribution $-\rho_f \partial\phi/\partial t$ to this pressure in the Bernoulli equation (4.15), that reflects the inertial effects. For a rigid structure, the inertial effects are predominant, and this remains true even if the structure is deformable (the inertial contribution then constitutes more than 99 % of the pressure). This is a well-known fact in the naval industry (Hunter and Geers, 2004; Leblond, 2007). In this thesis, we nonetheless wanted to compute the pressure through the Bernoulli equation, rather than just rely on the approximation $p \simeq -\rho_f \partial\phi/\partial t$, to check and confirm that this approximation is valid. For engineering analyses, the user is offered the option of using the approximation, which slightly speeds up the computation as $\nabla\phi$ no longer needs to be computed on Γ.

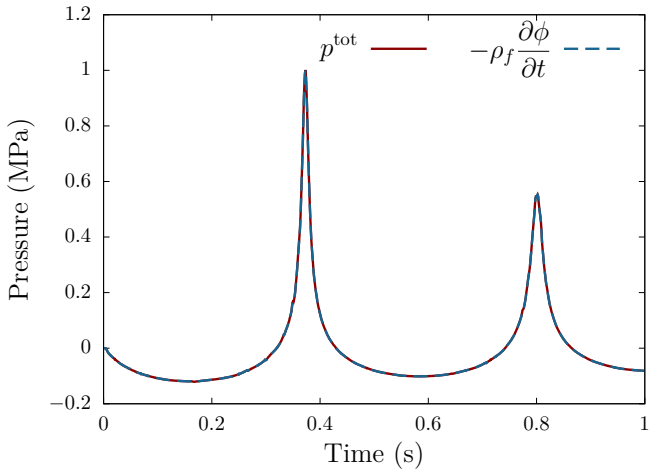

Figure 4.20: Total pressure and inertial contribution to the pressure on the new time interval $[T_{\mathcal{W}}, T_{\mathcal{B}}]$. Smoothing process applied with $T_{\text{smooth}} = 10$ ms.

Remark 23 *The hypothesis of an infinite remote water surface is valid for the considered time interval, because the maximum bubble depth variation, of approximately 15 m, remains small compared to $\xi_{exp} = 100$ m. The standoff distance $d_s = 46.7$ m is approximately 6 times the maximum bubble radius (4.24), so reducing the distance between the explosion and the structure could violate the hypotheses of remote UNDEX, as the bubble dynamics should then take into account the presence of the ship. This is why we consider an unrealistic mass of explosive*[3]*, to increase the severity of the explosion (measured by the shock factor) without reducing the standoff distance.*

4.6.3 Numerical solution of the FSI problem

Parameters. For the fluid BEM part, the FSI interface is less refined than for the structure (see Section 4.6.1): $N_f \simeq 10^4$ fluid DOFs. The fields are interpolated from the BE mesh to the FE mesh (and *vice versa*) using the software feflo.a (Loseille, 2017). The results of this section are obtained with the following numerical parameters:

- $T_{\mathcal{W}} = 50$ ms, $T_{\text{smooth}} = 10$ ms, $T = 0.93$ s, number of time steps $M = 930$.
- For the BEM: $\varepsilon_{\text{GMRES}} = 10^{-4}$; we use $P1$ Lagrange boundary elements; the $\mathcal{H}$-matrix threshold is set to $\varepsilon_{\mathcal{H}} = 10^{-4}$. Blocks containing less than $n_{\text{leaf}} = 200$ points are considered as leaves, and therefore no longer subdivided.
- For the FEM: 5 integration points along the thickness for each shell (hull, flange, web). We set `nlgeom = no` (that notably assumes small strains) and use the default direct solver of Abaqus®. Default time-stepping scheme used by Abaqus® implicit: Hilber-Hugues-Taylor (HHT) with $\alpha = 0.05$, $\beta = 0.275625$, $\gamma = 0.55$ (Géradin and Rixen, 1997; Hughes, 1987; Dassault Systèmes SIMULIA, 2017).
- The sub-cycles at each time step are performed with a constant guess for the velocity, and $\varepsilon_{\text{sc}} = 10^{-2}$ (see Section 4.5.2).

Global deformation: bending. Figure 4.21 shows 9 snapshots of the structure state, one every 100 ms. The structure deformations are magnified by a factor of 70. As expected, the most noticeable deformation mode is bending. This bending may be explained by

[3]The explosive charge of a torpedo is typically around 200 kg.

at least two (cumulative) factors. Firstly, it may be related to the dependence of the bubble ambient flow (4.25) on the distance to the bubble centre. The cylinder extremities being farther to the bubble centre than the cylinder centre, the pressure magnitude is larger at the cylinder centre. This effect is more and more pronounced as the standoff distance reduces. Secondly, the ambient flow may stimulate the natural structure mode corresponding to bending.

The structure is driven by a back-and-forth motion, following the ebb and flow generated by the bubble motion, alternating between positive and negative pressures (see Figure 4.20). The stiffeners play a small role in the bending process, and more generally in the structure response. Indeed, contrary to the shock wave case, the global deformation predominates the local ones. For that reason, some submarine hulls are stiffened with longitudinal stiffeners (parallel to the cylinder axis), that improve the hull resistance to bending.

Remark 24 *In the Abaqus® model used, we allowed for the possibility of plasticity, setting the elasticity limit to $\sigma_{lim} = 355$ MPa. However, in the above the results, where the initial state does not take into account the effects of the shock wave, we observed (a posteriori) that the deformations remained elastic, despite the high explosion charge.*

Convergence issues. For this example, the FSI iterative coupling suffered from convergence issues during the sub-cycling process (at each time step). To enhance the convergence, we introduce a relaxation coefficient α, possibly depending on the iteration k, such that the input of the fluid procedure at iteration $k+1$ is provided by

$$\partial_n \phi_n^{k+1} = \alpha^{k+1} \mathbf{v}_n^{k+1} \cdot \mathbf{n} + (1 - \alpha^{k+1}) \mathbf{v}_n^k \cdot \mathbf{n} \,,$$

where the notations are defined in Section 4.5.2, see Figure 4.1. To guarantee convergence, the relaxation parameter must be quite low. In this example, we set $\alpha = 0.1$, which allows a slow convergence, with typically $N_{sc} \sim 20$ sub-cycles at each time step, except near the bubble pulses, where $N_{sc} \sim 30$. The high value of N_{sc} hinders a finer discretisation of both space and time (to preserve acceptable computational times). This is the reason why we fixed $M \sim 10^3$ and used a rather coarse mesh for Γ. The discretisations yield smooth displacements, but disturbed velocities after the first bubble pulse (see Figure 4.22). This notably hinders the use of a linear or quadratic guess for the velocities, like performed in Section 4.5.2, because the guess is too far from the sought solution. We are currently looking for methods to reduce N_{sc}, so that M and/or N may be increased while preserving a reasonable computation time (less than a week).

Comparison to rigid case. The displacement and velocity obtained for a rigid (mobile) structure with the same procedure as in Section 4.5.2 (i.e., without using Abaqus® for the structure part) are also shown in Figure 4.22. It confirms, as illustrated in Figure 4.21 (see the colour scales), that the rigid displacement is high compared to the strains. This is consistent with our modelling hypotheses (large rigid displacements, small strains), and justifies that we re-used the same BEM operators at each time step (i.e., we never updated the BEM operators for this example).

Computational times. Each fluid BEM solution is quite fast (around 5 seconds), because (i) the number of BEM DOFs $N_f \simeq 10^4$ is rather low, (ii) the $\mathcal{H}$-matrix operators are computed only at the first time step, (iii) only about 7 GMRES iterations are needed, as we use the solution of the previous time step as initial guess, (iv) the $\mathcal{H}$-matrix-vector product is parallelised on 48 CPUs. Then, all other fluid treatments (computation of p

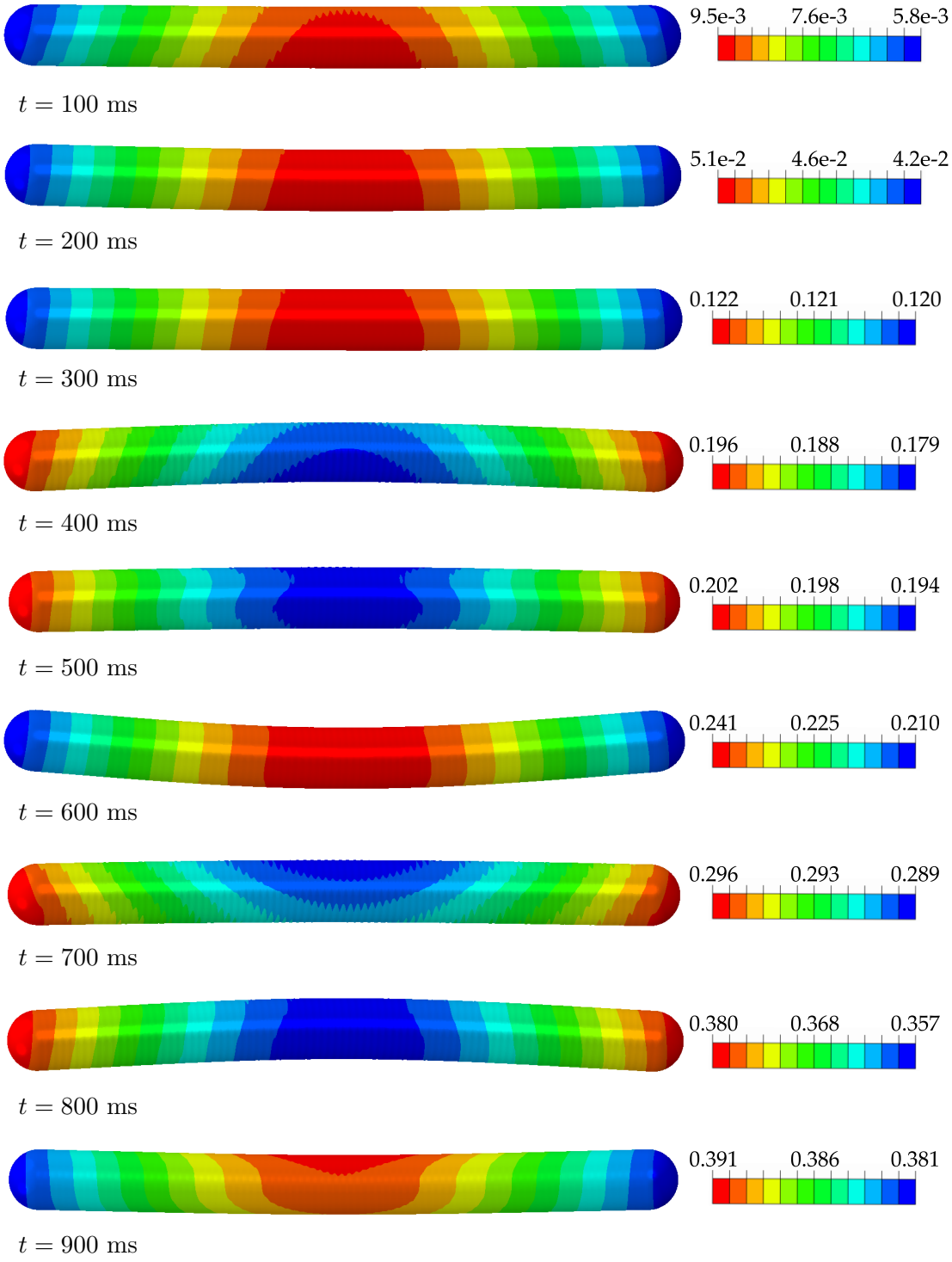

Figure 4.21: Snapshots of the structure state during the FSI, for $t \in [100\text{ ms}, 900\text{ ms}]$. The deformations are magnified by a factor of 70. The colours illustrate the magnitude of the displacement vector (m).

using the Bernoulli equation, computation of the nodal forces from the nodal pressures, field interpolations with the software feflo.a,...) last around 10 seconds. Unfortunately, each structure problem-solving lasts around 2 minutes, and so the $N_{sc}\, M \sim 2\ 10^4$ structure

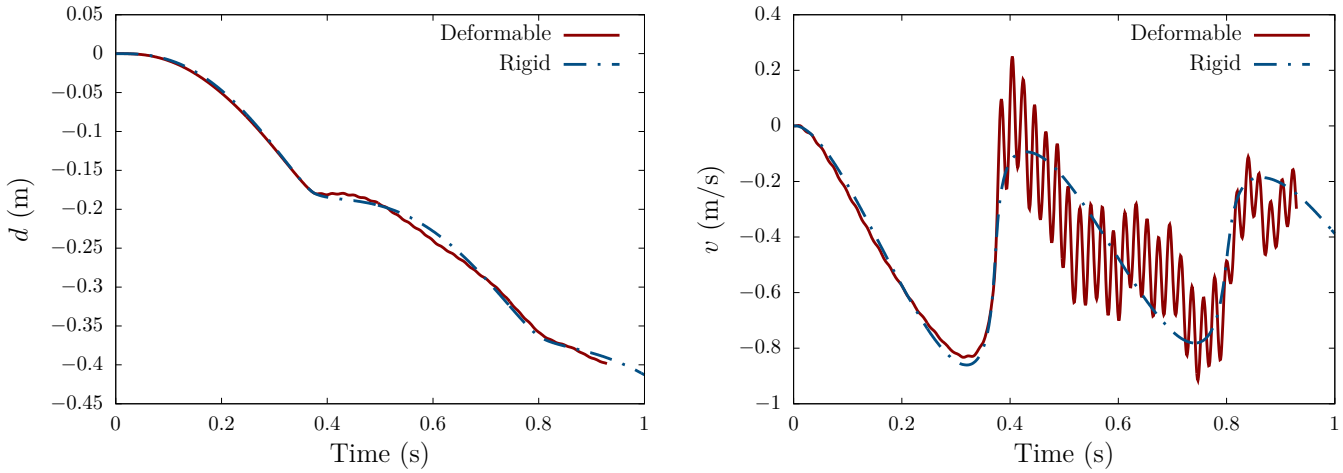

Figure 4.22: Displacement and velocity at the standoff point, component along OC, where O is the explosion locus and C is the initial structure centre. The results are not yet converged for the deformable case.

problem-solving account for the most of the overall computational cost of the FSI algorithm (the whole computation took around 30 days). The structure solving process could in principle be accelerated using CPU parallelisation. Unfortunately, one Abaqus® licence (*token*) is required for each new used CPU, which hinders massive parallelisation on, e.g., 48 CPUs (we believe massive parallelisation would reduce the whole computation time to a few days).

4.7 Conclusion and outlook

This chapter presented the FSI procedure we designed to deal with the bubble phenomenon. After explaining the differences with the shock wave case, we introduced the $\mathcal{H}$-matrix as a tool to efficiently deal with the multiple right-hand side problems governing the fluid behaviour in the context of a step-by-step FEM/BEM coupling, under the assumption of small strains. We presented and validated the FSI procedure on the simple problem of a rigid sphere in a uniform time-dependent flow. Then, we solved a concrete industrial case: the FSI between an UNDEX and a stiffened submarine hull.

We decided to first assess our procedure without taking into account the shock wave phenomenon. Of course, the next step, discussed in Chapter 5, is to treat the problem with the correct initial state. Nevertheless, we observed behaviours that conform to common expectations: (i) the global deformations are predominant compared to the local ones, (ii) bending is the most noticeable effect, and (iii) stiffeners do not play a substantial role. These observations suggest the structure response could be well approximated by a beam model, and we are currently validating the obtained results against those of an in-house procedure based on a beam model. These results will be presented in the future.

To be more realistic, the structure model (presented in Section 4.6.1) should be enhanced with some submarine key parts that significantly affect the structure response. Typically, adapting the submarine mass to the mass of the same volume of water would substantially modify the rigid displacement during the bubble coupling phase. Considering a more realistic model is then among our prospects for future work.

We are currently improving the computational procedure, so that it uses variable time steps, to improve the time discretisation only where it is necessary: around each bubble

pulses. Moreover, we keep studying methods for reducing the number of sub-cycles at each time step.

Comments on the fluid model hypotheses. To be relevant, the hypothesis of incompressible flow must be set only to model phenomena for which the fluid sound velocity may be considered infinite. For the bubble phenomenon, the bubble period T_b is typically of the order of 0.5 s, and the distances considered in our FSI context (length of the submarine, distance between the bubble and the submarine) are $L \sim 100$ m. A sound wave in water ($c = 1500$ m/s) travels 100 m in about $t_s \sim 0.07$ s. Therefore, assuming $t_s \ll T_b$ may be to some extent an oversimplification, which motivated Geers and Hunter (2002) to derive an integrated wave-effect model for the gas bubble. The authors use an approximation of the 3D wave equation called *Doubly Asymptotic Approximation (DAA)* (Geers and Toothaker, 2000; Lee et al., 2009; Geers and Felippa, 1983; Geers, 1978), that aims at providing a good order of magnitude of the solution, that is expected to be precise right after the explosion hits the hull (small times, large frequencies) and during the slower bubble process (long times, small frequencies), for cylindrical and spherical geometries. Two years later, in (Hunter and Geers, 2004), they proposed a modified relation (compared to (4.25)) to compute the ambient velocity potential in the fluid. It is sought in the form

$$\phi_{\mathcal{B}}(\mathbf{r},t) = \phi_S\left\{\mathbf{r},t|Q\right\} + \phi_D\left\{\mathbf{r},t|\mu\right\}\,,$$

where $\phi_S\left\{\mathbf{r},t|Q\right\}$ is the potential of a pulsating source of strength Q, and $\phi_D\left\{\mathbf{r},t|\mu\right\}$ is the potential of a translating dipole with strength μ. Hunter and Geers (2004) derived an approximation of ϕ_S and ϕ_D provided in (Leppington and Levine, 1987). Using the same notations as in Section 1.3.6 of (Leblond, 2007), the velocity potentials are then related to the bubble radius $R(t)$ and bubble depth variation $Z(t)$ through

$$\phi_S\left\{\mathbf{r},t|Q\right\} = -\frac{q(t')}{r'(\mathbf{r},t')}\left[1+\frac{\dot{Z}(t')}{c}\gamma'(\mathbf{r},t')\right] + \mathcal{O}(c^{-2}), \tag{4.27}$$

$$\phi_D\left\{\mathbf{r},t|\mu\right\} = -\frac{\mu(t')}{r'^2(\mathbf{r},t')}\left\{\left[1+3\frac{\dot{Z}(t')}{c}\gamma'(\mathbf{r},t')\right]\gamma'(\mathbf{r},t') - \frac{\dot{Z}(t')}{c}\right\} - \frac{\dot{\mu}(t')\gamma'(\mathbf{r},t')}{cr'(\mathbf{r},t')} + \mathcal{O}(c^{-2}), \tag{4.28}$$

where c denotes the sound velocity and

$$\begin{aligned}
\mathbf{r} &= z\,\mathbf{e}_z + x\,\mathbf{e}_x + y\,\mathbf{e}_y\,, \quad r = \|\mathbf{r}\|\,,\\
z'(\mathbf{r},t) &= z - Z(t)\,,\\
\mathbf{r}' &= z'(\mathbf{r},t)\,\mathbf{e}_z + x\,\mathbf{e}_x + y\,\mathbf{e}_y\,, \quad r' = \|\mathbf{r}'\|\,,\\
\gamma'(\mathbf{r},t) &= \cos\theta'(t) = \frac{z'(t)}{r'(t)}\,,\\
t' &= t - r'(\mathbf{r},t)/c\,,\\
q(t') &= R^2(t')\dot{R}(t')\,,\\
\mu(t') &= \frac{1}{2}R^3(t')\dot{Z}(t')\,, \quad \dot{\mu}(t') = \frac{1}{2}\left[R^3(t')\ddot{Z}(t') + 3R^2(t')\dot{R}(t')\dot{Z}(t')\right].
\end{aligned}$$

In the limit $c \to \infty$, the equation of incompressible flow (4.25) is retrieved. The first-order correction, proportional to $1/c$, permits to introduce causal effects, which allow a better modelling for the bubble pulses (Hunter and Geers, 2004; Leblond, 2007).

The ambient velocity potential ϕ^{amb} may be inferred from the bubble dynamics using either (4.27) and (4.28) or their simpler form (4.25) when $c \to \infty$. The relation (4.25) is consistent with our modelling choices, as we assume that ϕ^{per} is solution to the time-independent Laplace equation. Taking into account the $O(1/c)$ corrections proposed in (Hunter and Geers, 2004) would be interesting, since it introduces causal effects (for the bubble pulses). However, to be consistent, this would imply to change our modelling, and set a time-dependent equation for ϕ^{per}. For now, we wish to preserve the time-independence of the BEM operators, because of the computational advantages it offers. Then we could, like in (Geers and Hunter, 2002), use the DAA as the time-dependent equation satisfied by ϕ^{per}, instead of the Laplace equation, and compute ϕ^{amb} using the $O(1/c)$ corrections. Alternatively, we believe it could be interesting to compute ϕ^{amb} using the first-order corrections, but still preserve the Laplace equation for ϕ^{per}. Though it raises theoretical issues, the obtained results could be compared to experimental data, to see whether considering the $O(1/c)$ corrections only in the ambient flow ϕ^{amb} improves the results.

Chapter 5

Application to a stiffened hull subjected to an underwater explosion

This final chapter considers the main industrial application of interest in this PhD work: the fluid-structure interaction (FSI) between an underwater explosion (UNDEX) and a stiffened hull. The purpose is to demonstrate that the numerical tool we developed, based on the numerical procedures presented in Chapters 2 to 4, permits to deal with the complex phenomena introduced in Chapter 1. To this end, we follow the steps of an engineer that desires to simulate the effects of a given UNDEX on a well-chosen (submarine) hull. For confidentiality reasons, the explosion and the hull we consider are non-specific but representative, and the steps remain generic.

5.1 Numerical case study: stiffened hull facing an UNDEX

In Chapters 2 to 4 we have considered the design, implementation and validation of two numerical procedures. We briefly recall the main steps of the overall procedure (illustrated in Figure 5.4), so the problem-solving of the full fluid-structure interaction for both the shock wave and the oscillating bubble parts. For each step, we specify the chosen numerical parameters.

Prior step: specify the problem. We consider a stiffened hull similar to that presented in Section 4.6.1, but with smaller length $2L = 16.6$ m, subjected to an UNDEX of $W = 100$ kg of TNT at a standoff distance $d_s = 46.7$, with corresponding shock factor $K \simeq 0.2$. The cylindrical hull is stiffened as illustrated on Figures 4.16 and 4.17. The case considered is depicted in Figure 5.1.

Choose a model for the incident shock wave pressure. Deviating from the choice performed in Section 3.5, we use this time the double-exponential fit (1.4):

$$p_{\mathcal{W}}(r,t) = p_m\, f(t_r(r,t))H(t_r(r,t))\,,$$
$$f(t) = \alpha_1\, e^{-\beta_1\, t/\tau} + \alpha_2\, e^{-\beta_2\, t/\tau}\,,$$
$$p_m(r) = K_1 \left(\frac{W^{1/3}}{r}\right)^{a_1}\,, \qquad \tau(r) = K_2 W^{1/3} \left(\frac{W^{1/3}}{r}\right)^{a_2}\,,$$

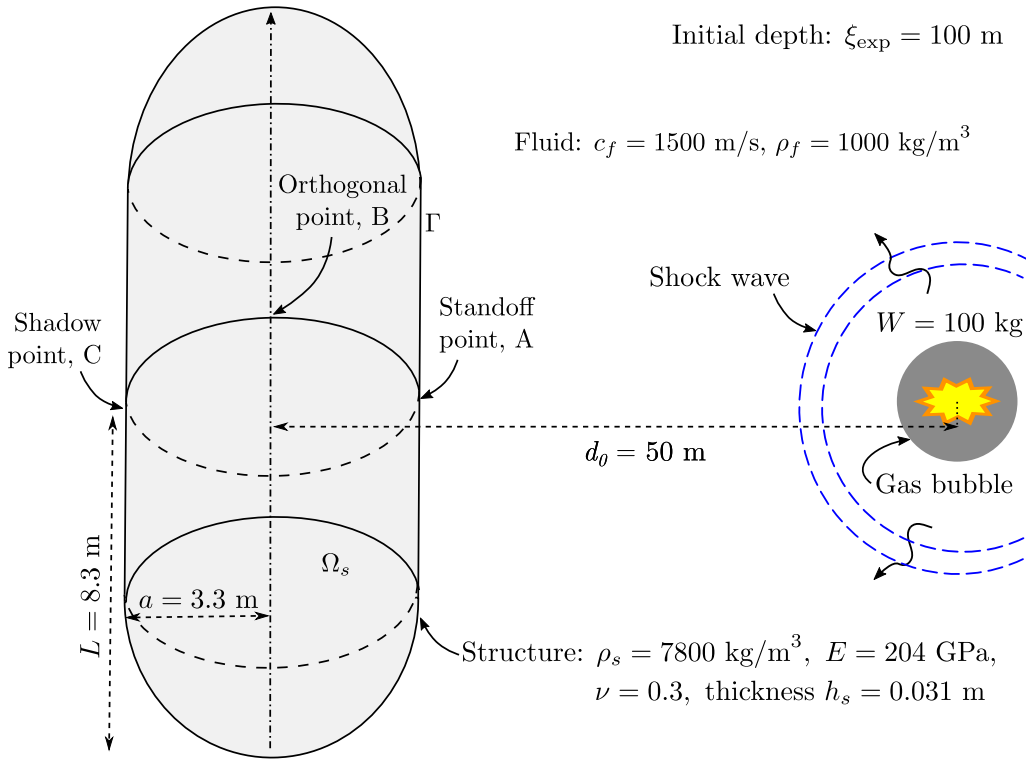

Figure 5.1: FSI between the stiffened hull and the underwater explosion (shock wave and gas bubble), notations and physical parameters.

for the shock wave incident pressure, because it is believed to be more accurate (Geers and Hunter, 2002). We choose the same explosive material parameters as in Section 3.5:

$$K_1 = 5.24\ 10^7 \text{ SI},\ a_1 = 1.13, \qquad K_2 = 8.4\ 10^5 \text{ SI},\ a_2 = -0.23,$$

and consider the common TNT parameters for the coefficients of the double-exponential decay (see Section 1.2.1):

$$\alpha_1 = 0.8251, \quad \beta_1 = 1.338, \quad \alpha_2 = 1 - \alpha_1 = 0.1749, \quad \beta_2 = 0.1805.$$

Choose a bubble model. We assume the flow is potential and incompressible, and choose the Hicks model to describe the bubble dynamics, similarly to Section 4.6, with the same explosive bubble parameters: $K_3 = 2.11$ SI and $K_4 = 3.50$ SI.

Choose how to blend the shock wave and gas bubble phenomena. As stated in Section 1.4, the junction between the shock wave and the gas bubble parts is a crucial step. In the context of a remote UNDEX, we choose to end the shock wave simulation once the input of the FEM/FEM coupling procedure $p^{\text{Ref}} = p^{\text{ref}} + p^{\text{inc}}$ is zero everywhere on the interface Γ. To ensure this behaviour, and prevent from small numerical instabilities (see for instance Figure 2.14), we smoothly enforce the pressure to be zero after a sufficiently long time. For the considered UNDEX of $W = 100$ kg at $d_s = 46.7$ m, the shock wave simulation duration is set to $T_{\mathcal{W}} = 25$ ms, but $p^{\text{Ref}} = p^{\text{ref}} + p^{\text{inc}}$ is smoothly set to zero, using (4.26), for $t \in [18 \text{ ms}, 23 \text{ ms}]$, and $p^{\text{Ref}} = 0$ for $t \in [23 \text{ ms}, 25 \text{ ms}]$. The bubble input is also smoothed at the beginning of the bubble procedure (see Section 4.6.2).

The two smoothing processes ensure a smooth numerical junction (in terms of induced pressures) between the two phenomena. Of course, the junction procedure introduces

a deviation between the numerical incident pressure experienced by the ship, and the expected *true* pressure curve (i.e., that would be experimentally measured if measurement errors are marginal), as illustrated in Figure 5.2. In particular, the closer the explosion, the less accurate the smoothing junction.

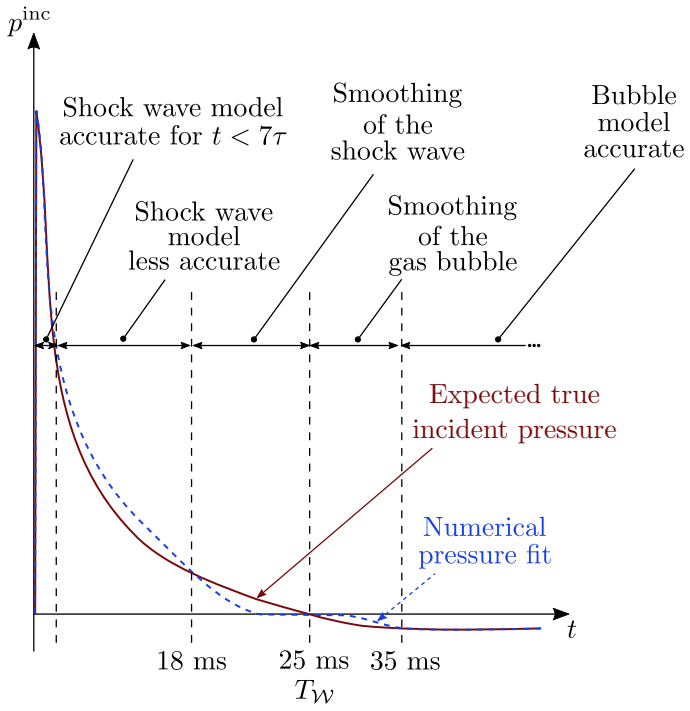

Figure 5.2: Schematic illustration of the smooth junction between the shock wave and bubble phenomena. Comparison between the smoothed numerical incident pressure and the expected *true* incident pressure.

Generate meshes of the fluid-structure interface Γ for the BEM. We use 10 meshes with uniform and decreasing mesh size (see Section 2.5.6). The most refined mesh has a mesh size $h \simeq 0.012$ m, corresponding to $N \simeq 2.6\ 10^6$ DOFs. The master mesh has a mesh size $h \simeq 0.06$ m, corresponding to $N \simeq 10^5$ DOFs. We use the rule of 8 points per wavelength, except for the most refined mesh, for which we carry the computation until 6 points per wavelength. The high frequency limit is therefore set to $f_{\text{HFA}} \simeq 21$ KHz, $k_{\text{HFA}}a/\pi \simeq 88$, $k_{\text{HFA}}L/\pi \simeq 230$. We recall that f_{HFA} is related to the most refined mesh, the latter being chosen according to the available computational resources.

Compute the reflected pressure for the shock wave part using the $\mathcal{Z}$-BEM. We set the simulation duration to $T_{\mathcal{W}} = 25$ ms and the number of time steps to $M = 5\ 10^4$. Similarly to Section 2.6, we set $\varepsilon_{\mathcal{Z}} = 10^{-5}$ (precision for the inverse $\mathcal{Z}$-transform), $L = 2M$ (number of frequencies), $\rho = \varepsilon^{1/L}$ (radius used in the CQM to compute the frequencies), $\varepsilon_{\text{GMRES}} = 10^{-5}$ (GMRES tolerance). We use the BDF2 (backward differential formula of order 2) scheme. The number of BEM problems actually solved with the FM-BEM is $M = 166$. The BEM input of the Abaqus® FEM/FEM solving, $p^{\text{Ref}} = p^{\text{ref}} + p^{\text{inc}}$, is smoothed with a Butterworth filter of order 5, with cut-off frequency $f_c = 20$ kHz (see Section 3.5.2).

Generate the structure and truncated fluid FEM models. The structure FEM model is similar to that of Section 4.6.1 (see Figures 4.16 and 4.17), except it has 13 regularly spaced stiffeners, positioned on the cylindrical part (the spherical parts are not stiffened). The whole model is made of Abaqus® shell elements (S4R). The mesh size ($h \simeq 0.06$ m) is such that the flange is meshed with 4 elements, the web with 6 elements, and 13 elements lie between two stiffeners for the cylindrical part. It leads to around 1.5 10^5 nodes for the structure part (5 DOFs per node), of which 10^5 are on the FSI interface Γ. The non-uniform fluid volume FE mesh is a water layer of 8 m surrounding the structure. Near the standoff point, at the fluid-structure interface Γ, the mesh size is set to 0.05 m. Elsewhere near Γ, the mesh size is set to 0.06 m. On the exterior boundary Γ_∞, the mesh size is set to 1.5 m, and Abaqus® absorbing conditions (cylindrical and spherical acoustic impedances) are set to reduce unphysical reflections. We use the Abaqus® acoustic tetra-element AC3D4. A snapshot of the meshes is provided in Figure 5.3.

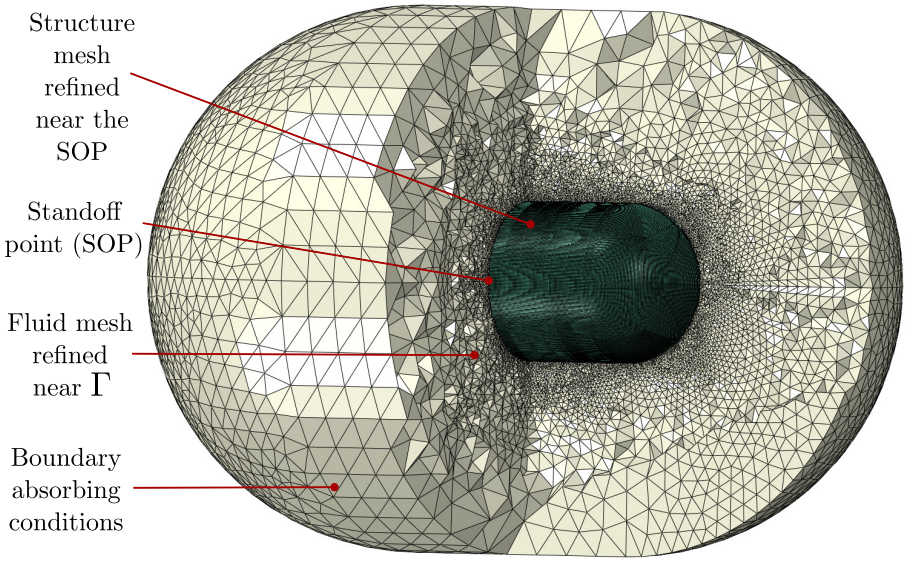

Figure 5.3: 3D view of the meshes used for the FEM/FEM coupling for the shock wave part. Both the 3D fluid and 2D structure meshes are refined near the standoff point.

Solve the FSI problem for the shock wave part using the hybrid $\mathcal{Z}$-BEM/FEM explicit approach, with $p^{\mathbf{Ref}}$ as input. The nodal forces related to p^{Ref} are computed using linear shape functions. We set $M = 5\ 10^5$ and use the explicit Abaqus® scheme with default parameters, similarly to Section 3.5.

Use the shock wave output state as input state for the bubble model. The practical junction between the two phenomena is performed using the `*Restart` and `*Import` functionalities of Abaqus® (Dassault Systèmes SIMULIA, 2017). They permit to load the state saved at the end of the shock wave procedure and use it as initial state in the bubble procedure.

Solve the FSI problem for the bubble model using the step-by-step coupling procedure. We use the same procedure as in Section 4.6, with the following numerical parameters:

- $T_{\mathcal{W}} = 25$ ms, $T_{\text{smooth}} = 10$ ms, $T_{\mathcal{B}} = 0.5$ s, number of time steps $M = 2000$.
- For the BEM: $\varepsilon_{\text{GMRES}} = 10^{-4}$; we use $P1$ Lagrange boundary elements; the $\mathcal{H}$-matrix threshold is set to $\varepsilon_{\mathcal{H}} = 10^{-4}$. Blocks containing less than $n_{\text{leaf}} = 200$ points are considered as leaves, and therefore no longer subdivided. The FSI interface Γ is less refined than for the FEM: $h \simeq 0.1$ m, $N_f \simeq 4\ 10^4$ fluid DOFs.
- For the FEM: 5 integration points along the thickness for each shell (hull, flange, web). We set `nlgeom = no` (that notably assumes small strains) and use the default direct solver of Abaqus®. Default time-stepping scheme used by Abaqus® implicit: Hilber-Hugues-Taylor (HHT) with $\alpha = 0.05$, $\beta = 0.275625$, $\gamma = 0.55$ (Géradin and Rixen, 1997; Hughes, 1987; Dassault Systèmes SIMULIA, 2017).
- The sub-cycles at each time step are performed with a constant guess for the velocity, and $\varepsilon_{\text{sc}} = 10^{-2}$ (see Section 4.5.2).

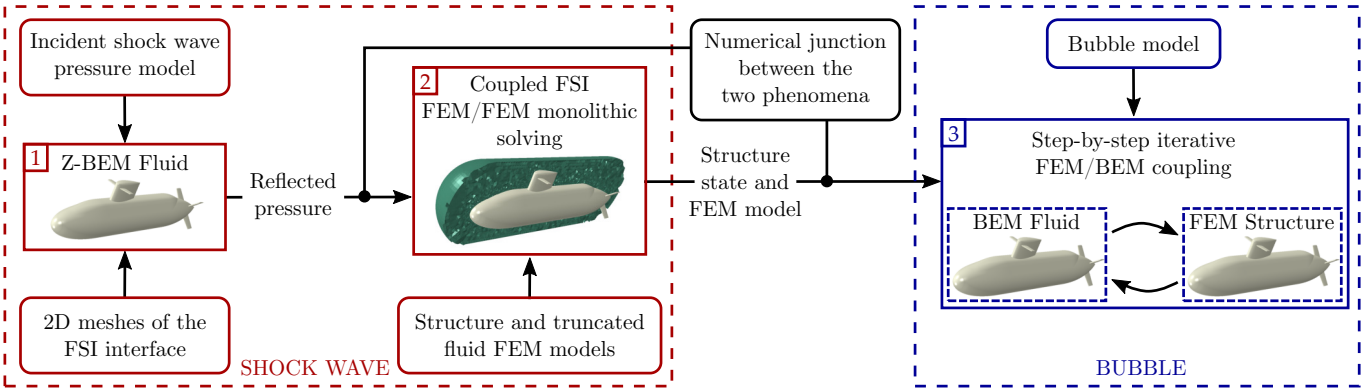

Figure 5.4: Main steps of the overall procedure solving the whole FSI problem (shock wave and gas bubble).

Remark 25 *We do not consider the effects of gravity, the buoyant force and the hydrostatic pressure, which are to be considered in the structure part, with a pre-computation (performed before the shock wave phenomenon) that sets the hull in the realistic environmental conditions.*

5.2 Results of the overall procedure, discussion

We separately comment the results of the $\mathcal{Z}$-BEM procedure, the FEM/FEM solving for the shock wave phase, and the FEM/BEM coupling for the gas bubble part.

5.2.1 Fluid-structure interaction for the shock wave phase

Uncoupled part (scattering problem). Firstly, p^{Ref} is computed using the $\mathcal{Z}$-BEM approach (step 1 in Figure 5.4). The computational time of this first step depends on the number of CPUs available. For example, this computation takes about 2 days on a standard computer with $O(500)$ GB of RAM and $O(100)$ threads. For industrial studies, it can be reduced by considering coarser meshes (that imply a lower value of f_{HFA}), depending on the target accuracy.

The result quality is illustrated on Figures 5.5 to 5.8 The computed time-dependent pressure response at the standoff (A) and orthogonal (B) points is rather smooth (not disturbed), as shown in Figure 5.5. This behaviour is observed everywhere in the front

region, as illustrated in Figures 5.6 and 5.7. We check that the maximum pressure at the standoff point conforms with its analytically-predicted value (3.18):

$$p^{\mathrm{Ref}}(t=0, P=A) = 2\, p_m(r=d_s) \simeq 7.7 \text{ MPa}.$$

The use of the Butterworth filter of order 5 (see Section 3.5.2) slightly increases this value, which reaches 8.3 MPa (see Figure 5.5). At the shadow (C) point, some numerical instabilities (non-causal effects, commented in Section 2.6.3) are still noticeable, especially on the snapshot Figure 5.7 at $t = 5.5$ ms. A second wave passage is noticeable at around $t = 10$ ms. It is visually explained on the snapshot in Figure 5.8 at $t = 9.35$ ms, and corresponds to the scattered waves coming from the structure extremities.

Remark 26 *In the line plots Figures 5.5 and 5.14 and the snapshots Figures 5.6 to 5.8, 5.10 to 5.13 and 5.15, the time instant $t = 0$ is set 0.1 ms before the shock wave hits the hull, so that the discontinuous jump at the standoff point is well observed (and not disturbed by the figure axes). However, in the comments, notably concerning the maximum pressure, we keep the convention that $t = 0$ corresponds to the instant the shock wave hits the hull.*

We are very satisfied with the result quality for this first step of the overall procedure. It provides a proper input for the next FEM/FEM solving, which is very important, because the entire procedure would suffer from a poorly computed p^{Ref}.

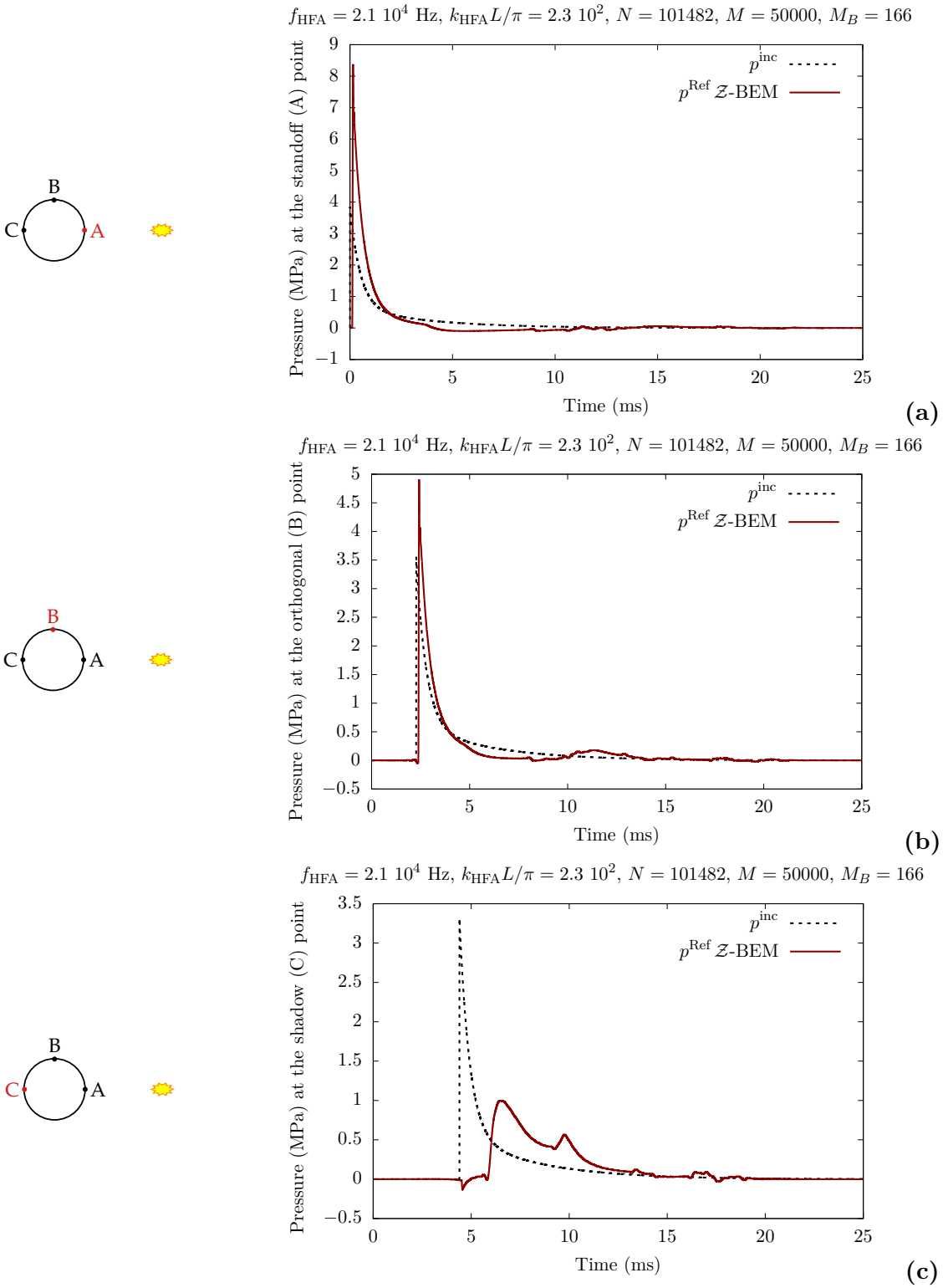

Figure 5.5: Scattering by the rigid hull, total field p^{Ref} in the cross-section containing the explosion, at the standoff (a), orthogonal (b) and shadow (c) points. The incident field at those points is also shown.

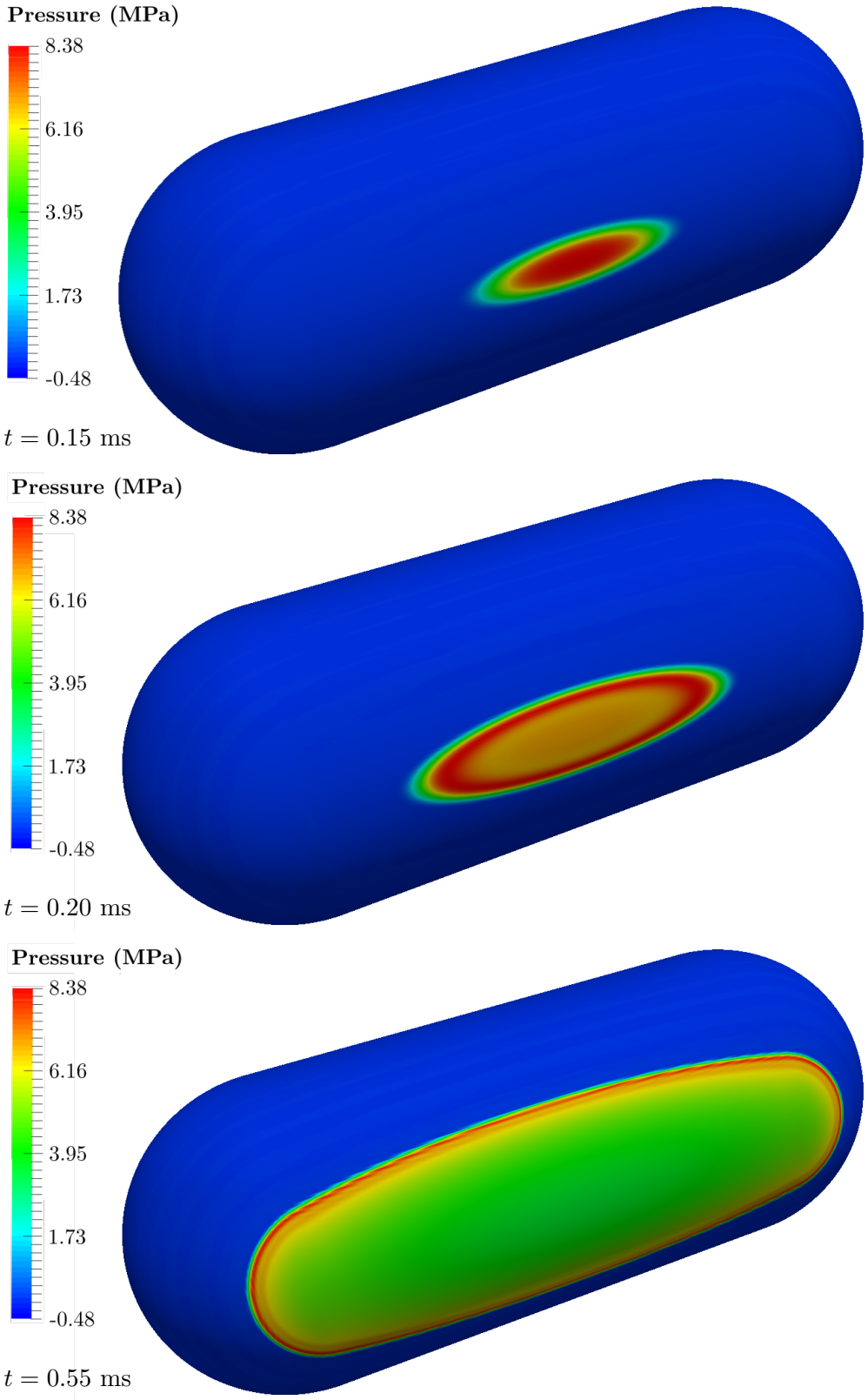

Figure 5.6: Snapshots of the total field p^{Ref} on the hull surface, in the front zone.

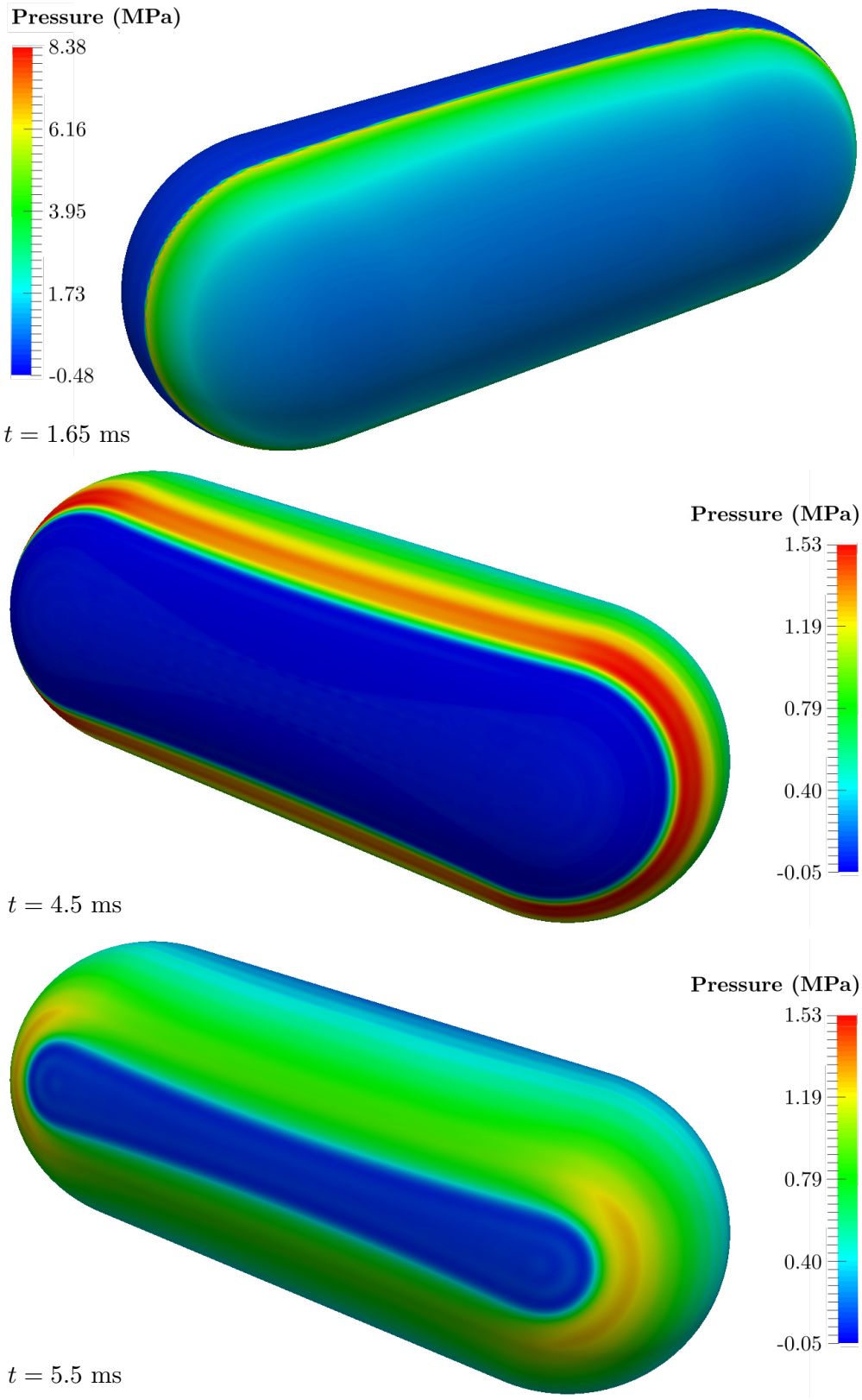

Figure 5.7: Snapshots of the total field p^{Ref} on the hull surface, in the front (top) and shadow (middle and bottom) zones.

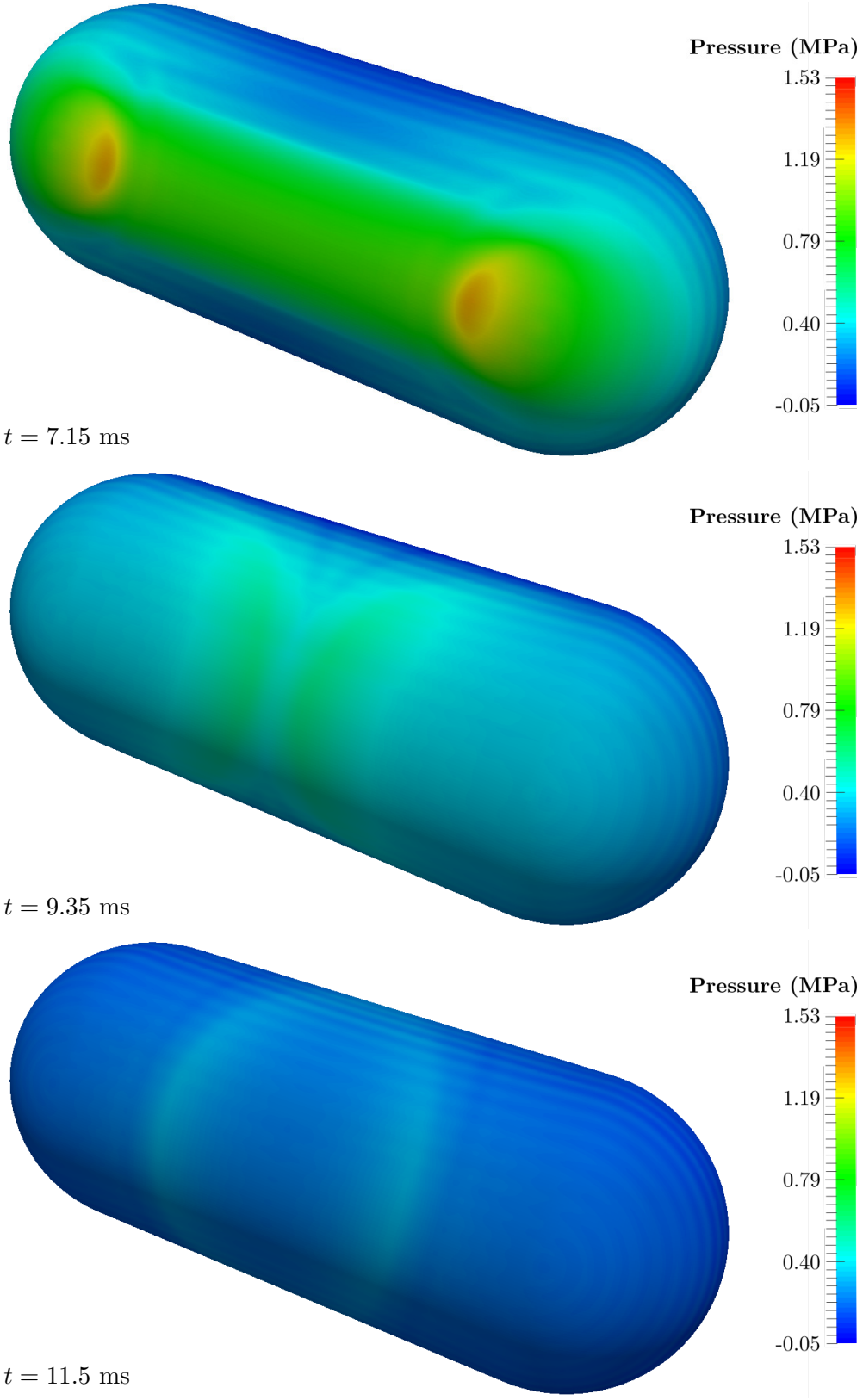

Figure 5.8: Snapshots of the total field p^{Ref} on the hull surface, in the shadow zone.

The role of stiffeners. Like in Section 3.5, p^{Ref} serves as input to compute the nodal forces and then solve the coupled FSI problem (step 2 in Figure 5.4). The structure kinematic response is illustrated by snapshots in Figures 5.10 to 5.12. As expected, the stiffeners play a major role in the local deformations: during the first milli-seconds, they reduce the displacement by a factor 2, compared to what is observed between two stiffeners (see Figure 5.12). The observed displacement reduction near the stiffeners induces (not surprisingly) stress concentrations in those regions, as illustrated by the von Mises stress map shown in Figure 5.13. As expected for the considered explosion, the stresses remain below the elastic limit $\sigma_{\text{lim}} = 355$ MPa.

Disturbed output state of the shock wave. When considering stiffened submarine hulls, the shock wave phenomenon may stimulate local structure modes, with natural frequency typically around $f \sim 100-500$ Hz. This makes the structure vibrate and leads to an output state that is quite disturbed. Line plots shown in Figure 5.14 illustrate these structure vibrations at the standoff point. In our context, this implies that the bubble FSI procedure would start with a disturbed initial state, with a typical time scale of the structure vibrations of $T \sim 10^{-2}-10^{-3}$ s. The bubble procedure is not designed to deal with that kind of vibrations, notably because the target time step is not small enough to treat them. To bypass this difficulty, some numerical damping may be introduced in the shock wave procedure, or during an intermediate computation inserted between the shock wave and the bubble phases, that aims at dissipating the structure vibrations. In Figure 5.14, we show results obtained with and without numerical Rayleigh damping introduced using the `*Damping` feature of Abaqus®. We use a stiffness proportional damping with $\beta_R = 10^{-5}$ (Dassault Systèmes SIMULIA, 2017, Section Material Damping). This kind of damping dissipates some of the energy of high frequency vibrations, and then provides an output state more suitable as initial state for the bubble procedure.

To evaluate potential unwanted effects of this artificially-introduced damping in our industrial context, we focus on the *Shock Response Spectrum (SRS)* introduced in Section 3.5.3. We recall that the purpose of the SRS is to provide an order of magnitude of the maximum acceleration experienced by an on-board equipment during the explosion. On-board equipment are sometimes attached to the flange, rather than the hull (see Figure 4.16). Therefore, the SRS is computed at the point in the middle of the flange (in the cross-section containing the explosion) instead of the standoff point. The SRS, provided in Figure 5.9, confirms that the main effect of the damping is to cut high frequencies. Under these conditions, SRS results remain reliable for equipment with natural frequencies below about 1 kHz.

Simulation duration. After only 25 ms of simulation, the structure vibrates too much (even with Rayleigh damping) for its state to be used as initial input for the bubble procedure. We could introduce stronger damping, but it could (i) affect too much the solution, (ii) imply a too-small stable time increment (Dassault Systèmes SIMULIA, 2017, Section Material Damping). Therefore, we continue the simulation until $T_{\mathcal{W}} = 100$ ms, to obtain a more stabilised state. This implies that we change the time parameters for the bubble procedure. We set $T_{\mathcal{W}} = 100$ ms, $T_{\text{smooth}} = 20$ ms, $T_{\mathcal{B}} = 0.5$ s, and $M = 2000$. For the shock wave procedure, this has the consequence that the simulation is 4 times longer, but the computational time remains below that of the preceding $\mathcal{Z}$-BEM procedure: about 40 hours divided by the number of CPUs (we used 4 CPUs). The consequences for the bubble part are discussed in the next section.

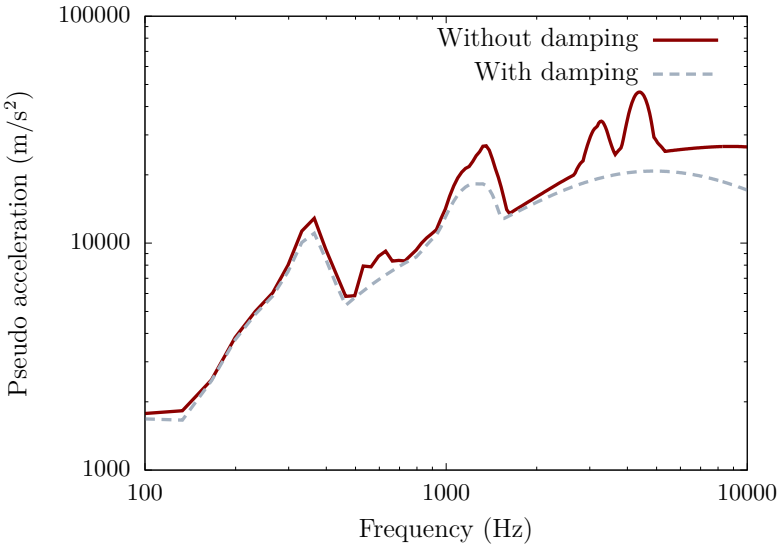

Figure 5.9: Shock response spectrum at the point in the middle of the flange, in the cross-section containing the explosion.

Efficiency of the boundary absorbing conditions. Figure 5.15 illustrates the propagation of the radiated pressure p^{rad} in the truncated 3D fluid domain. It permits to check that the Abaqus® boundary absorbing conditions do not introduce noticeable unphysical reflections. As expected, the result quality is poor in the fluid. This is due to the non-uniform mesh considered (see Figure 5.3), that is refined only near the FSI interface Γ. As explained in Section 3.3, this has no adverse effect in our FSI context, as a correct value of p^{rad} is required only on Γ.

Conclusion. We are mostly satisfied with the results obtained for the shock wave part. Though they are not perfect yet, they seem very promising and so we believe our method is quite competitive compared to other numerical methods (typically those presented in Section 3.4.2) on this specific case.

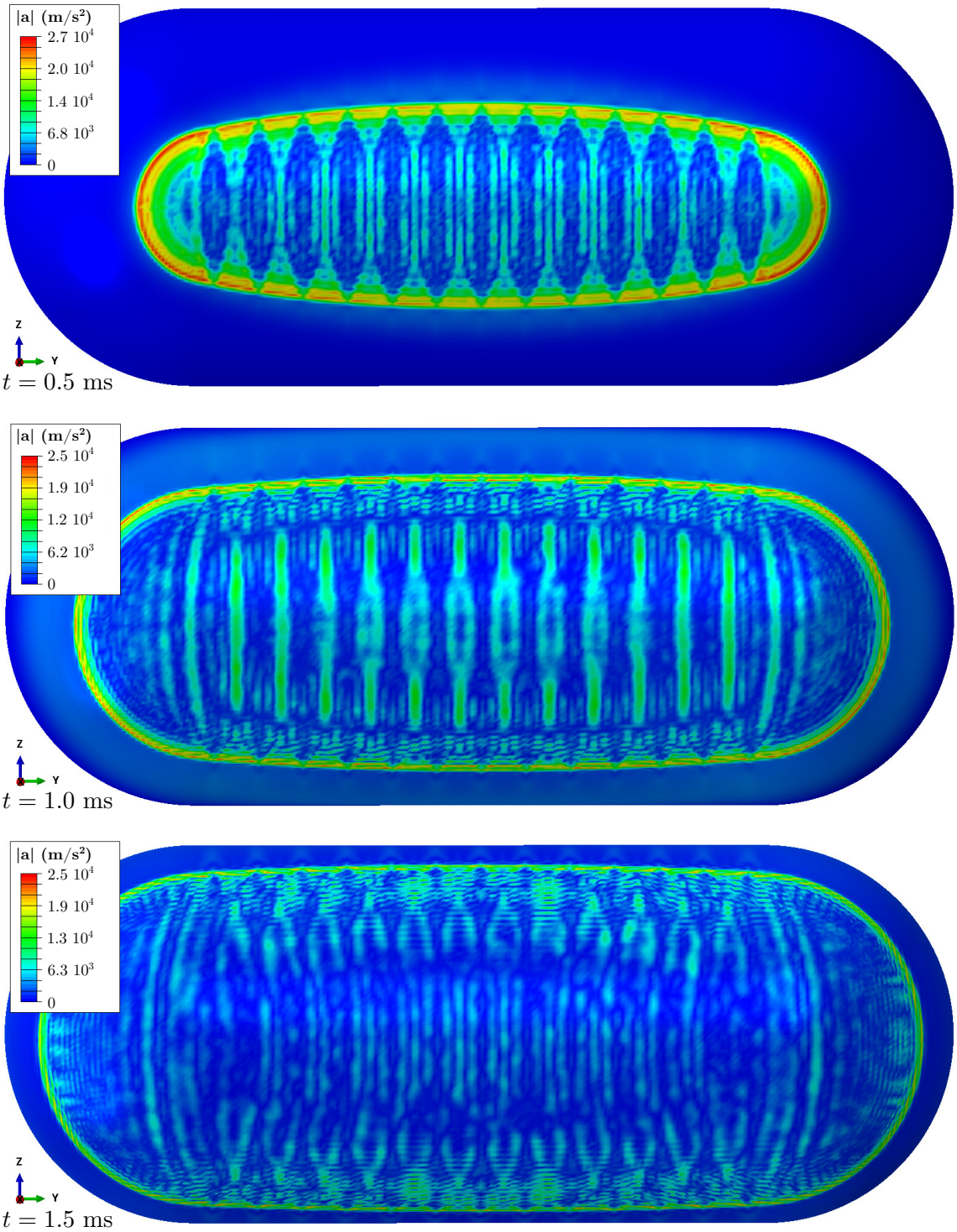

Figure 5.10: Snapshots of the acceleration magnitude |a| on the hull surface, in the front zone.

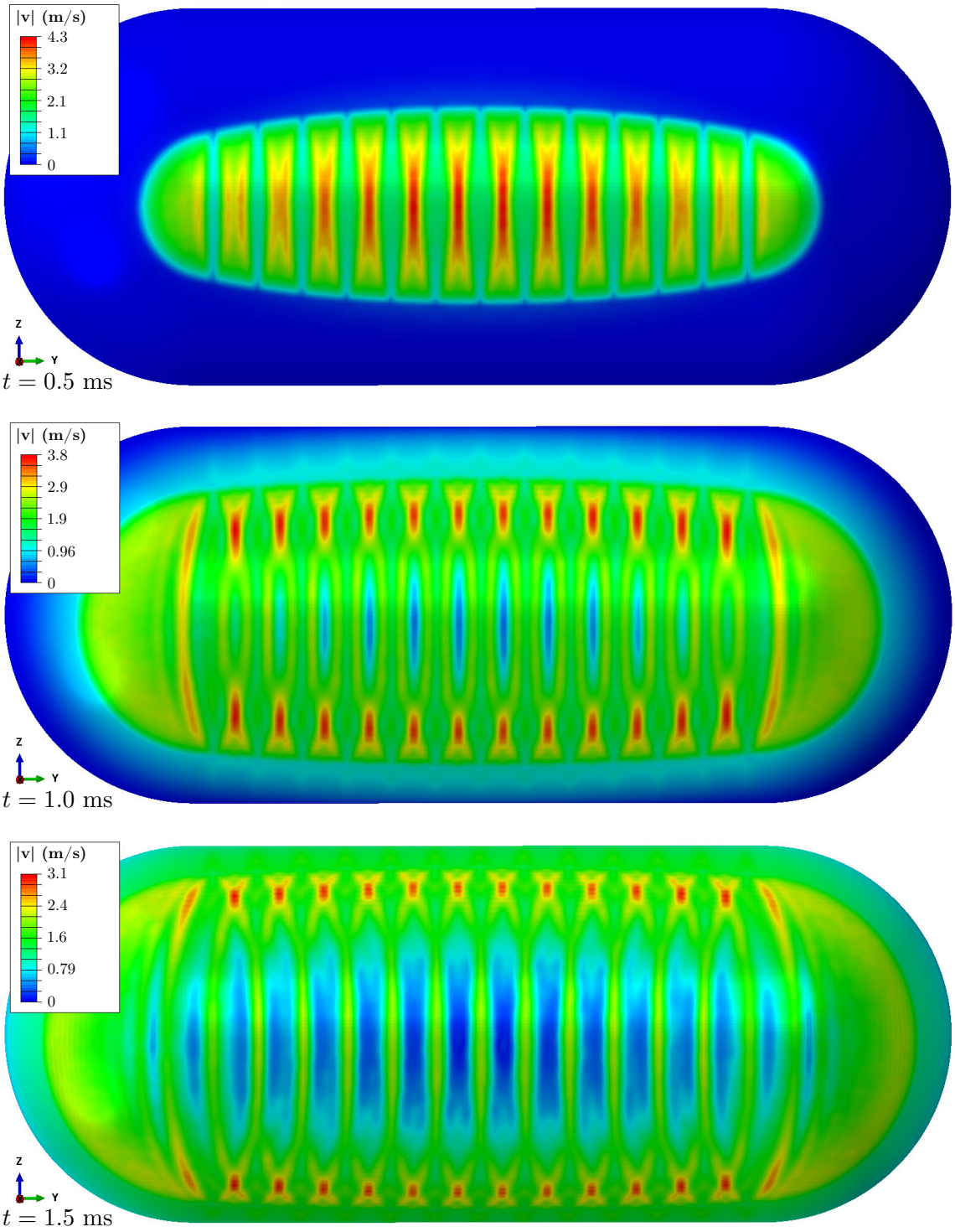

Figure 5.11: Snapshots of the velocity magnitude |v| on the hull surface, in the front zone.

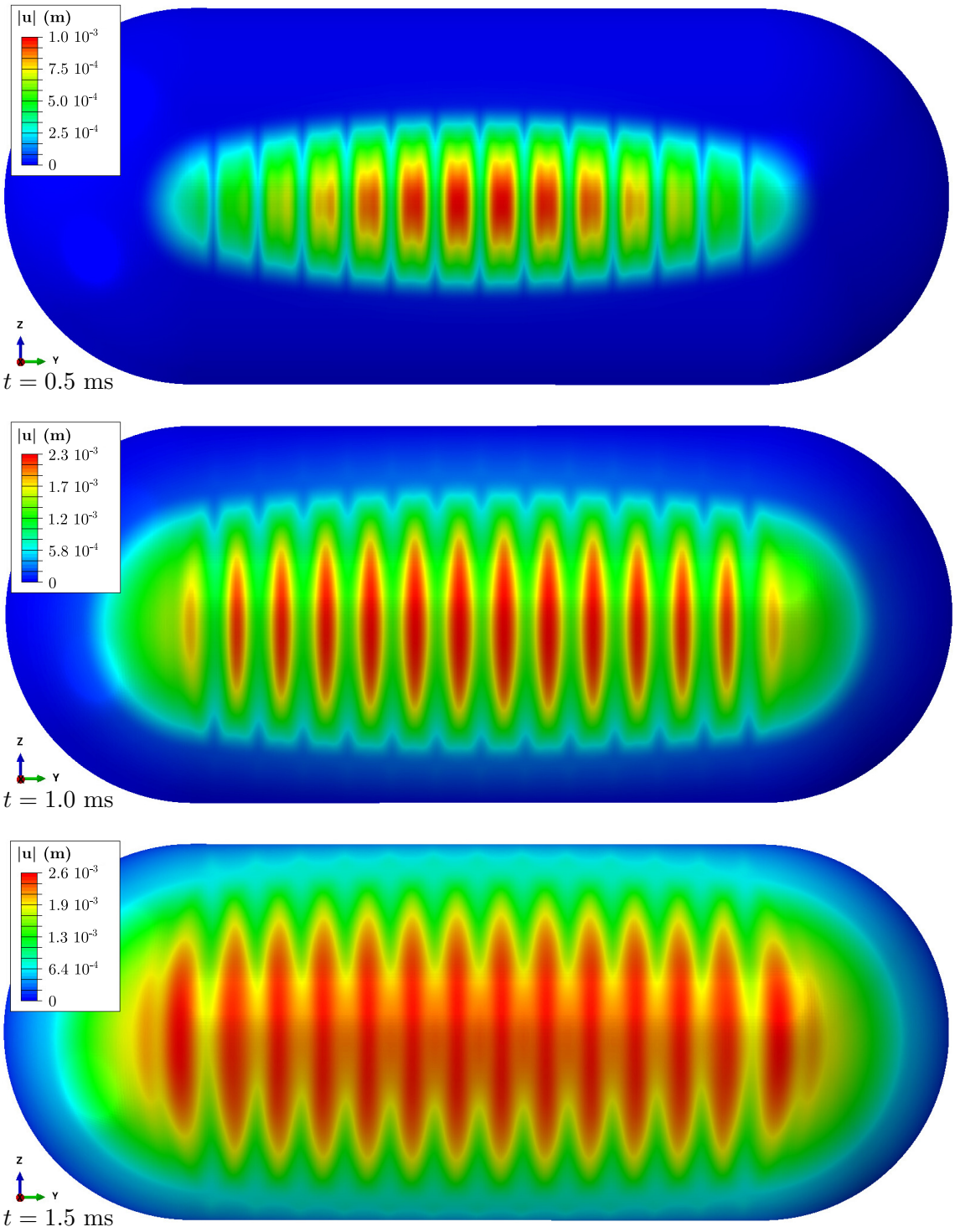

Figure 5.12: Snapshots of the displacement magnitude |u| on the hull surface, in the front zone.

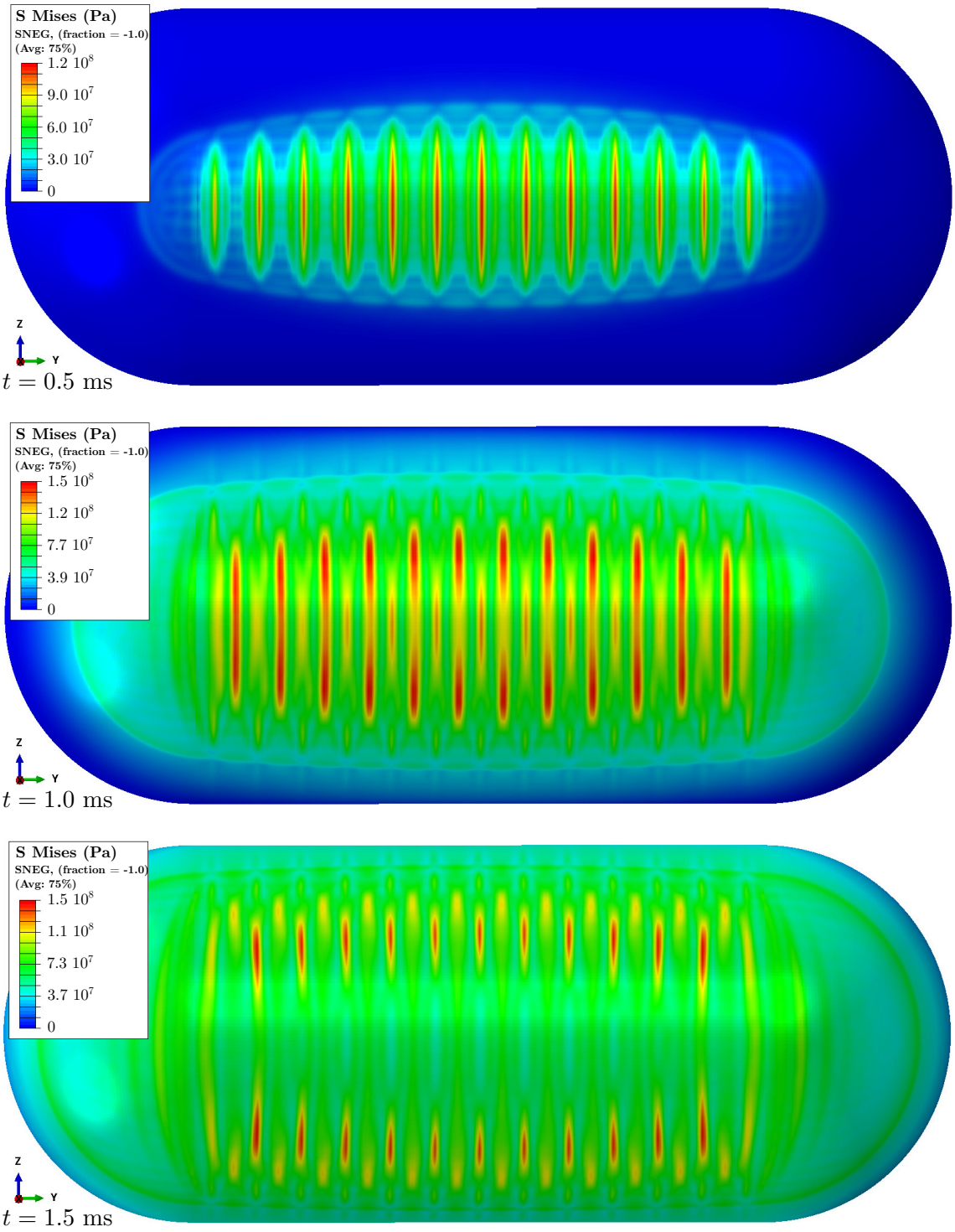

Figure 5.13: Snapshots of the Von Mises stress on the hull surface, in the front zone.

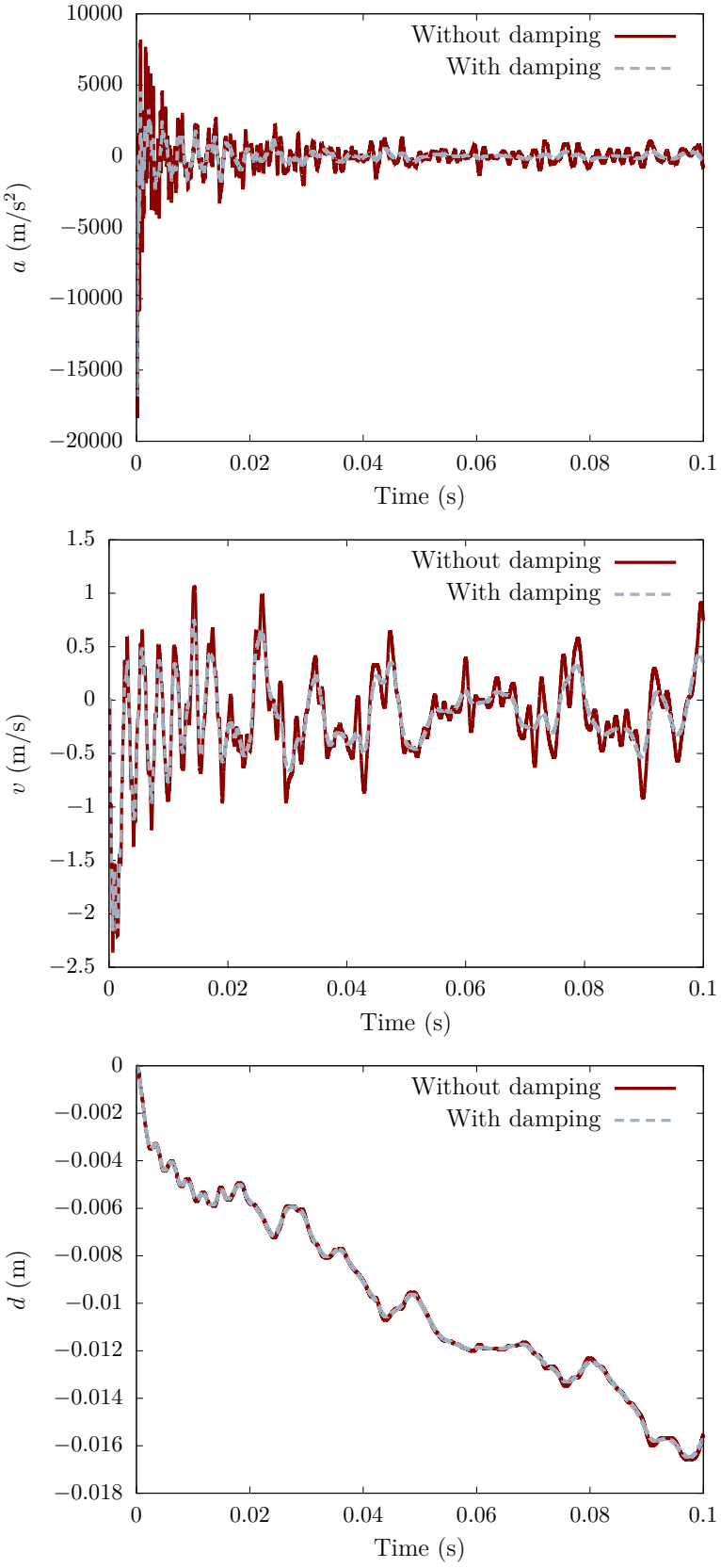

Figure 5.14: Acceleration, velocity and displacement at the standoff point, effects of the Rayleigh damping.

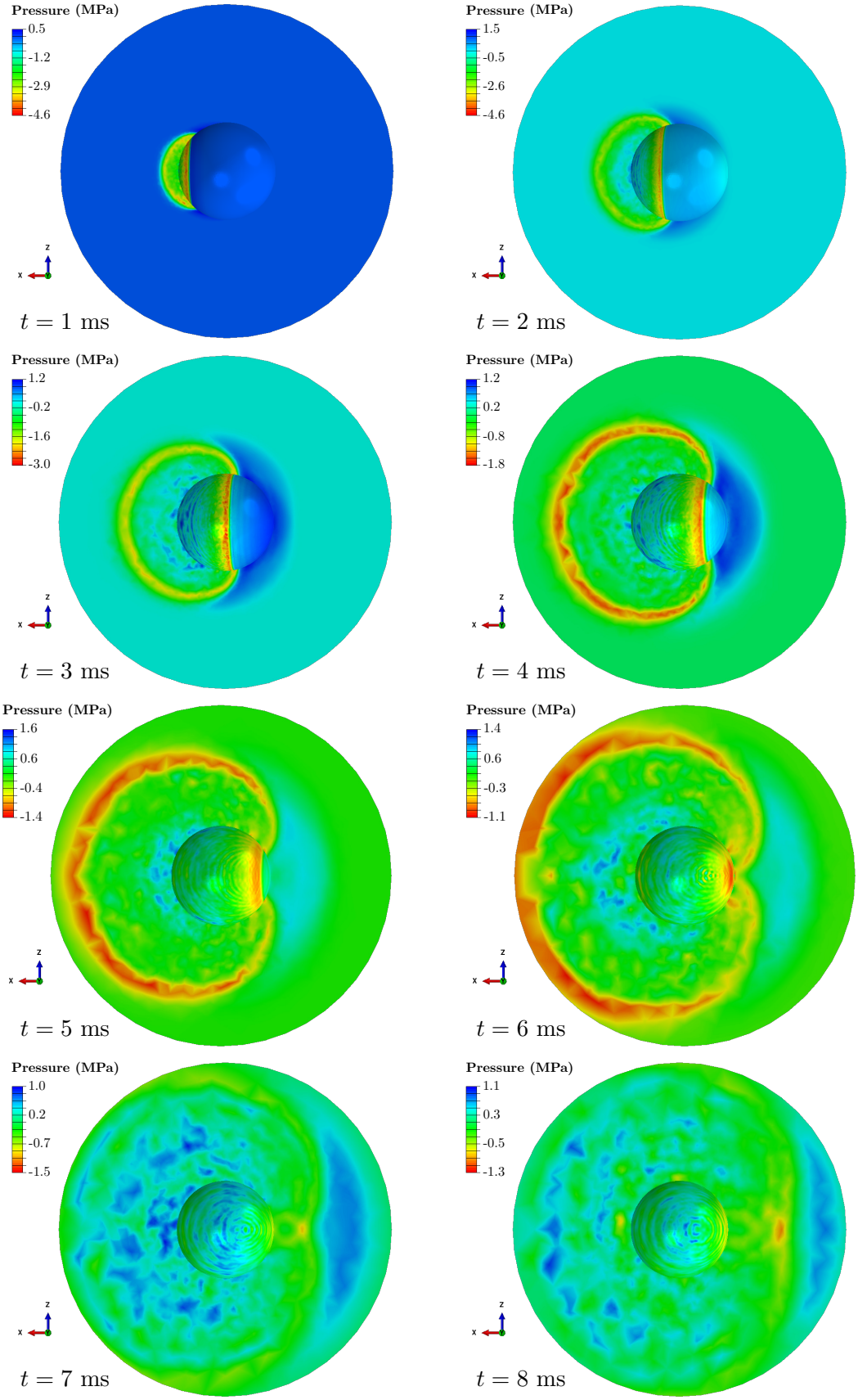

Figure 5.15: Snapshots of the radiated pressure p^{rad} in the FE fluid domain, in the cross-section containing the explosion. Illustration of the efficiency of the absorbing boundary conditions set on the exterior fluid surface Γ_∞.

5.2.2 Fluid-structure interaction for the gas bubble part

We now discuss the bubble part of the FSI problem (step 3 in Figure 5.4), and in particular the numerical junction with the shock wave phase.

The gas bubble of an UNDEX of 100 kg. Similarly to Section 4.6.2, we first study the effects of the bubble on the structure treated as rigid. The obstacle is meshed with $N_f \simeq 4.4\ 10^3$ fluid DOFs, $h \simeq 0.3$ m (we do not need a very refined mesh for the rigid motionless case), and $T_{\mathcal{B}} = 0.5$ s, $M = 2000$. The explosion of 100 kg of TNT at a water depth $\xi_{\text{exp}} = 100$ m generates a gas bubble of maximum radius and pseudo-period provided by (1.25) with $K_3 = 2.11$ SI and $K_4 = 3.50$ SI, so

$$T \simeq 0.19 \text{ s}, \quad R_{\max} \simeq 3.4 \text{ m}. \tag{5.1}$$

The Hicks model we use provides the time-dependent bubble radius and bubble depth shown in Figure 5.16. The model leads to a slightly smaller value of $R_{\max}$ than expected (see (5.1)), and underestimates energy losses (see Section 4.6.2).

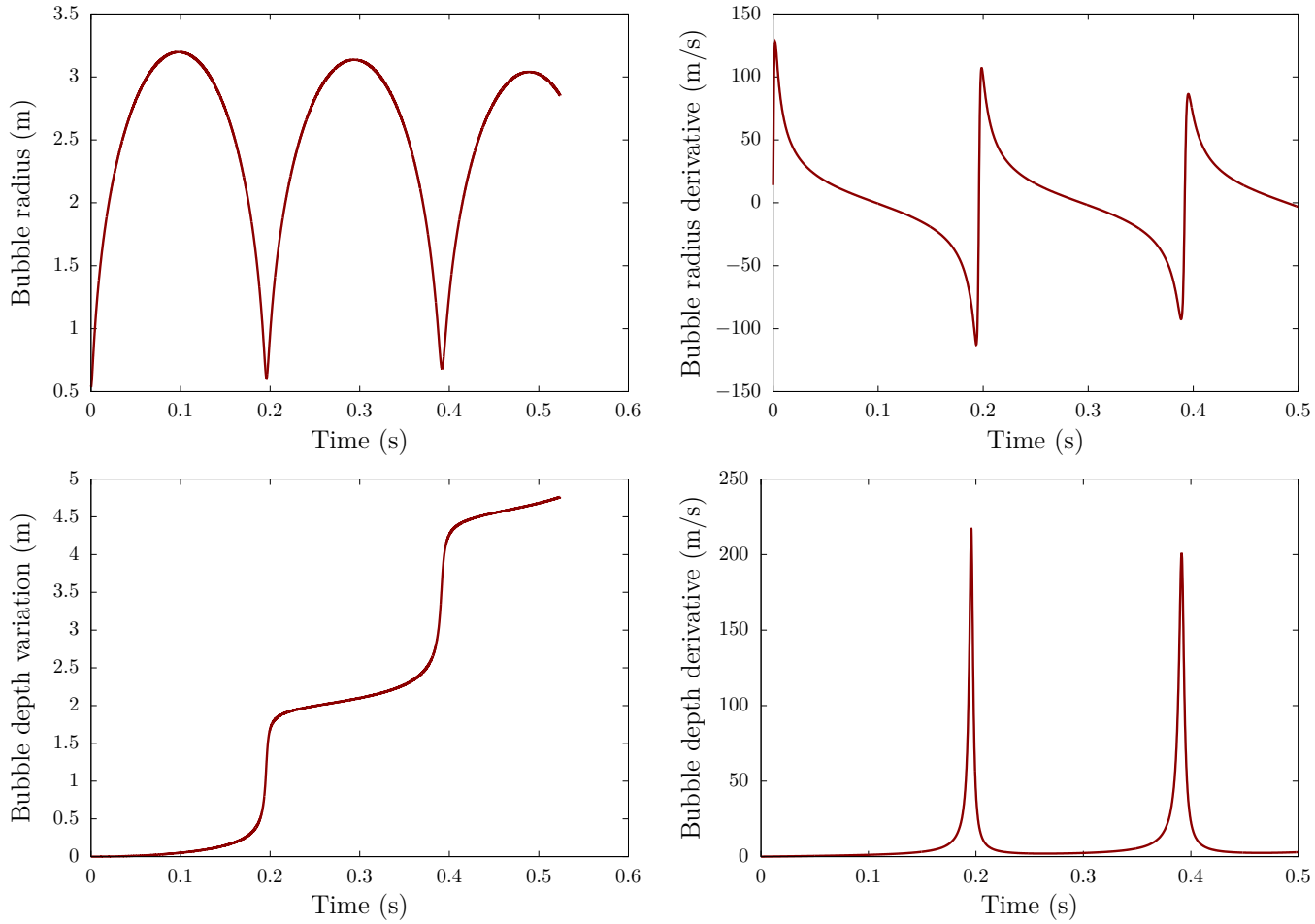

Figure 5.16: Bubble radius and depth variation obtained with the Hicks model, for an UNDEX of $W = 100$ kg of TNT at water depth $\xi_{\text{exp}} = 100$ m.

We compute the velocity potential and pressure at the obstacle surface Γ like in Section 4.5.1. The ambient velocity potential is given by (1.27) under our assumption of a

purely incompressible flow:

$$\phi^{\text{amb}}(r,\theta,t) = -\frac{R^2(t)\dot{R}(t)}{r} - \frac{R^3(t)\dot{Z}(t)}{2r^2}\cos\theta\,,$$

where θ is defined as in Figure 1.4. Figure 5.17 shows the pressure obtained on the time interval $[0, T = T_{\mathcal{B}} - T_{\mathcal{W}}]$. The high value of $T_{\mathcal{W}}$ (100 ms, instead of 25 ms, for the reasons previously explained in Section 5.2.1) implies that the beginning of the first bubble period is not taken into account. It also entails that the pressure varies significantly during the smoothing process, and compels us to increase the value of T_{smooth} (set to 20 ms instead of 10 ms).

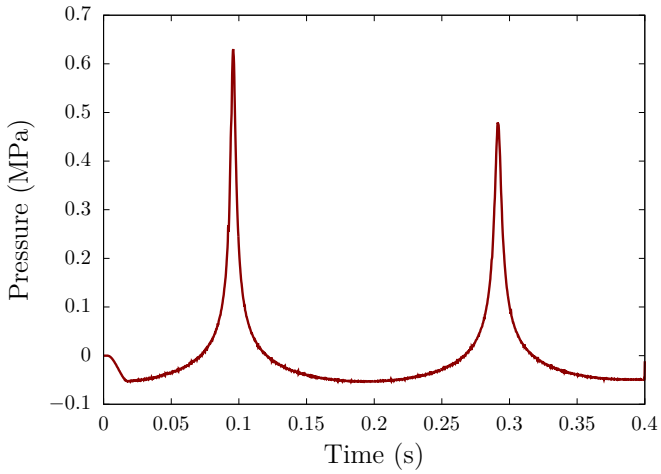

Figure 5.17: Total pressure on the time interval $[0, T = T_{\mathcal{B}} - T_{\mathcal{W}} = 400$ ms$]$. Smoothing process applied with $T_{\text{smooth}} = 20$ ms.

Coupled FSI part (work in progress). As of this writing, we have not obtained the results of the FSI coupling for the bubble phase, with the input state provided by the shock wave part. As explained in Sections 4.6.3 and 4.7, the bubble procedure is still a work in progress. In particular, we are facing convergence issues in the sub-cycling procedure, which we managed to overcome using relaxation techniques when the structure is at initial rest (see Section 4.6.3). Our procedure still needs refinement when applied with a disturbed initial state. We nonetheless achieved to get results when using a very short time step. However, a too-short time step implies a too-short time duration $T_{\mathcal{B}}$ (less than one bubble expansion), because we cannot consider more than $M \sim 2000$ time steps to preserve acceptable computational times.

We are currently working on a way to overcome this problem, i.e., make the procedure converge, by investigating numerical techniques, as well as modifications of the structure model. Typically, we are examining the influence of the overall structure model mass on the procedure convergence.

Alternatively, we could present results of the bubble phase without considering the shock wave part, like in Section 4.6, but they would not be very interesting for the specific case (structure and explosion) considered. Indeed, given the small structure length compared to the case studied in Section 4.6, we expect we would observe mostly rigid displacement, and less bending than in Section 4.6.

Though we cannot perform the junction yet, our procedure achieves the industrial goals. Indeed, in the case of elasticity (no plasticity), the results obtained by starting the bubble

procedure with a structure at initial rest (like in Section 4.6) are seen as satisfactory. When the shock wave induces plasticity, we can recourse to an *ad hoc* treatment in the wake of the shock wave procedure, to steady the structure response, and then use the deformed (but steady) structure state as input for the bubble procedure.

5.3 Conclusion and outlook

This chapter presented a typical engineering application of the numerical tool developed during this work, based on the numerical procedures presented in Chapters 2 to 4. We considered the example of a short (compared to a submarine) cylindrical stiffened hull closed by two half-spheres that is subjected to an explosion of 100 kg of TNT at a standoff distance $d_s = 46.7$ m. We first illustrated the efficiency of the $\mathcal{Z}$-BEM procedure to compute the reflected field induced by the shock wave. Then, we simulated the behaviour of the deformable stiffened hull during the shock wave phase. As expected, the stiffeners limit local deformations. The structure locally vibrates due to the high-frequency excitations. We had to introduce some numerical damping to reduce these vibrations before starting the bubble procedure. Despite the smoothing processes, we did not yet achieve to solve the FSI coupling during the bubble phase, when performing the junction with the shock wave phase. We are currently working on overcoming this problem. However, we stress that, even without the junction, the overall procedure achieves the industrial goals.

We are very satisfied with the results obtained for the shock wave part, especially given the rather challenging problem considered. To treat even more realistic (longer) geometries, we need to recourse to mesh interpolation.

Mesh interpolation between the two phenomena. Apart from the issues discussed in Section 5.2.2, our first prospect is to consider an industrial application with a realistic submarine hull, with dimensions similar to those presented in Section 4.6 (length $2L = 73.3$ m), enhanced with some submarine parts, notably in order to consider a realistic mass of the model (see Section 4.7). With current procedure developments, it is possible to separately treat the shock wave and bubble parts for this realistic industrial case. However, one improvement is required to treat the bubble part in the wake of the shock wave phase.

The bubble procedure can work with meshes coarser than those needed in the shock wave part. Therefore, an efficient way to perform the junction is to use meshes fine enough for the shock wave part, then interpolate the fields on coarser meshes for the bubble procedure. We are currently investigating the mesh-to-mesh solution mapping of Abaqus®. We did not yet achieve to set up the interpolation step, and therefore use the Abaqus® standard restart options (Dassault Systèmes SIMULIA, 2017). This compels us to use the same structure model (same meshes) for both procedures. As it is impossible (due to computational resource limitations) to treat the bubble phenomenon with too-fine meshes, we would have no choice but to use coarse meshes in the shock wave part, so that the following bubble procedure may be performed. This would lead to less precise results in the shock wave procedure, hence the need for mesh interpolation.

Conclusion and prospects

It is now time to conclude this PhD work. Firstly, we summarise all of the content presented in this dissertation. Secondly, we stress our contributions, notably by identifying our start and end points, in terms of both knowledge and software development. Thirdly, we discuss the consequences of some choices made in the industrial context. Finally, we give some prospects for future studies (some being already investigated).

Recalling initial question: how do we address the problem?

Our entire work was driven by the question raised in the introduction: *how do we address the problem of the fluid-structure interaction between a submarine and a remote underwater explosion?*

To answer this question, we first had to fully understand the physical phenomena taking part in the problem. In Chapter 1, we focused on the fluid component of the interaction, so the effects of an underwater explosion. We introduced the shock wave and gas bubble events, and showed that they both have to be taken into account in the context of fluid-structure interactions. For remote explosions, the shock wave propagation is approximately governed by the wave equation, in the framework of linear acoustics, whereas the gas bubble is modelled under the assumptions of potential and incompressible flow. At the end of the chapter, we proposed a way to perform the junction between the two mutually exclusive models, based on the multi-scale method, that turned out to reduce to a simple numerical junction for remote underwater explosions.

Chapter 2 was dedicated to the design, implementation and validation of an efficient numerical method for large-scale 3D rapid transient wave problems. Such problems are tricky because numerical methods based on geometry discretisation (mesh), such as the boundary element method (BEM) or the finite element method (FEM), often require to solve a linear system (from the spatial discretisation) for each time step. We proposed a numerical method to efficiently deal with 3D rapid transient acoustic problems set in large (infinite) exterior domains. Using the $\mathcal{Z}$-transform and the convolution quadrature method (CQM), we first presented a straightforward way to reframe the problem to the solving of a large amount (the number of time steps, M) of frequency-domain BEMs. Then, taking advantage of a well-designed high-frequency approximation (HFA), we drastically reduced the number of frequency-domain BEMs to be solved, with little loss of accuracy. The complexity of the resulting numerical procedure, labelled $\mathcal{Z}$-BEM, turns out to be $O(1)$ in regards to the time discretisation and $O(N \log N)$ for the spatial discretisation, the latter being prescribed by the complexity of the fast multipole-based BEM solver used by the $\mathcal{Z}$-BEM. Finally, we demonstrated the efficiency of the method on some examples of FSI applications, notably the scattering problem of an underwater explosion shock wave by a full-scale submarine.

The shock wave fluid-structure coupling was studied in Chapter 3. After a brief

presentation of monolithic and partitioned fluid-structure interaction (FSI) procedures, we presented the $\mathcal{Z}$-BEM/FEM coupling we intended to perform. Inspired by space-time domain decomposition methods (DDMs), it consists in alternately solving structure and fluid problems on the entire time interval $[0, T]$, instead of exchanging information at each time step. That kind of iterative procedures is known to be more efficient with Robin boundary conditions than Neumann ones. Unfortunately, a major practical constraint prevented us from using Robin boundary conditions in this work, and compelled us, *for the time being*, to design and switch to a hybrid $\mathcal{Z}$-BEM/FEM/FEM method in which the coupled part of the FSI problem is solved with a common monolithic FEM/FEM coupling. This hybrid method, that takes advantage of the fluid decomposition into a radiated (radiation problems) and a reflected (scattering problems) components, is nonetheless rather efficient – compared to the solutions produced using other methods –, as it was shown on the reference case of the FSI between a long cylinder and an underwater shock wave.

Chapter 4 focused on the subsequent oscillating bubble event. We first stressed the time-dependence of the geometric domains, by contrast to the shock wave case. Given the specificities of the fluid problem, that reduces to multiple right-hand side problem-solving (under the assumption of re-usable BEM operators), we adopted a step-by-step FEM/BEM coupling. In this context, the hierarchical matrices ($\mathcal{H}$-matrices) permit an efficient (fast and accurate) solving of the fluid equations, by re-using, at each time-step, already computed BEM operators. The procedure was validated on the simple problem of a rigid sphere in a uniform time-dependent flow, and we showed the importance of sub-cycling at each time step to guarantee the convergence to the correct FSI solution, while performing uncoupled fluid and structure problem-solving. Finally, we studied the FSI between a submarine stiffened hull and a powerful explosion ($W = 1000$ kg of TNT at $d_0 = 50$ m). As expected, the results showed that the gas bubble mainly causes rigid motion and bending, but very little local deformations, when the previous shock wave phenomenon is not considered.

This work concluded with the treatment of an industrial case: a stiffened hull subjected to a remote underwater explosion. The purpose of Chapter 5 was then to show the efficiency of the computational method, when gathering all the results obtained throughout Chapters 2 to 4. It demonstrated the capabilities of the shock wave procedure to deal with the realistic problems encountered in the naval industry. We are still working on the bubble phase, to solve the associated FSI problem in the wake of the shock wave phase. We explained the convergence issues we are facing in the FEM/BEM sub-cycling process for the bubble phase, and gave some insights on how to resolve them.

Review of our contributions

Given the industrial context of this work (supported by a mixed public-private funding in the French CIFRE doctorate framework), we would like to stress and summarise our contributions, in terms of both knowledge and practical software developments.

The content of Chapter 1 largely summarises available literature. However, we tried to enhance the way the concepts and results are introduced, notably by justifying any assumption or approximation. For instance, we paid particular attention to the validity of the linear acoustic model for the shock wave propagation, notably through computation of the associated acoustic energy in Section 1.2.2. Also, we tried to outline a theoretical basis to the unification between the bubble and shock wave phases, using the multi time scale method, in Section 1.4.

Chapter 2 (and its article version, Mavaleix-Marchessoux et al., 2020) presents a significant part of our contribution. Based on the (already known) convolution quadrature method (CQM) and the $\mathcal{Z}$-transform, we designed a procedure that can deal with large-scale rapid transient wave propagation problems by recourse to an *ad hoc* high frequency approximation (HFA). Contrary to traditional CQM-based BEMs, our procedure exhibits $O(1)$ time complexity (see Section 2.5.5). Once designed, we implemented our HFA-enhanced $\mathcal{Z}$-BEM in the frequency-BEM solver COFFEE developed at POEMS. We proved the feasibility of the method for uncoupled FSI on the simple problems of a pulsating sphere (radiation problem) and the scattering of a spherical wave by a small geometry. Then, we implemented some numerical improvements:

- Mesh interpolation (see Section 2.5.6) using the software feflo.a (Loseille, 2017).
- Efficient computation of the FFT required in the CQM on GPUs (CUDA cores).
- Optimised parallel computation of the frequency problems solved with the FM-BEM.

These improvements made possible a concrete application of the method: the scattering of an UNDEX shock wave by a complex submarine-shaped obstacle (see Section 2.7). Solving this challenging problem, we tuned the HFA to improve the results in the case of non-convex obstacles (see Section 2.7.2).

We now focus on our contribution in the case of coupled FSI problems, starting with the shock wave part in Chapter 3. We designed a coupling procedure, namely $\mathcal{Z}$-BEM/FEM procedure, inspired from domain decomposition methods (DDMs), that alternates fluid and structure solving on the entire time interval $[0, T]$ (see Section 3.2). We checked that the $\mathcal{Z}$-BEM/FEM coupling procedure is not well suited to Neumann boundary conditions in Section 3.2.2, but we did not have the opportunity to implement the procedure with Robin boundary conditions, because of practical constraints. Thereafter, we designed the hybrid $\mathcal{Z}$-BEM/FEM procedure presented in Section 3.3, that satisfies the industrial requirements, and proved its efficiency in the reference case of a long (infinite) cylinder subjected to an UNDEX shock wave. This latter numerical test is the result of a team work[1]: the analytical solution was obtained by Rakotomalala et al. (2021) and the FEM/FEM solution by Khoun (2021). We defined the reference case, obtained the solution of our hybrid $\mathcal{Z}$-BEM/FEM procedure, post-processed the results of all procedures, and carried out the result analyses. For the practical coupling with Abaqus®, we used the basis of the `C++` coupling simulation engine provided by Abaqus®, enhanced by the authors of (Véron, 2016), which we adapted to efficiently transfer data (in RAM memory) with the software COFFEE. We carried out the industrial application presented in Chapter 5, to confirm the efficiency of the hybrid $\mathcal{Z}$-BEM/FEM procedure.

We then used a rather straightforward step-by-step FEM/BEM coupling procedure to solve the FSI problem for the bubble part, in Chapter 4. The use of $\mathcal{H}$-matrices in the context of multiple right-hand sides is also known. Our contribution then rather lies in the efficient numerical implementation in the context of High Performance Computing. In particular, we developed a `Python` interface to connect the Abaqus® coupling engine to COFFEE. Similarly to the procedure developed for the shock wave phase, the python interface permits data transfers in RAM memory. Also, it allows to keep in RAM memory the time-independent BEM operators computed and stored at the first time step. A simpler (naive) procedure that would couple the fluid and structure codes without this `Python` interface would need to store in disk memory the BEM operators before leaving the fluid code, and then the saving/loading times would be detrimental. We validated the FSI coupling procedure in the simple case of a rigid sphere in a uniform time-dependent flow

[1] We thank again all the participants!

in Section 4.5, and demonstrated the procedure efficiency for the bubble FSI problem, in the case where the structure is at initial rest, in Section 4.6.

In the industrial context of this work, a useful practical contribution concerns the version control of the numerical tools we developed. We used `Git` for an efficient numerical development of our tools. Also, we thoroughly studied the numerical performance of our codes with two complementary set of tools recommended by the Performance Optimisation and Productivity (POP) institute (see https://pop-coe.eu/partners/tools):

- Extrae (captures information during the execution) and Paraver (visualises the traces generated by Extrae);
- Score-P (captures information during the execution) and Cube (incorporated in Score-P, visualises the traces).

Then, we deployed a clean stable version of our software on a cluster for industrial purposes, added simple configuration files so that engineers may use the code easily, and wrote a documentation for both installation and usage.

Comments on an important industrial choice

In this section, we summarise the consequences of an important industrial choice: the use of Abaqus® for the structure FEM part of the FSI. We believe it is important to objectively expose these consequences, so that future studies may be carried out in full knowledge of the facts.

The industrial context. The choice of Abaqus® is motivated by the industrial context. Abaqus® offers a user friendly interface that permits to easily design a model, using various available features, and solve common engineering problems. It is a very adequate tool in production engineering, which has to deal with various constraints, e.g., cost issues, deadlines,... The use of Abaqus® in this thesis offers the substantial advantage of a fast deployment of the numerical code we developed in production engineering units. Also, it permitted to take advantage from previous (PhD) works, e.g., (Véron, 2016).

Limitations of black-box uses. Abaqus® is not an open source software. This compels us to use it in a black-box manner, that leads to practical limitations. First, we were not able to implement the $\mathcal{Z}$-BEM/FEM procedure we designed in Section 3.2 for the shock wave FSI part, which requires the use of Robin boundary conditions (see Section 3.2.2). Unfortunately, these conditions could not be used in Abaqus® invoked in black-box fashion. Moreover, the CSE interface that allows to couple Abaqus® to an external code is very limited and not as user friendly as the common Abaqus® interface.

Limitations for massive parallel computing. The FSI bubble procedure we developed hit severe efficiency limitations caused by the licencing policy of Abaqus®. As explained in Section 4.6.3, the need for one "token" for each CPU hinders massive parallelisation, making the overall procedure computational time unattractive.

Our numerical tool in industry. Despite all the practical constraints and limitations induced by the choice of a not-open-source software to handle the structure part of the FSI problem, we conclude by stressing that it helped to quickly fulfil (within three years) the industrial goal: a numerical tool that can be used in production engineering (at least

for the shock wave part). We are glad we were able to achieve this ambitious target, and we reckon it is partly thanks to the industrial choices.

What's next?

As explained above, this PhD work results in the first version of a numerical tool to solve underwater explosion FSI problems. We see many prospects, which we now present in the natural order of short-term to longer-term objectives.

Short-term improvements of the bubble procedure. There remain some basic numerical improvements of our procedures, especially regarding the gas bubble part. Indeed, as explained in Chapters 4 and 5, the CPU time may be reduced by (i) using a variable time step and (ii) improving the sub-cycling convergence. We are currently investigating some methods available in the literature to improve the convergence of iterative methods, and hope to present in the near-future a bubble procedure made more efficient by faster sub-cycling. Once this is achieved, we will study the difference between the incompressible model and the model with $O(1/c)$ corrections presented in Section 4.7. Also, the bubble procedure results presented in Section 4.6 will be compared against a simple beam model. Lastly, we will solve the convergence issues faced when using the output shock wave state as input for the bubble FSI procedure (see details in Section 5.2.2).

Mid-term improvements of the shock wave procedure. As explained in Chapter 3, the hybrid $\mathcal{Z}$-BEM/FEM/FEM method we developed to solve the shock wave FSI part requires an arbitrary truncated volume FE fluid mesh. In contrast, the $\mathcal{Z}$-BEM/FEM coupling we initially intended to perform, presented in Section 3.2, is a purely FEM/BEM coupling that does not require any volume mesh of the exterior fluid. The collaboration between the POEMS laboratory and Naval Group continues with a new PhD thesis that notably aims to define and implement an algorithm performing the fluid-structure coupling on the basis of full BEM treatment of the fluid. Moreover, both the shock wave and bubble procedures will be improved to take into account the free surface and the sea bed, thus enlarging the scope to any kind of vessels and configurations.

Another interesting prospect concerns the FM-BEM solving process used in the $\mathcal{Z}$-BEM. The M_B BEM problems actually solved with the FM-BEM constitutes the most time-consuming task of the $\mathcal{Z}$-BEM. We considerably reduced the CPU time of the Fast Multipole Method (FMM) steps using parallel computing. While optimising the code performance using the tools of the POP institute (see `https://pop-coe.eu/partners/tools`), we realised that, when considering complex geometries, as in Section 2.7, there exist some FMM boxes that encapsulate a lot of geometrical nodes (e.g., near the back planes of a submarine). This effect is accentuated when considering non-uniform meshes, which is common for complex geometries. In that case, the near contribution part of the FMM process, usually dealt with using standard BEM techniques, becomes costly. A possible way to overcome this difficulty could be to artificially increase the number of levels of the FMM, but this leads to numerical errors and unwanted behaviours, as the number of levels must be set against a criterion related to the input frequency (Chaillat et al., 2017a, 2008). To speed up the near contribution part, we suggest to investigate a hybrid method in which the near contributions are dealt with using $\mathcal{H}$-matrices rather than standard BEM techniques.

Mid-term comparison with experimental data. To validate the tools we developed for industry, we must treat a concrete industrial configuration (full-scale submarine), following similar steps to those of Chapter 5, and compare the simulation results against (available) experimental data. This will notably allow to assess several available bubble models, and determine whether a new bubble model should be derived.

Long-term improvements of the junction between the two phenomena. In this work, we chose to separately treat the shock wave and bubble phases. If this offers many advantages, such as re-usable BEM operators for the fluid part of the bubble phase (see Section 4.3.1), it also compels us to artificially re-connect the shock wave and bubble phases. Despite the numerical (hence artificial) smoothing procedures we used, we did not yet succeed to practically blend the two phases (see Section 5.2.2) for realistic configurations. Then, we believe it could be interesting to investigate a unified numerical treatment of the shock wave and the bubble phenomena. Consider for instance the historical approach of the *Doubly Asymptotic Approximation (DAA)* (see Sections 3.1.2 and 4.7). The use of the same (approximate) equation for both the shock wave and bubble parts is a key advantage. Along the same lines, we could design a unified procedure that accounts for wave effects at small times (but more accurately than the DAA, given the advent and tremendous progress in fast BEMs since 1980) and smoothly turns to incompressible flows for larger times. A FEM-structure/BEM-fluid coupling procedure is well suited to this kind of treatment. This constitutes another argument in favour of implementing a full BEM-fluid/FEM-structure coupling, as outlined in Section 3.2.

Long-term prospect: an efficient tool for fluid-structure interaction in the naval industry. During this PhD, we had the great opportunity to discuss with experts of the naval industry, and discover a wide range of topics. Doing so, we realised that the scope of the $\mathcal{Z}$-BEM we developed is broader than expected. For instance, in addition to the study of underwater explosions, we may apply our method in the context of stealth technology, to solve the problem of a submarine subjected to acoustic sonars (that may use high frequencies), or to compute the submarine acoustic signature.

A very interesting prospect is then to adapt our code so that it may be used in any context for which the BEM is appropriate for the fluid part. Naval Group could then operate a unique BEM code whose improvements would simultaneously benefit the simulations of many fluid-structure problems and stealth analyses.

Bibliography

T. Abboud, J.-C. Nédélec, and B. Zhou. Méthode des équations intégrales pour les hautes fréquences. *Comptes rendus de l'Académie des sciences. Série 1, Mathématique*, 318(2): 165–170, 1994. 50, 51

T. Abboud, J.-C. Nédélec, and J. Volakis. Stable solution of the retarded potential equations. *17th Annual Review of Progress in Applied Computational Electromagnetics*, pages 146 – 151, 2001. 38

Z. Adnani. *Modélisation numérique tridimensionnelle de l'interaction sol-structure avec prise en compte des effets de site.* PhD thesis, Université Paris Saclay, 2018. 73

A. Aimi, M. Diligenti, C. Guardasoni, I. Mazzieri, and S. Panizzi. An energy approach to space-time Galerkin BEM for wave propagation problems. *Int. J. Numer. Meth. Engrg.*, 80(9):1196–1240, 2009. 38, 43

G. Allaire. *Analyse numérique et optimisation. Une introduction à la modélisation mathématique et à la simulation numérique.* École polytechnique, Paris, 2nd edition, 2012. 17, 34

F. Alouges, M. Aussal, and E. Parolin. FEM-BEM coupling for electromagnetism with the sparse cardinal sine decomposition. *ESAIM: ProcS*, 63:44–59, 2018. 74

F. Amlani, S. Chaillat, and A. Loseille. An efficient preconditioner for adaptive Fast Multipole accelerated Boundary Element Methods to model time-harmonic 3D wave propagation. *Computer Methods in Applied Mechanics and Engineering*, 352:189 – 210, 2019. 108

T. G. Anderson. *Hybrid Frequency-Time Analysis and Numerical Methods for Time-Dependent Wave Propagation.* PhD thesis, California Institute of Technology, 2020. 53

T. G. Anderson, O. P. Bruno, and M. Lyon. High-order, dispersionless "fast-hybrid" wave equation solver. Part I: O(1) sampling cost via incident-field windowing and recentering. *SIAM Journal on Scientific Computing*, 42(2):A1348–A1379, 2020. 53, 127

H. Antes. A boundary element procedure for transient wave propagations in two-dimensional isotropic elastic media. *Finite Elem. Anal. Des.*, 1:313 – 322, 1985. 38

A. B. Arons and D. R. Yennie. Energy partition in underwater explosion phenomena. *Review of Modern Physics*, 20(3):519 – 536, 1948. xiii, 6, 7, 9, 11, 14, 15, 24, 188, 189, 190, 191, 198, 200

A. B. Arons, J. P. Slifko, and A. Carter. Secondary pressure pulses due to gas globe oscillation in underwater explosions. *J. Acoustical Society of America*, 20(3):271 – 276, 1948. 9

B. B. Baker and E. T. Copson. *The mathematical theory of Huygens' principle*. Chelsea Publishing Company, 1950. 50

P. K. Banerjee. *The Boundary Element Methods in Engineering*. McGraw-Hill, 2nd edition, 1994. v, 32, 43, 44, 104

L. Banjai and S. Sauter. Rapid solution of the wave equation in unbounded domains. *SIAM Journal on Numerical Analysis*, 47(1):227–249, 2009. 38, 41

L. Banjai, M. Messner, and M. Schanz. Runge-Kutta convolution quadrature for the Boundary Element Method. *Comput. Methods Appl. Mech. Engrg.*, 245/246:90 – 101, 2012. 38

G. Barras. *Interaction fluide-structure : Application aux explosions sous-marines en champ proche*. PhD thesis, Université des Sciences et Technologies de Lille 1, 2012. iii, 6, 31

G. Barras, M. Souli, N. Aquelet, and N. Couty. Numerical simulation of underwater explosions using an ALE method. The pulsating bubble phenomena. *Ocean Engineering*, 41:53 – 66, 2012. iv, 19

A. Bayliss, M. Gunzburger, and E. Turkel. Boundary conditions for the numerical solution of elliptic equations in exterior regions. *SIAM Journal on Applied Mathematics*, 42(2): 430–451, 1982. 84, 212

M. Bebendorf. *Hierarchical Matrices*, volume 63 of *Lecture Notes in Computational Science and Engineering*. Springer, 2008. 108

M. Bebendorf and S. Rjasanow. Adaptive low-rank approximation of collocation matrices. *Computing*, 70:1 – 24, 2003. 111

M. Bebendorf, C. Kuske, and R. Venn. Wideband nested cross approximation for Helmholtz problems. *Numerische Mathematik*, 130:1 – 34, 2015. 111

E. Bécache, D. Givoli, and T. Hagstrom. High-order Absorbing Boundary Conditions for anisotropic and convective wave equations. *Journal of Computational Physics*, 229(4): 1099–1129, 2010. 81

J. P. Best. The effect of non-spherical collapse on determination of explosion bubble parameters. Technical Report DSTO-RR-0238, Defence Science & Technology, Australia, 2002. 8, 21, 22, 198, 199, 200

T. Betcke, N. Salles, and W. Smigaj. Overresolving in the Laplace domain for convolution quadrature methods. *SIAM J. Sci. Comput.*, 39(1):A188 – A213, 2017. v, 38, 41

G. Bianchi and R. Sorrentino. *Electronic Filter Simulation & Design*. McGraw-Hill Education, 2007. 93

J. Bielak and R. C. Maccamy. Symmetric finite-element and boundary integral coupling methods for fluid-solid interaction. *Quart. Appl. Math.*, 49:107 – 119, 1991. 43

M. Bonnet. *Boundary integral equation methods in solids and fluids*. John Wiley & sons, 1999. v, 32, 35, 36, 43, 104

M. Bonnet, G. Maier, and G. Polizzotto. Symmetric Galerkin boundary element methods. *Appl. Mech. Rev.*, 51:669 – 704, 1998. 43

M. Bouajaji, B. Thierry, X. Antoine, and C. Geuzaine. A quasi-optimal domain decomposition algorithm for the time-harmonic Maxwell's equations. *Journal of Computational Physics*, 294:38–57, 2015. 76

L. Brančik. Programs for fast numerical inversion of Laplace transforms in MATLAB language environment. Technical report, Institute of Theoretical and Experimental Electrical Engineering, 1999. 205

J. Bremer, A. Gillman, and P.-G. Martinsson. A high-order accurate accelerated direct solver for acoustic scattering from surfaces. *BIT Numer. Math.*, 55:367–397, 2013. 38

J. M. Brett, M. Buckland, T. Turner, C. G. Killoh, and P. Kiernan. An experimental facility for imaging of medium scale underwater explosions. Technical Report DSTO-TR-1432, Defence Science & Technology, Australia, 2003. iv, xiii, 7, 8, 10, 22

S. R. Brinkley and J. G. Kirkwood. Theory of the propagation of shock waves. *Physical Review*, 72(9):606 – 611, 1947a. iv, 6, 188

S. R. Brinkley and J. G. Kirkwood. Theory of the propagation of shock waves from infinite cylinders of explosive. *Physical Review*, 72(11):1109 – 1113, 1947b. iv, 6, 188

K. Brochard. *Modélisation analytique de la réponse d'un cylindre immergé à une explosion sous-marine*. PhD thesis, École Centrale de Nantes, 2018. xiii, 7, 11, 31, 83

O. P. Bruno, C. A. Geuzaine, J. A. Monro Jr, and F. Reitich. Prescribed error tolerances within fixed computational times for scattering problems of arbitrarily high frequency: the convex case. *Philosophical Transactions of the Royal Society of London. Series A: Mathematical, Physical and Engineering Sciences*, 362(1816):629–645, 2004. 50, 51

S. Butterworth. On the theory of filter amplifiers. *Experimental Wireless and the Wireless Engineer*, 7:536–541, 1930. 92

B. Caudron. *Couplages FEM-BEM faibles et optimisés pour des problèmes de diffraction harmoniques en acoustique et en électromagnétisme* . PhD thesis, Université de Lorraine; Université de Liège, Belgique, 2018. 77

S. Chaillat. *Fast Multipole Method for 3-D elastodynamic boundary integral equations. Application to seismic wave propagation.* PhD thesis, École Nationale des Ponts et Chaussées, Paris, France, 2008. v, 32, 45, 47, 53, 54, 75

S. Chaillat, M. Bonnet, and J.-F. Semblat. A multi-level fast multipole BEM for 3-D elastodynamics in the frequency domain. *Comput. Methods Appl. Mech. Engrg.*, 197(49): 4233 – 4249, 2008. 46, 54, 161

S. Chaillat, M. Darbas, and F. Le Louer. Fast iterative boundary element methods for high-frequency scattering problems in 3D elastodynamic. *J. Comput. Phys.*, 341:429 – 446, 2017a. 38, 161

S. Chaillat, L. Desiderio, and P. Ciarlet. Theory and implementation of $\mathcal{H}$-matrix based iterative and direct solvers for Helmholtz and elastodynamic oscillatory kernels. *J. Comp. Phys.*, 351:165 – 186, 2017b. vi, xv, 45, 75, 108, 109, 110, 111

S. N. Chandler-Wilde and S. Langdon. A Galerkin boundary element method for high frequency scattering by convex polygons. *SIAM Journal on Numerical Analysis*, 45(2): 610–640, 2007. 50, 51

D. Clouteau, R. Cottereau, and G. Lombaert. Dynamics of structures coupled with elastic media – A review of numerical models and methods. *Journal of Sound and Vibration*, 332(10):2415 – 2436, 2013. 73

Code_Aster Open Source. General FEA software, EDF R&D, code_aster documentation. 2020. URL https://www.code-aster.org/V2/doc/default/en/index.php?man=commande. vi, 84, 207

COFFEE. Accelerated BEM software, developed at POEMS laboratory. 2020. URL https://uma.ensta-paris.fr/soft/COFFEE/. 45, 48, 75, 84, 111, 159

R. H. Cole. *Underwater explosions*. Princeton University Press, 1948. iii, 6, 7, 12, 13, 18, 31, 56, 83, 187, 188

J. S. Coles, E. A. Christian, J. P. Slifko, C. R. Niffennegger, and M. A. Rogers. Shock-wave parameters from spherical TNT charges detonated underwater. Published in *Underwater Explosion Research, Office of Naval Research*, 1:1085 – 1105, 1946. 12, 13

M. Costabel. Time-dependent problems with the boundary integral equation method. In *Encyclopedia of Computational Mechanics*, chapter 25. 2004. 38

J. Cousteix and J. Mauss. *Analyse asymptotique et couche limite*, volume 56 of *Mathématiques & applications*. Springer, 2006. 25, 26

M. Darbas, E. Darrigrand, and Y. Lafranche. Combining analytic preconditioner and fast multipole method for the 3-D Helmholtz equation. *J. Comput. Phys.*, 236:289–316, 2013. 38, 45, 75

E. Darve. The fast multipole method: Numerical implementation. *Journal of Computational Physics*, 160:195 – 240, 2000. v, 38, 45, 75

Dassault Systèmes SIMULIA. Abaqus documentation, example problems manual. 2009. URL https://classes.engineering.wustl.edu/2009/spring/mase5513/abaqus/docs/v6.6/books/exa/default.htm. 92

Dassault Systèmes SIMULIA. Abaqus documentation, theory, analysis and user guides. 2017. URL https://abaqus-docs.mit.edu/2017/English/SIMACAEEXCRefMap/simaexc-c-docproc.htm. 81, 84, 128, 138, 139, 145, 155, 207

E. de Langre. *Fluides et Solides*. Les éditions de l'École Polytechnique, 2001. 179

B. Després. *Méthodes de décomposition de domaine pour la propagation d'ondes en régime harmonique. Le théorème de Borg pour l'équation de Hill vectorielle*. PhD thesis, Université Pais IX Dauphine, Paris, France, 1991. 77

A. A. Doinikov. Translational motion of a spherical bubble in an acoustic standing wave of high intensity. *Physics of fluids*, 14(4):1420 – 1425, 2002. 195

V. Dolean, P. Jolivet, and F. Nataf. *An introduction to domain decomposition methods: algorithms, theory, and parallel implementation*, volume 144. SIAM, 2015. v, 76

J. Dominguez. *Boundary Elements in Dynamics*. Elsevier Applied Science Publishers, 1993. 32, 38, 44

M. A. Epton and B. Dembart. Multipole translation theory for the three-dimensional Laplace and Helmholtz equations. *SIAM J. Sci. Comput.*, 16(4):865 – 897, 1995. 45

A. A. Ergin, B. Shanker, and E. Michielssen. Fast evaluation of three-dimensional transient wave fields using diagonal translation operators. *J. Comput. Phys.*, 146:157 – 180, 1998. 38

S. Falletta, G. Monegato, and L. Scuderi. A space-time BIE method for nonhomogeneous exterior wave equation problems. The Dirichlet case. *IMA Journal of Numerical Analysis*, 32:202 – 226, 2012. 38

C. A. Felippa, K.-C. Park, and C. Farhat. Partitioned analysis of coupled mechanical systems. *Computer Methods in Applied Mechanics and Engineering*, 190(24):3247 – 3270, 2001. 74, 75, 104

W. Fong and E. Darve. The black-box fast multipole method. *J. Comput. Phys.*, 228(23): 8712 – 8725, 2009. 38

S. François, H. R. Masoumi, and G. Degrande. A time domain coupled boundary element - finite element method for dynamic response of structures. *12th International Congress on Sound and Vibration*, 2005. 73

M. Gander, L. Halpern, and F. Nataf. Optimal schwarz waveform relaxation for the one dimensional wave equation. *SIAM J. Numerical Analysis*, 41:1643–1681, 2003. 76

T. L. Geers. Doubly asymptotic approximations for transient motions of submerged structures. *J. Acoust. Soc. Am.*, 64(5):1500 – 1508, 1978. 75, 132

T. L. Geers and C. A. Felippa. Doubly asymptotic approximations for vibration analysis of submerged structures. *J. Acoust. Soc. Am.*, 73, 1983. 75, 132

T. L. Geers and K. S. Hunter. An integrated wave-effects model for an underwater explosion bubble. *J. Acoustical Society of America*, 111(4):1584 – 1601, 2002. iv, 9, 13, 19, 22, 23, 57, 132, 133, 136

T. L. Geers and C.-K. Park. Optimization of the G&H bubble model. Published in *Shock and Vibration*, 12(1):3 – 8, 2005. 197

T. L. Geers and B. J. Toothaker. Third-order doubly asymptotic approximations for computational acoustics. *Journal of Computational Acoustics*, 8(1):101 – 120, 2000. 75, 132

M. Géradin and D. Rixen. *Théorie des vibrations : Application à la dynamique des structures*. Masson, 2nd edition, 1997. 92, 128, 139

D. Givoli. Non-reflecting boundary conditions. *Journal of Computational Physics*, 94(1):1 – 29, 1991. 81

G. H. Golub and C. F. Van Loan. *Matrix Computations*. The Johns Hopkins University Press, third edition, 1996. 111

D. Graham, J. Hobson, P. Murphy, C. Toole, S. Cross, and J. Farnworth. Efficient modelling of the structural response of submarine pressure hulls to underwater explosions. In *Warship 2017: Naval Submarines & UUVs, The Royal Institution of Naval Architects*, 2017. 9, 81

L. Greengard. *The rapid evaluation of potential fields in particle systems*. MIT Press, 1988. 45

L. Greengard and V. Rokhlin. A fast algorithm for particle simulations. *J. Comp. Phys.*, 73:325 – 348, 1987. 45

H. Guillard and R. Abgrall. *Modélisation numérique des fluides compressibles*, volume 5 of *Series in Applied Mathematics*. Gauthier-Villars, 2001. 26

J. Gwinner and E. P. Stephan. *Advanced boundary element methods*. Springer International Publishing, 2018. 38

S. T. Ha, L. C. Ngo, M. Saeed, B. J. Jeon, and H. Choi. A comparative study between partitioned and monolithic methods for the problems with 3D fluid-structure interaction of blood vessels. *Journal of Mechanical Science and Technology*, 31(1):281 – 287, 2017. 74

T. Ha-Duong. On retarded potential boundary integral equations and their discretisation. In *Topics in Computational Wave Propagation: Direct and Inverse Problems*, pages 301–336. Springer Berlin Heidelberg, 2003. 38, 43

W. Hackbusch. A sparse matrix arithmetic based on H-matrix. Part I: Introduction to H-matrices. *Computing*, 62:89 – 108, 1999. vi, 45, 75, 108

W. Hackbusch. *Hierarchical Matrices: Algorithms and Analyses*, volume 49. Springer, 2015. 109

L. Halpern, J. Szeftel, and C. Japhet. Optimized Schwarz Waveform Relaxation and Discontinuous Galerkin Time Stepping for Heterogeneous Problems. *SIAM Journal on Numerical Analysis*, 50(5):2588–2611, 2012. 76

S. Hassan, C. Japhet, and M. Vohralik. A posteriori stopping criteria for space-time domain decomposition for the heat equation in mixed formulations. *ETNA - Electronic Transactions on Numerical Analysis*, 49:151 – 181, 2018. 77

A. Henrot and M. Pierre. *Shape Variation and Optimization: a Geometrical Analysis*. Number 28 in Tracts in Mathematics. European Mathematical Society, 2018. 107

A. N. Hicks. Effect of bubble migration of explosion-induced whipping of ships. Technical Report Washington, D.C., Naval Ship Research and Development Center, 1970. vi, 101, 197

T. T. P. Hoang, J. Jaffré, C. Japhet, M. Kern, and J. Roberts. Space-time domain decomposition methods for diffusion problems in mixed formulations. *SIAM Journal on Numerical Analysis*, 51:3532–3559, 2013. 76

T. J. R. Hughes. *The Finite Element Method: Linear Static and Dynamic Finite Element Analysis*. Prentice-Hall, 1987. 44, 92, 128, 139

H. Hugoniot. Mémoire sur la propagation des mouvements dans les corps et spécialement dans les gaz parfaits. *Journal de l'École Polytechnique*, volumes 57 and 58, 1887 - 1888. 15, 187, 188

K. S. Hunter and T. L. Geers. Pressure and velocity fields produced by an underwater explosion. *J. Acoust. Soc. Am.*, 115(4):1483 – 1496, 2004. 127, 132, 133

S. Iakovlev. Influence of a rigid coaxial core on the stress-strain state of a submerged fluid-filled circular cylindrical shell subjected to a shock wave. *Journal of Fluids and Structures*, 19(7):957 – 984, 2004. 204

C. Japhet, Y. Maday, and F. Nataf. Robin Schwarz algorithm for the NICEM Method: the Pq finite element case. *SIAM Journal on Numerical Analysis*, 52, 2014. 77

M. C. Junger and D. Feit. *Sound, Structures, and Their Interaction*. The MIT Press, 2nd edition, 1986. 48, 83, 203

E. I. Jury. *Theory and application of the Z-transform method*. Krieger, 1973. 39

L. F. Kallivokas, T. Juneja, and J. Bielak. A symmetric Galerkin BEM variational framework for multi-domain interface problems. *Comp. Meth. Appl. Mech. Engng.*, 194: 3607 – 3636, 2005. 43

L. Khoun. *Réduction de modèles pour les problèmes vibro-acoustiques transitoires*. PhD thesis, Sorbonne Université, Paris, France, 2021. To be published. vi, 81, 84, 159

G. Kirchhoff. Zur theorie der lichtstrahlen. *Annalen der Physik (German)*, 254(4):663 – 695, 1883. 33

F. Kpadonou, S. Chaillat, and P. Ciarlet. On the efficiency of nested GMRES preconditioners for 3D acoustic and elastodynamic H-matrix accelerated Boundary Element Methods. *Computers & Mathematics with Applications*, 80(3):471 – 489, 2020. 108, 111

S. Kurz, J. Fetzer, and G. Lehner. Three-dimensional transient BEM-FEM coupled analysis of electrodynamic levitation problems. *IEEE Transactions on Magnetics*, 32(3): 1062–1065, 1996. 74

I. Labarca, L. M. Faria, and C. Pérez-Arancibia. Convolution quadrature methods for time-domain scattering from unbounded penetrable interfaces. *Proceedings of the Royal Society A*, 475(2227):20190029, 2019. 38

P. Ladevèze, J.-C. Passieux, and D. Néron. The LATIN multiscale computational method and the Proper Generalized Decomposition. *Computer Methods in Applied Mechanics and Engineering*, 199(21):1287 – 1296, 2010. Multiscale Models and Mathematical Aspects in Solid and Fluid Mechanics. 77

C. Lalanne. Mechanical shock. In *Mechanical Vibration and Shock Analysis*, volume 2, pages 369 – 396. 2nd edition, 2010. 93

H. Lamb. *Hydrodynamics*. University Press, Cambridge, 6th edition, 1932. 14

L. D. Landau and E. M. Lifshitz. *Fluid mechanics*. Pergamon Press, English 2nd edition, 1987. 20, 196

R. Le Mestre, O. Doaré, and J.-S. Schotté. Modélisation des effets des fluides externes et internes sur le comportement dynamique des dirigeables déformables. *CSMA, 14ème Colloque National en Calcul des Structures*, 2019. 75

C. Leblond. *Modélisation de phénomènes fortement instationnaires en milieux couplés. Application au dimensionnement de structures immergées aux explosions sous-marines.* PhD thesis, Université de Nantes, 2007. iv, vi, 9, 20, 21, 22, 23, 24, 31, 50, 83, 97, 101, 125, 127, 132, 199, 200

C. Leblond and J.-F. Sigrist. A reduced basis approach for the parametric low frequency response of submerged viscoelastic structures. *Finite Elements in Analysis and Design*, 119:15 – 29, 2016. 84, 212

C. Leblond, S. Iakovlev, and J.-F. Sigrist. A fully elastic model for studying submerged circular cylindrical shells subjected to a weak shock wave. *Mécanique & Industries*, 10: 275–284, 2009. vi, 83

M. Lecouvez. *Méthodes itératives de décomposition de domaine sans recouvrement avec convergence géométrique pour l'équation de Helmholtz.* PhD thesis, Ecole Polytechnique, 2015. 77

M. Lee, Y.-S. Park, Y. Park, and K. C. Park. New approximations of external acoustic-structural interactions: Derivation and evaluation. *Computer Methods in Applied Mechanics and Engineering*, 198(15):1368 – 1388, 2009. 75, 132

M. Lenoir. *Équations Intégrales et Problèmes de Diffraction.* ENSTA ParisTech, UMA, Poems, 2016. iv, 32

F. G. Leppington and H. Levine. The sound field of a pulsating sphere in unsteady rectilinear motion. *Proc. R. Soc. Lond., Ser. A*, 412:199 – 221, 1987. 132

A. Lieu, P. Marchner, G. Gabard, H. Beriot, X. Antoine, and C. Geuzaine. A non-overlapping Schwarz domain decomposition method with high-order finite elements for flow acoustics. *Computer Methods in Applied Mechanics and Engineering*, 369, 2020. 76

P. L. Lions. On the Schwarz alternating method III: A variant for nonoverlapping subdomains. In Tony F. Chan, R. Glowinski, J. Périaux, and O. B. Widlund, editors, *Third International Symposium on Domain Decomposition Methods for Partial Differential Equations*, pages 202–223. Society for Industrial and Applied Mathematics, 1990. 77

Y. L. Liu, A. M. Zhang, Z. L. Tian, and S. P. Wang. Numerical investigation on global responses of surface ship subjected to underwater explosion in waves. *Ocean Engineering*, 161:277 – 290, 2018. 107

Livermore Software Technology Corp. Ls-dyna documentation. 2020. URL https://www.dynasupport.com/manuals. 207

P. Longère, A.-G. Geffroy-Grèze, B. Leblé, and A. Dragon. Ship structure steel plate failure under near-field air-blast loading: Numerical simulations vs experiment. *International Journal of Impact Engineering*, 62:88 – 98, 2013. 31

A. Loseille. Chapter 10 - unstructured mesh generation and adaptation. In Rémi Abgrall and Chi-Wang Shu, editors, *Handbook of numerical methods for hyperbolic problems*,

volume 18 of *Handbook of Numerical Analysis*, pages 263 – 302. Elsevier, 2017. 53, 128, 159

C. Lubich. Convolution quadrature and discretized operational calculus. I. *Numer. Math*, 52:129 – 145, 1988a. v, 38, 41

C. Lubich. Convolution quadrature and discretized operational calculus. II. *Numer. Math*, 52:413 – 425, 1988b. v, 38, 41, 42

D. Mavaleix-Marchessoux, M. Bonnet, S. Chaillat, and B. Leblé. A fast boundary element method using the Z-transform and high-frequency approximations for large-scale three-dimensional transient wave problems. *International Journal for Numerical Methods in Engineering*, 121(21):4734 – 4767, 2020. 31, 159

W. McLean. *Strongly Elliptic Systems and Boundary Integral Equations*. Cambridge, Univ. Press, 2000. 35

A. Modave, C. Geuzaine, and X. Antoine. Corner treatments for high-order local absorbing boundary conditions in high-frequency acoustic scattering. *Journal of Computational Physics*, 401, 2020a. 81

A. Modave, A. Royer, X. Antoine, and C. Geuzaine. A non-overlapping domain decomposition method with high-order transmission conditions and cross-point treatment for Helmholtz problems. *Computer Methods in Applied Mechanics and Engineering*, 368, 2020b. 76

H. J.-P. Morand and R. Ohayon. *Fluid-Structure Interaction: Applied Numerical Methods*. Wiley, 1995. 74

D. Néron. *Sur une stratégie de calcul pour les problèmes multiphysiques*. PhD thesis, École normale supérieure de Cachan - ENS Cachan, 2004. v, 77

A. Nieto Ferro. *Nonlinear dynamic soil-structure interaction in earthquake engineering*. PhD thesis, École Centrale Paris, Paris, France, 2013. 38, 73

N. Nishimura. Fast multipole accelerated boundary integral equation methods. *Appl. Mech. Rev.*, 55:299 – 324, 2002. v, 45, 75

J. C. Nédélec. *Acoustic and Electromagnetic Equations, Integral Representations for Harmonic Problems*. Applied Mathematical Sciences 144. Springer-Verlag New York, 2001. iv, 32

R. Ohayon and C. Soize. *Structural acoustics and vibration*. Academic Press, 1998. 49

F. W. J. Olver, D. W. Lozier, R. F. Boisvert, and C. W. Clark. *NIST Handbook of Mathematical Functions*. Cambridge University Press, 2010. 46, 205

B. Overpelt, B. Nienhuis, and B. Anderson. Free running manoeuvring model tests on a modern generic SSK class submarine (BB2). *Pacific International Maritime Conference, Sydney, Australia*, 2015. 66

E. Parolin. *Non overlapping domain decomposition methods with non local transmission conditions for electromagnetic wave propagation*. PhD thesis, IPP, POEMS, Palaiseau, France, 2020. 76

R. S. Price. Similitude equations for explosives fired underwater. Technical Report NSWC TR 80 - 299, Naval Surface Warfare Center, Dahlgren, Virginia, 1979. 13

A. Quarteroni, R. Sacco, and F. Saleri. *Numerical mathematics*. Springer, 2007. 39, 52, 53

Q. Rakotomalala, L. Khoun, C. Leblond, and J.-F. Sigrist. An advanced semi-analytical model for the study of naval shock problems. To be published, 2021. vi, 83, 159

W. J. M. Rankine. On the thermodynamic theory of waves of finite longitudinal disturbance. *Philosophical Transactions of the Royal Society of London*, 160:277 – 288, 1870. 15, 187, 188

Y. Saad and M. H. Schultz. GMRES: A generalized minimal residual algorithm for solving nonsymmetric linear systems. *SIAM J. Sci. Stat. Comput.*, 7(3):856 – 869, 1986. 44, 108

F. J. Sayas. *Retarded Potentials and Time Domain Boundary Integral Equations. A Road Map*, volume 50 of *Springer Series in Computational Mathematics*. Springer International Publishing, 2016. iv, v, 32, 33, 38, 40, 41

J.-S. Schotté. *Influence de la gravité sur les vibrations linéaires d'une structure élastique contenant un liquide incompressible*. PhD thesis, Conservatoire National des Arts et Métiers, Paris, France, 2001. 112

A. Seghir, A. Tahakourt, and G. Bonnet. Coupling FEM and symmetric BEM for dynamic interaction of dam - reservoir systems. *Engineering Analysis with Boundary Elements*, 33(10):1201 – 1210, 2009. 74

D.H. Sharp. An overview of Rayleigh-Taylor instability. *Physica D: Nonlinear Phenomena*, 12(1):3 – 18, 1984. 20

R. P. Shaw. Diffraction of acoustic pulses by obstacles of arbitrary shape with a robin boundary condition. *J. Acoustical Society of America*, 41(4):855 – 859, 1966. 32

J.-F. Sigrist. *Fluid-Structure Interaction: An Introduction to Finite Element Coupling*. Wiley, 2015. 74

J.-F. Sigrist and C. Leblond. Une méthode semi-analytique pour l'analyse de l'interaction entre une onde de choc et une coque élastique immergée. application au pré-dimensionnement de coques de sous-marins. (French). *Mécanique & Industries*, 9(6): 543–550, 2008. vi, 83

V. Simoncini and E. Gallopoulos. An iterative method for nonsymmetric systems with multiple right-hand sides. *SIAM J. Sci. Comput*, 16:917–933, 1995. 108

H. G. Snay. Hydrodynamics of underwater explosions. Published in *Symposium on Naval Hydrodynamics, National Academy of Sciences, Washington D.C.*, pages 325 – 346, 1956. iii, xiii, 8

H. G. Snay. Underwater explosion phenomena: the parameters of migrating bubbles. Technical report, U. S. Naval Ordnance Laboratory, White Oak, Maryland, 1962. 7, 19

D. Soares Jr. and W. J. Mansur. An efficient time-domain BEM/FEM coupling for acoustic-elastodynamic interaction problems. *Tech Science Press, CMES*, 8(2):153 – 164, 2005. 73

M. M. Swisdak. Explosion effects and properties. Part II. Explosion effects in water. Technical Report NSWC/WOL TR 76 - 116, Naval Surface Weapons Center, Dahlgren, Virginia, 1978. xvii, 7, 15, 16, 19, 20, 57

T. Takahashi, N. Nishimura, and S. Kobayashi. A fast BEM for three-dimensional elastodynamics in time domain. *Engrg. Anal. Bound. Elem.*, 28:165 – 180, 2004. 38

P. Le Tallec and J. Mouro. Fluid structure interaction with large structural displacements. *Computer Methods in Applied Mechanics and Engineering*, 190(24):3039 – 3067, 2001. Advances in Computational Methods for Fluid-Structure Interaction. 74

A. Toselli and O. Widlund. *Domain decomposition methods – algorithms and theory*, volume 34. Springer Science & Business Media, 2006. v, 76

E. Véron. *Calcul numérique des grandes déformations de structures minces en contact avec des fluides lourds*. PhD thesis, Université de Nantes, 2016. 73, 74, 75, 81, 84, 104, 112, 114, 159, 160

A. Vion and C. Geuzaine. Improved sweeping preconditioners for domain decomposition algorithms applied to time-harmonic Helmholtz and Maxwell problems. *ESAIM: ProcS*, 61:93–111, 2018. 76

O. Von Estorff. On FEM/BEM coupling for fluid-structure interaction analyses in the time domain. *International journal for numerical methods in engineering*, 31:1151 – 1168, 1991. 73

C. Wang and B. C. Khoo. An indirect boundary element method for three-dimensional explosion bubbles. *Journal of Computational Physics*, 194(2):451 – 480, 2004. iv, 19

X. Wang, X. Li, X. Ma, and G. Du. Numerical analysis on spectrum dip characteristics of shock response spectrum of submarine equipment. *Chinese Journal of Ship Research*, 14 (3):31–37, 2019. 93

L. Ying. A pedestrian introduction to fast multipole methods. *Science China Mathematics*, 55(5):1043 – 1051, 2012. 32, 45

A.-M. Zhang and X.-L. Yao. Interaction of underwater explosion bubble with complex elastic-plastic structure. *Applied Mathematics and Mechanics*, 29(1):89 – 100, 2008. iv, 7, 74

A.-M. Zhang, L.-Y. Zeng, X.-D. Cheng, S.-P. Wang, and Y. Chen. The evaluation method of total damage to ship in underwater explosion. *Applied Ocean Research*, 33(4):240 – 251, 2011. 107

Z. Zong. A hydroplastic analysis of a free-free beam floating on water subjected to an underwater bubble. *Journal of Fluids and Structures*, 20:359 – 372, 2005. iv, 7

R. Zorrilla, R. Rossi, R. Wüchner, and E. Oñate. An embedded finite element framework for the resolution of strongly coupled fluid-structure interaction problems. Application to volumetric and membrane-like structures. *Computer Methods in Applied Mechanics and Engineering*, 368:113179, 2020. 74

Glossary

Boundary Element Method (BEM) – *méthode des éléments de frontière* – Numerical method based on boundary integral formulations, that only requires the discretisation of a surface when dealing with 3D problems. 3, 28

Doubly Asymptotic Approximation (DAA) – *approximation doublement asymptotique* – Approximative relation between the normal fluid-particle velocity, the surface pressure and their temporal derivatives. It is obtained from asymptotic analysis arguments and approximation of Kirchhoff's retarded potential formula (2.17). 75, 132, 162

Equation of state – *équation d'état* – Thermodynamic equation relating state variables such as pressure, mass density, temperature or internal energy. 187

Equilibrium – *équilibre* – Rest state used as a reference. Usually, an object is termed *at equilibrium* if it is motionless and/or not subjected to any stress. 7

Euler equations – *équations d'Euler* – Set of quasilinear hyperbolic equations governing adiabatic and inviscid flow. It expresses conservation of mass, momentum and energy. 7, 176

Far-field/remote underwater explosion – *explosion sous-marine en champ lointain* – When considering a structure affected by an underwater explosion, the explosion is qualified as *far-field* or *remote* if (i) the presence of the structure only marginally affects the explosion, especially the behaviour of the bubble of hot gases, and (ii) the influence of the shock wave can be temporally separated from that of the bubble. 1, 12

Finite Element Method (FEM) – *méthode des éléments finis* – Numerical method used to solve problems governed by partial differential equations, based on the discretisation of the continuous domains involved. 3, 28

Homogeneous medium – *milieu homogène* – A medium is qualified as homogeneous if its mass density ρ is constant. 12

Irrotational/potential flow – *écoulement irrotationnel/potentiel* – A flow is qualified as irrotational if the curl of its velocity vector vanishes at any point, at any time. Then, it may be expressed as the gradient of a function termed velocity potential, and the flow may also be qualified as potential. 12

Isotropic medium – *milieu isotrope* – A medium is qualified as isotropic if it shows the same properties in all directions. 12

Oscillating gas bubble – *bulle de gaz oscillante* – Bubble of hot gases resulting from the chemical reaction of an explosion. Seeking a balance between its internal pressure and the surrounding water pressure, the bubble surface oscillates. It also migrates towards the water surface. 12

Perfect fluid – *fluide parfait* – A fluid is qualified as perfect fluid if it has no viscosity and is adiabatic (no heat conduction). Flows are then described by the *Euler equations*. 12

Quasi-periodic – *quasi-périodique* – An evolution is qualified as quasi-periodic when it displays an irregular periodicity, typically a slightly variable period or a slightly diminishing amplitude. This often occurs when dealing with dissipative systems. 7

Shock factor – *facteur de choc* – Figure estimating the severity of an underwater explosion, as experienced by a naval target, as a function of explosive charge weight and standoff distance. 7

Shock Response Spectrum (SRS) – *spectre de réponse aux chocs* – Plot showing the maximum displacement, velocity or acceleration, as a function of the natural frequency, of damped spring-mass systems for a given solicitation. 93, 145

Shock wave/primary wave/blast – *onde de choc/onde primaire/souffle* – Destructive wave spreading outwards from an explosion. The name *primary wave* is given by analogy with the P-waves in seismology, defined as the first waves resulting from an earthquake to arrive at a seismograph. 6, 12

Standoff distance and standoff point – Shortest distance between a considered structure Ω_s (submarine) and an explosion locus O, denoted d_s. The standoff point $A \in \partial\Omega_s$ is the closest point to the explosion, such that $d_s = \|AO\|$. xx

Wave – *onde* – Propagating perturbation accompanied by a transfer of energy, but no transport of matter, that travels through a medium. 1, 6

Wave equation – *équation des ondes* – Second-order linear hyperbolic partial differential equation governing the propagation of acoustic waves. 6

Acronyms

$\mathcal{H}$-matrices hierarchical matrices. 3

BE boundary element. 43

BEM boundary element method. 3

BIE boundary integral equation. 32

CPU central processing unit. 109

CQM convolution quadrature method. 3

CSE coupling simulation engine of Abaqus®. 81

DAA doubly asymptotic approximation. 75

DDM domain decomposition method. 76

DOF degree of freedom. 32

FE finite element. 84

FEM finite element method. 3

FFT fast Fourier transform. 42

FM-BEM fast multipole-based boundary element method. 32

FMM fast multipole method. 3

FSI fluid-structure interaction. 1

GPU graphics processing unit. 159

HFA high frequency approximation. 3

LATIN large time increment (method). 77

RAM random-access memory. 67

SRS shock response spectrum. 93

TNT trinitrotoluene. 5

UNDEX underwater explosion. 5

USA underwater shock analysis (software). 75

Appendix A

Dimensional analysis for fluid-structure interaction

FLUID-structure interaction is surely one of the most important notions when investigating the coupling caused by a far-field underwater explosion. This appendix, dedicated to the dimensional analysis for fluid-structure interaction problems, is largely inspired from the course on fluid-structure interaction conducted by E. de Langre at École Polytechnique (de Langre, 2001).

The purpose is to perform dimensional analyses for the shock wave and bubble phenomena. For a given problem, the values of some well-chosen dimensionless physical parameters indicate the relevant approximations and assumptions to be performed, and therefore highlight the proper method to be used to deal with the problem. We first define these numbers, as we recall the notion of fluid-structure coupling using the Buckingham π theorem. In the case of a submarine submerged in water and submitted to a far-field UNDEX, we show that the primary wave and the oscillating bubble are two different phenomena whose values of the various dimensionless physical parameters differ.

A.1 Hypotheses

The study of the fluid-structure interaction between submerged shell and water requires some hypotheses:

- The fluid and solid domains do not intersect;
- There is no mass exchange between the two domains;
- The temperature is assumed to be uniform and constant over time within each domain, and so there is no heat exchange between solid and fluid.

In particular, the first hypothesis implies that the structure does not rupture under the load induced by the far-field underwater explosion.

A.2 Variables and parameters

The independent variables are the coordinates of the current point $\mathbf{x} = (x, y, z)$ and time t. The denomination "current point" refers to a point in either Lagrangian or Eulerian specification. The dependent variables are the following:

- For the fluid: velocity $\mathbf{v}$, pressure p, density ρ_f;
- For the solid: displacement $\mathbf{u}$, Cauchy stress tensor σ, mass density ρ_s.

The fluid-structure interaction also depends on some material parameters:

- Physical parameters of fluid: dynamic (shear) viscosity μ, sound speed c_f;
- Physical parameters of solid: Young's modulus E, Poisson's ratio ν.

These parameters are known and linked to the types of fluid and solid. Some other quantities have to be taken into account, depending on the considered situation:

- Quantities for both the solid and the fluid: characteristic length L, gravity $\mathbf{g}$;
- Quantities for the fluid: reference velocity v_0, reference mass density ρ_f^0, reference pressure p_0;
- Quantities for the solid: reference displacement u_0, reference mass density ρ_s^0.

These quantities depend on the problem considered, and are often determined using boundary conditions.

A.3 Coupling between a solid and a fluid

The fluid-structure coupling hypothesis stipulates that dependent variables defined in the fluid domain and in the solid domain depend on the physical parameters and the quantities related to both domains. For instance, it implies that the fluid velocity is expressed as a function of all the parameters:

$$\mathbf{v} = f_v(\mathbf{x}, t\,; g, \mu, c_f, L\,; v_0, p_0, \rho_f^0\,; E, \nu\,; u_0, \rho_s^0)\,. \tag{A.1}$$

A similar relation to (A.1) holds for each dependent variable: p, ρ_f, $\mathbf{u}$, σ, ρ_s. The Buckingham π theorem states that (A.1), involving a number $n = 14$ of physical variables, can be rewritten in terms of a set of $p = n - r$ dimensionless parameters constructed from the original variables, where r is the number of physical dimensions involved, namely the rank of the dimensional matrix:

$$\begin{array}{c} \\ \text{Length} \\ \text{Mass} \\ \text{Time} \end{array} \begin{array}{c} \begin{array}{cccccccccccccc} \mathbf{v} & \mathbf{x} & t & \mu & c_f & L & g & v_0 & p_0 & \rho_f^0 & E & \nu & u_0 & \rho_s^0 \end{array} \\ \left(\begin{array}{cccccccccccccc} 1 & 1 & 0 & -1 & 1 & 1 & 1 & 1 & 1 & -3 & -1 & 0 & 1 & -3 \\ 0 & 0 & 0 & 1 & 0 & 0 & 0 & 0 & 1 & 1 & 1 & 0 & 0 & 1 \\ -1 & 0 & 1 & -1 & -1 & 0 & -2 & -1 & -2 & 0 & -2 & 0 & 0 & 0 \end{array} \right) \end{array} \tag{A.2}$$

The dimensional matrix (A.2) is of rank $r = 3$, so the relation (A.1) may be rewritten as a relation between $p = 14 - 3 = 11$ non-dimensional parameters, for instance:

$$\frac{\mathbf{v}}{v_0} = F_v\left(\frac{\mathbf{x}}{L}, \frac{v_0 t}{L}\,; \frac{\rho_f^0 v_0^2}{p_0}, \frac{\rho_f^0 v_0 L}{\mu}, \frac{v_0}{\sqrt{Lg}}, \frac{v_0}{c_f}\,; \nu, \frac{u_0}{L}, \frac{\rho_s^0 g L}{E}\,; \mathcal{A}\right), \tag{A.3}$$

where

- $v_0 t/L$ is the *reduced time*, and $T_f \equiv L/v_0$ is the order of magnitude of the time the fluid takes to travel the distance L;
- $\Pi \equiv \rho_f^0 v_0^2/p_0$ is the *reduced dynamic pressure*, inverse of the *Euler number*;
- $\mathcal{R}_E \equiv \rho_f^0 v_0 L/\mu$ is the *Reynolds number*, it quantifies the relative magnitudes of convection and viscous diffusion velocities;
- $\mathcal{F}_R \equiv v_0/\sqrt{Lg}$ is the *Froude number*, it assesses the relative magnitudes of inertial and gravitational forces;
- $\mathcal{M}_{ach} \equiv v_0/c_f$ is the *Mach number*, it measures compressibility effects;

- $\mathcal{D} \equiv u_0/L$ is the *reduced displacement*, it quantifies the effects of large displacements;
- $\mathcal{G} \equiv \rho_s^0 g L/E$ is the *gravity number*, it assesses the deformations induced by the structure weight;
- $\mathcal{A}$ is a dimensionless number that compares characteristic quantities of the solid and the fluid. For instance, either the *mass number* $\mathcal{M} \equiv \rho_f^0/\rho_s^0$, or the *Cauchy number* $\mathcal{C}_Y \equiv \rho_f^0 v_0^2/E$, that quantifies the deformations due to the dynamic pressure $\rho_f^0 v_0^2$, may be used for $\mathcal{A}$.

A similar equation to (A.3) holds for each dependent variable, for instance the solid displacement is written as

$$\frac{\mathbf{u}}{u_0} = G_u\left(\frac{\mathbf{x}}{L}, \frac{v_0 t}{L}; \frac{\rho_f^0 v_0^2}{p_0}, \frac{\rho_f^0 v_0 L}{\mu}, \frac{v_0}{\sqrt{Lg}}, \frac{v_0}{c_f}; \nu, \frac{u_0}{L}, \frac{\rho_s^0 g L}{E}; \mathcal{A}\right). \tag{A.4}$$

Remark 27 *The dimensionless numbers chosen in* (A.3) *and* (A.4) *are not unique, other numbers could be obtained through a combination of the chosen ones. For instance, the gravity number* $\mathcal{G}$ *could be replace by the reduced velocity* $\mathcal{V}_R = F_R\sqrt{\mathcal{G}} = v_0/c_s$ *, where* $c_s = \sqrt{E/\rho_s^0}$ *is the wave speed in the solid; or the reduced time could be defined using* c_s *instead of* v_0 *:* $T_s = L/c_s$*. Another interesting physical parameter is the ratio between* c_s *and* c_f*, denoted as* $\mathcal{U}_R \equiv c_s/c_f = \mathcal{M}_{ach}/\mathcal{V}_R$*.*

The fluid-structure coupling is expressed in the relations set in this section. Indeed, the involvement of the dimensionless numbers $\nu, \mathcal{D}, \mathcal{G}, \mathcal{A}$ in (A.3); and $\Pi, R_E, F_R, \mathcal{A}$ in (A.4) reveals the influence of the solid on the fluid and *vice versa*.

A.4 Fluid-structure coupling caused by the shock wave

When the primary wave goes through the submarine, the global motion of water due to the oscillating bubble is not taken into account, and the reference fluid velocity v_0 is set to c_f. The reference pressure p_0 is set to the magnitude p_m of the pressure discontinuity, defined in (1.1). Typically, a detonation of $W = 100$ kg of TNT located at a distance of $d_s = 100$ m from the structure corresponds to $p_0 = 1$ MPa. To compute the global displacement of the structure, the typical length L is set to the submarine length, typically 100 m, and the material parameters are set to those of steel. Hence, the reduced time of the solid is $T_s = L/c_s \simeq 2\ 10^{-2}$ s, with $c_s \sim 5\ 10^3$ m/s.

The order of magnitude of the typical displacement is obtained using the second law of Newton: the shell is submitted to both the incident pressure forces, and an inertial force due to the water resistance, that the submarine has to push away. The drag force is not considered because the global shell motion is slow and so it is marginal compared to the inertial force. For a cylinder of radius R and length L, it holds

$$\rho_s \pi R^2 L\, \ddot{u} \simeq \underbrace{-\rho_f \pi R^2 L\, \ddot{u}}_{\text{added mass of fluid}} + \underbrace{2\pi R L\, p_m}_{\text{shock wave pressure}},$$

so that the order of magnitude of u_0 is evaluated as

$$u_0 \simeq \frac{2}{R}\frac{p_m}{\rho_s + \rho_f} T_s^2 \sim 10^{-2} \text{ m}.$$

The resulting orders of magnitude of the values of the various dimensionless parameters are given in Table A.1, as powers of 10.

Dimensional parameter	g	μ	c_f	L	v_0	ρ_f	E	u_0	ρ_s	p_0
Order of magnitude	1	-3	3	2	3	3	11	-2	4	6

Table A.1: Orders of magnitude of the various physical parameters for the shock wave, expressed in SI units. Explosion of $W = 100$ kg of TNT located at $d_s = 100$ m from the shell, at a water depth of $\xi_{\text{exp}} = 100$ m. Values in powers of 10.

Dimensionless parameter	$\mathcal{R}_E$	$\mathcal{M}_{ach}$	$\mathcal{F}_R^2$	$\mathcal{V}_R$	$\mathcal{C}_Y$	$\mathcal{M}$	$\mathcal{G}$	$\mathcal{D}$	$\mathcal{U}_R$	Π
Order of magnitude	11	0	3	0	-2	-1	-4	-4	0	3

Table A.2: Orders of magnitude of the various dimensionless parameters for the shock wave. Explosion of $W = 100$ kg of TNT located at $d_s = 100$ m from the shell, at a water depth of $\xi_{\text{exp}} = 100$ m. Values in powers of 10.

Using Table A.1, the orders of magnitude of the values of the various dimensionless parameters are given in Table A.2, in powers of 10.
The high value of the Reynolds number in Table A.2 confirms that the viscous effects can be neglected. The other values are typical of those for a wave. Table A.2 also stresses a low value of the Euler number, inverse to Π, which will be of use in Appendix B. Finally, $\mathcal{D} = u_0/L \sim 10^{-4}$ m indicates that the approximation of small displacements is valid.

A.5 Fluid-structure coupling caused by the bubble oscillations

For the bubble oscillation phenomenon, the order of magnitude of v_0 is obtained using (1.27), considering only the oscillating part

$$v_0 = \|\nabla\phi\| = \frac{R^2\dot{R}}{r^2}\,.$$

Hence, for $R \sim R_{\max}$ and $\dot{R} \sim 0.05\,c_f$, it holds

$$v_0 = \frac{(0.05\,c_f)R_{\max}^2}{r^2} \sim 10^{-1}\ \text{m/s}\,,$$

for an explosion of $W = 100$ kg of TNT, at a water depth of $\xi_{\text{exp}} = 100$ m, at a distance $d_s = 100$ m. The reference pressure p_0 corresponds to the hydrostatic pressure at a water depth of 100 m. The typical displacement u_0 due to the bubble oscillation is usually larger than the one due to the primary wave, because the shell globally vibrates due to the periodic loading. For the typical explosion considered, it is set to $u_0 \sim 10^{-1}$ m. Table A.3 provides an order of magnitude for each value of the various physical parameters, in powers of 10.
Using Table A.3, the orders of magnitude of the values of the various dimensionless parameters are given in Table A.4, also in powers of 10.
Like for the shock wave phenomenon, the Reynolds number is high enough to allow neglecting viscous effects. The other parameters are quite different from the ones obtained for the shock wave, in Table A.2. This confirms that the two phenomena behave differently, though emerging from the same physical phenomenon, namely an underwater explosion. For typical displacements $u_0 \sim 10^{-1}$ m, $\mathcal{D}$ indicates that the approximation of small displacements remains relevant.

Physical parameter	g	μ	c_f	L	v_0	ρ_f	E	u_0	ρ_s	p_0
Order of magnitude	1	-3	3	2	-1	3	11	-1	4	5

Table A.3: Orders of magnitude of the various physical parameters for the bubble oscillation, expressed in SI units. Explosion of $W = 100$ kg of TNT located at $d_s = 100$ m from the shell, at a water depth of $\xi_{exp} = 100$ m. Values in powers of 10.

Dimensionless parameter	$\mathcal{R}_E$	$\mathcal{M}_{ach}$	$\mathcal{F}_R^2$	$\mathcal{V}_R$	$\mathcal{C}_Y$	$\mathcal{M}$	$\mathcal{G}$	$\mathcal{D}$	$\mathcal{U}_R$	Π
Order of magnitude	6	-5	-4	-5	-12	-1	-4	-3	0	-6

Table A.4: Orders of magnitude of the various dimensionless parameters for the bubble oscillation. Explosion of $W = 100$ kg of TNT located at $d_s = 100$ m from the shell, at a water depth of $\xi_{exp} = 100$ m. Values in powers of 10.

Appendix B

Additional study of the shock wave phenomenon

This appendix presents a complementary study to Section 1.2, using the notations defined in Notations. In Appendix B.1, we introduce a crucial theory for near-field UNDEX: the Kirkwood-Bethe theory of propagation of shock waves. For far-field UNDEX, this theory in not used, as the linear acoustic theory is adequate enough. However, it is instructive to stress the differences between the two models, and especially check that the Kirkwood-Bethe theory of propagation reduces to linear acoustics under certain assumptions. Then, in Appendix B.2, we introduce the Rankine-Hugoniot conditions, which provide three equations relating the fluid quantities at the shock front. We show that extending these conditions during the relaxation phase (after the shock wave front has passed) is relevant for far-field UNDEX. This extension at any time permits the computation of the total energy related to the shock wave, in Appendix B.3.

B.1 Kirkwood-Bethe theory of propagation of shock waves

In Section 1.2.3, we showed that the shock wave propagation is not exactly governed by the common wave equation. Then, a question naturally arises: what are the propagation equations for the shock wave produced by an underwater explosion? To obtain these equations, the starting point is the Euler equations of fluid dynamics: for a perfect fluid whose state is described at any time t and point M by mass density $\rho(M,t)$, total pressure $p(M,t)$, velocity $\mathbf{v}(M,t)$, internal energy per unit of mass of fluid $e(M,t)$, the conservations of mass, momentum and energy lead to the following set of equations:

$$\begin{cases} \dfrac{\mathrm{d}\rho}{\mathrm{d}t} + \rho\nabla\cdot\mathbf{v} = \dfrac{\partial\rho}{\partial t} + \rho\nabla\cdot\mathbf{v} + (\mathbf{v}\cdot\nabla)\rho = 0 & \text{conservation of mass,} \quad \text{(B.1a)} \\ \dfrac{\mathrm{d}\mathbf{v}}{\mathrm{d}t} + \dfrac{1}{\rho}\nabla p = \dfrac{\partial\mathbf{v}}{\partial t} + (\mathbf{v}\cdot\nabla)\mathbf{v} + \dfrac{1}{\rho}\nabla p = \mathbf{g} & \text{conservation of momentum,} \quad \text{(B.1b)} \\ \dfrac{\mathrm{d}e}{\mathrm{d}t} + \dfrac{p}{\rho}\nabla\cdot\mathbf{v} = \dfrac{\partial e}{\partial t} + (\mathbf{v}\cdot\nabla)e + \dfrac{p}{\rho}\nabla\cdot\mathbf{v} = 0 & \text{conservation of energy,} \quad \text{(B.1c)} \end{cases}$$

where $\mathbf{g}$ is the gravity. These equations are more general than the wave equation (1.20), since the latter equation may be obtained from (B.1) by considering a small perturbation $(\delta\rho, \delta p, \delta\mathbf{v}, \delta e)$ with respect to an unperturbed reference state, and then linearising the system (B.1).

The Kirkwood-Bethe theory is an analytical approach to shock wave propagation in water that relies on fundamental equations, such as (B.1) or the laws of thermodynamics. First, instead of manipulating the total pressure p in the fluid, the enthalpy H is used, defined as

$$H := e + \frac{p}{\rho}\,.$$

Only the variation ω of enthalpy is relevant: $\omega \equiv \Delta H = H - H_0$, where $H_0 = e_0 + p_h/\rho_0$ is the enthalpy of the unperturbed state. An elementary variation of ω is provided by

$$\mathrm{d}\omega = \mathrm{d}e + \frac{\mathrm{d}p}{\rho} + p\,\mathrm{d}\left(\frac{1}{\rho}\right) - \mathrm{d}H_0\,,$$

where the term $-\mathrm{d}H_0$ is kept because $\nabla H_0 = \nabla p_h/\rho_0 = \mathbf{g} \neq 0$. Using the second law of thermodynamics

$$\mathrm{d}e = T\mathrm{d}S - p\,\mathrm{d}\left(\frac{1}{\rho}\right),$$

it comes

$$\mathrm{d}\omega = T\mathrm{d}S + \frac{1}{\rho}\,\mathrm{d}p - \mathrm{d}H_0\,.$$

Behind the shock wave front, the relaxation is assumed to be **isentropic**, namely $\mathrm{d}S = 0$. This implies

$$\nabla p = \rho\nabla\omega + \rho\mathbf{g}\,, \quad \frac{\mathrm{d}p}{\mathrm{d}t} = \rho\frac{\mathrm{d}\omega}{\mathrm{d}t}\,, \tag{B.2}$$

$$\frac{\mathrm{d}\rho}{\mathrm{d}t} = \frac{\mathrm{d}\rho}{\mathrm{d}p}\frac{\mathrm{d}p}{\mathrm{d}t} = \frac{1}{c^2}\frac{\mathrm{d}p}{\mathrm{d}t} = \frac{\rho}{c^2}\frac{\mathrm{d}\omega}{\mathrm{d}t}\,, \tag{B.3}$$

where $c^2 = \left(\frac{\mathrm{d}p}{\mathrm{d}\rho_f}\right)_S$ is not necessary constant. Using (B.2) and (B.3), (B.1a) and (B.1b) are rewritten as

$$\nabla\cdot\mathbf{v} = -\frac{1}{c^2}\frac{\mathrm{d}\omega}{\mathrm{d}t}\,, \tag{B.4}$$

$$\frac{\mathrm{d}\mathbf{v}}{\mathrm{d}t} = \frac{\partial\mathbf{v}}{\partial t} + (\mathbf{v}\cdot\nabla)\mathbf{v} = -\nabla\omega\,. \tag{B.5}$$

A new function of the variation of enthalpy ω and the velocity $\mathbf{v}$ may be introduced, named kinetic enthalpy, defined as

$$\Omega := \omega + \frac{1}{2}v^2. \tag{B.6}$$

Assuming the flow is potential, the velocity is expressed using a velocity potential ϕ as $\mathbf{v} = \nabla\phi$, and so $\nabla\times\mathbf{v} = 0$. This notably implies

$$\nabla\omega = \nabla\Omega - (\mathbf{v}\cdot\nabla)\mathbf{v}\,.$$

(B.5) then becomes

$$\frac{\partial\nabla\phi}{\partial t} = -\nabla\Omega \Longrightarrow \Omega = -\frac{\partial\phi}{\partial t} + \tilde{\phi}\,,$$

where $\tilde{\phi}$ depends only on time t. Redefining the velocity potential $\phi \to \phi + \mathcal{F}(\tilde{\phi})$, where $F(\tilde{\phi})$ is an antiderivative of $\tilde{\phi}$, allows to write

$$\Omega = -\frac{\partial\phi}{\partial t}\,. \tag{B.7}$$

Note that the velocity potential is now defined up to an additive constant with respect to both spatial coordinates and time. Eventually, (B.4) provides

$$\Delta\phi \overset{(B.6)}{=} -\frac{1}{c^2}\left(\frac{\partial\Omega}{\partial t} + \mathbf{v}\cdot\nabla\Omega - \mathbf{v}\cdot\frac{\mathrm{d}\mathbf{v}}{\mathrm{d}t}\right) \overset{(B.7)}{=} -\frac{1}{c^2}\left(-\frac{\partial^2\phi}{\partial t^2} - \mathbf{v}\cdot\left(\frac{\partial\mathbf{v}}{\partial t} + \frac{\mathrm{d}\mathbf{v}}{\mathrm{d}t}\right)\right),$$

$$\Delta\phi - \frac{1}{c^2}\frac{\partial^2\phi}{\partial t^2} = \frac{1}{c^2}\left(\frac{\partial v^2}{\partial t} + \mathbf{v}\cdot(\mathbf{v}\cdot\nabla)\mathbf{v}\right),$$

$$\boxed{\Delta\phi - \frac{1}{c^2}\frac{\partial^2\phi}{\partial t^2} = \frac{1}{c^2}\left(\frac{\partial v^2}{\partial t} + \frac{1}{2}(\mathbf{v}\cdot\nabla)v^2\right)}, \tag{B.8}$$

where $v = \|\mathbf{v}\| = \|\nabla\phi\|$. (B.8) clearly shows a correction compared to the wave equation for the velocity potential

$$\Delta\phi - \frac{1}{c^2}\frac{\partial^2\phi}{\partial t^2} = 0\,,$$

since a (non-zero) right hand side is considered in (B.8). It also reflects that the wave equation is obtained from a linearisation of the Euler equations, since the right-hand side of (B.8) is composed of terms of order at least $O(v^2)$. (B.8) may be used to numerically quantify the error in considering the propagation of a far-field UNDEX as given by the wave equation, by checking that the right-hand side is marginal compared to the term $\frac{1}{c^2}\frac{\partial^2\phi}{\partial t^2}$ of the left-hand side.

So far, the analyses carried out in this thesis focused on the incident pressure induced by the shock wave, and the variation of fluid velocity $u_{\mathcal{W}}$ through the acoustic approximation (1.12). The other physical quantities related to the shock wave, namely the variation of density $\rho_{\mathcal{W}}$, and specific internal energy $e_{\mathcal{W}}$ have not been studied yet. Appendix B.2 aims to relate the quantities $\rho_{\mathcal{W}}$, $u_{\mathcal{W}}$ and $e_{\mathcal{W}}$ to the incident pressure $p_{\mathcal{W}}$, because the latter is the quantity that is effectively measured in experiments, and characterised using (1.4).

B.2 Approximated relations for the physical quantities of the shock wave

In view of the analysis carried out so far, it seems interesting to obtain a relation – at least an approximated relation – between the variation of density $\rho_{\mathcal{W}}$ and the incident pressure $p_{\mathcal{W}}$. Such a relation is commonly termed *equation of state*. In fluid mechanics, a common equation of state is the adiabatic Tait equation (Cole, 1948)

$$p = \frac{\rho_0 c_f^2}{m}\left(\frac{\rho_f}{\rho_0}\right)^m - \frac{\rho_0 c_f^2}{m}, \tag{B.9}$$

where $m \simeq 7$ and $\rho_0 c_f^2/m \simeq 3.2\ 10^8$ Pa in water. The water depths considered in this thesis are those of submarine immersions, and so do not exceed 500 meters. Therefore $p_h < 5\ 10^6$ Pa and $p_h + \rho_0 c_f^2/m \simeq \rho_0 c_f^2/m$. Then, (B.9) may be approximated by

$$p_{\mathcal{W}} = \frac{\rho_0 c_f^2}{m}\left(\frac{\rho_0 + \rho_{\mathcal{W}}}{\rho_0}\right)^m - \frac{\rho_0 c_f^2}{m}. \tag{B.10}$$

To check whether the equation of state (B.10) is consistent with the shock wave analysis, the Rankine-Hugoniot conditions are useful (Hugoniot, 1887 - 1888; Rankine, 1870). These

conditions express the conservations of mass, momentum and energy between the states on both sides of a shock wave, that is, between the unperturbed fluid, $p^{\text{tot}} = p_h$, and the perturbed one at the shock front, where $p^{\text{tot}} = p_{\mathcal{W}}(t = t_r) + p_h = p_m + p_h$. The Rankine-Hugoniot conditions are, **at distance $\boldsymbol{R}$ and time $\boldsymbol{t{=}R/c_f}$**, (Hugoniot, 1887 - 1888; Rankine, 1870; Cole, 1948; Brinkley and Kirkwood, 1947a,b)

$$p_m = \rho_0 U u_{\mathcal{W}} \qquad \text{conservation of momentum,} \tag{B.11a}$$

$$\rho_0 U = \rho_f (U - u_{\mathcal{W}}) \qquad \text{conservation of mass,} \tag{B.11b}$$

$$e_{\mathcal{W}} = \frac{1}{2}\left(p_m + 2\,p_h\right)\left(\frac{1}{\rho_0} - \frac{1}{\rho_f}\right) \qquad \text{conservation of energy,} \tag{B.11c}$$

where U is the shock wave velocity. As stated previously, the shock wave is highly supersonic near the explosion, and so it is likely that, far from the initial bursting point, the shock wave propagates slightly quicker than a classical wave. Empirically, the shock wave velocity is approximated by the linear relation (Arons and Yennie, 1948)

$$U(R) \simeq c_f \left(1 + 7.7\ 10^{-8} p_m(R)\right), \tag{B.12}$$

where the magnitude pressure, defined in (1.5), is expressed in Pa. (B.12) remains correct for values of p_m up to approximatively 300 MPa. Given the orders of magnitude of the pressure considered in the case of far-field underwater explosions, it is a fair approximation to set $U \simeq c_f$, and so (B.11) becomes, **at distance $\boldsymbol{R}$ and time $\boldsymbol{t{=}R/c_f}$**,

$$p_m = \rho_0\, c_f\, u_{\mathcal{W}}\,, \tag{B.13a}$$

$$\rho_0\, c_f = (\rho_0 + \rho_{\mathcal{W}})(c_f - u_{\mathcal{W}})\,, \tag{B.13b}$$

$$e_{\mathcal{W}} = \frac{1}{2}\left(p_m + 2\,p_h\right)\left(\frac{1}{\rho_0} - \frac{1}{\rho_0 + \rho_{\mathcal{W}}}\right). \tag{B.13c}$$

These conditions (B.13) do not provide a relation between the quantities during the relaxation, after the shock front passed through the fluid, but only at the shock front. Therefore, (B.13) provides a relation between maximum pressure, maximum particle velocity and maximum density. Arons and Yennie (1948) proposed to extend the Rankine-Hugoniot conditions during the relaxation, after the shock wave front, as an approximation, **at distance $\boldsymbol{R}$, at any time**

$$p_{\mathcal{W}} \simeq \rho_0\, c_f\, u_{\mathcal{W}}\,, \tag{B.14a}$$

$$\rho_0 c_f \simeq (\rho_0 + \rho_{\mathcal{W}})(c_f - u_{\mathcal{W}})\,, \tag{B.14b}$$

$$e_{\mathcal{W}} \simeq \frac{1}{2}\left(p_{\mathcal{W}} + 2\,p_h\right)\left(\frac{1}{\rho_0} - \frac{1}{\rho_0 + \rho_{\mathcal{W}}}\right). \tag{B.14c}$$

The extension of (B.13a) at any time, (B.14a), results in the plane wave approximation, which is a relevant approximation in our case, as it corresponds to (1.12), because the after flow term in (1.12) is negligible (see Section 1.2.2). Assuming the validity of (B.14b) at any time must be consistent with the Tait equation (B.10), because only one equation of state can be set. For the shock wave phenomenon, the Tait equation (B.10) provides

$$\rho_{\mathcal{W}} = \rho_0 \left(1 + m\,\frac{p_{\mathcal{W}}}{\rho_0 c_f^2}\right)^{1/m} - \rho_0\,. \tag{B.15}$$

In the plane wave approximation, (B.14b) is rewritten at any time as

$$\rho_{\mathcal{W}} \simeq \rho_0 \left(1 - \frac{p_{\mathcal{W}}}{\rho_0 c_f^2}\right)^{-1} - \rho_0 \,. \tag{B.16}$$

For $p_{\mathcal{W}} \ll \rho_0 c_f^2$ ($\simeq 2$ GPa in water), namely at low value of the *Euler number*, the Tait equation (B.15) coincides with the extension of the Rankine-Hugoniot condition (B.16) in the plane wave approximation, leading to the approximate relation

$$\rho_{\mathcal{W}} \simeq \frac{p_{\mathcal{W}}}{c_f^2} \,. \tag{B.17}$$

Finally, (B.14c) at any time provides

$$e_{\mathcal{W}} \simeq \frac{1}{2} \frac{p_{\mathcal{W}} + 2\,p_h}{\rho_0} \left(1 - \left(1 + \frac{\rho_{\mathcal{W}}}{\rho_0}\right)^{-1}\right),$$

using (B.17) and the fact that $p_{\mathcal{W}} \ll \rho_0 c_f^2$, it comes

$$e_{\mathcal{W}} \simeq \frac{1}{2} \frac{p_{\mathcal{W}} + 2\,p_h}{\rho_0} \left(\frac{p_{\mathcal{W}}}{\rho_0 c_f^2}\right).$$

Conclusion. In a configuration such that $p_m(r) \ll \rho_0 c_f^2$ ($\simeq 2$ GPa in water), which is the case in this work, the quantities characterising the shock wave are approximated, at a distance r from the explosion, for any time such that $t - r/c_f \leq 7\tau(r)$, by

$$p_{\mathcal{W}}(r,t) = p_m(r) \left(\alpha_1\, e^{-\beta_1\, t_r/\tau(r)} + \alpha_2\, e^{-\beta_2\, t_r/\tau(r)}\right) H(t_r) \,, \tag{B.18a}$$

$$\rho_{\mathcal{W}} \simeq \frac{p_{\mathcal{W}}}{c_f^2} \,, \tag{B.18b}$$

$$u_{\mathcal{W}} \simeq \frac{p_{\mathcal{W}}}{\rho_0\, c_f} \,, \tag{B.18c}$$

$$e_{\mathcal{W}} \simeq \frac{1}{2} \frac{p_{\mathcal{W}} + 2\,p_h}{\rho_0} \left(\frac{p_{\mathcal{W}}}{\rho_0 c_f^2}\right), \tag{B.18d}$$

$$p_{\mathcal{W}} \sim 10^6 \text{ Pa} \ll \rho_0 c_f^2 \sim 10^9 \text{ Pa} \,, \quad \rho_{\mathcal{W}} \sim 1 \text{ kg/m}^3 \ll \rho_0 \sim 10^3 \text{ kg/m}^3 \,, \tag{B.18e}$$

$$e_{\mathcal{W}} \sim 1 \text{ m}^2/\text{s}^2 \ll c_f^2 \sim 10^6 \text{ m}^2/\text{s}^2 \,, \quad u_{\mathcal{W}} \sim 1 \text{ m/s} \ll c_f \sim 10^3 \text{ m/s} \,, \tag{B.18f}$$

where $t_r \equiv t - r/c_f$ is the retarded time. The set of relations (B.18) permits the computation of the total energy related to the shock wave. This computation is performed in Appendix B.3, where, for once, we do not assume the UNDEX to be remote.

B.3 Computation of the total energy related to the shock wave

In this section, we summarise the steps carried out in (Arons and Yennie, 1948) to compute the total energy flow related to the shock wave (see Figure 1.3), based on the Rankine-Hugoniot conditions. In the whole section, we do not assume the explosion to be remote. The total energy flow due to the shock wave that goes through a sphere of radius R and centre the initial bursting point is composed of three terms:

- the compressional acoustic energy, computed in Section 1.2.2, that corresponds to an energy travelling through the fluid, not stored in the latter but radiated at infinity;
- the kinetic energy of the mass of fluid moving past the point of observation;
- the elevation of internal energy of the mass of fluid relatively to the initially unperturbed state. This elevation notably manifests itself in the variation of temperature of the fluid.

Using the notations defined in Notations, the total energy flux F due to the shock wave, through a sphere of radius R and centre the initial bursting point, is then given by

$$F(R) = \int_0^{t_1} \Bigg(\underbrace{\frac{p_{\mathcal{W}}(R,t)}{\rho_f(R,t)}}_{\text{acoustic}} + \underbrace{\frac{1}{2} u_{\mathcal{W}}(R,t)^2}_{\text{kinetic}} + \underbrace{e_{\mathcal{W}}(R,t)}_{\text{internal}} \Bigg) \rho_f(R,t)\, u_{\mathcal{W}}(R,t)\, \mathrm{d}t\,, \tag{B.19}$$

where $e_{\mathcal{W}}$ denotes the increase in internal energy per unit of mass of fluid relatively to the unperturbed state, and t_1 is an arbitrary upper limit of integration, that is, for instance, set such that the retarded time $t_1 - R/c_f$ is equal to 7τ (see Section 1.2.1). Note that the dependence of the fluid density on R and t is taken into account. The density of the initially unperturbed fluid is denoted ρ_0 in the following. The acoustic approximation (1.12) is rewritten as

$$u_{\mathcal{W}}(R,t) = \frac{p_{\mathcal{W}}(R,t)}{\rho_0\, c_f} + \frac{1}{R\,\rho_0} \int_0^t p_{\mathcal{W}}(R,\theta)\, \mathrm{d}\theta \equiv \frac{p_{\mathcal{W}}(R,t)}{\rho_0\, c_f} + \frac{I(R,t)}{R\,\rho_0}\,, \tag{B.20}$$

where the second term in (B.20) is often referred to as the after-flow term in the particle velocity (Arons and Yennie, 1948). Using (B.20), the total flow of energy associated to the flux (B.19) holds as

$$E = 4\pi R^2 \left[\int_0^{t_1} \left(\frac{p_{\mathcal{W}}}{\rho_f} + \frac{u_{\mathcal{W}}^2}{2} + e_{\mathcal{W}} \right) \frac{\rho_f p_{\mathcal{W}}}{\rho_0 c_f}\, \mathrm{d}t + \frac{1}{R} \int_0^{t_1} \frac{\rho_f}{\rho_0} \left(\frac{p_{\mathcal{W}}}{\rho_f} + \frac{u_{\mathcal{W}}^2}{2} + e_{\mathcal{W}} \right) I(R,t)\, \mathrm{d}t \right]. \tag{B.21}$$

(B.21) is composed of two terms that depend on the incident pressure $p_{\mathcal{W}} = p - p_h$, the particle velocity $u_{\mathcal{W}}$ and the increment $e_{\mathcal{W}}$. The extension of the Rankine-Hugoniot conditions (B.11) at any time is then useful: **at distance $\boldsymbol{R}$ and time $\boldsymbol{t{=}R/c_f}$**,

$$p_{\mathcal{W}} \simeq \rho_0 U u_{\mathcal{W}} \qquad \text{conservation of momentum,} \tag{B.22a}$$

$$\rho_0 U \simeq \rho_f (U - u_{\mathcal{W}}) \qquad \text{conservation of mass,} \tag{B.22b}$$

$$e_{\mathcal{W}} \simeq \frac{1}{2} (p_{\mathcal{W}} + 2\, p_h) \left(\frac{1}{\rho_0} - \frac{1}{\rho_f} \right) \qquad \text{conservation of energy.} \tag{B.22c}$$

Using (B.22), the term $u_{\mathcal{W}}^2/2 + e_{\mathcal{W}}$ is compared to $p_{\mathcal{W}}/\rho_f$ in (B.21):

$$\frac{p_{\mathcal{W}}/\rho_f}{u_{\mathcal{W}}^2/2} \overset{\text{(B.22a)}}{\simeq} 2\, \frac{\rho_0}{\rho_f}\, \frac{\rho_0\, U^2}{p_{\mathcal{W}}}\,, \tag{B.23}$$

$$e_{\mathcal{W}} \overset{\text{(B.22c)}}{\simeq} \frac{p_{\mathcal{W}} + 2\, p_h}{2} \left(\frac{1}{\rho_0} - \frac{1}{\rho_f} \right) \overset{\text{(B.22b)}}{\simeq} \frac{p_{\mathcal{W}} + 2\, p_h}{2}\, \frac{u_{\mathcal{W}}}{U \rho_0} \overset{\text{(B.22a)}}{\simeq} \frac{p_{\mathcal{W}} + 2\, p_h}{2}\, \frac{p_{\mathcal{W}}}{(U\rho_0)^2}\,, \tag{B.24}$$

$$\frac{p_{\mathcal{W}}/\rho_f}{e_{\mathcal{W}}} \simeq 2\, \frac{\rho_0}{\rho_f}\, \frac{\rho_0\, U^2}{p_{\mathcal{W}} + 2\, p_h}\,. \tag{B.25}$$

It is noticeable that the extension of the Rankine-Hugoniot conditions implies that $e_{\mathcal{W}} \simeq u_{\mathcal{W}}^2/2$ when $p_{\mathcal{W}} \gg p_h$. At low values of $p_{\mathcal{W}}$ compared to $\rho_0 U^2 \simeq \rho_0 c_f^2$ ($\simeq 2$ GPa in water),

i.e., at low values of the *Euler number*, the ratios (B.23) and (B.25) show that $u_{\mathcal{W}}^2/2 + e_{\mathcal{W}}$ is marginal compared to $p_{\mathcal{W}}$. Then, the contribution $u_{\mathcal{W}}^2/2 + e_{\mathcal{W}}$ in (B.21) has to be taken into account only for very high values of $p_{\mathcal{W}}$.

Therefore, the second term in the right-hand side of (B.21) does not need to take into account the sum $u_{\mathcal{W}}^2/2 + e_{\mathcal{W}}$, because the quantity $I(t, R)$ is initially 0 and does not have an appreciable value before a certain amount of time, during which the pressure $p_{\mathcal{W}}$ is exponentially plummeting, and so after which it is reasonable to consider $p_{\mathcal{W}} \ll \rho_0 c_f^2$.

When the shock wave velocity U may be associated to c_f, the total flow of energy holds as, in the approximation $e_{\mathcal{W}} \simeq u_{\mathcal{W}}^2/2 \simeq {p_{\mathcal{W}}}^2/(2\, c_f^2 \rho_0^2)$ and $\rho_f \simeq \rho_0$,

$$E(R) \simeq \frac{4\pi R^2}{\rho_0} \left[\int_0^{t_1} \frac{(p_{\mathcal{W}})^2}{c_f} \left(1 + \frac{p_{\mathcal{W}}}{\rho_0 c_f^2} \right) \mathrm{d}t + \frac{1}{R} \int_0^{t_1} p_{\mathcal{W}} I(t, R)\, \mathrm{d}t \right] . \tag{B.26}$$

The right-hand side of (B.26) is composed of two terms: the first one is a radiated energy, whereas the second one represents an energy stored reversibly in the region covered by the shock wave. This second term shows that the shock wave is not an ideal wave, an issue discussed in Section 1.2.3. Obtaining (B.26) is the first step to be performed to get the values presented in Figure 1.3. We will not go further into the theoretical partitioning of the energy for the shock wave, and we kindly suggest the reader to refer to (Arons and Yennie, 1948) for more details.

Appendix C

Proofs and calculations

C.1 Wave equation for the shock wave incident pressure

This section checks to what extent the shock wave incident pressure (1.3) satisfies the wave equation (1.20). We consider only the regular exponential part, so the pressure discontinuity is not taken into account. For the double-exponential fit, the incident pressure is written in the form

$$\begin{aligned} &p_{\mathcal{W}}(r,t) = Pr^{-a_1}\left(\alpha_1 \exp\left(-A\, r^{a_2}(t-r/c_f)\right) + \alpha_2 \exp\left(-B\, r^{a_2}(t-r/c_f)\right)\right), \\ &p_{\mathcal{W}}(r,t) \equiv p_{\mathcal{W}1}(r,t) + p_{\mathcal{W}2}(r,t)\,, \end{aligned}$$

where some new letters have been introduced to ease the notations:

$$P \equiv K_1 W^{a_1/3}\,, \quad A \equiv \beta_1\, K_2^{-1} W^{-(1+a_2)/3}\,, \quad B \equiv \beta_2\, K_2^{-1} W^{-(1+a_2)/3}\,.$$

First, the Laplacian is computed in spherical coordinates:

$$\Delta p_{\mathcal{W}} = \frac{2}{r}\frac{\partial p_{\mathcal{W}}}{\partial r} + \frac{\partial^2 p_{\mathcal{W}}}{\partial r^2}\,,$$

$$\frac{\partial p_{\mathcal{W}}}{\partial r} = -\frac{a_1}{r} p_{\mathcal{W}} + \left(-a_2\, t\, r^{a_2-1} + (a_2+1)\,\frac{r^{a_2}}{c_f}\right)\left(A\, p_{\mathcal{W}1} + B\, p_{\mathcal{W}2}\right),$$

$$\begin{aligned} \frac{\partial^2 p_{\mathcal{W}}}{\partial r^2} = {} & \frac{a_1}{r^2} p_{\mathcal{W}} - \frac{a_1}{r}\frac{\partial p_{\mathcal{W}}}{\partial r} + \left(a_2(1-a_2) t\, r^{a_2-2} + a_2(a_2+1)\,\frac{r^{a_2-1}}{c_f}\right)\left(A\, p_{\mathcal{W}1} + B\, p_{\mathcal{W}2}\right) \\ & + \left(-a_2\, t\, r^{a_2-1} + (a_2+1)\,\frac{r^{a_2}}{c_f}\right)\left(A\,\frac{\partial p_{\mathcal{W}1}}{\partial r} + B\,\frac{\partial p_{\mathcal{W}2}}{\partial r}\right). \end{aligned}$$

For $k \in \{1,2\}$,

$$\frac{\partial p_{\mathcal{W}k}}{\partial r} = -\frac{a_1}{r} p_{\mathcal{W}k} + \left(-a_2\, t\, r^{a_2-1} + (a_2+1)\,\frac{r^{a_2}}{c_f}\right)\gamma_k\, p_{\mathcal{W}k}\,,\ \gamma_k \equiv A\,\delta_{1k} + B\,\delta_{2k}\,.$$

The time derivatives of $p_{\mathcal{W}}$ are

$$\frac{\partial p_{\mathcal{W}}}{\partial t} = -r^{a_2}(A\, p_{\mathcal{W}1} + B\, p_{\mathcal{W}2})\,, \quad \frac{\partial^2 p_{\mathcal{W}}}{\partial t^2} = r^{2a_2}(A^2\, p_{\mathcal{W}1} + B^2\, p_{\mathcal{W}2})\,.$$

The left-hand side of the wave equation is composed of a sum of terms of different powers of r. This sum is zero for all r if and only if the coefficient of each power is zero, that is

$$p_{\mathcal{W}}\, r^{-2} \left(a_1 + a_1^2 - 2a_1\right) = 0\,, \tag{C.1a}$$

$$\left(A\, p_{\mathcal{W}1} + B\, p_{\mathcal{W}2}\right) r^{a_2-2} \left(a_1 a_2 + a_2(1-a_2) + a_2 a_1 - 2a_2\right) t = 0\,, \tag{C.1b}$$

$$\left(A\, p_{\mathcal{W}1} + B\, p_{\mathcal{W}2}\right) r^{a_2-1} \left(-a_1(a_2+1) + a_2(a_2+1) - a_1(a_2+1) + 2(a_2+1)\right) \frac{1}{c_f} = 0\,, \tag{C.1c}$$

$$\left(A^2\, p_{\mathcal{W}1} + B^2\, p_{\mathcal{W}2}\right) r^{2a_2-2} \left(a_2^2\right) t^2 = 0\,, \tag{C.1d}$$

$$\left(A^2\, p_{\mathcal{W}1} + B^2\, p_{\mathcal{W}2}\right) r^{2a_2-1} \left(-2a_2(a_2+1)\right) \frac{t}{c_f} = 0\,, \tag{C.1e}$$

$$\left(A^2\, p_{\mathcal{W}1} + B^2\, p_{\mathcal{W}2}\right) r^{2a_2} \left((a_2+1)^2 - 1\right) \frac{1}{c_f^2} = 0\,, \tag{C.1f}$$

and so the system to be satisfied is

$$\begin{cases} a_1 + a_1^2 - 2a_1 = 0\,, \\ a_1 a_2 + a_2(1-a_2) + a_2 a_1 - 2a_2 = 0\,, \\ -a_1(a_2+1) + a_2(a_2+1) - a_1(a_2+1) + 2(a_2+1) = 0\,, \\ a_2^2 = 0\,, \\ -2a_2(a_2+1) = 0\,, \\ (a_2+1)^2 - 1 = 0\,, \end{cases} \tag{C.2}$$

whose unique solution is $(a_1 = 1, a_2 = 0)$.

C.2 Derivation of a simple spherical bubble model, incompressible flow

C.2.1 Hypotheses of the modelling

In this section, the dynamics of an oscillating bubble $\mathcal{B}$ that migrates toward an **infinitely remote** water surface is considered. The equations of motion are obtained in the case of a **spherical bubble**, moving in an **infinite perfect fluid**, where the flow is assumed to be **incompressible** and **potential**. In particular, the last two hypotheses imply

$$\mathbf{v} = \nabla\phi\,, \quad \nabla\cdot\mathbf{v} = 0 \quad \Longrightarrow \quad \Delta\phi = 0\,,$$

where ϕ is the velocity potential and Δ denotes the spatial Laplacian. For a function $f(r,\theta,\varphi)$, it is recalled that

$$\Delta f = \frac{1}{r^2}\frac{\partial}{\partial r}\left(r^2\frac{\partial f}{\partial r}\right) + \frac{1}{r^2\sin\theta}\frac{\partial}{\partial\theta}\left(\sin\theta\frac{\partial f}{\partial\theta}\right) + \frac{1}{r^2\sin^2\theta}\frac{\partial^2 f}{\partial\varphi^2}\,.$$

To take advantage of the spherical and axial symmetries, the study is performed in a vertical plane section containing the bubble centre, and so the initial bursting point (see Figure C.1). The velocity potential ϕ must satisfy

$$\begin{cases} \phi(r,\theta,0) = 0 & \forall r > a_c\,, \forall\theta\in[0,\pi]\,, \\ \lim\limits_{r\to\infty}\phi(r,\theta,t) = 0 & \forall t\geq 0\,, \forall\theta\in[0,\pi]\,. \end{cases} \tag{C.3}$$

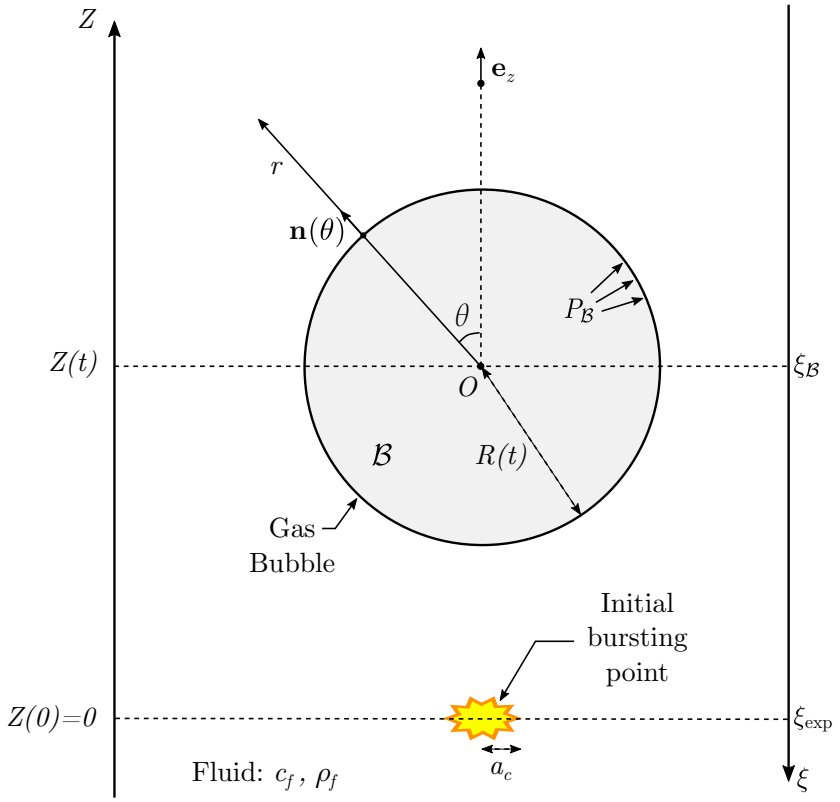

Figure C.1: Cross-section of the (assumed spherical) gas bubble created by an underwater explosion.

The first condition of (C.3) reflects the fact that the system is at initial rest, when the explosion occurs. The second condition, termed decay condition, means that, very far away, the fluid is not affected by the explosion.

The equations of motion of the bubble can be obtained either using a Lagrangian formalism, like e.g., in (Doinikov, 2002), or directly from the principle of conservation of the total energy. In both methods, the velocity potential ϕ must be specified beforehand.

C.2.2 Velocity potential

The system considered is a spherical gas bubble that moves vertically, along $\mathbf{e}_z$, toward the water surface, and whose surface oscillates. In spherical coordinates (r, θ, φ), with a moving origin at the centre of the bubble, the continuity of the normal velocity at the bubble surface implies, at any non-negative time t,

$$\nabla\phi \cdot \mathbf{e}_r|_{r=R(t)} = \left.\frac{\partial\phi}{\partial r}\right|_{r=R(t)} = \left(\dot{R}(t)\mathbf{e}_r + \dot{Z}(t)\mathbf{e}_z\right) \cdot \mathbf{e}_r = \dot{R}(t) + \dot{Z}(t)\cos(\theta)\,, \tag{C.4}$$

with $R(t)$ being the bubble radius and $Z(t)$ the bubble centre position, defined as $Z(t) = \xi_{\text{exp}} - \xi_{\mathcal{B}}(t)$, where ξ_{exp} is the positive depth of the original bursting point, and $\xi_{\mathcal{B}}(t)$ is the positive depth of the bubble centre. For now, we set *a priori* $Z(0) = 0$ and $\dot{Z}(0) = 0$. Because of the axial symmetry, it is useful to decompose the velocity potential in the form

$$\phi(r, \theta, t) = \sum_{n=0}^{\infty} \phi_n(r, t) P_n(\cos\theta)\,,$$

where P_n are Legendre polynomials, defined as solutions to Legendre's differential equations:

$$(1-x^2)\frac{\mathrm{d}^2P_n(x)}{\mathrm{d}x^2} - 2x\frac{\mathrm{d}P_n(x)}{\mathrm{d}x} + n(n+1)P_n(x) = 0\,,\ \forall x \in [-1,1]\,,\ \forall n \in \mathbb{N}\,. \tag{C.5}$$

The Laplacian of ϕ is then given by

$$\begin{aligned}
\Delta\phi &= \frac{1}{r^2}\frac{\partial}{\partial r}\left(r^2\frac{\partial\phi}{\partial r}\right) + \frac{1}{r^2\sin\theta}\frac{\partial}{\partial\theta}\left(\sin\theta\frac{\partial\phi}{\partial\theta}\right)\\
&= \sum_{n=0}^{\infty}\left(\frac{\partial^2\phi_n}{\partial r^2}P_n(\cos\theta) + \frac{2}{r}\frac{\partial\phi_n}{\partial r}P_n(\cos\theta) + \frac{1}{r^2\sin\theta}\phi_n\frac{\partial}{\partial\theta}\left(-(\sin\theta)^2P_n'(\cos\theta)\right)\right)\\
&= \sum_{n=0}^{\infty}\left(\frac{\partial^2\phi_n}{\partial r^2}P_n(\cos\theta) + \frac{2}{r}\frac{\partial\phi_n}{\partial r}P_n(\cos\theta)\right.\\
&\quad\left. + \frac{1}{r^2}\phi_n\left((1-(\cos\theta)^2)P_n''(\cos\theta) - 2\cos\theta P_n'(\cos\theta)\right)\right),
\end{aligned}$$

using (C.5) with $x = \cos\theta$, it holds

$$\Delta\phi = \sum_{n=0}^{\infty}\left(\frac{\partial^2\phi_n}{\partial r^2}P_n(\cos\theta) + \frac{2}{r}\frac{\partial\phi_n}{\partial r}P_n(\cos\theta) - \frac{n(n+1)}{r^2}\phi_nP_n(\cos\theta)\right). \tag{C.6}$$

(C.6) provides a set of uncoupled equations:

$$r^2\frac{\partial^2\phi_n}{\partial r^2} + 2r\frac{\partial\phi_n}{\partial r} - n(n+1)\phi_n = 0\,,\quad \forall n \in \mathbb{N}\,. \tag{C.7}$$

The solutions of (C.7) that allow ϕ to satisfy (C.3) are

$$\phi_n = \frac{a_n(t)}{r^{n+1}}\,.$$

The coefficients a_n are obtained using the equation of continuity (C.4):

$$\left.\frac{\partial\phi}{\partial r}\right|_{r=R(t)} = \sum_{n=0}^{\infty}\frac{\partial\phi_n}{\partial r}(R,t)P_n(\cos\theta) = \dot{R}(t) + \dot{Z}(t)\cos\theta\,,\quad \forall t \geq 0\,.$$

The Legendre polynomials are $L^2([-1,1])$-orthogonal functions, so using $P_0(X) = 1$ and $P_1(X) = X$, it comes

$$-\frac{1}{R^2(t)}\,a_0(t) = \dot{R}(t)\,,\quad -\frac{2}{R^3(t)}\,a_1(t) = \dot{Z}(t)\,,\quad a_n(t) = 0\,,\ \forall n \geq 2\,,$$

and then

$$\phi(r,\theta,t) = -\frac{R^2(t)\dot{R}(t)}{r} - \frac{R^3(t)\dot{Z}(t)}{2r^2}\cos\theta\,. \tag{C.8}$$

This result is obtained under the hypothesis that the water surface is remote, and hence disregarded. (C.8) shows that in the case of a spherical oscillating bubble, vertically translating towards a surface located infinitely far away, the solution to $\Delta\phi = 0$ is composed of only two terms: a source term ϕ_0 for the bubble oscillation and a dipole $\phi_1\cos(\theta)$ for the translation (Landau and Lifshitz, 1987). In the following, the total energy of the system is obtained using (C.8), and the equations of motion are inferred from the law of conservation of this total energy.

C.2.3 Equations of motion from the energy conservation law

The kinetic energy of the fluid is defined as

$$E_k := \frac{\rho_f}{2}\int_V |\mathbf{v}|^2\,\mathrm{d}V = \frac{\rho_f}{2}\int_R^\infty\int_0^\pi |\nabla\phi|^2\,2\pi r^2\sin\theta\,\mathrm{d}\theta\,\mathrm{d}r\,.$$

Using (C.8), it comes

$$\begin{aligned} E_k &= \frac{\rho_f}{2}\,2\pi\int_R^\infty 2\frac{R^4(t)\dot{R}^2(t)}{r^2} + \frac{2}{3}\frac{R^6(t)\dot{Z}^2(t)}{r^4} + \frac{4}{3}\frac{R^6(t)\dot{Z}^2(t)}{4r^4}\,\mathrm{d}r \\ &= \frac{1}{2}\left(\frac{4}{3}\pi R^3\rho_f\right)\left(3\,\dot{R}^2 + \frac{\dot{Z}^2}{2}\right). \end{aligned} \tag{C.9}$$

Since $\dot{R}$ is the velocity of the oscillation and $\dot{Z}$ that of the translation, the quantities $4\pi\rho_f R^3$ and $(2\pi/3)\rho_f R^3$ correspond to the added masses of oscillating and translational motions, respectively. The purpose is now to compute the power of the various forces. First, the power of the pressure forces, derivative of the work W_p with respect to the time, is computed:

$$\frac{\mathrm{d}W_p}{\mathrm{d}t} = -\int_{\Gamma_f}\mathbf{v}\cdot\mathbf{n}\,p\,\mathrm{d}S\,,$$

where p is the fluid pressure, Γ_f is the boundary of the fluid domain Ω_f, and $\mathbf{n}$ is the outward normal to Ω_f. Considering a large enough sphere S_r of radius $r > \sup_{t>0}[R(t)]$, centred at O, the time derivative of the work W_b is

$$\frac{\mathrm{d}W_p}{\mathrm{d}t} = \int_{S_R}\frac{\partial\phi}{\partial r}\,P_{\mathcal{B}}\,\mathrm{d}S - \lim_{r\to\infty}\int_{S_r}\frac{\partial\phi}{\partial r}\,p\,\mathrm{d}S\,,$$

where S_R and $P_{\mathcal{B}}$ denote the bubble surface and the pressure on this surface, respectively. The pressure p at point $M(r,\theta,\psi)\in S_r$, far away from the bubble, is the hydrostatic pressure: $p = \rho_f g\xi_M + P_0$ where ξ_M is the water depth at M and P_0 is the atmospheric pressure. Using $\xi_M = \xi_{\mathrm{exp}} - Z(t) - r\cos\theta$, it comes $p = \rho_f g(\xi_{\mathrm{atm}} + \xi_{\mathrm{exp}} - Z(t) - r\cos\theta)$, with $\xi_{\mathrm{atm}} \equiv P_0/(\rho_f g)$, $\xi_{air} \simeq 10$ m. Therefore, using (C.8),

$$\begin{aligned} \frac{\mathrm{d}W_p}{\mathrm{d}t} &= 4\pi R^2\dot{R}P_{\mathcal{B}} - 4\pi R^2\dot{R}\rho_f g(\xi_{\mathrm{atm}} + \xi_{\mathrm{exp}} - Z) + \frac{2}{3}\,2\pi R^3\rho_f g\dot{Z} \\ &= 4\pi R^2\dot{R}(P_{\mathcal{B}} - P_{\mathrm{exp}}) + 4\pi R^2\dot{R}\rho_f g Z + \frac{4}{3}\pi R^3\rho_f g\dot{Z}\,, \end{aligned}$$

where $P_{\mathrm{exp}} \equiv \rho_f g(\xi_{\mathrm{atm}} + \xi_{\mathrm{exp}})$ is the hydrostatic pressure at the initial bursting point. The associated work is then simply given by

$$W_p = \frac{4}{3}\pi R^3(P_{\mathcal{B}} - P_{\mathrm{exp}} + \rho_f g Z) + C\,,$$

where C is a constant independent of time t. In order to be closer to the experimental results, a force reflecting the fluid resistance has to be taken into account: a drag force of magnitude $F_D = (1/2)\rho_f\pi R^2 C_D\dot{Z}^2$, opposed to the motion, proportional to the cross section area of the sphere and to the square of the vertical migration velocity. C_D is termed drag coefficient, and is set to 2.25 on the basis of experimental results. According to (Geers and Park, 2005) this value of C_D was first obtained in (Hicks, 1970). The power of the drag force is

$$\frac{\mathrm{d}W_D}{\mathrm{d}t} = \mathbf{F}_D\cdot\dot{Z}\mathbf{e}_z = -\frac{1}{2}\rho_f\pi C_D R^2\dot{Z}^3\,.$$

If the energy losses due to both thermal exchanges and radiation of secondary waves are not taken into account, the conservation of the total energy of the fluid over time provides (denoting by U the potential energy):

$$\frac{\mathrm{d}}{\mathrm{d}t}(E_k + U) = \frac{\mathrm{d}}{\mathrm{d}t}(E_k - W_P - W_D) = 0\,.$$

After division by $2/3\pi R^3\rho_f$, it comes

$$0 = \frac{6}{R}\dot{R}\left(\frac{3}{2}\,\dot{R}^2 + \frac{\dot{Z}^2}{4}\right) + 6\dot{R}\ddot{R} + \dot{Z}\ddot{Z} - \frac{6}{R\rho_f}\dot{R}(P_{\mathcal{B}} - P_{\mathrm{exp}}) - \frac{6}{R}\dot{R}\,gZ - 2g\dot{Z} + \frac{3}{4}\,C_D\frac{\dot{Z}^3}{R}\,. \tag{C.10}$$

Actually, (C.10) does not suffice to obtain the equations of motion of the bubble. It is then useful to also consider the momentum p_z of the bubble in the direction $\mathbf{e}_z$:

$$p_z = \frac{\mathrm{d}E_k}{\mathrm{d}\dot{Z}} = \frac{2}{3}\,\pi R^3\rho_f\dot{Z}\,, \tag{C.11}$$

and then, applying the second law of Newton to the bubble subjected to the buoyancy and drag forces, it comes

$$\frac{\mathrm{d}p_z}{\mathrm{d}t} = \frac{4}{3}\,\pi R^3\rho_f g - \frac{1}{2}\,\rho_f\pi C_D R^2\dot{Z}^2\,. \tag{C.12}$$

Combining the time derivative of (C.11) and (C.12), it holds, after division by $2/3\pi R^3\rho_f$,

$$3\frac{\dot{R}}{R}\dot{Z} + \ddot{Z} = 2g - \frac{3}{4}\,C_D\frac{\dot{Z}^2}{R}\,. \tag{C.13}$$

Hence, some terms in (C.10) vanish, and the latter becomes, after division by $6\dot{R}/R$,

$$R\ddot{R} + \frac{3}{2}\dot{R}^2 = \frac{1}{\rho_f}(P_{\mathcal{B}} - P_{\mathrm{exp}}) + \frac{\dot{Z}^2}{4} + gZ\,. \tag{C.14}$$

Equations (C.13) and (C.14) are the coupled equations of motion for the spherical sphere under the hypotheses of perfect fluid, incompressible and potential flow. To solve (C.14), it is necessary to specify $P_{\mathcal{B}}$, the pressure at the bubble surface. For a perfect fluid, $P_{\mathcal{B}}$ is linked to the internal pressure within the gas P_g and the surface tension σ. For an underwater explosion, the pressure values are so high that the effects of surface tension are marginal, and so $P_{\mathcal{B}}$ is simply set to the internal pressure of the gas. In the simplest case, considering the pressure within the gas as uniform and the process expansion/contraction as adiabatic, the relation of a polytropic process holds

$$P_{\mathcal{B}} = \kappa_c\left(\frac{V_c}{V}\right)^{\gamma} = \kappa_c\left(\frac{a_c}{R}\right)^{3\gamma}\,, \tag{C.15}$$

where γ is the ratio of the heat capacity at constant pressure to heat capacity at constant volume, and κ_c is a coefficient related to the charge. For instance, for TNT, the empirical values of these coefficients are (Best, 2002; Arons and Yennie, 1948) (assuming a typical TNT density of 1.654 g/cm^3)

$$\gamma \simeq 1.23 \text{ to } 1.25\,, \quad \kappa_c \simeq 1.35\ 10^9 \text{ Pa}\,.$$

Finally, the equations of motion are:

$$3\frac{\dot{R}}{R}\dot{Z} + \ddot{Z} + \frac{3}{4}C_D\frac{\dot{Z}^2}{R} = 2g\,, \tag{C.16a}$$

$$R\ddot{R} + \frac{3}{2}\dot{R}^2 - \frac{\kappa_c}{\rho_f}\left(\frac{a_c}{R}\right)^{3\gamma} = -\frac{P_{\text{exp}}}{\rho_f} + \frac{\dot{Z}^2}{4} + gZ\,. \tag{C.16b}$$

To be numerically implemented, the set of equations (C.16) must be supplemented with initial conditions.

C.2.4 Initial conditions of the bubble model

The equations of motion (C.16) are solvable if suitable initial conditions are also provided. Basic intuition would suggest to set those initial conditions to $Z(0) = 0$, $\dot{Z}(0) = 0$, $R(0) = a_c$ and $\dot{R}(0) = 0$. However, these initial conditions lead to numerical results that differ from the experimental ones, notably regarding the maximum radius of the bubble (Best, 2002; Leblond, 2007).

To deal with this issue, the initial conditions are instead set such that the maximum radius numerically predicted corresponds to the one experimentally measured, given by (1.25). This maximum radius may be obtained via energy conservation arguments, following the steps given in (Best, 2002).

If the vertical motion is not taken into account during the first oscillation, the velocity potential and the kinetic energy of the fluid are given by (C.8) and (C.9) with $\dot{Z} = 0$:

$$\phi(r,\theta,t) = -\frac{R^2(t)\dot{R}(t)}{r}\,, \quad E_k = 2\pi\rho_f R^3\dot{R}^2\,.$$

The potential energy of the bubble when it has a radius R corresponds to the work done in expanding radius from zero to R, against the hydrostatic pressure,

$$W_p = \frac{4}{3}\pi R^3 P_{\text{exp}}\,,$$

where P_{exp} is the hydrostatic pressure at the initial bursting point. The internal energy of the gas within the bubble is equal to the work done in compressing this gas from infinite volume, zero pressure, to the bubble volume $V_{\mathcal{B}}$ at radius R adiabatically:

$$U_i = -\int_{\infty}^{V_{\mathcal{B}}} P_g\,\mathrm{d}V\,.$$

Using (C.15) and recalling that $P_{\mathcal{B}} = P_g$ because surface tension effects are marginal, it comes

$$U_i = -\int_{\infty}^{V_{\mathcal{B}}} \kappa_c\left(\frac{V_c}{V}\right)^{\gamma}\mathrm{d}V = \left(\frac{4}{3}\,\pi\right)^{1-\gamma}\frac{\kappa_c(V_c)^{\gamma}}{\gamma-1}\,R^{3(1-\gamma)}\,.$$

It is noticed in (Best, 2002) that photographic records of underwater explosions suggest that the explosive mass is not totally converted to gas upon detonation, some solid remnants being observed. Assuming that a given proportion l of the explosive mass is converted to gas, the internal energy is written as

$$U_i = \left(\frac{4}{3}\,\pi\right)^{1-\gamma}\frac{\kappa W^{\gamma}}{\gamma-1}\,R^{3(1-\gamma)}\,,$$

where $\kappa \equiv \kappa_c(\rho_e^{-1}l)^\gamma$ and ρ_e denotes the mass density of the explosive material. If ε denotes the (unknown) amount of energy provided to the bubble per unit of explosive mass, then the total energy in the bubble oscillation is εW, and we have

$$E_k + W_p + U_i = \varepsilon W \tag{C.17}$$

The dimensionless form of (C.17) is obtained using distance and time scales

$$R_{sc} = \left(\frac{3\varepsilon W}{4\pi P_{\text{exp}}}\right)^{1/3}, \quad T_{sc} = R_{sc}\left(\frac{3\rho_f}{2P_{\text{exp}}}\right)^{1/2},$$

and is then given by

$$\tilde{R}^3\dot{\tilde{R}}^2 + \tilde{R}^3 + \mu\tilde{R}^{-3(\gamma-1)} = 1\,, \tag{C.18}$$

where $\tilde{R} \equiv R/R_{sc}$ and $\mu \equiv \kappa P_{\text{exp}}^{\gamma-1}\varepsilon^{-\gamma}/(\gamma-1)$. The maximum and minimum radii solve (C.18) with $\dot{\tilde{R}} = 0$; i.e.:

$$\tilde{R}^3 + \mu\tilde{R}^{-3(\gamma-1)} = 1\,. \tag{C.19}$$

In the case where $\mu \ll 1$, an approximation of $\tilde{R}_{\text{min}}$ and $\tilde{R}_{\text{max}}$ is given by (Best, 2002)

$$\tilde{R}_{\text{min}} \simeq \mu^{1/(3(\gamma-1))}\,, \quad \tilde{R}_{\text{max}} \simeq 1 - \mu/3 + (2-3\gamma)\mu^2/9\,, \tag{C.20}$$

and so the values of $\tilde{R}_{\text{min}}$ and $\tilde{R}_{\text{max}}$ may be obtained by numerically solving (C.19) with a fixed-point iteration method with initial guesses given by (C.20). Then, once the value of $\tilde{R}_{\text{max}}$ has been obtained, the value of ε is set so that the maximum radius R_{max} matches that observed experimentally. For TNT, the values of κ, ε and γ are approximately (Best, 2002; Arons and Yennie, 1948)

$$\gamma \simeq 1.25\,, \quad \varepsilon \simeq 2.05\ 10^6\ \text{J/kg}\,, \quad \kappa \simeq 1.45\ 10^5\ \text{SI}.$$

Remark 28 *At a water depth $\xi_{exp} = 100$ m, the order of magnitude of μ is*

$$\mu \simeq \frac{1.5\ 10^5 \cdot \left(10^6\right)^{0.25} \cdot \left(2\ 10^6\right)^{-1.25}}{0.25} \simeq 0.25\,,$$

so the approximation $\mu \ll 1$ is not exactly valid, which implies that the initial guess would not be very efficient.

Now that the initial conditions have been set, the bubble model developed in this section can be numerically computed using e.g., an explicit Runge-Kutta fourth-order algorithm (Leblond, 2007). This numerical solution notably allows to compute the pressure induced by the oscillating bubble.

C.2.5 Pressure induced by the oscillating sphere

The effect of the gas bubble on a remote submarine hull is characterised by the pressure load $p_{\mathcal{B}}$ it generates. At a given point $P(r,\theta,\psi)$ in the fluid, the usual Euler momentum equation provides, in terms of total quantities,

$$\frac{\partial \mathbf{v}}{\partial t} + (\mathbf{v}\cdot\nabla)\,\mathbf{v} = -\frac{1}{\rho_f}\nabla p + \mathbf{g}\,, \tag{C.21}$$

which becomes, since the flow is potential,

$$\nabla\left(\frac{\partial\phi}{\partial t}+\frac{1}{2}\,\mathbf{v}\cdot\mathbf{v}+\frac{1}{\rho_f}\,p-g\,\xi_P\right)=\mathbf{0}\,,$$

and so the generalised Bernoulli equation holds as

$$\frac{\partial\phi}{\partial t}+\frac{1}{2}\,\mathbf{v}\cdot\mathbf{v}+\frac{1}{\rho_f}\,p-g\,\xi_P=C(t)\,, \tag{C.22}$$

where the constant C does not depend on the spatial coordinates and the limit of (C.22) for $r\to\infty$ provides $C(t)=0$. Note that the partial time derivative $\partial/\partial t$ in (C.22) is expressed in a fixed coordinate system. In the bubble frame (r,θ,φ), the convected time derivative $\left[\frac{\partial\phi}{\partial t}\right]_{\mathcal{B}}$ is linked to $\frac{\partial\phi}{\partial t}$ through

$$\frac{\partial\phi}{\partial t}=\left[\frac{\partial\phi}{\partial t}\right]_{\mathcal{B}}-\dot{Z}\,\nabla\phi\cdot\mathbf{e}_z.$$

Hence, (C.22) is rewritten

$$\frac{p}{\rho_f}=-\left[\frac{\partial\phi}{\partial t}\right]_{\mathcal{B}}+\dot{Z}\,\frac{\partial\phi}{\partial Z}-\frac{1}{2}|\nabla\phi|^2+g\,\xi_P\,.$$

The various terms are computed using (C.8):

$$\begin{aligned}-\left[\frac{\partial\phi}{\partial t}\right]_{\mathcal{B}}&=\frac{1}{r}\frac{\partial(R^2\dot{R})}{\partial t}+\frac{1}{2r^2}\frac{\partial(R^3\dot{Z})}{\partial t}\cos\theta\,,\\ \nabla\phi\cdot\mathbf{e}_z&=\frac{\partial\phi}{\partial r}\cos\theta-\frac{1}{r}\frac{\partial\phi}{\partial\theta}\sin\theta\,,\end{aligned}$$

where it was used that $\mathbf{e}_z=\cos\theta\mathbf{e}_r-\sin\theta\mathbf{e}_\theta$. Finally, the pressure is expressed as

$$\begin{aligned}\frac{p}{\rho_f}&=g\,\xi_P+\frac{R}{r}\left(2\dot{R}^2+R\ddot{R}\right)+\frac{R^2}{2r^2}\left(3\dot{R}\dot{Z}+R\ddot{Z}\right)\cos\theta\\&\quad+\dot{Z}\left(\frac{R^2\dot{R}}{r^2}+\frac{R^3\dot{Z}}{r^3}\cos\theta\right)\cos\theta-\frac{\dot{Z}}{r}\frac{R^3\dot{Z}}{2r^2}\sin^2\theta\\&\quad-\frac{1}{2}\left(\frac{R^4\dot{R}^2}{r^4}+2\frac{R^5\dot{R}\dot{Z}}{r^5}\cos\theta+\frac{R^6\dot{Z}^2}{r^6}\cos^2\theta+\frac{R^6\dot{Z}^2}{4r^6}\sin^2\theta\right).\end{aligned} \tag{C.23}$$

What is of interest in the following is the behaviour of the pressure far from the explosion, namely for $r\gg\sup_{t>0}[R(t)]$. In that case, (C.23) provides the approximation

$$p(P(r,\theta,\psi),t)\underset{r\to\infty}{\sim}\rho_f g\,\xi_P+\frac{\rho_f}{r}\frac{\partial(R^2\dot{R})}{\partial t}=\rho_f g\,\xi_P+\frac{\rho_f}{4\pi r}\frac{\partial^2 V_{\mathcal{B}}}{\partial t^2}\,,$$

where $V_{\mathcal{B}}(t)=\frac{4\pi}{3}R^3(t)$ is the bubble volume.

C.3 Kirchhoff's retarded potential formula

In this section, it is shown that the Kirchhoff retarded potential formula (2.17)

$$4\pi\varepsilon(P)\phi(P,t)=-\int_\Gamma\left\{\frac{1}{r}\frac{\partial\phi}{\partial n}(Q,t_r)+\frac{1}{r^2}\frac{\partial r}{\partial n}\phi(Q,t_r)+\frac{1}{cr}\frac{\partial r}{\partial n}\dot{\phi}(Q,t_r)\right\}\mathrm{d}S_Q\,,$$

corresponds to the BIE (2.14)

$$\varepsilon(P)\phi(P,t) = -\int_\Gamma \left\{ \left(G(r,\cdot) \star \frac{\partial \phi}{\partial n}(Q,\cdot) \right)(t) - \left(\frac{\partial G}{\partial n}(r,\cdot) \star \phi(Q,\cdot) \right)(t) \right\} \mathrm{d}S_Q \,, \tag{C.24}$$

the fundamental solution G being given by (2.4), i.e.:

$$G(\mathbf{y},t,\mathbf{x}) \equiv G(r,t) = \frac{\delta(t-r/c)}{4\pi r} \,.$$

Going back to a mathematical formalism, we recall that a causal distribution S is a member of $\mathcal{D}'(\mathbb{R}^+)$, dual space of $\mathcal{D}(\mathbb{R}^+)$, the latter denoting the space of smooth (infinitely differentiable) functions with compact support in $\mathbb{R}^+$. We also recall that the convolution product $S \star T$ of two causal distributions is a causal distribution defined by

$$\langle S \star T, \varphi \rangle := \langle S, \langle T, \varphi(x+y) \rangle_x \rangle_y \qquad \forall \varphi \in \mathcal{D}(\mathbb{R}^+) \,,$$

where $\langle T, \varphi \rangle$ denotes the application of the distribution T on the test function φ. Then, (C.24) is to be understood in the sense of distributions, and the first term in its right-hand side is directly computed using the property of the δ distribution

$$\delta \star T = T \qquad \forall T \in \mathcal{D}'(\mathbb{R}^+) \,,$$

which leads to

$$G(r,t) \star \frac{\partial \phi}{\partial n}(Q,t) = \frac{1}{4\pi r} \frac{\partial \phi}{\partial n}(Q, t-r/c) \,. \tag{C.25}$$

For the second term in the right-hand side of (C.24), it comes:

$$\begin{aligned} \frac{\partial G}{\partial n}(r,t) \star \phi(Q,t) &= \frac{\partial r}{\partial n} \frac{\partial G}{\partial r}(r,t) \star \phi(Q,t) \\ &= \frac{\partial r}{\partial n} \left(-\frac{\delta(t-r/c)}{4\pi r^2} + \frac{1}{4\pi r} \frac{\partial L}{\partial r}(r) \right) \star \phi(Q,t), \end{aligned} \tag{C.26}$$

where

$$L : \begin{array}{ccc}]0,\infty] & \longrightarrow & \mathcal{D}'(\mathbb{R}^+) \\ r & \longmapsto & \delta(t-r/c) \,. \end{array}$$

We then compute:

$$\begin{aligned} \frac{\partial L}{\partial r}(r) \star \phi(Q,t) &= \left(\lim_{h \to 0} \frac{L(r+h) - L(r)}{h} \right) \star \phi(Q,t) \\ &= \lim_{h \to 0} \left(\frac{\delta(t-(r+h)/c) - \delta(t-r/c)}{h} \right) \star \phi(Q,t) \\ &= \lim_{h \to 0} \left(\frac{\phi(Q,t-(r+h)/c) - \phi(Q,t-r/c)}{h} \right) \\ &= \frac{\partial K_t}{\partial r}(r) \,, \end{aligned} \tag{C.27}$$

where, for any $t \in \mathbb{R}^+$,

$$K_t : \begin{array}{ccc}]0,\infty] & \longrightarrow & \mathbb{R} \\ r & \longmapsto & \phi(t-r/c) \,. \end{array}$$

Then, if $\dot{\phi}(\cdot)$ denotes the derivative of $\phi(\cdot)$ with respect to its variable,

$$\frac{\partial K_t}{\partial r}(r) = \frac{\partial (t-r/c)}{\partial r} \dot{\phi}(t-r/c) = -\frac{1}{c} \dot{\phi}(t-r/c) \,. \tag{C.28}$$

Combining all the previous results (C.25), (C.26), (C.27), (C.28), the sought equation is obtained:

$$\varepsilon(P)\phi(P,t) = -\int_\Gamma \frac{1}{4\pi r}\frac{\partial\phi}{\partial n}(Q,t_r) + \frac{\partial r}{\partial n}\left(\frac{1}{4\pi r^2}\phi(Q,t_r) + \frac{1}{4\pi cr}\dot\phi(Q,t_r)\right) \mathrm{d}S_Q\,,$$

which is meaningful in the sense of functions, and precisely corresponds to (2.17).

C.4 The acoustic breathing sphere: analytical solution

In this appendix, the (radially symmetric) analytical solution of the breathing sphere is derived in a convenient format, following classical techniques (see e.g., Junger and Feit, 1986). The notations defined in Section 2.6.1 are used. The prescribed velocity (2.41) being a linear combination of data $u(t)$ of the form $u(t) = u(t;\omega) = u_0\sin(\omega t)$ $(t \geq 0)$, it is sufficient here to consider one of such data. The Laplace transform $\bar\phi(r,s)$ of the velocity potential solves the radially symmetric wave equation

$$\frac{1}{r^2}\frac{\partial}{\partial r}\left(r^2\frac{\partial\bar\phi}{\partial r}\right) = \frac{s^2}{c^2}\bar\phi\,,$$

with boundary condition

$$\frac{\partial\bar\phi}{\partial r}(a,s) = \bar u(s) = u_0\,\frac{\omega}{s^2+\omega^2},$$

and vanishes as $r\to\infty$; a straightforward derivation yields the solution

$$\bar\phi(r,s) = -\frac{a^2\,e^{sa/c}}{1+sa/c}\,\frac{e^{-sr/c}}{r}\,\bar u(s;\omega)\,.$$

The pressure field is then

$$\bar p(r,s) = -\rho c\bar\phi(r,s) = \rho c\,\frac{sa^2}{(c+sa)r}\,e^{s(a-r)/c}\,\bar u(s;\omega)\,.$$

In particular, we have on the surface

$$\bar p(a,s) = \rho c\,\frac{sa}{c+sa}\,\bar u(s;\omega)\,. \tag{C.29}$$

The solution in the time domain can then be retrieved by inverse Laplace transformation. In particular, the pressure on the surface is

$$p(a,t) = \rho ca\mathcal{L}^{-1}\left(\frac{1}{c+sa}\right)\star\left(\dot u(t;\omega)+u(0;\omega)\right) = \rho cu_0\,\omega\,e^{-ct/a}\star\cos(\omega t)\,, \tag{C.30}$$

where $\star$ denotes the time convolution of causal functions, defined by

$$(u\star v)(t) = \int_0^t u(t-\tau)v(\tau)\,\mathrm{d}\tau = \int_0^t v(t-\tau)u(\tau)\,\mathrm{d}\tau = (v\star u)(t)\,,\quad t\geq 0\,.$$

After effecting two integrations by parts, we finally obtain

$$p(a,t) = \rho cu_0\,\frac{\kappa}{1+\kappa^2}\left(\kappa\sin(\omega t)+\cos(\omega t)-e^{-\omega t/\kappa}\right),\qquad \kappa := \frac{\omega a}{c}\,. \tag{C.31}$$

For a fixed value of ω, the analytical expressions (C.29) and (C.31) allow to assess the accuracy of the frequency-domain FM-BEM and the $\mathcal{Z}$-BEM procedure, respectively.

Remark 29 *The analytical expression of $p(a,t)$ can be obtained for any prescribed velocity $u(t)$ provided the convolution in (C.30) can be computed analytically. In particular, the accuracy of the $\mathcal{Z}$-BEM procedure presented in Chapter 2 was checked with various choices for $u(t)$, such as a combination of cosines and sines or a delayed unit step function.*

Remark 30 *The limiting case $\kappa \to \infty$ in (C.31) yields the high-frequency behaviour of the surface pressure. We find $p(a,t) = \rho c u(t) + o(\kappa^{-1})$, which is the expected behaviour for a radiation problem.*

C.5 Semi-analytical solution for a rigid infinite cylinder

This section briefly summarises the steps to obtain the semi-analytical solution for a rigid infinite cylinder, see e.g., (Iakovlev, 2004) for more details. Consider a rigid infinite cylinder, of radius a and axis $\mathbf{e}_z$, facing the wave generated by a remote underwater explosion. The plane perpendicular to the cylinder containing the explosion locus is denoted $\mathcal{P} \equiv \{z = 0\}$ (see Figure C.2).

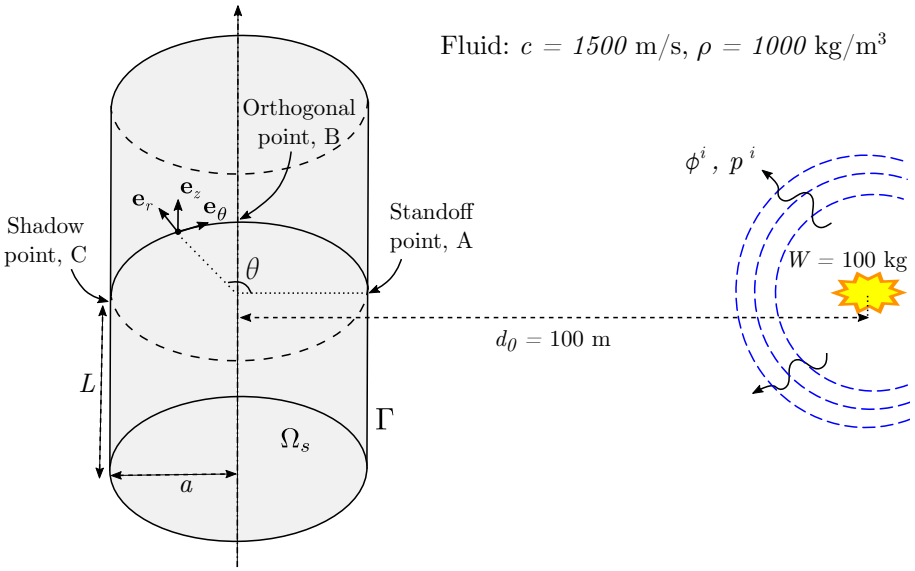

Figure C.2: Infinite cylinder facing an underwater explosion.

The problem is studied for $z \in [-L, L]$, using cylindrical coordinates (r, θ, z). Using a classical separation of variables approach in (2.1), the incident (known) and reflected (unknown) pressures are expressed as Fourier series in z and θ:

$$p^{\text{ref}}(r,\theta,z,t) = \sum_{m=0}^{\infty}\sum_{n=0}^{\infty} p^{\text{ref}}_{m,n}(r,t)\cos(n\theta)\cos(\hat{m}z)\,, \tag{C.32a}$$

$$p^{\text{inc}}(r,\theta,z,t) = \sum_{m=0}^{\infty}\sum_{n=0}^{\infty} p^{\text{inc}}_{m,n}(r,t)\cos(n\theta)\cos(\hat{m}z)\,, \tag{C.32b}$$

where $\hat{m} \equiv \pi m/L$. The above decomposition implicitly assumes the pressures to be $2L$-periodic in z. For underwater explosions, the incident pressure, obtained by expressing (2.43) in cylindrical coordinates, is not $2L$-periodic (since it is a spherical wave). To bypass this difficulty, the problem is artificially set as periodic by considering simultaneous explosions with sources along the z direction separated by a distance $2L$ and of identical

strength. Then, for a short enough duration T, the solution for $z \in [-L, L]$ results only from the source located in the $z = 0$ plane, because of the finite wave velocity. Conversely, for a chosen time interval $[0, T]$, the length L, which may be arbitrarily chosen, must be set large enough so that the solution for $z \in [-L, L]$ is not influenced by the other sources.

Using the expression of the Laplacian in cylindrical coordinates

$$\Delta f = \frac{1}{r}\frac{\partial}{\partial r}\left(r\frac{\partial f}{\partial r}\right) + \frac{1}{r^2}\frac{\partial^2 f}{\partial \theta^2} + \frac{\partial^2 f}{\partial z^2}\,,$$

the wave equation for the Laplace transforms $\bar{p}^{\mathrm{ref}}_{m,n}(\cdot, s)$ of the reflected pressure reads

$$\left[\frac{\partial^2}{\partial r^2} + \frac{1}{r}\frac{\partial}{\partial r} - \left(\frac{n^2}{r^2} + k_m^2\right)\right]\bar{p}^{\mathrm{ref}}_{m,n} = 0\,, \qquad m, n \geq 0\,, \tag{C.33}$$

with $k_m := \sqrt{\hat{m}^2 + s^2/c^2}$. The solution to (C.33) that decays as $r \to \infty$ and satisfies the boundary condition

$$\frac{\partial \bar{p}^{\mathrm{ref}}_{m,n}}{\partial r}(a, s) = -\frac{\partial \bar{p}^{\mathrm{inc}}_{m,n}}{\partial r}(a, s)$$

is given by

$$\bar{p}^{\mathrm{ref}}_{m,n}(r, s) = -\frac{1}{k_m}\frac{\partial \bar{p}^{\mathrm{inc}}_{m,n}}{\partial r}(a, s)\frac{K_n(k_m r)}{K_n'(k_m a)}\,, \tag{C.34}$$

where K_n denotes the modified Bessel function of the second kind, of order n (Olver et al., 2010, Chap. 10). The semi-analytical expression of $\bar{p}^{\mathrm{ref}}$ is then obtained by inserting (C.34) into (C.32a). The semi-analytical solution does **not** in practice provide exact values: its accuracy is often much lower than the machine precision and depends on many factors. The steps of the semi-analytical method are

- Perform a fast numerical Laplace transform of p^{inc}, or use an analytical expression;
- Decompose $\bar{p}^{\mathrm{inc}}$ as a truncated series (with finite numbers $N^{\theta}_{\mathrm{modes}}, N^{z}_{\mathrm{modes}}$ of modes);
- Compute the Fourier components of $\bar{p}^{\mathrm{ref}}$ using (C.34);
- Reconstruct $\bar{p}^{\mathrm{ref}}$ using the truncated Fourier basis;
- Perform a fast numerical inverse Laplace transform to get p^{ref} in the time domain (Brančik, 1999).

Numerical errors arise from both the fast numerical inverse Laplace transform and the fact that the Fourier basis is truncated. While not yielding an exact solution for those reasons, the semi-analytical method provides results that are accurate enough to serve as a reference for checking the validity (if not the precision) of the $\mathcal{Z}$-BEM procedure on this configuration.

Remark 31 *The incident pressure given by (2.43) is discontinuous in time, and a Gibbs phenomenon arises near that discontinuity. To avoid nonphysical oscillations, a typical procedure, implemented in the Naval Group code that evaluates the above solution, consists in setting to zero quantities (e.g., $p^{ref}(\mathbf{x}, t)$) that are known to vanish due to causality. This improves the overall quality of the results.*

Appendix D

Summary tables for the FSI problem of Section 3.5

This appendix gathers summary tables for the FSI problem studied in Section 3.5, providing information on the numerical methods used, and the numerical parameter values. For details on Abaqus®, code_aster® or LS-DYNA®, refer to (Dassault Systèmes SIMULIA, 2017), (Code_Aster Open Source, 2020), (Livermore Software Technology Corp., 2020), respectively.

$\mathcal{Z}$-BEM/Abaqus® FEM/FEM	Semi-analytical	code_aster® FEM/FEM	LS-DYNA® FEM/USA BEM
Method			
$\mathcal{Z}$-BEM to get p^{ref} from p^{inc}, then FEM/FEM to solve the fluid-structure interaction.	Semi-analytical approach to solve the 2D fluid-structure interaction.	FEM/FEM to solve the fluid-structure interaction.	USA-BEM to solve the fluid part of the problem, and FEM for the structure part.
Monolithic/iterative			
Once p^{Ref} is obtained from the $\mathcal{Z}$-BEM, it becomes an input for the monolithic FEM/FEM solving.	Modal decomposition. Fluid and structure components obtained for each mode, then reconstruction on a truncated basis.	Monolithic FEM/FEM solving.	Iterative procedure. Successive solving of the BEM-fluid and the FEM-structure equations at each time step.
Equations solved			
Fluid: 3D linear wave equation. Structure: any equation, related to the modelling.	Fluid: 2D linear wave equation. Structure: 2D equations of the Love-Kirchhoff shell theory.	Fluid: 3D linear wave equation. Structure: any equation, related to the modelling.	Fluid: approximation of the 3D linear wave equation, DAA1 or DAA2. Structure: any equation, related to the modelling.
Solvers			
$\mathcal{Z}$-BEM: FM-BEM with Krylov iterative solver. Abaqus® implicit solver. Abaqus® explicit: diagonal lumped mass matrix.	Use of Bessel's functions to obtain an analytical form of the solution for each mode. When considering equipment, small linear systems are solved by computing an inverse matrix (not too costly).	MUMPS implicit solver.	Standard BEM and LS-DYNA® solvers.
Time-stepping schemes			
$\mathcal{Z}$-BEM: related to the one chosen for the CQM, typically bdf2. Abaqus® implicit: HHT with $\alpha = -0.05$ by default. Abaqus® explicit: central difference + small damping.	Related to the one chosen for the CQM, typically bdf2.	θ-Wilson, or Newmark with coefficients set to introduce some numerical damping, or HHT.	Those available in LS-DYNA®.

Table D.1: Comparison between the three used methods and LS-DYNA®/USA. Part I: modelling.

$\mathcal{Z}$-BEM/Abaqus® FEM/FEM	Semi-analytical	code_aster® FEM/FEM	LS-DYNA® FEM/USA BEM
Smoothness of the input pressure			
$\mathcal{Z}$-BEM: handle discontinuous inputs. Abaqus® explicit: the input p^{Ref} must be smoothed, either using a (Butterworth) filter or with common UNDEX procedure (with $\tau/10$). Abaqus® implicit: need to use a time-stepping scheme that naturally filters the signal.	Handle discontinuous inputs. The $\mathcal{Z}$-transform is used to reformulate the problem in the frequency domain, rather than the Laplace transform. It then reduces Gibbs phenomena.	Need to use a time-stepping scheme that naturally filters the signal to improve the results.	Need to smooth the input signal with the common UNDEX procedure (with $\tau/10$).
Hypotheses on the deformations			
$\mathcal{Z}$-BEM: naturally solves the problem in the mobile referential following the rigid structure motion, so allows rigid displacement (as long as p^{inc} remains correct) and small strains. Abaqus® implicit: small strains and small rigid displacement. Abaqus® explicit: no limitation. Elasticity or plasticity.	Small strains, possibly large 2D rigid displacement. Elasticity only.	Small strains and small rigid displacement. Elasticity only.	USA BEM: naturally solves the problem in the mobile referential following the rigid structure motion, so allows rigid displacement (as long as p^{inc} remains correct) and small strains. LS-DYNA®: no limitation a priori. Elasticity or plasticity.
Far-field explosions			
Valid as long as the model used for p^{inc} is correct. So near- and far-field explosions.	Only far-field explosions, because the 2D solution is representative of the 3D behaviour only when the wave front is almost cylindrical (not spherical).	Valid as long as the model used for p^{inc} is correct. So near- and far-field explosions.	Valid as long as the model used for p^{inc} is correct. So near- and far-field explosions.
Sea bed and water surface			
The $\mathcal{Z}$-BEM procedure could take into account the sea bed or the water surface using the image technique. Abaqus®: theoretically possible but not yet tested.	Not implemented in the procedure.	Not implemented in the procedure.	Can be taken into account. The sea bed is a wall (pure reflections).

Table D.2: Comparison between the three used methods and LS-DYNA®/USA. Part II: hypotheses.

$\mathcal{Z}$-BEM/Abaqus® FEM/FEM	Semi-analytical	code_aster® FEM/FEM	LS-DYNA® FEM/USA BEM
Structure model complexity			
$\mathcal{Z}$-BEM: no limitation. Can handle full-scale submarine. Abaqus®: no limitation other than the number of DOFs.	Shell theory. Stiffened shell with equivalent model. Use of a spring-mass system to model an equipment fixed on the shell.	No limitation other than the number of DOFs.	USA-BEM: standard BEM, so important limitation on the number of DOFs. LS-DYNA®: no limitation other than the number of DOFs.
Structure shape			
Any.	Only cylinders. Infinite in theory, large in practice (causality).	Any.	Only cylinders or spheres, because of the DAA approximation of the USA-BEM.
Complexity			
$\mathcal{Z}$-BEM: - space: $O(N \log N)$ - time: $O(1)$ Abaqus®: - space: depends on the structure model, for surface shells, 5 DOFs per nodes, for volume mesh, 1 DOF per node - time: $O(M)$	- time: O(M) For complex model (equipment), the complexity regarding the number of spatial modes N^θ is related to the way the linear system is solved (at worse: $(N^\theta)^3$). Anyway, $N^\theta \sim 50$, so the whole time of the procedure does not exceed a few minutes.	- space: the complexity of the LU-factorisation of a sparse matrix - time: $O(MN^2)$	USA-BEM: - space: $O(N^2)$ - time: $O(M)$ LS-DYNA®: - space: depends on the structure model - time: $O(M)$
Dimensions of the structure			
Can handle full-scale industrial cases with acceptable time computation and result precision. For a fixed mesh size, if the structure dimensions are multiplied by 2, the number of elements for the fluid is multiplied by 4. Same for the structure.	No limitation, because 2D model.	Difficult to handle full-scale industrial cases with acceptable time computation and result precision. For a fixed mesh size, if the structure dimensions are multiplied by 2, the number of elements for the fluid is multiplied by 4. Same for the structure.	Limitations coming from the standard BEM of USA prevent from dealing with full-scale industrial cases with acceptable time computation and result precision. It nonetheless provides a good order of magnitude with an acceptable time computation.

Table D.3: Comparison between the three used methods and LS-DYNA®/USA. Part III: limitations.

$\mathcal{Z}$-BEM/Abaqus® FEM/FEM	Semi-analytical	code_aster® FEM/FEM	LS-DYNA® FEM/USA BEM
Type of elements			
$\mathcal{Z}$-BEM: P0, P1 and P2 triangle elements. Abaqus® explicit: linear (reduced) shell elements, triangles and quadrangles, linear tetra and hexa fluid elements. Abaqus® implicit: linear and quadratic shell elements, triangles or quadrangles, linear and quadratic tetra and hexa fluid elements.	2D discretisation related to the θ discretisation.	Linear and quadratic shell elements, triangles and quadrangles, linear and quadratic tetra and hexa fluid elements. At the interface Γ, the fluid mesh and the structure mesh must be compatible.	Any element type available in LS-DYNA®.
Mesh generation			
$\mathcal{Z}$-BEM: 2D uniform mesh. Abaqus® structure: 2D or 3D meshes. Abaqus® fluid: 3D mesh refined only near Γ. Difficult to generate when dealing with complex interface shapes Γ.	No mesh.	Structure: 2D or 3D meshes. Fluid: 3D mesh refined only near Γ. Difficult to generate when dealing with complex interface shapes Γ.	Structure: 2D or 3D meshes. Fluid: 2D mesh.

Table D.4: Comparison between the three used methods and LS-DYNA®/USA. Part IV: some numerical characteristics.

$\mathcal{Z}$-BEM/Abaqus® FEM/FEM	code_aster® FEM/FEM
Fluid	
$\mathcal{Z}$-BEM: P1 triangle elements. Most refined mesh: uniform mesh size $h \approx 0.027$ m, 10^6 DOFs. Abaqus® explicit: linear tetra elements (AC3D4), mesh refined near Γ, and near the standoff point, where $h \approx 0.04$ m. Fluid domain truncated, 6 m of water encapsulates the shell. Near Γ_∞, $h \approx 1$ m. See Figure 3.5. Abaqus® implicit: quadratic tetra elements (AC3D10), mesh refined near Γ, and near the standoff point, where $h \approx 0.08$ m. The fluid domain is truncated so that 6 m of water encapsulates the structure. Near Γ_∞, $h \approx 2$ m. On Γ_∞, the absorbing conditions are the cylindrical or spherical acoustic impedances of Abaqus®.	Quadratic tetra elements, mesh refined near Γ, where $h \approx 0.1$ m. Model 3D_FLUID. The fluid domain is truncated so that 7.5 m of water encapsulates the structure. Near Γ_∞, $h \approx 5$ m. On Γ_∞, the absorbing condition is $BGT1$ (Bayliss et al., 1982; Leblond and Sigrist, 2016).
Structure	
Abaqus® explicit: linear triangle shell elements (S3), 5 integration points in the thickness. Mesh refined near Γ, and near the standoff point, where $h \approx 0.03$ m. Abaqus® implicit: linear triangle shell elements (S3), 5 integration points in the thickness. Mesh refined near Γ, and near the standoff point, where $h \approx 0.06$ m.	Quadratic triangle shell elements. Model COQUE_3D. Uniform mesh with $h \approx 0.1$ m.

Table D.5: Numerical parameter values for the case of validation. Part I.

$\mathcal{Z}$-BEM/Abaqus® FEM/FEM	code_aster® FEM/FEM
Time-stepping scheme	
$\mathcal{Z}$-BEM: bdf2. $T = 20$ ms, $dt = 2\ 10^{-3}$ ms.	Newmark with $\gamma = (1-\alpha)/4$ and $\beta = 1/2-\alpha$, with
Abaqus® explicit: default central difference, $T = 20$ ms, $dt = 1\ 10^{-3}$ ms.	$\alpha = -0.2$. $dt = 1.6\ 10^{-2}$ ms, $T = 8$ ms.
Abaqus® implicit: HHT with $\alpha = -0.05$, $T = 5$ ms, $dt = 10^{-2}$ ms.	

Table D.6: Numerical parameter values for the case of validation. Part II.

For the semi-analytical approach, the number of spatial nodes of the truncated basis is set to $N^\theta = 65$, and $T = 20$ ms, $dt = 2\ 10^{-3}$ ms.

Apart from the semi-analytical approach, the meshes of each procedure have been chosen so that the computations last around 5 days. For instance, for the $\mathcal{Z}$-BEM/Abaqus® FEM/explicit FEM procedure, it leads to around 10^7 tetra linear elements for the fluid FE mesh, and the structure shell has around $3\ 10^5$ nodes (with 5 DOFs per node). To improve the results, the fluid and structure FE meshes have been refined near the standoff point. A screenshot of the used meshes illustrates these refinements, Figure 3.5.

Fondation mathématique
FMJH
Jacques Hadamard

Titre : Modélisation du couplage entre une structure et un fluide lors d'une explosion sous-marine en champ lointain

Mots clés : Interaction fluide-structure ; explosion sous-marine ; méthode des éléments de frontière accélérée ; couplage FEM/BEM ; méthode de quadrature de convolution ; approximation haute fréquence

Résumé : Les sous-marins militaires doivent résister aux sollicitations induites par une explosion sous-marine. Pour s'en assurer, la simulation numérique est d'une importance capitale, compte tenu du coût très élevé des campagnes expérimentales. Une explosion sous-marine lointaine est un événement complexe qui a deux effets distincts : elle libère une onde de choc, puis crée une bulle de gaz oscillante qui pousse une grande quantité d'eau plus lentement. Les deux phénomènes ont des caractéristiques et des échelles de temps assez différentes. Dans ce travail, nous supposons que l'explosion est suffisamment éloignée pour (i) que la présence du navire affecte peu l'explosion, et (ii) permettre une séparation temporelle des deux phénomènes, tels que perçus par le navire. Dans ces conditions, notre objectif est de concevoir, implémenter (dans le cadre du calcul haute performance) puis valider une méthodologie de simulation numérique pour le problème d'interaction fluide-structure prenant en compte les deux phénomènes. Pour ce faire, nous commençons par étudier les deux perturbations en l'absence du sous-marin, pour déduire une modélisation et des méthodes numériques adaptées. Nous développons ensuite une procédure éléments de frontière (BEM) accélérée, basée sur une combinaison de la méthode de quadrature de convolution avec une approximation haute fréquence empirique originale. Plus largement, cette procédure permet de simuler efficacement des problèmes transitoires rapides 3D de propagation d'ondes en milieu non-borné, et offre une complexité très favorable : $O(1)$ par rapport à la discrétisation temporelle et $O(N \log N)$ par rapport à la discrétisation spatiale. Enfin, nous mettons en place des stratégies performantes de couplage éléments finis/éléments de frontière (FEM/BEM) pour la phase d'interaction fluide-structure de l'onde de choc (acoustique linéaire) et celle de la bulle de gaz (écoulements incompressibles). La procédure globale, validée sur des problèmes académiques, fournit des résultats très prometteurs sur des cas industriels réalistes.

Title: Modelling the fluid-structure coupling caused by a far-field underwater explosion

Keywords: Fluid-structure interaction; underwater explosion; fast boundary element method; FEM/BEM coupling; convolution quadrature method; high frequency approximation

Abstract: Submarines must withstand the effects of rapid dynamic loads induced by underwater explosions. Due to the very high cost of experimental campaigns, numerical simulations are very important. A remote underwater explosion is a complex event that has two distinct effects: it sends a shock wave, then creates an oscillating gas bubble that sets water in slower motion. The two phenomena have quite different characteristics and time scales. In this work, we consider remote enough underwater explosions so that (i) the presence of the submarine only marginally affects the explosion, and (ii) there is a temporal separation of the two phenomena, as experienced by the ship. Under these conditions, our overall goal is to design, implement (in the context of high performance computing) then validate a computational methodology for the fluid-structure interaction problem, taking into account both phenomena. With this aim, we first study the two perturbations without considering the submarine, to propose appropriate modelling and numerical methods. Then, we design a fast boundary element (BEM) procedure, based on the combination of the convolution quadrature method and an original empirical high frequency approximation. The procedure allows to efficiently simulate 3D rapid transient wave propagation problems set in an unbounded domain, and shows advantageous complexity: $O(1)$ in regards to the time discretisation and $O(N \log N)$ for the spatial discretisation. Finally, we implement adequate finite element/boundary element (FEM/BEM) coupling strategies for the shock wave fluid-structure interaction phase (linear acoustics) and that of the gas bubble (incompressible flow). The overall procedure, validated on academic problems, provides very promising results when applied on realistic industrial cases.

Institut Polytechnique de Paris
91120 Palaiseau, France

INSTITUT POLYTECHNIQUE DE PARIS